OPTICAL TECHNIQUES FOR THE INVESTIGATION OF A MECHANICAL ROLE FOR FRMD6/WILLIN IN THE HIPPO SIGNALLING PATHWAY

Frances Elizabeth Goff

A Thesis Submitted for the Degree of PhD
at the
University of St Andrews

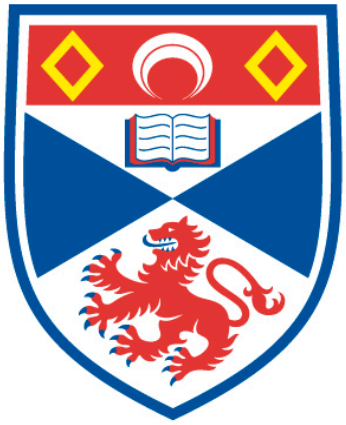

2019

Optical techniques for the investigation of a mechanical role for FRMD6/Willin in the Hippo signalling pathway

Frances Elizabeth Goff

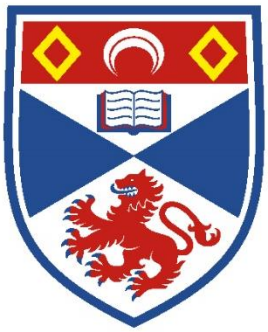

University of St Andrews

This thesis is submitted in partial fulfilment for the degree of

Doctor of Philosophy (PhD)

at the University of St Andrews

January 2019

Declarations

Candidate's declaration

I, Frances Elizabeth Goff, do hereby certify that this thesis, submitted for the degree of PhD, which is approximately 50,000 words in length, has been written by me, and that it is the record of work carried out by me, or principally by myself in collaboration with others as acknowledged, and that it has not been submitted in any previous application for any degree.

I was admitted as a research student at the University of St Andrews in September 2014.

I received funding from an organisation or institution and have acknowledged the funder(s) in the full text of my thesis.

Date Signature of candidate

Supervisor's declaration

I hereby certify that the candidate has fulfilled the conditions of the Resolution and Regulations appropriate for the degree of PhD in the University of St Andrews and that the candidate is qualified to submit this thesis in application for that degree.

Date Signature of supervisor

Permission for publication

In submitting this thesis to the University of St Andrews we understand that we are giving permission for it to be made available for use in accordance with the regulations of the University Library for the time being in force, subject to any copyright vested in the work not

being affected thereby. We also understand, unless exempt by an award of an embargo as requested below, that the title and the abstract will be published, and that a copy of the work may be made and supplied to any bona fide library or research worker, that this thesis will be electronically accessible for personal or research use and that the library has the right to migrate this thesis into new electronic forms as required to ensure continued access to the thesis.

I, Frances Elizabeth Goff, have obtained, or am in the process of obtaining, third-party copyright permissions that are required or have requested the appropriate embargo below.

The following is an agreed request by candidate and supervisor regarding the publication of this thesis:

Printed copy

Embargo on all of print copy for a period of 2 years on the following ground(s):

- Publication would preclude future publication

Supporting statement for printed embargo request

Research in this thesis is due for future publication

Electronic copy

Embargo on all of electronic copy for a period of 2 years on the following ground(s):

- Publication would preclude future publication

Supporting statement for electronic embargo request

Research in this thesis is due for future publication

Title and Abstract

- I agree to the title and abstract being published.

Date Signature of candidate

Date Signature of supervisor

Underpinning Research Data or Digital Outputs

Candidate's declaration

I, Frances Elizabeth Goff, hereby certify that no requirements to deposit original research data or digital outputs apply to this thesis and that, where appropriate, secondary data used have been referenced in the full text of my thesis.

Date Signature of candidate

Abstract

The mammalian hippo signalling pathway controls cell proliferation and apoptosis via transcriptional co-activators YAP and TAZ, and as such is a key regulator of organ and tissue growth. Multiple cellular components converge in this pathway, including the actin cytoskeleton, which is required for YAP/TAZ activity. The precise mechanism by which the mechanical actomyosin network regulates Hippo signalling, however, is unknown.

Optical methods provide a non-invasive way to image and study the biomechanics of cells. In the past two decades, super-resolution fluorescence microscopy techniques that break the diffraction limit of light have come to the fore, enabling visualisation of intracellular detail at the nanoscale level. Optical trapping, on the other hand, allows precise control of micron-sized objects such as cells. Here, super resolution structured illumination microscopy (SIM) and elastic resonator interference stress microscopy (ERISM) were used to investigate a potential role for the FERM-domain protein FRMD6, or Willin, in the mechanical control of the Hippo pathway in a neuronal cell model. A double optical trap was also integrated with the Nikon-SIM with the aim of cell stretching.

Willin expression was shown to modify the morphology, neuronal differentiation, actin cytoskeleton and forces of SH-SY5Y cells. Optical trapping from above the SIM objective, however, was demonstrated to be ineffective for manipulation of adherent cells. The results presented here indicate a function for Willin in the assembly of actin stress fibres that may be the result of an interaction with the Hippo pathway regulator AMOT. Further investigation, for example by direct cell stretching, is required to elucidate the exact role of Willin in the mechanical control of YAP/TAZ.

Acknowledgements

I would firstly like to thank my supervisors, Professor Kishan Dholakia and Professor Frank Gunn-Moore, for their support and guidance throughout the duration of my PhD. I would also like to thank Dr Jonathan Nylk – without your expertise, tuition and encouragement, this endeavour would not have been possible. Thank you also for your patience. Thank you too to Dr Fatma Zohra Bioud for your helpful discussion and practical advice during the early days of my optical trapping experiments.

I would like to thank Dr Nils Kronenberg for your collaboration on the ERISM investigation. It was a pleasure to work with you.

To the physics workshop engineers who produced parts for my optomechanical setups – thank you for all of your time and help.

This research was kindly funded by the EPSRC.

I would like to thank Dr Andrew Lunel for helping me set up in the lab and for all of the laughs, Dr Patrick Guest for helping me to become a better scientist, Dr Laura Aitken for the pep talks, and everybody in labs 248/9 for your friendship. Best of luck to the newest PhD students, Vanya Metodieva and Elsa Yu – you can do it!

I would like to thank my parents for all the opportunities you have given me, for which I am incredibly grateful. Special thanks to my father for having always instilled in me a sense of scientific curiosity. Thank you to friends, old and new, for all the good times and bearing with me for the past four years.

Lastly, I would like to thank my fiancé Dr Luke Thompson – you were and are my rock.

Contents

List of figures

List of tables

Abbreviations

2D – Two-dimensional

3D – Three-dimensional

AJ – Adherens junction

AJC – Apical junctional complex

AMOT – Angiomotin

AMOTL1 – Angiomotin like-1

AMOTL2 – Angiomotin like-2

AMP – Adenosine monophosphate

AMPK – AMP-activated protein kinase

ANOVA – Analysis of variance

aPKC – Atypical protein kinase C

ATP – Adenosine triphosphate

BCA – Bicinchonic acid

BDNF – Brain-derived neurotrophic factor

BSA – Bovine serum albumin

CAP – Cyclase-associated protein

CC – Coiled-coil

CCD – Charge-coupled device

CCND1 – Cyclin D1

CIP – Contact inhibition of cell proliferation

CP – Capping protein

CRB – Crumbs

CRB3 – Crumbs isoform 3

CTGF – Connective tissue growth factor

cw – Continuous wave

DM – Dichroic mirror

DMEM/F12 – Dulbecco's Modified Eagle Medium: Nutrient Mixture F-12

DNA – Deoxyribonucleic acid

ECM – Extracellular matrix

EGF – Epidermal growth factor

EGFR – Epidermal growth factor receptor

EMCCD – Electron multiplying CCD

EMT – Epithelial-mesenchymal transition

Ena – Enabled

ER – Endoplasmic reticulum

ERISM – Elastic resonator interference stress microscopy

Ex – Expanded

F-actin – Filamentous actin

FACS – Fluorescence-activated cell sorting

FAK – Focal adhesion kinase

FBM – FERM-binding motif

FERM – 4.1 Ezrin Radixin Moesin

FISH – Fluorescence in situ hybridization

FOXM1 – Forkhead box M1

FRET – Fluorescnce resonance energy transfer

FRMD6 – FERM domain-containing protein 6

FSS – Fluid shear stress

FWHM – Full-width at half-maximum

G-actin – Globular actin

GPCR – G-protein-coupled receptor

GPER – G protein-coupled estrogen receptor

GRIN – Gradient-index

GTPases – Guanosine triphosphatases

HEK – Human embryonic kidney

Hpo – Hippo

Hppy – Happyhour

HRP – Horseradish peroxidase

HWP – Half-wave plate

I^2M – Image interference microscopy

I^3 – Incoherent interference illumination

ICC – Immunocytochemistry

Ig – Immunoglobulin

IP – Immunoprecipitation

IR – Infrared

ISIM – Instant SIM

JFR – Juxta-FERM domain region

JNK– c-Jun N-terminal kinase

Kibra – Kidney/brain protein

LATS – Large tumour suppressor

LATS1/2 – Large tumour suppressor 1/2

LB – Luria broth

LIFR – Leukemia inhibitory factor receptor

LIMD1 – LIM domain-containing protein 1

LKB1 – Liver kinase B1

LLSM – Lattice light sheet microscopy

LPA – Lysophosphatidic acid

Lrp4 – Lipoprotein-related receptor-4

MAP4K – Mitogen-activated protein kinase kinase kinase kinase

Mats – Mob as tumour suppressor

MCD – Minimal change disease

MOB1A/B – Mps one binder kinase activator 1A/B

MSC – Mesenchymal stem cell

MSIM – Multifocal SIM

Msn – Misshapen

MST1/2 – Mammalian sterile like-20 kinases 1/2

MuSK – Muscle-specific kinase

N-SIM – Nikon-structured illumination microscope

NA – Numerical aperture

ND – Neutral density

NES – Nuclear export signal

NF2 – Neurofibromatosis type 2

NGF – Nerve growth factor

NL-SIM – Nonlinear SIM

NOS1AP – Nitric oxide synthase 1 adaptor protein

NSOM – Near-field scanning optical microscopy

OS-SIM – Optical sectioning SIM

OTF – Optical transfer function

PAINT – Point accumulation for imaging in nanoscale topography

PALM – Photoactivated localization microscopy

PA NL-SIM – Patterned-activation nonlinear SIM

PAR – Protease-activated receptor

PATJ – PALS-associated tight junction protein

PBS – Phosphate-buffered saline/polarizing beamsplitter

PBS-T – Phosphate-buffered saline-Triton X-100

PCA – Principal component analysis

PDZ – Post-synaptic density 95/Discs Large/zonula occludens-1 domain

PDZ-BM – PDZ binding motif

PFA – Paraformaldehyde

PH – Pleckstrin homology

PKC – Protein kinase C

PML – Promyelocytic leukaemia

PSD – Power spectral density

PSF – Point-spread function

PTB – Phosphotyrosine binding

PTPN14 – Non-receptor tyrosine phosphatase 14

PVDF – Polyvinylidene fluoride

qPCR – Quantitative polymerase chain reaction

QPD – Quadrant photodiode

RA – Retinoic acid

RASSF – Ras association domain family

RBC – Red blood cell

RESOLFT – Reversible saturable/switchable optical fluorescence transitions

RNA – Ribonucleic acid

RNAP – Ribonucleic acid polymerase

ROCK – Rho-associated protein kinase

ROS – Reactive oxygen species

RPM – Revolutions per minute

RT-DC – Real-time deformability cytometry

RT-PCR – Real-time polymerase chain reaction

S – Serine

S1P – Sphingosine 1-phosphate

SARAH – SAV-RASSF-HPO

Sav – Salvador

SAV1 – Salvador homologue 1

Sd – Scalloped

SDD – Slit diaphragm density

SDS – Sodium dodecyl sulphate

SDS-PAGE – Sodium dodecyl sulphate-polyacrylamide gel electrophoresis

SH3 – Src homology 3

SH3-BM – Src homology 3-binding motif

ShRNA – Short-hairpin RNA

ShScr – Scrambled shRNA

ShWillin – ShRNA targeting Willin mRNA

SIM – Structured illumination microscopy/microscope

SLM – Spatial light modulator

SM – Single mode

SMLM – Single molecule localization microscopy

SNR – Signal-to-noise-ratio

SOC – Super Optimal broth with Catabolite repression

SRRF – Super-resolution radial fluctuations

SSIM – Saturated SIM

STED – Stimulated emission depletion

STORM – Stochastic optical reconstruction microscopy

T – Threonine

TAD – Transcriptional activation domain

TAZ – Transcriptional co-activator with PDZ-binding motif

TBD – TEAD-binding domain

TBS – Tris-buffered saline

TBS-T – TBS-Tween

TBX5 – T-box transcription factor 5

TEAD – TEA-domain

TFM – Traction force microscopy

TGFβ – Transforming growth factor beta

Tgi – Tondu domain-containing growth inhibitor

TIRF – Total internal reflection fluorescence

TJ – Tight junction

TPA – *12-O-Tetradecanoylphorbol-13-acetate*

UPR – Unfolded protein response

USS – Unidirectional shear stress

VASP – Vasodilator-stimulated phosphoprotein

VGLL4 – Vestigial-like 4

WB – Western blotting

Wts – Warts

YAP – Yes-associated protein

Yki – Yorkie

ZO – Zonula occludens

1 Introduction

1.1 Preface

Since the discovery of DNA, a concerted effort was invested in the second half of the 20th Century in unravelling the biochemical workings of the cell. It was perhaps overlooked that cells exist not only in a chemical environment, but also one that is three-dimensional, and are therefore subjected to pulling and pushing from neighbouring cells as well as forces from the extracellular matrix (ECM) and fluid flow.

How a cell senses mechanical forces and converts them into a biochemical response is termed mechanotransduction (Alenghat & Ingber, 2002). One well-known example is the bending of stereocilia in the hair cells of the inner ear by sound waves, causing mechanically-gated ion channels to open and activate downstream signalling pathways (Chalfie, 2009); another is the detection of blood flow-generated friction by mechanosensors on the surface of endothelial cells, triggering vascular adaptive responses (Hsieh *et al*., 2014). But in fact, mechanical forces affect all cells, and modulate such fundamental functions as proliferation, migration and differentiation (Dupont *et al*., 2011; Lauffenburger & Horwitz, 1996; Engler *et al*., 2006). Consequently, defects in mechanotransduction are implicated in a diverse range of diseases, from hearing loss to atherosclerosis and cancer (Jaalouk & Lammerding, 2009). There is a need therefore to dissect the complexity of biomechanical pathways to fully understand the pathology of these disorders and identify potential drug targets.

Several principal cellular mechanosensors have been identified, including the actin cytoskeleton and focal adhesion complexes (Figure 1.1). However, many of the individual proteins and molecules involved in mechanotransduction are yet to be elucidated, perhaps due to the nature of the fundamental question of how cells respond in a *biochemical* manner to *physical* forces? The answers must therefore exist at the interface of biology and physics, and therein lies the motivation behind this thesis.

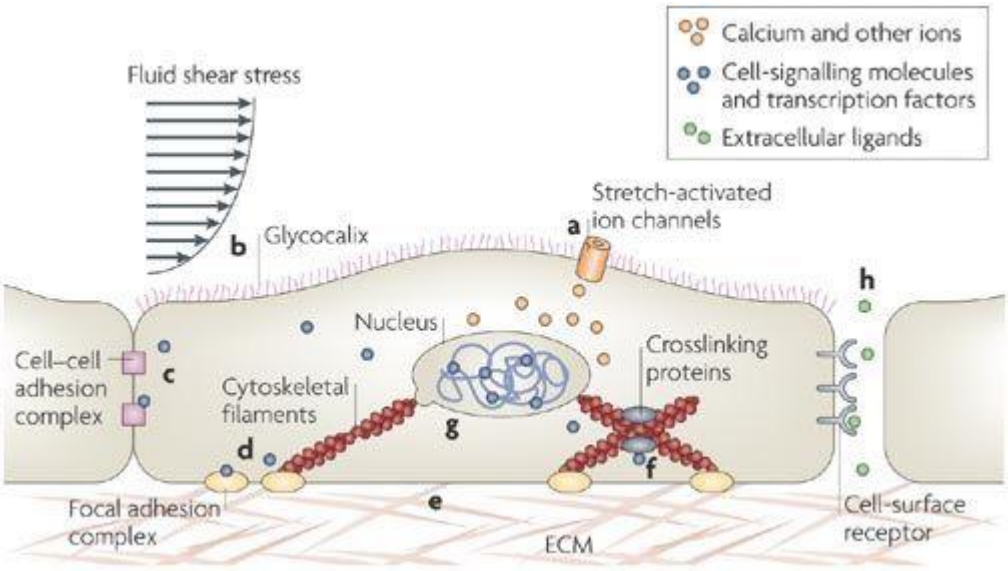

Figure 1.1 Schematic of mechanosensors within a representative cell. **(a)** Stretch-activated ion channels open in response to membrane tension, causing influx of ions e.g. Ca^{2+} into the cell (Ranade, Syeda & Patapoutian, 2015). **(b)** Glycoproteins on the surface of endothelial cells sense and respond to fluid shear stress (Pahakis *et al.*, 2007). **(c)** Cell-cell junctions and **(d)** focal adhesion complexes that link cells to the ECM mediate mechanotransduction via the cytoskeleton. **(e)** ECM proteins e.g. Agrin act as transducers of matrix rigidity and regulate intracellular signalling pathways (Chakraborty *et al.*, 2017). **(f)** Actin cross-linking proteins e.g. alpha-actinin localize to stress fibres and co-ordinate cell responses (Tseng *et al.*, 2005). **(g)** Mechanical forces from the ECM are relayed to the nucleus and influence chromatin organisation and gene transcription (Cho, Irianto & Discher, 2017). **(h)** Membrane receptors e.g. G-protein-coupled receptors (GPCRs) act as mechanosensors of fluid flow at the cell surface (Chachisvilis, Zhang & Frangos, 2006). Figure adapted from Jaalouk & Lammerding, 2009.

Optical techniques offer many advantages for biochemical and biomechanical studies: light microscopy can be used to observe living specimens, as opposed to electron microscopy which requires a vacuum; fluorescent light microscopy enables studies of the dynamics of molecules and structures of interest labelled with specific "tags"; and light is relatively non-toxic to live samples. Due to the diffraction of light waves, the resolution of a light microscope is limited to approximately 200nm. Many subcellular structures are smaller than this and therefore cannot be resolved by conventional light microscopy. Confocal microscopy uses a pinhole to remove out-of-focus light, thereby achieving optical sectioning and lending a 1.4x improvement in lateral resolution (Wilson, 2011). The arrival of a number of super-resolution fluorescence microscopy techniques in the last decade, however, has truly shattered the diffraction limit of the light microscope, paving the way for imaging at the protein and molecular level (Sydor *et al.*, 2015).

In addition to super-resolution microscopy, optical techniques that measure and apply mechanical forces to biological samples have been developed. Optical trapping is a powerful tool that allows particles on the order of a few microns to be held in the focus of a laser beam and moved at will or used as handles to manipulate other objects (Neuman & Block, 2004; Dholakia, Reece & Gu, 2008). Optical traps have been used for various innovative biomechanical studies at both the cellular and single-molecule level, for instance the detection of cancer cells by optical deformation (Guck *et al*., 2005) and measurement of forces generated by RNA polymerase during real-time DNA transcription (Davenport *et al*., 2000). Forces exerted by cells on the ECM can be characterised by substrate deformation using traction force microscopy (TFM) (Style *et al*., 2014) or deflections of elastic micropillars (Schoen *et al*., 2010). Elastic resonator interference stress microscopy (ERISM) has recently emerged as a novel method for yielding cell stress maps that allows for long-term experiments and post-imaging assays e.g. immunocytochemistry (Kronenberg *et al*., 2017). A number of studies have combined mechanical manipulation techniques with super-resolution microscopy (Heller *et al*., 2013; Diekmann *et al*., 2016; Colin-York, Eggeling & Fritzsche, 2017). However, tools for the biologist to examine biomechanical pathways in real-time are still lacking.

This is a revolutionary time for biophysics, which has already exposed the mechanics of molecular motors (Block, Goldstein & Schnapp, 1990), made vast leaps for neuroimaging (Livet *et al*., 2007), and revealed the true complexity of proteins present in our cells (Wilhelm *et al*., 2014). Disentangling the web of mechanotransduction seems a daunting task, but we are now in a better position than ever to do so.

1.2 Synopsis

This thesis examines the question of whether the protein Willin is involved in the Hippo pathway in a mechanical and neurological context. Optical techniques including super-resolution structured illumination microscopy (SIM) are used to answer this question. A double optical trap for integration with the commercial Nikon-SIM (N-SIM), designed for simultaneous manipulation and imaging of neuronal model cells expressing live fluorescent probes, is described. In addition, the effects of Willin expression on the cytoskeleton and cell forces are examined.

Chapter 2 describes the Hippo signalling pathway, a key regulator of tissue growth, and its biochemical and mechanical regulators, including Willin. Chapter 3 discusses super-resolution

microscopy techniques, including SIM, and the theory and practical biological applications of optical trapping. Chapter 4 details the biological methods used in this thesis. Chapter 5 introduces SIM for use in two different biological studies: investigation of the effect of Willin expression on neuronal differentiation, and the quantitative diagnosis of nephrotic syndrome. Chapter 6 discusses the construction and characterisation of a double optical trap designed for integration with the N-SIM. Chapter 7 investigates the relationship between Willin and the actin cytoskeleton, and Chapter 8, the effect of Willin expression on cellular forces using ERISM.

2 The Hippo signalling pathway: biochemical and mechanical regulators

2.1 Introduction

The development of multicellular organisms to the correct size necessitates a fine balance between cell division and death. Over the past two decades, the Hippo signalling pathway has emerged as a key mediator of cell proliferation, responsible for limiting tissue and organ growth (Harvey & Tapon, 2007; Pan, 2010; Zhao, Tumaneng & Guan, 2011; Yu, Zhao & Guan, 2015). As such, the Hippo pathway, also known as the Hippo tumour suppressor pathway, is implicated in many forms of human cancer (Harvey, Zhang & Thomas, 2013). The core components of the pathway were first identified in the fruit fly (*Drosophila melanogaster*) from genetic screens for mutations resulting in overgrowth but are highly conserved in mammals (Hilman & Gat, 2011). Numerous upstream regulators, both biochemical and mechanical, have been discovered that feed into the pathway and activate or inhibit the Hippo pathway effectors, Yorkie (Yki) in *Drosophila*, and yes-associated protein (YAP) and transcriptional co-activator with PDZ-binding motif (TAZ) in mammals (Meng, Moroishi & Guan, 2016).

This chapter first describes the delineation of the Hippo pathway in *Drosophila,* before focusing on the mammalian Hippo pathway and its upstream regulators, including the 4.1 Ezrin Radixin Moesin (FERM) domain protein, Willin. The involvement of the Hippo pathway in stem cell renewal and its potential as a therapeutic target for tissue regeneration and cancer treatment is also discussed.

2.2 Overview of the Hippo pathway in *Drosophila*

The core Hippo pathway consists of a kinase signalling cascade, the discovery of which led to the characterisation of a novel growth control pathway. The key kinase of the Hippo kinase cascade, Warts/Large tumour suppressor (Wts/LATS), was isolated in 1995 from genetic mosaic screens in *Drosophila* for mutations that caused abnormal larval tissue overgrowth (Justice *et al.*, 1995; Xu *et al.*, 1995). Nearly a decade later, the proteins Hippo (Hpo), Salvador (Sav) and Mob as tumour suppressor (Mats) were identified as tumour suppressors that phenocopy Wts (Harvey, Pfleger & Hariharan, 2003; Jia *et al.*, 2003; Pantalacci, Tapon &

Léopold, 2003; Udan *et al.*, 2003; Wu *et al.*, 2003; Kango-Singh *et al.*, 2002; Tapon *et al.*, 2002; Lai *et al.*, 2005) and interact with one another and Wts as part of a signalling complex known as the Salvador-Warts-Hippo pathway (Harvey & Tapon, 2007). Within this pathway, the serine/threonine kinase Hpo, together with the scaffold protein Sav, phosphorylates and activates the serine/threonine kinase Wts (Figure 2.1). Sav contains both a SAV-RASSF-HPO (SARAH) domain that interacts with Hpo (Scheel & Hofmann, 2003), and two WW domains that mediate binding to Wts (Tapon *et al.*, 2002). Phosphorylation of Sav by Hpo promotes their physical binding, allowing the phosphorylation of Wts (Wu *et al.*, 2003), and in addition prevents Sav ubiquitylation and degradation (Aerne *et al.*, 2015). Similarly, phosphorylation of Mats by Hpo promotes the formation of a Mats-Wts complex and stimulates Wts kinase activity (Lai *et al.*, 2005; Wei, Shimizu & Lai, 2007).

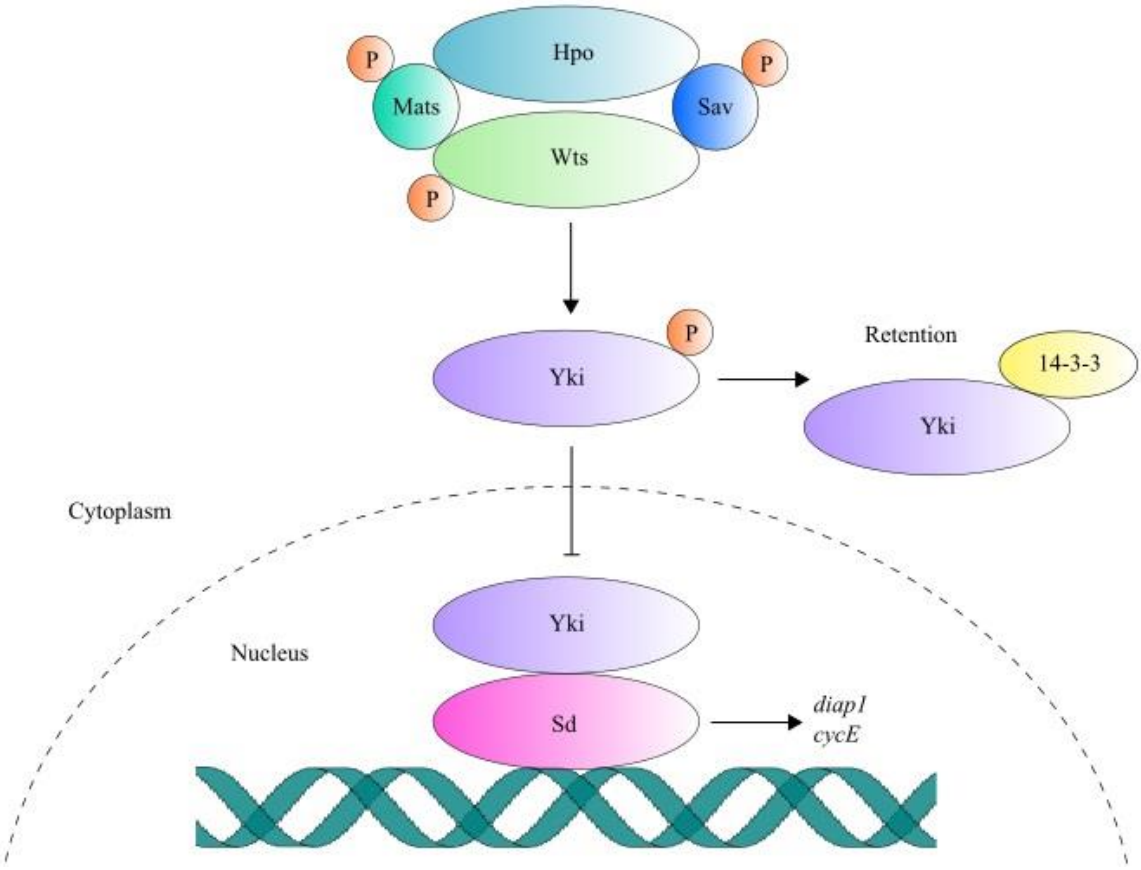

Figure 2.1 The Hippo kinase signalling cascade in *Drosophila*. When Hippo signalling is turned on, activated Hpo phosphorylates the scaffold proteins Sav and Mats to promote the phosphorylation of Wts. Wts in turn phosphorylates Yki at S168 to promote its cytoplasmic retention by 14-3-3 proteins. When Hippo signalling is turned off, Yki binds to the transcription factor Sd in the nucleus and facilitates transcription of genes that induce cell proliferation.

The *Drosophila* downstream Hippo effector, Yki, was identified in 2005 by a yeast two-hybrid screen as a Wts binding partner and homologue of the previously characterised mammalian transcriptional coactivator YAP (Huang *et al.*, 2005). Yki activity causes increased cell proliferation and decreased apoptosis by upregulating transcription of apoptosis inhibitor *diap1* and cell cycle regulator *cycE*, and is negatively regulated by Hippo signalling (Huang *et al.*, 2005). Phosphorylation of Yki by Wts at amino acid residue S168 causes its exclusion from the nucleus and subsequent inactivation via interactions with cytoplasmic 14-3-3 proteins (Dong *et al.*, 2007) (Figure 2.1). Yki lacks a DNA-binding domain, but partners with the TEA-domain (TEAD) transcription factor Scalloped (Sd) to regulate gene transcription (Goulev *et al.*, 2008; Wu *et al.*, 2008; Zhang *et al.*, 2008). By default, Sd transcriptional activity is repressed by Tondu domain-containing growth inhibitor (Tgi) but is stimulated upon replacement of Tgi with Yki (Koontz *et al.*, 2013).

Direct activation of Hpo can occur by phosphorylation of residue T195 by the Sterile 20 family kinase, Tao-1 (Boggiano, Vanderzalm & Fehon, 2011; Poon *et al*., 2011). However, multiple regulatory factors have been found to function upstream of the *Drosophila* core Hippo kinase cascade, including the FERM domain proteins Merlin and Expanded (Ex) (Hamaratoglu *et al*., 2006), and Kidney/brain protein (Kibra) (Baumgartner *et al*., 2010; Genevet *et al*., 2010; Yu *et al*., 2010), the roles of which are described in Sections 2.5.1.1 and 2.5.1.2. In addition, many other proteins, such as those located at cell-cell junctions and within polarity complexes (Irvine & Harvey, 2015), are involved in the control of Yki activity, as discussed in Section 2.5.1.2.

2.3 The core Hippo pathway in mammals

The core Hippo pathway as described in Section 2.2 is largely conserved in mammals. Many of the mammalian homologues of the *Drosophila* components had been discovered prior to their connection to Hippo signalling (Piccolo, Dupont & Cordenonsi, 2014), but it was the elucidation of the Hippo pathway in *Drosophila* that pushed forward the idea that these factors were part of a parallel mechanism of growth control in mammals (Dong *et al*., 2007): Mammalian sterile 20-like kinases 1/2 (MST1/2) are homologues of Hpo, Large tumour suppressor 1/2 (LATS1/2) are homologues of Wts, and YAP and TAZ are homologues of Yki. MST1/2 binds to and phosphorylates SAV1, homologue of Sav, which has been proposed to act as a regulatory subunit of MST1/2 (Chan *et al*., 2005; Callus, Verhagen & Vaux, 2006; Galan & Avruch, 2016). The adaptor protein MOB1A/B, homologues of Mats, binds to MST1/2 autophosphorylated docking motifs to form the MST1/2-MOB1A/B complex, enabling phosphorylation of MOB1A/B by MST1/2 (Praskova, Xia & Avruch, 2008; Ni *et al*., 2015) (Figure 2.2). Phosphorylated MOB1A/B binds to LATS1/2, which is in turn activated by phosphorylation at multiple sites by MST1/2, including critical residues T1079 and S909 within the LATS1/2 activation loop (Chan *et al*., 2005; Hergovich, Schmitz & Hemmings, 2006). Activated LATS1/2/-MOB1A/B phosphorylates YAP and TAZ at HxRxxS motifs, including critical residues S127 and S89 in YAP and TAZ respectively, leading to their inhibition via cytoplasmic translocation, sequestration by 14-3-3 proteins and proteasomal degradation (Dong *et al*., 2007; Lei *et al*., 2008; Liu *et al*., 2010; Zhao *et al*., 2007; Zhao *et al*., 2010).

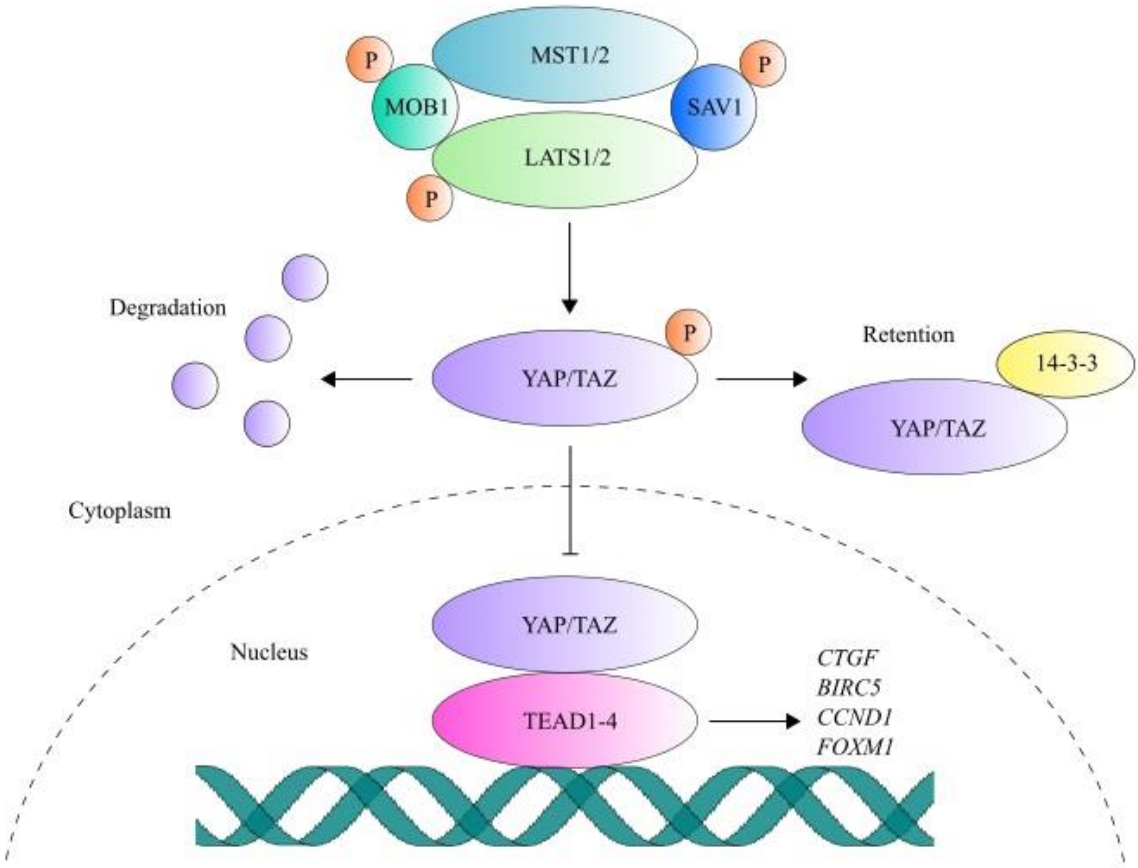

Figure 2.2 The Hippo kinase signalling cascade in mammals. Activated MST1/2 phosphorylates the scaffold proteins SAV1 and MOB1A/B to activate LATS1/2. Activated LATS1/2 phosphorylates YAP/TAZ at HxRxxS motifs, leading to their cytoplasmic sequestration by 14-3-3 proteins and degradation via ubiquitination. In the nucleus, YAP/TAZ bind to TEAD transcription factors and induce expression of cell proliferation/anti-apoptotic genes.

MST1/2 is activated by phosphorylation of critical residues T183/T180 in MST1 and MST2 respectively (Praskova *et al*., 2004). In parallel to Hpo activation in *Drosophila*, phosphoactivation of MST1/2 can occur directly via Tao-1 homologues TAO1/3 (Boggiano, Vanderzalm & Fehon, 2011; Poon *et al*., 2011), but also via autophosphorylation by MST1/2 dimerization (Glantschnig, Rodan & Reszka, 2002; Praskova *et al*., 2004).

2.4 Transcriptional roles of YAP/TAZ

YAP and TAZ, like Yki, are transcriptional co-activators that in the nucleus bind to a range of transcription factors to regulate gene transcription. YAP/TAZ mediate Hippo-induced growth and oncogenic transformation via interaction with TEA-domain (TEAD) transcription factors

1-4, homologues of Sd (Zhao *et al*., 2008; Chan *et al*., 2009; Zhang *et al*., 2009). In a parallel mechanism to that of *Drosophila*, TEAD1-4 by default bind to the transcriptional repressor vestigial-like 4 (VGLL4) but are activated upon binding to YAP/TAZ (Koontz *et al*., 2013). Mechanistically, YAP/TAZ regulate TEAD transcriptional activity by binding the SWI/SNF chromatin-remodeling complex and recruiting a methyl transferase complex to the transcription factor, thus promoting histone methylation and gene transcription (Hansen, Moroishi & Guan, 2015). TEAD1-4-YAP/TAZ target genes include *CTGF* (Zhao *et al*., 2008; Zhang *et al*., 2009), a gene that regulates cell adhesion, proliferation and migration and is required for cell growth, *BIRC5*/*Survivin*, an inhibitor of apoptosis (Bai *et al*., 2012), and cell cycle regulators *CCND1* and *FOXM1* (Mizuno *et al*., 2012). In addition to TEADs, YAP/TAZ interact with the transcription factors Smad, p73 (see Section 2.5.1.2), Runx1/2, Pax3 and T-box transcription factor 5 (TBX5) to mediate the expression of a diverse array of genes (Hansen, Moroishi & Guan, 2015).

The key structural domains of YAP/TAZ are shown in Figure 2.3. Of particular importance are the WW domains that mediate interactions between YAP/TAZ and proteins that contain PPxY motifs (see below). Both YAP and TAZ also contain a highly conserved C-terminal post-synaptic density 95/Discs Large/zonula occludens-1 domain (PDZ)-binding motif which is critical for YAP/TAZ nuclear localization and TEAD-mediated transcription (Shimomura *et al*., 2014).

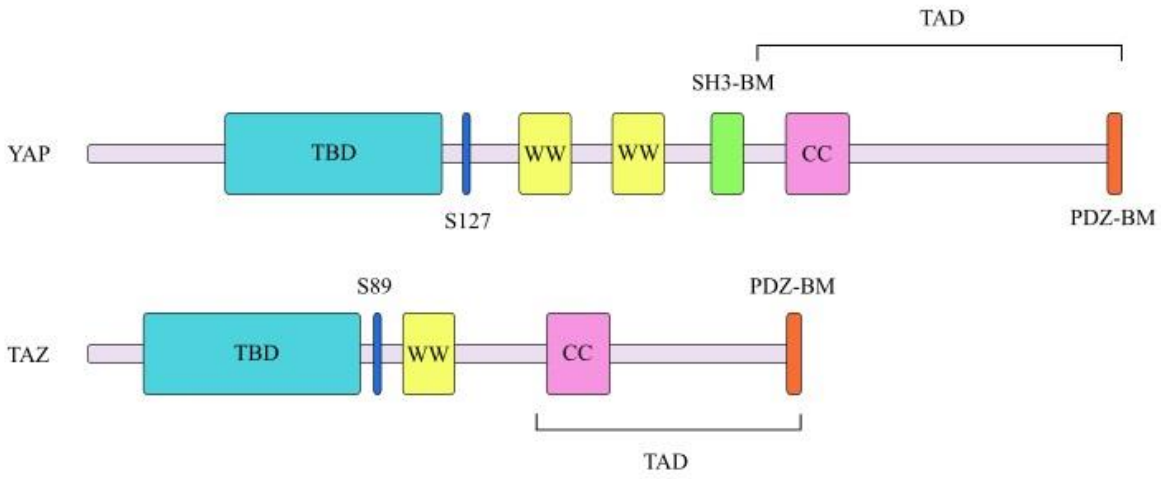

Figure 2.3 Schematic representation of YAP/TAZ regulatory domains. YAP contains an N-terminal TEAD-binding domain (TBD), a 14-3-3 binding site (phospho-S127), two WW domains, a Src homology 3 (SH3)-binding motif (SH3-BM) and a transcriptional activation domain (TAD) which includes a coiled-coil (CC) region and a C-terminal PDZ binding motif (PDZ-BM). The WW domains consist of two tryptophan residues separated by 20-23 amino acids and recognise and bind to PPxY motifs in other proteins. TAZ has a similar structure to YAP that includes S89 as a 14-3-3 binding site, but lacks the second WW domain and SH3-BM. Drawing not to scale.

2.5 Upstream regulators of the mammalian Hippo pathway

The classical Hippo pathway consists of the serine/threonine kinase cascade as described in Sections 2.2 and 2.3. However, in recent years, a plethora of studies have demonstrated that Hippo signalling extends far beyond a simple linear pathway. YAP/TAZ activity can be controlled in both a LATS-dependent and independent manner by a diverse set of such intrinsic cellular machineries as the actin cytoskeleton and G-protein-coupled receptors (GPCRs) (Meng, Moroishi & Guan, 2016). The Hippo pathway is regulated both positively and negatively: positive regulators of the Hippo pathway switch on Hippo signalling and suppress YAP/TAZ activity, whilst negative regulators switch off Hippo signalling and promote YAP/TAZ activity and cell proliferation.

2.5.1 LATS-dependent regulation of YAP/TAZ

The following sections describe factors and mechanisms involved in the regulation of YAP/TAZ that function through the core Hippo signalling kinase cascade.

2.5.1.1 FERM proteins

Merlin, a tumour suppressor encoded by the neurofibromatosis type 2 (NF2) gene *NF2*, and Willin, or FERM domain-containing protein 6 (FRMD6), are both FERM family proteins that act upstream of the mammalian core Hippo kinase cascade. FERM proteins link the actin cytoskeleton to the plasma membrane via an N-terminal FERM domain that binds cell membrane-associated proteins and lipids, and typically a C-terminal spectrin/actin binding domain, thus helping to maintain structural integrity of the sub-membrane region (Chishti *et al*., 1998; Bretscher, Edwards & Fehon, 2002; Moleirinho *et al.*, 2013a). The FERM protein superfamily has expanded rapidly over the last few years and now consists of over 50 members, the functions of which, e.g. in cell movement and cancer metastasis, are slowly being elucidated (Bosanquet *et al*., 2014).

The FERM domain contains approximately 300 amino acids and is composed of three lobes, F1, F2 and F3, which have structural similarities to other proteins and protein domains (Figure 2.4): the F1 lobe is structurally related to ubiquitin, the F2 lobe to an acyl-CoA binding protein, and F3 to a pleckstrin homology (PH)/phosphotyrosine-binding (PTB) domain (Pearson *et al*., 2000). FERM protein activity is regulated by intramolecular masking of the FERM domain by the C-terminal tail in the cytoplasm, yielding the protein inactive via concealing of protein and lipid binding sites (Pearson *et al*., 2000). At the plasma membrane, this head-tail interaction is weakened by exposure to phosphoinositides and phosphorylation, allowing the active protein to bind to molecules within the membrane and the actin cytoskeleton (Fievet *et al*., 2004).

2.5.1.1.1 Merlin

The *Drosophila* homologue of Merlin together with Ex (see Section 2.5.1.1.2) function upstream of the Hippo kinase cascade as tumour suppressors that are required for proliferation arrest and apoptosis (Hamaratoglu *et al*., 2006). Prior to the discovery of the Hippo pathway, human *NF2* loss of function mutations or deletions were already known to cause neurofibromatosis type 2, a disease that leads to formation of multiple tumours within the central nervous system (Rouleau *et al*., 1993; Trofatter *et al*., 1993). It was later shown that loss of Merlin prevented contact inhibition of cell proliferation (CIP), the arrest of cell proliferation at high cell density (see Section 2.5.2.1.1), and promoted nuclear YAP localization and cell proliferation in human meningioma brain tumour cells (Striedinger *et al*.,

2008). A parallel study demonstrated that co-transfection of *NF2* and *YAP* into NF2-null mesothelioma cells induced phosphorylation of YAP at S127 and reduction of nuclear YAP (Yokoyama *et al*., 2008). Merlin is also required for Hippo signalling and antagonism of YAP in the mouse liver (Zhang *et al*., 2010). In contrast to other FERM proteins, Merlin is active in the closed state and inactivated by phosphorylation of C-terminal residue S518 via several different kinases (Kissil *et al*., 2002).

Merlin inhibits YAP/TAZ activity both at the cell membrane and in the nucleus (Petrilli & Fernández-Valle, 2016). Merlin, aided by SAV1, directly binds and targets LATS1/2 to the plasma membrane and promotes its phosphorylation by MST1/2 without enhancing MST1/2 enzymatic activity (Yin *et al*., 2013). Within the nucleus, Merlin binds to and inhibits the E3 ubiquitin ligase $CRL4^{DCAF1}$, a regulator of cell proliferation and survival, to suppress cell proliferation (Li *et al*., 2010; Mori *et al*., 2014). Active $CRL4^{DCAF1}$ ubiquitinates and promotes proteasomal degradation of LATS1 and inhibition of LATS2 in the nucleus, thereby allowing YAP-activated oncogenic gene transcription (Li *et al*., 2014). Thus, loss of Merlin results in increased YAP activity via a lack of LATS1/2 recruitment to the plasma membrane and repression of $CRL4^{DCAF1}$. In confluent cells, Merlin is recruited to adherens junctions (AJs) at the cell boundary, and this localization is critical for its role as a tumour suppressor (Lallemand *et al*., 2003). Merlin also interacts with angiomotin (AMOT) at tight junctions (TJs) as part of a protein complex to control CIP (Yi *et al*., 2011).

In addition to acting upstream of the Hippo pathway, Merlin also regulates cell proliferation via epidermal growth factor receptor (EGFR) signalling (Yi & Kissil, 2010; Benhamouche *et al*., 2010). In *Drosophila*, Merlin and Ex are required to limit the abundance of membrane receptors including EGFR, with loss of Merlin and Ex causing aberrant hyperactivation of the associated receptor pathways (Maitra *et al*., 2006). Similarly in mammalian cells, upon cell-cell contact, Merlin restrains EGFR into an intracellular compartment and prevents its association with effector proteins; inhibition of EGFR by pharmacological compounds also blocks cell proliferation in *NF2*-null cells, thus indicating a second mechanism by which Merlin controls cell growth (Curto *et al*., 2007).

Merlin has been shown to have a role in the migration of epithelial cells (Das *et al*., 2015). Within stationary epithelial monolayers, Merlin localizes to cell-cell junctions. During collective migration of a number of cells, however, the intercellular pulling force from movement of the leading cell triggers translocation of a fraction of Merlin to the cytoplasm,

which in turn activates Rac1. Thus, Merlin has been proposed to act as a mechanotransducer that facilitates coordinated cell movement (Das *et al*., 2015).

2.5.1.1.2 Willin/FRMD6

Willin/FRMD6 was discovered in the rat sciatic nerve as a novel FERM domain-containing protein from a yeast two-hybrid screen for binding partners of the transmembrane L1 family member neurofascin (Gunn-Moore *et al*., 2005). Willin contains 614 amino acids, with the FERM domain residing between residues 14 and 322. The FERM domain of Willin shares high sequence homology with that of FERM proteins ezrin, radixin and moesin, and the predicted 3D structure is highly similar to the known crystal structure of the FERM domain of moesin (Figure 2.4).

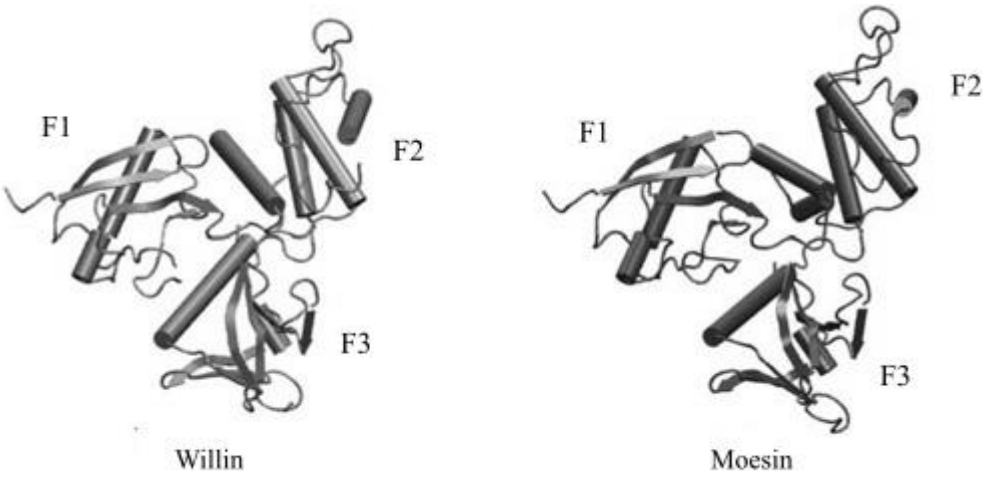

Figure 2.4 Predicted three-dimensional structure of the FERM domain of Willin. The predicted FERM domain of Willin is comparable to the three-lobed crystal structure of the FERM domain of moesin. F1 – ubiquitin-like subdomain; F2 - acyl-CoA binding protein-like subdomain; F3 – PH/PTB-like subdomain. Image adapted from Moleirinho *et al*., 2013a.

Willin is expressed in a diverse range of organs within the human body including the brain, heart, liver and lung (http://www.genecards.org/cgi-bin/carddisp.pl?gene=FRMD6). Intracellularly, Willin is found both in the cytoplasm as indicated by punctate immunostaining, and at the cell membrane, particularly at regions of cell-cell contact (Gunn-Moore *et al*., 2005), though nuclear localization has also been reported (Madan *et al*., 2006). Localization of Willin in PC12 cells can be influenced by the addition of growth factors e.g. epidermal growth factor (EGF) and nerve growth factor (NGF), which cause a translocation of Willin from the

cytoplasm to the plasma membrane (Gunn-Moore *et al*., 2005). Willin, like other FERM proteins, colocalizes with actin despite lacking an actin-binding site, and binds to a profile of phospholipids identical to that of moesin (Gunn-Moore *et al*., 2005).

Willin is the closest human homologue of *Drosophila* Ex, a FERM protein and upstream regulator of the Hippo signalling pathway, as previously mentioned in Section 2.5.1.1.1. Ex acts upstream of Hpo and Wts and downstream of the atypical Fat cadherin to control Yki activity and in turn apoptosis and cell cycle arrest (Bennett & Harvey, 2006; Hamaratoglu *et al*., 2006; Silva *et al*., 2006; Willecke *et al*., 2006). Ex, in concert with 14-3-3 proteins, also directly binds and sequesters Yki in the cytoplasm via interaction of Ex C-terminal PPxY motifs and Yki WW domains (Badouel *et al*., 2009).

In light of the discovery that Ex acts as a regulator of Hippo signalling in *Drosophila*, a potential functional role for Willin in the mammalian Hippo pathway has been examined. Ectopic expression of Willin increases phosphorylation of MST1/2, LATS1 and YAP in human embryonic kidney (HEK)-293 cells, though cannot rescue growth defects associated with loss of *ex* in mutant *Drosophila* epithelial cells (Angus *et al*., 2012). Willin, whilst sharing high homology with Ex in the N-terminal FERM domain, lacks the C-terminus tail and therefore PPxY motifs present in Ex that bind Yki (Figure 2.5). It has been proposed that during evolution, Ex was split into two proteins, Willin and AMOT, as the latter contains two PPxY motifs that bind to YAP (Moleirinho *et al*., 2013a). The FERM domain of Willin, however, was found to be sufficient to antagonise YAP-induced epithelial-mesenchymal transition (EMT, a hallmark of cancer whereby epithelial cells are transformed into undifferentiated mesenchymal-like cells) in mammary epithelial cells, and knockdown of Willin expression phenocopies YAP overexpression (Angus *et al*., 2012). Therefore, Willin acts upstream of the mammalian Hippo pathway, though the exact mechanism by which it does so is yet to be elucidated. **Since Ex is implicated in regulating Hippo pathway activity at least partially via the actin cytoskeleton (see Section 2.5.2.1.3), it may be that Willin too plays a mechanical role upstream of YAP/TAZ.**

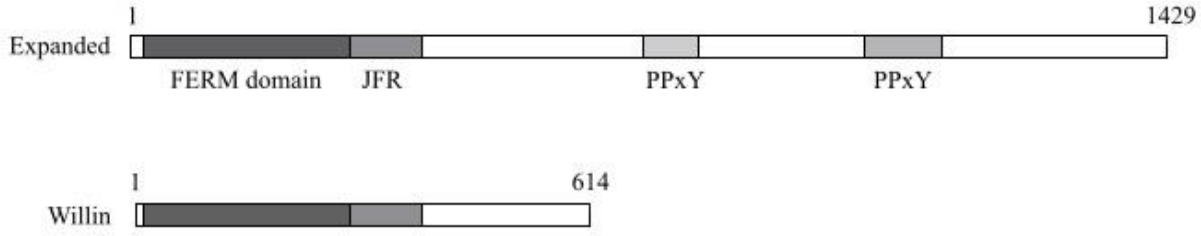

Figure 2.5 Structure of Ex vs. Willin. Willin lacks the C-terminal region of Ex that contains two PPxY motifs. The FERM domain is shown in dark grey, and the juxta-FERM domain region (JFR) in light grey. Image adapted from Hamaratoglu *et al*., 2006.

In addition to its role in Hippo signalling, Willin has been shown to be recruited to polarity complexes in epithelial cells, specifically the apical junctional complex (AJC) at the boundary between the apical and basolateral plasma membrane domains, by nectins, Ig-family proteins that associate with the AJC (Ishiuchi & Takeichi, 2012). Here, Willin cooperates with Par3 to regulate circumferential actomyosin contractility (Ishiuchi & Takeichi, 2011): Willin recruits atypical protein kinase C (aPKC) to the AJC via its juxta-FERM domain region (JFR) in a manner that is independent of Par3; deletion of both Willin and Par3 leads to removal of aPKC from the AJC and apical constriction of epithelial cells. The Par-aPKC complex is discussed in detail in Section 2.5.1.2.4. Willin has also been shown to have a potential role in the regeneration of the peripheral nervous system: in mammalian sciatic nerve fibroblasts, Willin, in addition to activating the Hippo pathway, also promotes cell migration and scratch wound closure (Moleirinho *et al*., 2013b).

2.5.1.2 Cell polarity & junction complexes

Apicobasal polarity, the differential positioning of membrane proteins, lipids and organelles along the apical-basolateral axis, is crucial for epithelial cells to sense and respond to cues from the extracellular environment and neighbouring cells (Martin-Belmonte & Perez-Moreno, 2012). Epithelial cells adhere to one another via adherens junctions (AJs) and tight junctions (TJs) to form a cohesive layer that acts as a barrier to the extracellular space. AJs and TJs, along with several polarity complexes, form distinct apical and basolateral domains of the plasma membrane, thus establishing apicobasal polarity. Loss of epithelial cell polarity is linked to both the early stages of tumorigenesis and advanced stages of cancer progression (Martin-Belmonte & Perez-Moreno, 2012). Interestingly, many of the proteins that make up AJs, TJs and polarity complexes are well-studied tumour suppressors and upstream regulators

of the Hippo pathway (Schroeder & Halder, 2012; Yu & Guan, 2013). Indeed, cell junctions act as platforms for Hippo signalling (Sun & Irvine, 2016). Cell-cell contact via AJs and TJs serves as a key regulatory mechanism for the control of cell proliferation. The polarized architecture of epithelial cells and polarity and junctional proteins that function upstream of mammalian Hippo signalling are shown in Figure 2.6 and described below.

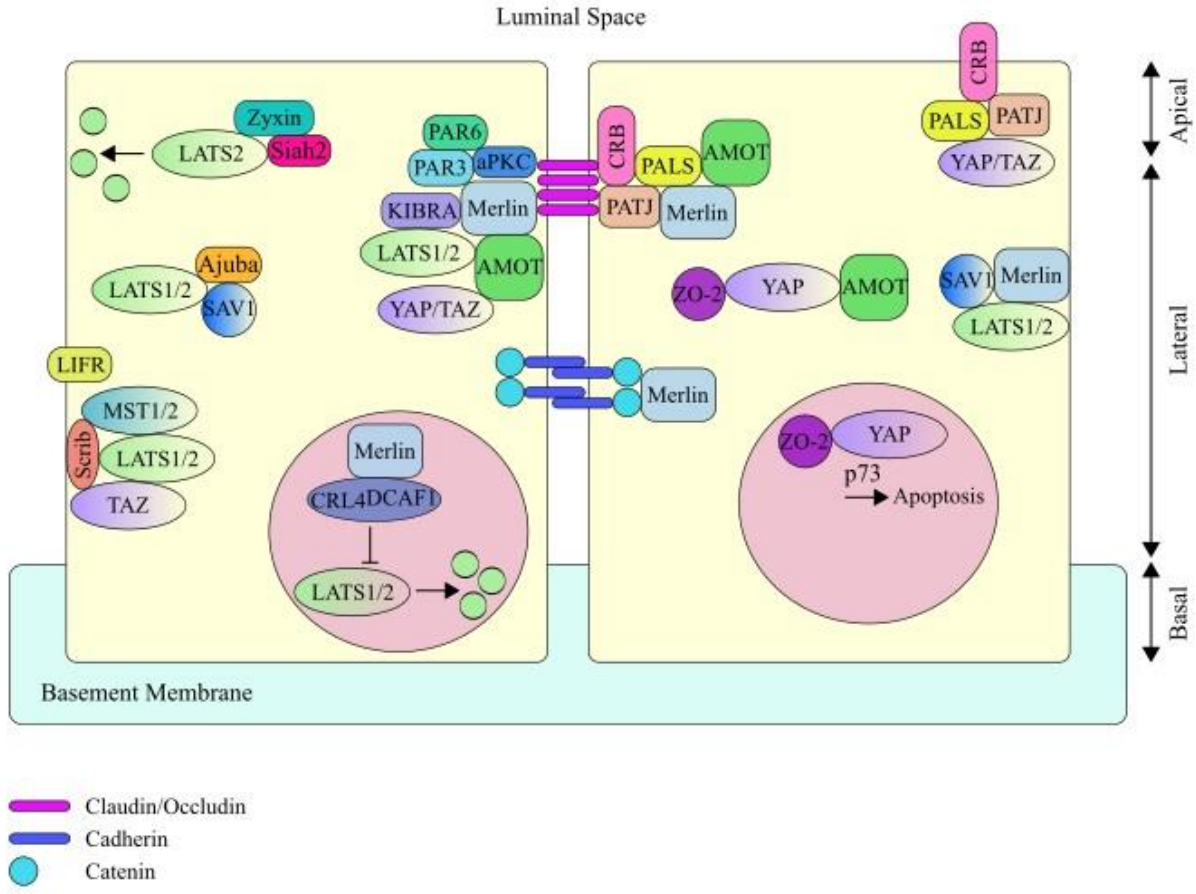

Figure 2.6 Graphical representation of mammalian Hippo pathway regulation by epithelial cell apicobasal polarity protein complexes. The plasma membrane of polarized epithelial cells is subdivided into apical (lumen facing) and basolateral (basement membrane facing) compartments by TJs (shown in purple just below the apical surface of the cell) and AJs (shown in blue/turquoise at the boundary between the apical and basolateral domains). Many polarity proteins act as scaffolds that promote interactions between YAP/TAZ and LATS1/2 e.g. CRB3, AMOT and Scribble, whilst others sequester LATS1/2 to prevent phosphorylation of YAP/TAZ e.g. Ajuba or promote the breakdown of LATS1/2 via ubiquitination and degradation e.g. zyxin. Willin may localize at the boundary between the apical and baslateral domains (Ishiuchi & Takeichi, 2012). Drawing not to scale.

2.5.1.2.1 KIBRA & Merlin

KIBRA is a WW-domain containing protein and upstream regulator of the Hippo pathway. In *Drosophila*, Kibra and Merlin colocalize at the apical domain of epithelial cells and recruit Sav and Hpo, thus activating Hpo signalling (Genevet *et al*., 2010; Yu *et al*., 2010; Su *et al*., 2017). It was previously thought that Kibra and Merlin also form a complex with Ex (Genevet *et al*., 2010; Yu *et al*., 2010); however, it has recently been shown that Kibra and Merlin recruit Sav, Hpo and Wts independently of and in a spatially distinct domain from Ex (Su *et al*., 2017).

In mammals, KIBRA regulates Hippo signalling independently of MST1/2: KIBRA interacts directly with and promotes phosphorylation of LATS1/2 at its hydrophobic motif, and loss of MST1/2 does not affect KIBRA-mediated phosphorylation of LATS1/2 (Xiao *et al*., 2011); in mammary epithelial cells, loss of KIBRA induces EMT, concomitant with decreased phosphorylation of LATS1/2 and YAP but not MST1/2 (Moleirinho *et al*., 2013c). The interaction between Kibra and Merlin observed in *Drosophila* appears to be conserved in human cells (Genevet *et al*., 2010; Xiao *et al*., 2011; Zhang *et al*., 2010).

2.5.1.2.2 The Crumbs complex

The Crumbs complex is composed of the transmembrane protein Crumbs (CRB) and cytoplasmic proteins PALS and PALS-associated tight junction protein (PATJ), and is located at the apical surface and cell junctions of polarized epithelial cells (Médina *et al*., 2002). In *Drosophila*, Crb is essential for establishment of apicobasal polarity in embryonic epithelial cells, with *crb* mutations leading to disruptions in the organisation of epithelia, and in some cases, cell death (Tepass, Theres & Knust, 1990; Tepass & Knust, 1990). Both loss and overexpression of Crb lead to tissue overgrowth characteristic of defective Hippo signalling and upregulation of Yki target genes (Chen *et al*., 2010; Grzeschik *et al*., 2010; Ling *et al*., 2010; Robinson *et al*., 2010). Crb has been shown to regulate Hippo signalling via the FERM protein Ex (Chen *et al*., 2010; Ling *et al*., 2010; Robinson *et al*., 2010): Crb binds directly to Ex via an intracellular FERM-binding motif (FBM) and leads to its apical localization and stabilisation; loss or overexpression of Crb results in basal mislocalization of Ex (Chen *et al*., 2010; Grzeschik *et al*., 2010; Ling *et al*., 2010; Robinson *et al*., 2010), and the FBM is essential for Crb-mediated regulation of Hippo signalling (Chen *et al*., 2010; Ling *et al*., 2010). Recently it was found that Crb localizes Ex specifically to cell junctions to promote Hippo activity (Su

et al., 2017). Conversely, Crb has also been shown to limit Ex activity by promoting its degradation via ubiquitination, and this degradation is inhibited by Hippo pathway activity (Ribeiro *et al*., 2014; Zhang *et al*., 2015). Crb also sequesters Kibra to cell junctions to suppress Kibra-mediated Hippo activity and thus promote cell proliferation (Su *et al*., 2017). Therefore, in *Drosophila*, Crb both positively and negatively regulates the Hippo pathway via Ex and Kibra to coordinate growth.

In mammalian cells, the apical CRB complex binds to YAP/TAZ, and CRB and PALS are required for their phosphorylation (Varelas *et al*., 2010). The CRB complex promotes the formation and is a structural component of TJs (Roh *et al*., 2002; Tilston-Lünel *et al*., 2016). Regulation of YAP/TAZ by the CRB complex is cell density dependent: at high cell density, PALS is present at TJs and TAZ is cytoplasmic; at low cell density, PALS is diffusely localized and TAZ is nuclear (Varelas *et al*., 2010). CRB isoform 3 (CRB3) also promotes the interaction between YAP and LATS1/2, and thus YAP phosphorylation at apical cell junctions in airway epithelial cells (Szymaniak *et al*., 2015); loss of CRB3 leads to unrestricted nuclear YAP and prevents differentiation of airway epithelial progenitors.

There is evidence to suggest that CRB relays signals from outside of the cell: firstly, in *Drosophila*, mutations in *crb* cause mislocalization of Ex in neighbouring cells that express Crb (Chen *et al*., 2010); and secondly, the density-dependent regulation of YAP/TAZ by the CRB complex in mammalian cells suggests a role for CRB in CIP (Varelas *et al*., 2010). It is noteworthy, that unlike *Drosophila* Crb which binds Ex, mammalian CRB does not appear to bind Willin (Tilston-Lünel *et al*., 2016), and thus the role of Crb in Hippo signalling in *Drosophila* is unlikely to be fully conserved in humans, though it has recently been reported that CRB3 expression upregulates transcription of Willin mRNA (Mao *et al*, 2017).

2.5.1.2.3 The Par-aPKC complex

The apical Par-aPKC polarity complex consists of aPKC, Par3 and Par6. Overexpression of aPKC in *Drosophila* imaginal discs causes aberrant Yki activity and tissue overgrowth (Grzeschik *et al*., 2010). In mammals, aPKC is associated with oncogenic cell transformation via nuclear YAP activity, and in human cancers, increased aPKC activity is correlated with increased nuclear YAP (Archibald *et al*., 2015). In addition, active aPKC has been shown to prevent CIP of polarized epithelial cells and cause a loss of apicobasal polarity (Archibald *et al*., 2015). It has previously been shown that MST1/2 is recruited to the plasma membrane

where it couples with LATS1/2 to phosphorylate YAP (Yin *et al*., 2013); gain-of-function aPKC associates with MST1/2 and SAV1 and prevents their localization at the plasma membrane, thus uncoupling MST1/2 from LATS1/2 (Archibald *et al*., 2015). The Par-aPKC complex also binds directly to and targets KIBRA to epithelial cell TJs and apical domains (Yoshihama *et al*., 2011).

2.5.1.2.4 AMOT

The angiomotin family consists of AMOT, AMOTL1 and AMOTL2, which localize to the apical membrane of cells where they act as scaffold proteins and interact with multiple TJ components and members of the Hippo pathway (Wells *et al*., 2006). AMOT is expressed as two different isoforms, AMOT-p130 and AMOT-p80, the larger of which, AMOT-p130, contains an extended N-terminal domain. AMOT-p130 has been shown to bind YAP/TAZ via AMOT PPxY motifs and YAP/TAZ WW domains, leading to YAP/TAZ recruitment to TJs and cytoplasmic sequestration (Chan *et al*., 2011; Wang, Huang & Chen, 2011; Zhao *et al*., 2011). In addition, both isoforms form a TJ-associated complex with Merlin, PALS and PATJ (Yi *et al*., 2011). AMOT also binds and promotes kinase activity of LATS2 (Paramasivam *et al*., 2011; Hirate & Sasaki, 2014), and promotes the interaction of Merlin with LATS1/2 (Li *et al*., 2015a). AMOT has emerged as an important regulator of Hippo signalling via the actin cytoskeleton, as discussed in Section 2.5.2.1.3. No AMOT homologues have been reported in *Drosophila*, suggesting an evolutionary divergence of Hippo regulation by cell polarity proteins between *Drosophila* and mammals. A potential interaction between AMOT and Willin is investigated in Chapter 7.

2.5.1.2.5 Scribble

Scribble is a cell polarity protein and Hippo tumour suppressor located within the basolateral domain of polarized epithelial cells (Skouloudaki *et al*., 2009). In *Drosophila*, Scribble acts downstream of Fat, a transmembrane protein and cadherin (see Section 2.5.1.2.6), to regulate Yki activity (Verghese *et al*., 2012). In mammals, loss of Scribble disrupts epithelial cell polarity and promotes mammary tumorigenesis via inhibition of apoptosis (Zhan *et al*., 2008). Scribble forms a complex with TAZ, MST1/2 and LATS1/2, and is required for the recruitment of MST1/2 to the TAZ/LATS1/2 complex and thus inhibition of TAZ activity (Cordenonsi *et al*., 2011). In addition, ectopic expression of Scribble induces formation of tight junctions and

supresses EMT in mammary epithelial cells (Elsum, Martin & Humbert, 2013). Scribble has also been shown to directly associate with the nitric oxide synthase 1 adaptor protein (NOS1AP) to control Hippo pathway activity and restrict cell proliferation (Clattenburg *et al*., 2015).

Like Merlin, the tumour suppressor role of Scribble is dependent upon its localization at the cell membrane: Scribble mislocalization in the cytoplasm is sufficient to promote cell transformation and allow evasion of TAZ from MST1/2-LATS1/2 inhibition (Zhan *et al*., 2008; Cordenonsi *et al*., 2011). Scribble localization is regulated by the tumour suppressor liver kinase B1 (LKB1) and the Par-1 family of proteins, which in turn regulate YAP activity (Mohseni *et al*., 2014), and by leukemia inhibitory factor receptor (LIFR), which promotes enrichment of Scribble at the cell membrane (Chen *et al*., 2012).

2.5.1.2.6 Adherens junctions

AJs join adjacent cell plasma membranes via homophilic cadherin dimers (Figure 2.6). Cadherins associate with catenins, which in turn bind to cytoskeletal actin filaments and microtubules (Harris & Tepass, 2010). Two key components of AJs, E-cadherin and α-catenin, act as upstream regulators of the Hippo pathway. Cell-cell contact mediated by E-cadherin homophilic binding decreases cell proliferation via regulation of YAP subcellular localization (Kim *et al*., 2011). In keratinocytes, α-catenin was identified as a crucial negative upstream regulator of the Hippo pathway that binds directly to YAP to prevent its dephosphorylation and activation (Schlegelmilch *et al*., 2011). Knockdown of either α-catenin or E-cadherin expression induces nuclear YAP localization and cell proliferation (Yang *et al*., 2015).

2.5.1.2.7 Tight junctions

Many of the proteins described above function at TJs, which provide a platform for Hippo signalling (Figure 2.6). In addition, zonula occludens (ZO) proteins that make up TJs have themselves been shown to be involved in YAP/TAZ regulation. ZO-2, through its PDZ domain, forms a complex with YAP2 and facilitates its nuclear translocation and induction of apoptosis via p73 (Oka *et al*., 2010). ZO-2 also binds to AMOTL1, and this association is mediated by YAP (Oka *et al*., 2012); AMOTL1 opposes the actions of ZO-2 by retaining YAP

in the cytoplasm. Both ZO-1 and ZO-2 have also been shown to interact with TAZ and control its nuclear localization (Remue *et al*., 2010).

2.5.1.2.8 LIM-domain proteins

Zyxin and Ajuba (Jub in *Drosophila*) are LIM-domain proteins and negative regulators of the Hippo signalling pathway (Rauskolb *et al*., 2011; Thakur *et al*., 2010). In *Drosophila*, zyxin localizes to the sub-apical membrane and binds to Wts to promote Yki activity and tissue growth (Rauskolb *et al*., 2011); in mammals, it forms a complex with LATS2 and the E3 ubiquitin ligase Siah2 to promote hypoxia-induced LATS2 ubiquitination and degradation, and is upregulated in human breast cancers (Ma *et al*., 2016). Ajuba/Jub associates with LATS1/2/Wts and SAV1/Sav to inhibit phosphorylation of YAP/Yki and enhance cell proliferation (Thakur *et al*., 2010). The roles of both zyxin and Ajuba/Jub in the regulation of the Hippo pathway have been linked to the actin cytoskeleton, as discussed in Section 2.5.2.1.3.

2.5.2 LATS-independent regulation of YAP/TAZ

The following sections describe mechanisms of YAP/TAZ regulation that are independent/semi-independent of the Hippo kinase cascade.

2.5.2.1 Mechanical cues

The binding of growth factors to receptors present on the outside of the cell represents the initiation of the classical signalling pathway. However, in addition to soluble factors, cells are subjected to constant mechanical forces from neighboring cells and the physical environment in which they grow. A ground-breaking study identified YAP and TAZ as sensors and mediators of extracellular mechanical cues, paving the way for a new area of Hippo pathway research (Dupont *et al*., 2011). The following sections describe the mechanical regulation of Hippo signalling by cell-cell contact, the ECM, the actin cytoskeleton and mechanical stress. Together, these factors have been found to be fundamental in the control of YAP/TAZ activity.

2.5.2.1.1 Contact Inhibition of Cell Proliferation

CIP, the arrest of cell proliferation upon cells reaching confluency (Levine *et al*., 1965), is a well-known phenomenon in cell culture. Evasion of CIP is one of the hallmarks of cancer, whereby cells continue to proliferate despite physically contacting neighboring cells (Hanahan & Weinberg, 2011). The Hippo pathway is a key mediator of CIP: YAP is nuclear and active at low cell density, and cytoplasmic and inactive at high cell density; furthermore, overexpression of YAP leads to inhibition of CIP (Zhao *et al*., 2007). Control of YAP activity by cell density is mediated by cell junction proteins E-cadherin, together with Merlin and Kibra (Kim *et al*., 2011), α-catenin (Schlegelmilch *et al*., 2011) and CRB3 (Mao *et al*., 2017). Merlin is a potent mediator of CIP: loss of Merlin leads to reduced cadherin-mediated cell-cell contact, impaired intercellular adhesion and blocked CIP (Lallemand *et al*., 2003; Flaiz *et al*., 2008). In addition, non-receptor tyrosine phosphatase 14 (PTPN14) has been shown to associate with YAP via WW-PPxY interactions and promote its cytoplasmic localization at high cell density (Wang *et al*., 2012; Liu *et al*., 2013).

2.5.2.1.2 Regulation of Hippo signalling by the ECM

The ECM is an essential and highly changeable component of tissues and organs composed of water, proteins and polysaccharides (Frantz, Stewart & Weaver, 2010). The ECM provides a physical scaffolding and adhesion surface for cells, and its unique biochemical and biophysical composition mediates such fundamental processes as cell growth, differentiation and migration. Cells adhere to the ECM via integrins, transmembrane receptors which couple the actin cytoskeleton of the cell to protein fibrils of the ECM (Schwartz, 2010). Clusters of integrins together with multiple other proteins form focal adhesions that are located on the lower surface of the cell (Figure 2.7).

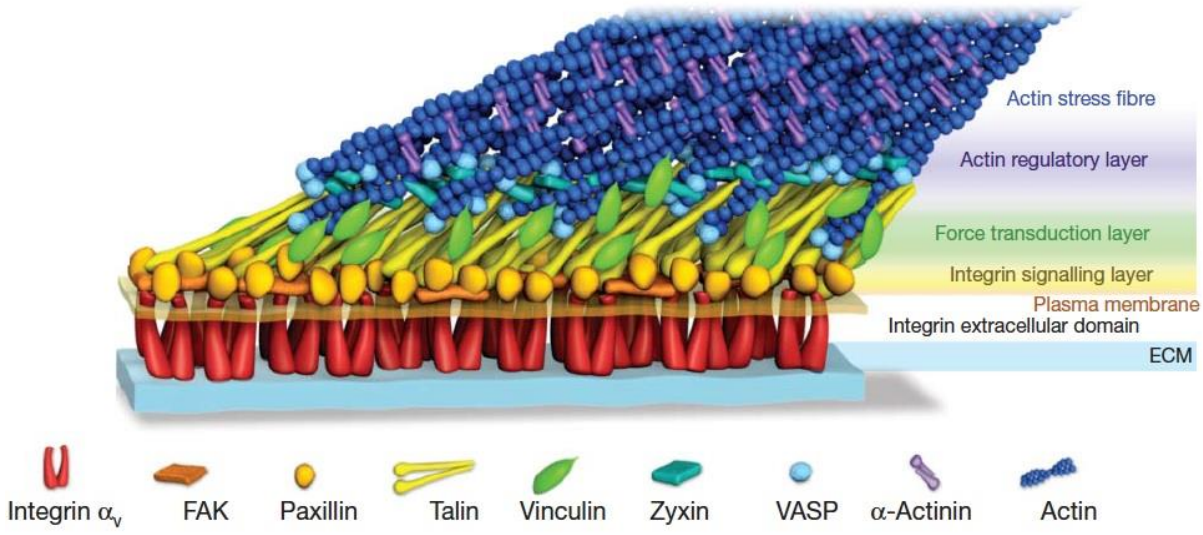

Figure 2.7 Molecular architecture of focal adhesions. Focal adhesions are composed of many different proteins that form vertically stratified layers perpendicular to the plasma membrane. Focal adhesion kinase (FAK) and paxillin link integrins to the actin cytoskeleton via the force-transducing proteins talin, vinculin and zyxin. Vasodilator-stimulated phosphoprotein (VASP), also known as Enabled (Ena), promotes polymerisation of actin filaments, which are crosslinked by α-actinin to form stress fibres. Image adapted from Kanchanawong *et al.*, 2010.

Attachment of cells to the ECM itself is sufficient to induce YAP activity: during cell attachment, YAP is dephosphorylated and mobilises to the nucleus; after detachment by trypsinization, YAP is phosphorylated and shifts to the cytoplasm (Zhao *et al*., 2012). Focal adhesions have been found to play an important role in regulating YAP/TAZ. Attachment of mammary epithelial cells to fibronectin, an ECM glycoprotein, induces YAP nuclear accumulation via stimulation of focal adhesion kinase (FAK)-Src signalling (Kim & Gumbiner, 2015), and integrin-linked kinase inhibits Merlin activation by preventing its dephosphorylation to promote nuclear YAP/TAZ (Serrano *et al*., 2013). YAP has also been shown to regulate the formation of focal adhesions by inducing transcription of focal adhesion-related genes (Nardone *et al*., 2017).

Stem cell fate can be modulated by substrate elasticity: mesenchymal stem cells (MSCs) grown on soft matrices that mimic the elasticity of the brain differentiate into neuronal cell types, and those on stiff matrices that mimic bone, into osteocytes (Engler *et al*., 2006). ECM stiffness translates into YAP/TAZ activity, whereby high stiffness promotes nuclear YAP/TAZ and high transcriptional activity, and low stiffness, cytoplasmic YAP/TAZ and low transcriptional

activity (Dupont *et al*., 2011; Aragona *et al*., 2013) (Figure 2.8). On stiff substrates, YAP/TAZ depletion inhibits MSC osteogenic differentiation, and conversely enables adipogenic differentiation, thus mimicking a soft environment. In addition, overexpression of active YAP rescues osteogenic differentiation on soft matrices. Thus YAP/TAZ is required for mediating stem cell fate by ECM stiffness (Dupont *et al*., 2011).

ECM stiffness and adhesive area define cell geometry, or the amount that a cell 'spreads out': cells growing on stiff substrates or large adhesive areas are well spread, whereas those grown on soft substrates or small areas display a rounded morphology (Fu *et al*., 2010). Cell geometry alone has been shown to be sufficient to regulate YAP/TAZ activity: single cells grown on large fibronectin-coated islands display a spread morphology and predominantly nuclear YAP/TAZ localization; in contrast, YAP/TAZ is largely cytoplasmic in cells grown on smaller fibronectin islands (Dupont *et al*., 2011; Wada *et al*., 2011) (Figure 2.8).

Factors present within the ECM are also able to transduce mechanical signals. The ECM proteoglycan Agrin has recently been found to mechanically activate YAP (Chakraborty *et al*., 2017). Agrin functions at the neuromuscular junction, where it binds to lipoprotein-related receptor-4 (Lrp4) and muscle-specific kinase (MuSK) and plays a critical role in synaptic differentiation (Kim *et al*., 2008). In liver cancer cells, Agrin maintains focal adhesion integrity via Lrp4 and MuSK to enhance cell proliferation, migration and oncogenesis (Chakraborty *et al*., 2015). Agrin promotes YAP activity via matrix rigidity: cells respond to stiff hydrogel substrates by increasing Agrin expression, and thus Agrin may serve as a signaller of tissue rigidity (Chakraborty *et al*., 2017). Exogenous Agrin is also sufficient to activate YAP on soft hydrogels and in cells grown on small adhesive islands, thus mimicking the effects of a stiff ECM and large growth area. The mechano-activation of YAP by Agrin occurs through focal adhesions: Agrin requires FAK to mechanoactivate YAP, and restricts association of Hippo components with focal adhesions, whilst simultaneous blocking of MuSK and integrins leads to inactivation of YAP in a similar manner to during Agrin depletion (Chakraborty *et al*., 2017).

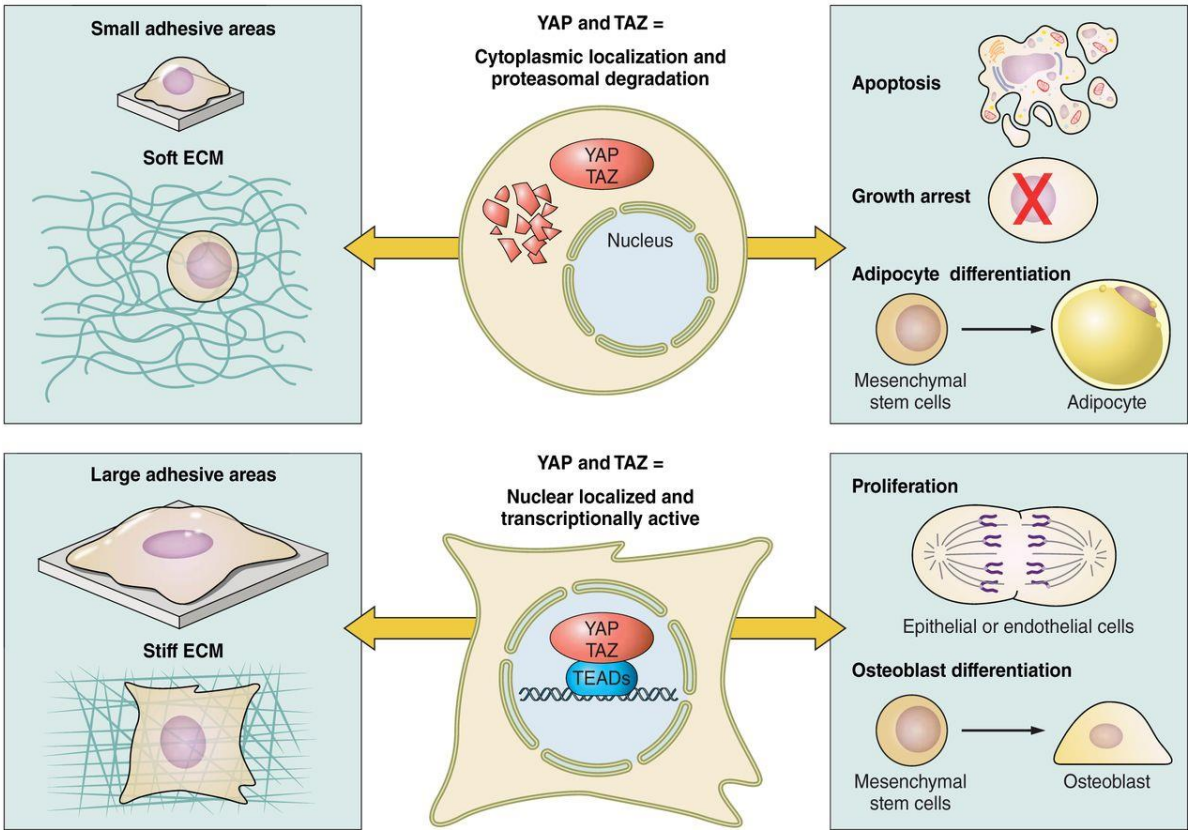

Figure 2.8 Regulation of YAP/TAZ activity and Hippo-mediated cell fate by the ECM. A restricted growth area or soft ECM results in cytoplasmic YAP/TAZ and growth arrest. Conversely, a large growth area or stiff ECM induces nuclear localization of YAP/TAZ and cell proliferation. Low ECM stiffness stimulates differentiation of mesenchymal stem cells into adipocytes, whereas high ECM stiffness promotes osteoblast differentiation. Image adapted from Piccolo, Dupont & Cordenonsi, 2014.

The effect of cell substrate elasticity on Willin expression and localization is investigated in Chapter 7.

2.5.2.1.3 Regulation of Hippo signalling by the actin cytoskeleton

The actin cytoskeleton is a major component of the internal cell machinery and the main determinant of cell architecture. Actin exists in both monomeric (G-actin) and polymeric or filamentous (F-actin) form, the latter of which develops a network throughout the cell that is constantly assembled and disassembled by the addition/subtraction of G-actin monomers via numerous actin polymerising and depolymerising factors e.g. actin capping proteins (Figure 2.9). Actin polymerisation/depolymerisation is regulated by the Rho family of small guanosine triphosphatases (GTPases), including Rho, Rac and Cdc42, and their effectors, the Rho-associated protein kinases (ROCKs) (Hall, 1998; Sit & Manser, 2011). In non-muscle cells,

bundles of 10-30 actin filaments crosslinked by a periodic distribution of α-actinin and the motor protein non-muscle myosin II form contractile stress fibres that generate mechanical tension (Burridge & Wittchen, 2013). The dynamic nature of actin filaments drives cell motility, migration and muscle contraction. In addition, the actin cytoskeleton plays a key role in signal transduction, including Hippo signalling.

YAP/TAZ activity requires both the actin cytoskeleton and Rho: treatment of MSCs with the actin inhibitor latrunculin A or the Rho inhibitor C3 greatly diminishes YAP/TAZ nuclear localization and transcriptional activity (Dupont *et al*., 2011). Conversely, overexpression of the actin-polymerising factor diaphanous promotes YAP/TAZ activity. Moreover, cytoskeletal tension is required for YAP/TAZ activity, as demonstrated by inhibition of myosin II (Dupont *et al*., 2011). The presence of actin stress fibres is correlated with ECM stiffness and adhesive area: cells grown on stiff hydrogels or large islands have more prominent stress fibres compared to those on soft hydrogels or small islands (Dupont *et al*., 2011). This study showed that inhibition of YAP/TAZ by mechanical cues did not involve the Hippo kinase cascade, as phosphorylation of YAP at S127, a key target of LATS1/2, was not increased upon treatment with cytoskeletal inhibitors, and depletion of LATS1/2 had only marginal effects on YAP/TAZ inactivation by the same treatment.

F-actin depolymerising factors have been shown to act as potent inhibitors of YAP/TAZ. Depletion of F-actin severing proteins cofilin and gelsolin and actin capping protein CapZ rescues formation of stress fibres and YAP/TAZ activity in cells grown on soft hydrogels and in dense monolayers (Aragona *et al*., 2013). Similarly, in *Drosophila*, two separate studies demonstrated that actin capping proteins inhibit Yki activity: loss of capping proteins led to abnormal F-actin accumulation, reduced Hippo pathway activity, and strong imaginal disc overgrowth (Fernández *et al*., 2011; Sansores-Garcia *et al*., 2011). It has been proposed that rather than acting through the canonical Hippo cascade, F-actin regulates YAP/TAZ activity in parallel by a distinct, albeit unknown mechanism (Aragona *et al*., 2013).

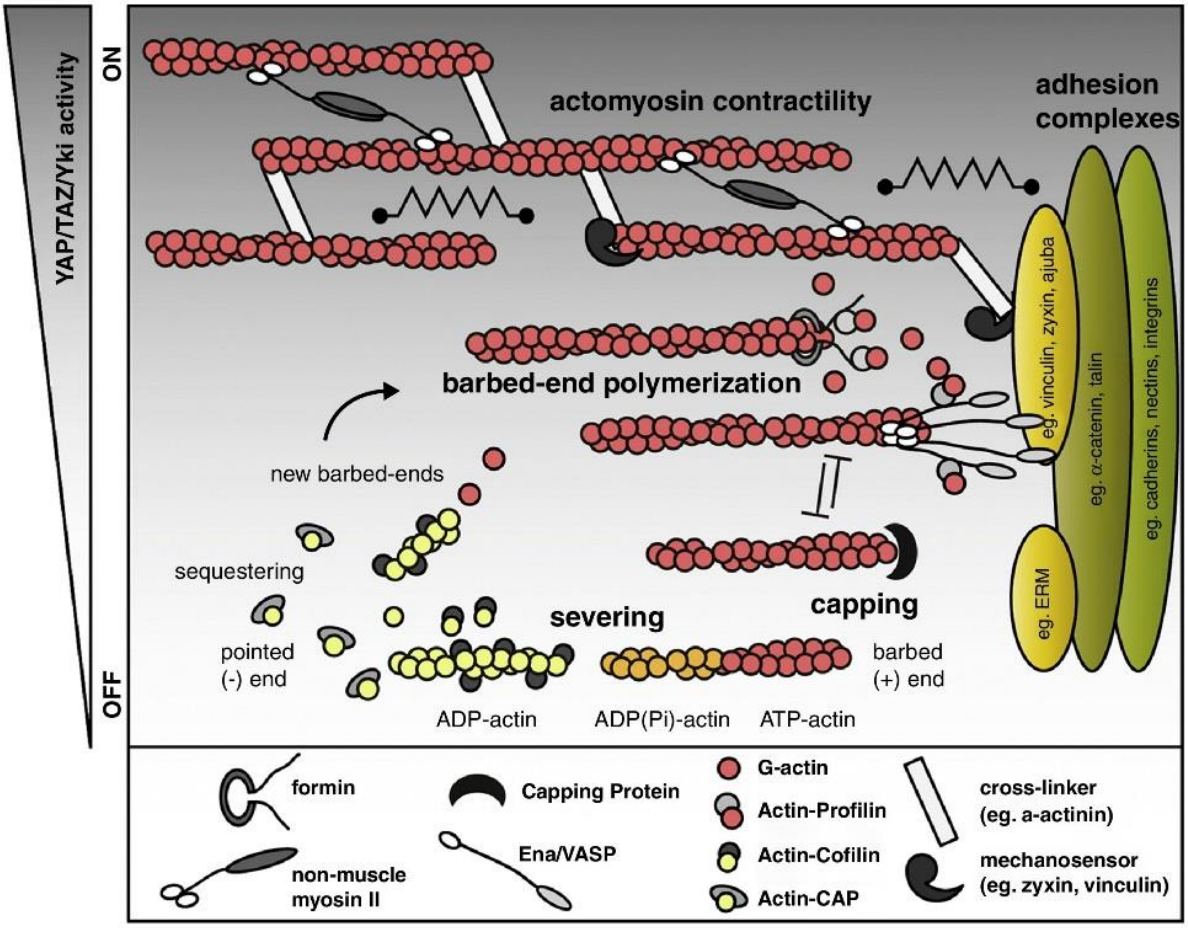

Figure 2.9 Dynamics of the actin cytoskeleton and Hippo signalling. Polymerisation of F-actin occurs by the addition of G-actin monomers at the 'barbed', or fast-growing (positive) end of actin filaments and is facilitated by formins, proteins that promote actin filament elongation by forming a donut-shaped complex around terminal actin subunits, resulting in removal of capping proteins that otherwise block polymerisation, and by Ena/VASP, actin and focal adhesion-associated proteins that antagonize filament capping by capping protein. Profilin binds to both formins and G-actin monomers to promote the addition of actin subunits. G-actin monomers that bind ATP polymerise faster than those that bind ADP, and so are preferentially added to the actin filament barbed end. After polymerisation, ATP bound to actin (ATP-actin) (red subunits) is hydrolysed to ADP and inorganic phosphate (Pi), resulting in the formation of ADP(Pi)-actin (orange subunits); Pi is then released to form ADP-actin (yellow subunits), destabilising the actin filament. Actin depolymerisation, or disassembly, occurs at the 'pointed' (negative) end of F-actin via the severing actions of cofilin and cyclase-associated protein (CAP) that result in the shortening of actin filaments and release of free G-actin monomers into the cytosol. Hippo signalling is correlated with the polymerisation state of the actin cytoskeleton: YAP/TAZ activity is high (drives cell proliferation) in the presence of contractile actin stress fibres and barbed-end polymerisation, and low (corresponding to reduced cell proliferation) when actin filaments are capped or destabilized. Image adapted from Gaspar & Tapon, 2014.

Interestingly, overexpression of Ex can partially reverse the accumulation of apical F-actin in *Drosophila* cells depleted in Capping Protein (CP). Furthermore, CP and Ex colocalize, and endogenous Ex is upregulated in cells lacking CP, suggesting a role for Ex in the regulation of Hippo signalling by F-actin (Fernández *et al*., 2011). Indeed, zyxin has been found to antagonize Ex in the regulation of Yki by F-actin (Gaspar *et al*., 2015). In mammalian cells, zyxin is a component of focal adhesions that in response to mechanical stress mobilises to actin filaments to aid fibre repair via recruitment of actin polymerisation factor Enabled (Ena) and the cross-linking protein α-actinin (Yoshigi *et al*., 2005; Smith *et al*., 2010). In addition, zyxin mediates actin reorganisation around endothelial exocytotic granules (Han *et al*., 2017). Zyxin also promotes Yki gene expression and tissue growth and compensates for phenotypes elicited by Ex loss (Gaspar *et al*., 2015). The growth-promoting effects of zyxin depend on its interaction with Ena, and are reduced by CP; moreover, the interaction between zyxin and Ena is required for zyxin to antagonize Ex in growth control, and zyxin antagonizes the restriction of apical F-actin by Ex (Gaspar *et al*., 2015). Taken together, zyxin and Ex may co-ordinate growth control through their antagonistic effects on F-actin (Gaspar *et al*., 2015).

Cell polarity proteins are also implicated in actin-mediated Hippo signalling. In *Drosophila*, cytoskeletal tension modulates the Hippo pathway via the LIM-domain protein Jub (Rauskolb *et al*., 2014). Cytoskeletal tension is controlled by myosin II activity, which is in turn regulated by ROCK. Myosin II activity promotes Yki activity in a Jub-dependent manner, and cytoskeletal tension causes a shift in Jub localization to AJs where it associates with α-catenin and recruits and inhibits Wts (Rauskolb *et al*., 2014). AMOT-p130, the long isoform of AMOT, binds to F-actin via a conserved actin-binding domain; YAP and F-actin compete for binding to AMOT-p130, and F-actin inhibits the cytoplasmic retention of YAP by AMOT-p130 (Mana-Capelli *et al*., 2014). Indeed, angiomotins are required for cytoplasmic localization of YAP after actin cytoskeleton disruption, for example by treatment with latrunculin B. The association of F-actin with AMOT-p130 is regulated by LATS1/2, which phosphorylates AMOT-p130 at S175 to inhibit F-actin binding (Dai *et al*., 2013; Mana-Capelli *et al*., 2014). In addition, disruption of the actin cytoskeleton or inhibition of Rho GTPase enhances Merlin-Wts interactions in *Drosophila* (Yin *et al*., 2013).

In contrast to previous studies which showed that cytoskeletal tension is required for YAP/TAZ/Yki nuclear localization (Dupont *et al*., 2011, Rauskolb *et al*., 2014), contraction of circumferential actin belts that underlie and link AJs in polarized mammalian epithelial cells was recently shown to supress YAP/TAZ activity in a Merlin-dependent manner (Furukawa *et*

al., 2017). Merlin contains nuclear export signal (NES) sequences that allow it to shuttle between the cytoplasm and the nucleus. Whilst YAP/TAZ lack NES consensus sequences, they can bind directly to Merlin and be transported from the nucleus. Tension in circumferential actin belts decreases the association between E-cadherin and Merlin at AJs, releasing Merlin into the cytoplasm and thus facilitating nuclear export of YAP/TAZ (Furukawa *et al*., 2017). These findings imply that cytoskeletal tension at sites of cell-cell and cell-ECM adhesion regulate YAP/TAZ activity in a distinct and opposite manner.

The effects of Willin expression on the actin cytoskeleton, and in addition the potential interaction of Willin and F-actin, are investigated in Chapters 7 and 8.

2.5.2.1.4 Regulation of Hippo signalling by mechanical stress

Cells *in vivo* are exposed to frequent mechanical strain, e.g. lung tissue and smooth muscle cells to cyclic stretch, and vascular endothelial cells to fluid shear stress (FSS). Both stretch and FSS are important regulators of Hippo signalling. Contact inhibition of epithelial cells growing in a dense monolayer, for example, can be overcome via YAP/TAZ activation by 3-6 hours of static stretching (Aragona *et al*., 2013). Cyclic stretch of cells grown on soft substrates results in cell spreading, formation of stress fibres and nuclear localization of YAP, mimicking growth on stiff substrates (Cui *et al*., 2015). YAP activation induced by cyclic stretch has been shown to occur through c-Jun N-terminal kinase (JNK)-dependent inhibition of LATS1/2 by the LIM domain-containing protein 1 (LIMD1) (Codelia, Sun & Irvine, 2014).

When fluid flows over a surface, for example the endothelial wall of a blood vessel, it exerts a frictional force parallel to the surface, defined as shear stress. FSS controls stem cell fate via YAP/TAZ: MSCs exposed to constant fluid flow undergo osteogenic differentiation via TAZ activation in a Rho-ROCK dependent manner (Kim *et al*., 2014), and FSS-mediated osteogenesis of MSCs and dedifferentiation of chondrocytes has been shown to occur via enhanced expression of YAP (Zhong *et al*., 2013a). Recently, FSS characteristic of lymphatic flow has been shown to promote migration of cancer cells via YAP activation (Lee *et al*., 2017).

In the vasculature, different shear forces caused by blood flow induce distinct cellular responses (Wang *et al*., 2016). Disturbed blood flow is associated with inflammation and atherosclerosis, whereas unidirectional shear stress (USS) is atheroprotective. YAP/TAZ have been implicated in atherosclerosis. A recent investigation demonstrated that USS promotes the interaction of integrin β3, a sensor of shear force, and the G-protein subunit $G\alpha_{13}$, resulting in

RhoA inhibition and YAP phosphorylation (Wang *et al*., 2016). YAP/TAZ inhibition supresses JNK signalling and diminishes pro-inflammatory gene expression. Conversely, disturbed flow promotes YAP/TAZ activity and endothelial activation, and YAP overexpression promotes atherosclerotic plaque formation in mice (Wang *et al*., 2016).

2.5.2.2 GPCRs & Rho GTPases

As mentioned in Section 2.5.2.1.3, YAP/TAZ activity can be regulated by Rho-GTPases (Dupont *et al*, 2011). Rho-GTPases act downstream of GPCRs, a large family of cell membrane receptors that couple to small heteromeric G proteins. Several GPCRs have been shown to mediate YAP/TAZ activity through Rho-GTPases. Serum lysophosphatidic acid (LPA) and sphingosine 1-phosphate (S1P) for example act through $G\alpha_{12/13}$ to activate YAP/TAZ via LATS1/2 inhibition (Yu *et al*., 2012). Similarly, thrombin activates $G\alpha_{12/13}$ through GPCR protease-activated receptors (PARs) to supress YAP/TAZ phosphorylation (Mo *et al*., 2012). In contrast, glucagon and epinephrine stimulate Gs-coupled receptors to activate LATS1/2 and repress YAP activity (Yu *et al*., 2012). Estrogen acts through G protein-coupled estrogen receptor (GPER) to inhibit LATS1/2 and activate YAP/TAZ, thus providing a possible mode of pathogenesis in breast cancer (Zhou *et al*., 2015).

The universal involvement of LATS1/2 in GPCR and Rho-GTPase mediated Hippo signalling is controversial. Rho-GTPases are key regulators of the actin cytoskeleton, which is itself key in YAP/TAZ activity (see Section 2.5.2.1.3) and thus represents an alternative mechanism for Rho-GTPase-mediated control of YAP/TAZ. Overexpression of $G\alpha_q$ through mutations in *GNAQ* and *GNA11* promotes uveal melanoma tumorigenesis via YAP activation (Yu *et al*., 2014). This activation of YAP has been shown to be independent of the Hippo kinase cascade, but instead requires activation of the guanine nucleotide exchange factor, Trio, and subsequent activation of RhoA and Rac1 (Feng *et al*., 2014). Indeed, activation of YAP in uveal melanoma cells is dependent upon the actin cytoskeleton, as reduced actin polymerisation decreases YAP activity even when cells are deficient in LATS1/2. As mentioned in Section 2.5.2.1.3, F-actin and YAP compete for binding to AMOT-p130. The authors show that the accumulation of F-actin causes YAP to dissociate from AMOT, thus contributing to its nuclear translocation (Feng *et al*., 2014). Interestingly, F-actin dependent GPCR signalling inhibits S175 phosphorylation of AMOT by LATS1/2, and AMOT phosphorylation prevents its interaction with F-actin (Dai *et al*, 2013). Regulation of YAP/TAZ activity by LPA and S1P has also been shown to be

controlled by Rho-GTPase activity and the actin cytoskeleton independently of LATS1/2 (Miller *et al*., 2012). Recently it has been shown that FSS activates $G\alpha_{q/11}$ independently of GPCRs in endothelial cells (dela Paz, Melchior & Frangos, 2017).

2.5.2.3 Cell stressors

The role of mechanical stress in the regulation of YAP/TAZ activity has already been discussed (Section 2.5.2.1.4). However, multiple other forms of cellular stress, including energy starvation and oxidative stress, have been found to affect Hippo signalling (Mao *et al*., 2014).

It is not surprising that a lack of energy restricts cell growth; indeed, glucose starvation and inhibitors of glucose metabolism and ATP production induce YAP phosphorylation and suppression via LATS1/2 inactivation and AMOT phosphorylation by AMP-activated protein kinase (AMPK) (DeRan *et al*., 2014; Mo *et al*., 2015). AMPK also phosphorylates YAP directly at multiple sites including S94, a critical residue for YAP-TEAD interactions, thus inhibiting transcription of YAP target genes (Mo *et al*., 2015; Wang *et al*., 2015). In *Drosophila*, AMPK inhibits Yki in the developing central brain/ventral nerve cord independently of Hpo/Wts (Gailite, Aerne & Tapon, 2015).

The status of intracellular molecules such as proteins and DNA has been shown to affect YAP/TAZ regulation. The accumulation of unfolded proteins in the endoplasmic reticulum (ER) lumen, referred to as ER stress, activates the unfolded protein response (UPR) which reduces the unfolded protein load in the ER (Schröder & Kaufman, 2005). During the adaptive stage of the UPR, YAP expression is increased to prevent cell death, while prolonged ER stress promotes apoptosis via activation of the Hippo pathway (Wu *et al*., 2015). Reactive oxygen species (ROS) cause oxidative damage to lipids, proteins and DNA. Oxidative stress in mammalian neurons activates MST1, which in turn phosphorylates the FOXO3 transcription factor to induce apoptosis (Lehtinen *et al*., 2006). YAP physically interacts with FOXO1 to promote transcription of antioxidants catalase and MnSOD, and protects against oxidative stress induced by ischemia/reperfusion in the heart (Shao *et al*., 2014). In contrast, hypoxia deactivates the Hippo pathway by promoting LATS2 ubiquitylation and degradation via the the E3 ubiquitin ligase Siah2 and zyxin (Ma *et al*., 2015; Ma *et al*., 2016). Following DNA damage, YAP is phosphorylated at Y357 by ABL1 to promote its interaction with tumor suppressor p73 and enhance p73-dependent apoptosis (Basu *et al*., 2003; Levy *et al*., 2008).

Additionally, YAP-p73 promotes transcription of the promyelocytic leukaemia (PML) tumour suppressor, which stabilises YAP in a pro-apoptotic positive feedback loop (Lapi *et al*., 2008).

2.6 The Hippo pathway in stem cell renewal and tissue regeneration

In addition to controlling organ size, the Hippo pathway plays a role in stem cell-self renewal and expansion (Zhao, Tumaneng & Guan, 2011). YAP, for example, has been shown to promote stem cell pluripotency by inducing expression of genes involved in stem cell maintenance (Lian *et al*., 2010). Furthermore, YAP is inactive in differentiating mouse embryonic stem cells, and elevated during induced pluripotent stem cell reprogramming (Lian *et al*., 2010). Similarly, TAZ mediates self-renewal of human embryonic stem cells via TGFβ-stimulated binding to Smad2/3-4 transcription factors, and loss of TAZ leads to differentiation into a neuroectoderm lineage (Varelas *et al*., 2008). In the mouse intestine, YAP expression is largely restricted to progenitor cells, and transgenic YAP expression causes expansion of the progenitor cell compartment (Camargo *et al*., 2007). The expansion of human embryonic stem cells has been shown to require the Rho signalling pathway, which in turn promotes the continuous nuclear localization of YAP/TAZ via reorganization of the actin cytoskeleton (Ohgushi, Minaguchi & Sasai, 2015).

The Hippo pathway is also involved in tissue regeneration in response to injury. Damage in the *Drosophila* midgut leads to inactivation of Hippo signalling and Yki activation in differentiated enterocytes, when Yki activity is normally restricted to intestinal stem cells (Karpowicz, Perez & Perrimon, 2010). In mammals, YAP activity declines to a basal level after birth. However, intestinal damage leads to a marked increase in YAP expression, and loss of YAP is detrimental to dextran sodium sulfate-stimulated intestinal regeneration (Cai *et al*., 2010). YAP also induces cardiac regeneration: ectopic expression of active YAP in the adult heart stimulates cardiac repair and improves contractility after myocardial infarction (Xin *et al*., 2013). Recently, Merlin has been found to play a critical role in Schwann cell plasticity and peripheral nerve repair post-injury through activation of the Hippo pathway, as loss of Merlin results in failure of axons to regenerate in the peripheral nervous system, whereas loss of YAP restores axonal growth (Mindos *et al*., 2017).

Regenerative medicine seeks to repair damaged tissues using a multifaceted approach that includes tissue engineering but also stimulation of intrinsic repair mechanisms (Mao & Mooney, 2015). As described above, YAP is activated upon tissue injury. Thus, stimulation

of YAP activity may represent a potential strategy for promoting tissue regeneration. There have already been promising results in this field, for example the enhancement of liver and intestinal regeneration by inhibition of MST1/2 (Fan *et al*., 2016). The fabrication of intestinal organoids for transplantation has also been optimised based on matrix stiffness and associated YAP activity (Gjorevski *et al*., 2016), and transient activation of YAP/TAZ in differentiated mouse cells induces their conversion into tissue specific stem cells with the potential for use in tissue regeneration (Panciera *et al*., 2016).

2.7 The Hippo pathway in cancer

Many of the properties of cancer, such as uncontrolled proliferation and insensitivity to apoptosis, are mediated by the Hippo pathway (Harvey, Zhang & Thomas, 2013). YAP overexpression, for example, causes ectopic cell proliferation and tissue overgrowth in mammals (Camargo *et al*., 2007) and blocks tumour-necrosis factor/CD95-induced apoptosis (Dong *et al*., 2007). Tumour cells have been likened to stem cells in that they display high potential for self-renewal and loss of differentiation markers (Reya *et al*., 2001). YAP/TAZ promote embryonic stem cell pluripotency (Varelas *et al*., 2008; Lian *et al*., 2010) (Section 2.6), and YAP/TAZ activity is increased in breast cancer cells that have stem-cell like properties (Cordenonsi *et al*., 2011). Thus, YAP/TAZ hyperactivity has been proposed to promote tumorigenesis through enhancing a stem-cell-like phenotype (Harvey, Zhang & Thomas, 2013). As discussed in Section 2.5.2.1, YAP/TAZ are sensitive to the mechanical characteristics of the extracellular environment. Tumour tissues display an altered, more rigid ECM, which may be partly responsible for YAP/TAZ hyperactivation observed in human tumours (Butcher, Alliston & Weaver, 2009). The Hippo pathway may also contribute to metastasis of advanced tumours, as YAP overexpression promotes epithelial-mesenchymal transition (EMT) (Overholtzer *et al*., 2006).

Dysregulation of the Hippo pathway has been reported in many different human carcinomas (Harvey, Zhang & Thomas, 2013). However, few germline or somatic mutations have been found in Hippo pathway genes in human cancers, a notable exception being inherited mutations in *NF2* (Merlin) that lead to type 2 neurofibromatosis. The amplification and overexpression of YAP and TAZ have also been reported in various human tumours (Zender *et al*., 2006; Cordenonsi *et al*., 2011). In contrast, oncogenic mutations in pathways that crosstalk with Hippo signalling have been shown to be far more common (Harvey, Zhang & Thomas, 2013).

The Wnt pathway, for example, shows frequent mutations in gastrointestinal cancers (White, Chien & Dawson, 2012); activated β-catenin may hyperactivate YAP via direct binding and promotion of its nuclear accumulation (Imajo *et al*., 2012). The GPCR ligand LPA that stimulates YAP activity (see Section 2.5.2.2) is a powerful carcinogen, and its receptor is required for tumour formation (Lin *et al*., 2009). High rates of mutations have been reported in GPCRs in human cancers (Onken *et al*., 2008; Prickett *et al*., 2011), and cancer-associated $G\alpha_q$ and $G\alpha_{11}$ mutants have been shown to activate YAP (Feng *et al*., 2014; Yu *et al*., 2014).

The findings described above make the Hippo pathway an ideal target for anticancer treatments. Kinases are considered among the best targets for small-molecule therapeutics (Moroishi, Hansen & Guan, 2015). However, the core Hippo kinases are tumour suppressors. The most attractive option, therefore, is direct targeting of YAP/TAZ. Verteporfin blocks the interaction between YAP and TEADs to disrupt YAP-mediated transcription, and has been shown to prevent YAP-induced liver tumorigenesis (Liu-Chittenden *et al*., 2012). A peptide-based YAP inhibitor that mimics VGLL4, a natural suppressor of TEAD transcription, has been developed and shown to reduce growth of human gastric cancer cells grown in mice (Jiao *et al*., 2014). Statins may potentially be used to sequester YAP and TAZ in the cytoplasm via inhibition of the mevalonate pathway (Sorrentino *et al*., 2014), and a negative association of statins with cancer occurrence has already been demonstrated in animal models (Gronich & Rennert, 2013). Treatment of metastasis will be paramount to curing advanced cancers. A preliminary study has shown that LIFR-mediated YAP inhibition suppresses metastasis of breast cancer cells in mice (Chen *et al*., 2012), providing a potential new window for therapeutic intervention.

2.8 Concluding remarks

The Hippo pathway, once considered to be linear in behaviour, has been recharacterized as a network that links biochemical signals to physical forces to direct gene transcription and cell fate via multiple branches. The definition of Hippo signalling is no longer restricted to the canonical kinase cascade that was outlined early in the history of the pathway, but includes the direct regulation of Yki/YAP/TAZ by a multitude of factors, including the cytoskeletal architecture of the cell. The actin cytoskeleton is involved in many aspects of YAP/TAZ regulation, for example by AMOT, zyxin, GPCRs and focal adhesions, and is required for YAP/TAZ transcriptional activity. However, the exact mechanisms by which F-actin controls

Hippo signalling, and the extent to which they are connected to canonical regulation of YAP/TAZ, remain unknown. Elucidation of the complete Hippo pathway and its relationship to other cell signalling processes will provide a major leap forward for regenerative medicine and treatment of certain cancers.

In this thesis, the effect of Willin expression on the actin cytoskeleton is examined to determine whether Willin, like Ex, may have a role in the mechanical regulation of the mammalian Hippo pathway (Chapters 5, 7 and 8). In addition, a potential interaction between Willin and AMOT is explored (Chapter 7). Super-resolution structured illumination microscopy (SIM), as discussed in the next Chapter, is used as an imaging tool to aid in these investigations.

3 Light microscopy and optical manipulation of cells

3.1 Introduction

Light microscopy has been key to some of the most significant biological advances in the past few centuries. For instance, the term 'cell' was first used in 1665 by Robert Hooke when he observed honeycomb-like units in cork, and in 1873, Golgi staining of neuronal processes gave rise to modern neuroscience. Despite the development of other imaging techniques such as electron microscopy in 1931 (Ruska, 1986), light microscopy continues to be highly relevant today due to its use in live-cell imaging and the discovery and development of fluorophores for fluorescence microscopy. The diffraction limit of the light microscope, however, often acts as a barrier for capturing the fine structure of the cell. A number of super-resolution fluorescence microscopy techniques have successfully broken this barrier, improving resolution by up to an order of magnitude. The first half of this chapter discusses and compares three of the most widely-used of these techniques - structured illumination microscopy (SIM), stimulated emission depletion (STED) microscopy, and single molecule localization microscopy (SMLM), which can take the form of photoactivated localization microscopy (PALM) and stochastic optical reconstruction microscopy (STORM).

The latter half of this chapter introduces the phenomenon of optical trapping and discusses its applications for micromanipulation in the biosciences. The notion that light exerts a force is not a new one: Johannes Kepler observed that the tail of a comet always points away from the Sun, which he ascribed to solar pressure (Dholakia, Reece & Gu, 2008). However, it is the invention of the laser, an intense source of coherent photons in a narrow beam, in 1960 that marks the advent of optical trapping experiments, as pioneered by Ashkin ten years later. Now, optical traps are often employed as a method for mechanical characterisation both at the single molecule and whole cell level (Dholakia, Reece & Gu, 2008).

3.2 The diffraction limit of the light microscope

To understand the diffraction limit of the optical microscope, we must first consider how an image is formed. In 1873, Ernst Abbe proposed what is currently the widely accepted theory of image formation (Abbe, 1873). When incident light interacts with an object within a specimen, it diffracts due to its transverse wave nature. The smaller the object (higher the

object spatial frequency), the greater the diffraction of the light. The resulting diffracted waves, each corresponding to a given order (0, ±1, ±2 etc.) are collected by the microscope objective lens. Using periodic gratings, Abbe demonstrated that the objective lens acts as a transform lens, producing a Fraunhofer diffraction pattern at its back focal plane (Figure 3.1). The waves travel beyond the back focal plane and arrive at the image plane where they interfere to form an inverted image of the object. Due to its limited aperture, the objective lens acts as a spatial low-pass filter: only waves of low diffraction order are collected and thus transmitted, whereas waves of diffraction order (and therefore object spatial frequencies) above a given value are not collected and so do not contribute to image formation in the image plane.

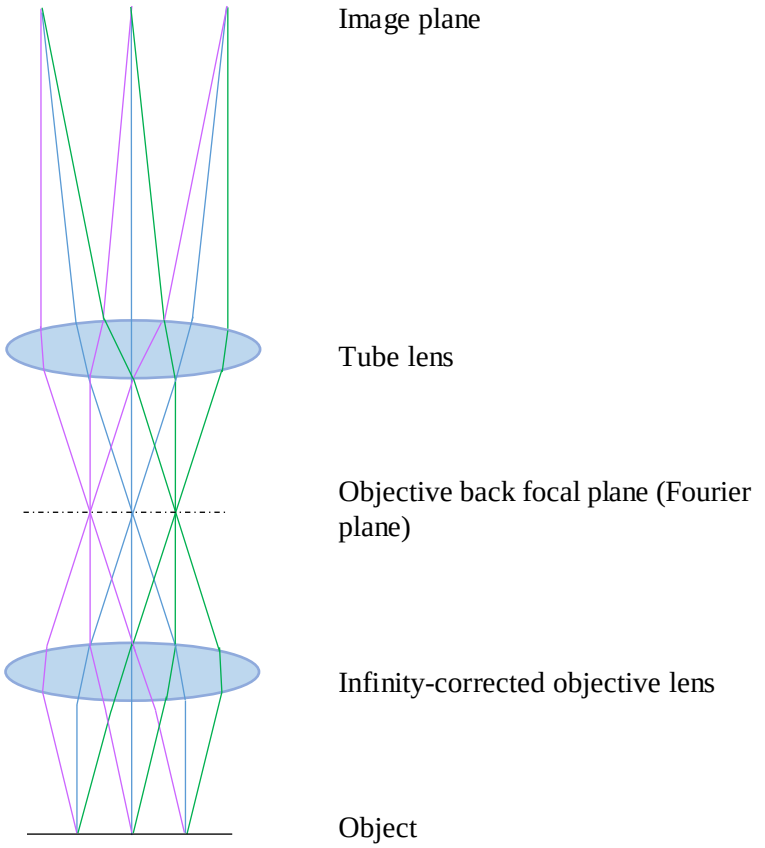

Figure 3.1 Abbe theory of image formation. Incident light is diffracted off a grating and focused by an infinity-corrected objective lens at the back focal plane, also known as the Fourier plane. A tube lens then focuses the rays to form an image of the object in the image plane.

Each point in the specimen is imaged not as a point, but as a finite three-dimensional diffraction pattern referred to as an Airy pattern, composed of a central bright region (the Airy disk) surrounded by concentric rings of decreasing intensity. The Airy pattern is also known as the

point-spread function (PSF). The size of the PSF determines the resolution of the microscope and depends on both the wavelength of light (λ) and the numerical aperture (NA) of the microscope objective, or the ability of the objective lens to gather diffracted light. The NA of the objective is related to the acceptance angle of light, and is defined as:

$$NA = nsin\alpha \tag{3.1}$$

where n is the refractive index of the medium between the objective aperture and coverslip protecting the specimen (1.0 for air, 1.5 for oil), and α is half the aperture angle of the objective lens. Abbe determined the minimum lateral ($r_{x,y}$) and axial (r_z) distance between two objects for those objects to be resolved to be:

$$r_{x,y} = \frac{\lambda}{2NA} \tag{3.2}$$

$$r_z = \frac{2\lambda}{NA^2} \tag{3.3}$$

The full-width at half-maximum (FWHM) method for defining resolution was proposed by Houston in 1927 (Houston, 1927), which states that the resolution is equal to the full-width of the PSF where the PSF intensity is equal to half its maximum value. The FWHM method is advantageous in that it allows a reliable quantification of resolution when the PSF intensity profile does not fall to zero, as is often the case due to background noise.

The Rayleigh criterion for resolution is similar to that of Abbe, and states that two point sources are just resolved when the maximum of one PSF coincides with the first minimum of the second PSF (Rayleigh, 1874). The minimum lateral distance between two objects for those objects to be resolved ($r_{x,y}$) is defined as:

$$r_{x,y} = \frac{0.61\lambda}{NA} \tag{3.4}$$

3.3 Fluorescence microscopy

The development of fluorescence microscopy in the twentieth century represents a major step forward for cell biology, enabling the specific labelling and visualisation of proteins, lipids and other cellular structures using fluorescent probes (fluorophores) and fluorescently-labelled antibodies (Coons, 1951; Giepmans *et al*., 2006). Furthermore, these structures can be targeted in both fixed (dead) and living samples, allowing tracking of their movement and behaviour during live-cell imaging. Fluorescence resonance energy transfer (FRET) is a fluorescence technique used to determine molecular interactions between proteins labelled with donor and

acceptor fluorophores (Fernandez & Berlin, 1976; Sekar & Periasamy, 2003), and fluorescence *in situ* hybridisation (FISH) can detect chromosomal abnormalities using fluorophores that bind specific DNA sequences (Pinkel *et al*., 1988).

The process of fluorescence can be described as the emission of light by atoms and molecules following the absorption of light energy in the form of one or more photons. Absorbed photons excite electrons from the ground state, S_0, to higher energy singlet states, $S_{1, 2...}$. When excited electrons return to the ground state, the excess energy is released as photons (Figure 3.2). Due to non-radiative energy loss by electrons in the excited state, the emitted photons have less energy and thus a longer wavelength than the absorbed photons. The shift in wavelength between the absorbed and emitted light is known as the Stoke's shift.

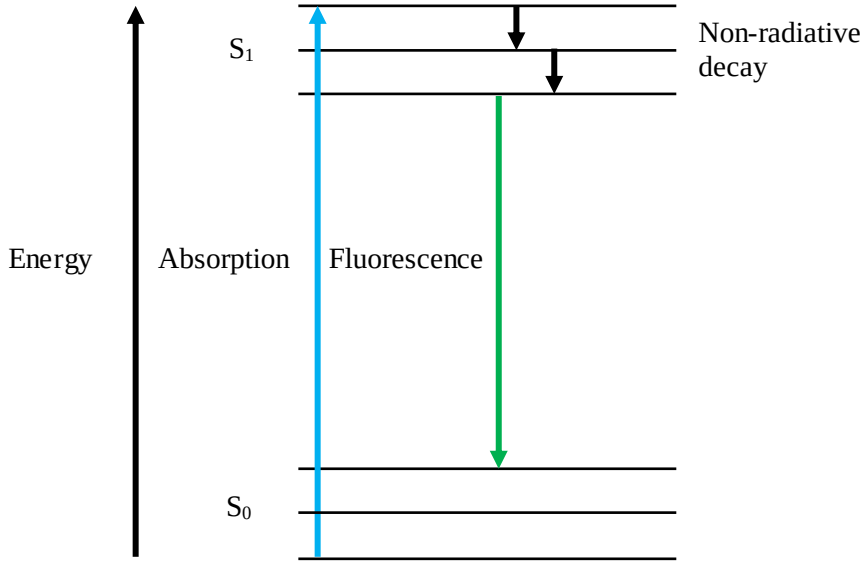

Figure 3.2 Jablonski diagram of fluorescence. Absorption of a photon by a fluorophore leads to excitation of an electron from the ground state (S_0) to the first singlet state (S_1). The excited electron loses some energy through vibrational relaxation, before returning to S_0 and emitting excess energy in the form of a photon.

The fluorescence microscope is designed such that emitted light is separated from excitation light using a dichroic mirror and optical filters, as shown in Figure 3.3. Visible light is depicted as the light source; however, many fluorescence microscopes use lasers with specific wavelengths as sources of excitation light e.g. 405nm, 488nm and 561nm.

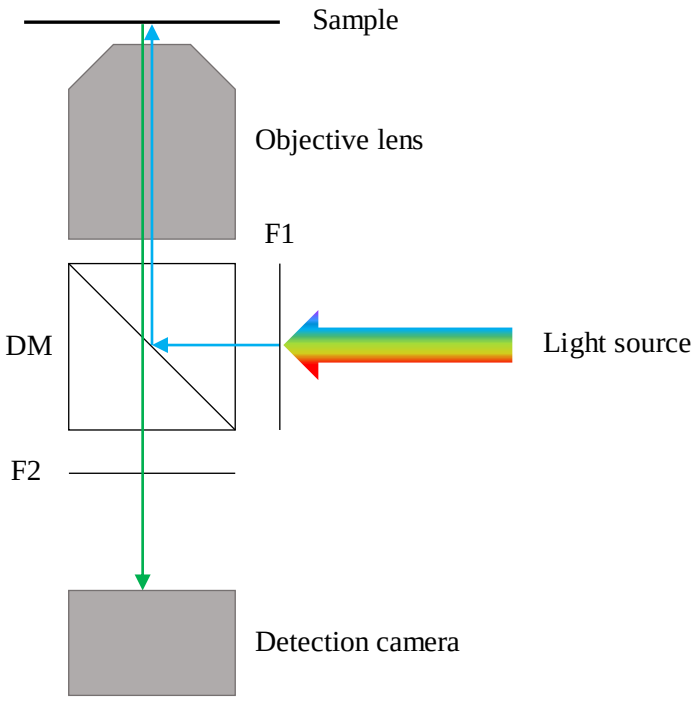

Figure 3.3 Light paths of a basic fluorescent microscope. Visible light from a bulb is filtered into blue excitation light using a filter (F1) and reflected off a dichroic mirror (DM) towards the specimen. Emitted green fluorescence is transmitted through the DM and filtered using an emission filter (F2) to remove unwanted wavelengths before being detected by the camera.

The diffraction barrier of light microscopy as discussed in Section 3.2 limits the lateral and axial resolution to approximately 220nm and 520nm respectively when imaging with green light ($\lambda \sim 550$nm) and an oil immersion objective with NA = 1.40 for example. However, many subcellular structures are smaller than this resolution limit, necessitating methods that improve the spatial resolution of the fluorescence light microscope. A number of such techniques have been developed, as described below in Section 3.4. Super-resolution fluorescence microscopy techniques that truly increase resolution far beyond the diffraction limit are discussed in Section 3.5.

3.4 Extending the diffraction limit in optical microscopy

The loss of high frequency information due to diffraction can be circumvented by exciting fluorophores close to the surface of an object, or in the near-field, and collecting non-propagating evanescent light. Near-field scanning optical microscopy (NSOM) uses a sharp probe tip that is scanned across the specimen and can achieve a lateral resolution of tens of

nanometres (Ash & Nicholls, 1972; Betzig *et al*., 1986). However, NSOM is constrained to examining near-surface features of samples only and is unable to image at depth. The discussion of imaging methods is henceforth limited to far-field techniques that collect emitted light at a distance greater than the light wavelength.

Confocal microscopy scans a focused excitation laser across a specimen and uses a small detection pinhole to remove out-of-focus fluorophore emission light from other parts of the sample and achieve 'optical sectioning', or the production of high contrast images of thin sections from thick samples (Paddock, 1999). Whilst confocal imaging produces a sharper image than widefield microscopy, in which the whole sample is illuminated, the image is also dimmer due to the loss of emission light at the detection pinhole.

Two-photon microscopy uses excitation light of half the energy of single-photon microscopy, such that two photons are needed to excite a single electron and cause fluorescence (Denk, Strickler & Webb, 1990). Fluorophore excitation and emission are thus largely restricted to the focal volume, as it is here that two photons are likely to be absorbed at the same time by the same fluorophore. A high temporal and spatial density of photons is required for this method and is achieved by using a high-powered pulsed laser that packages the photons. Two-photon microscopy is particularly useful for deep tissue imaging, as longer wavelength light is scattered less within tissues than shorter wavelength light (Helmchen & Denk, 2005).

An alternative method for improving axial resolution is to use two opposing objective lenses for excitation and detection. Both 4Pi microscopy (Hell & Stelzer, 1992) and I^5M (Gustaffson, Agard & Sedat, 1999) make use of theis setup. 4Pi microscopy is a laser-scanning technique that coherently illuminates the sample through two juxtaposed lenses to produce excitation light at a common focal plane. Constructive interference of the two wavefronts reduces the focal volume of the excitation light in the z direction such that an axial resolution of ~100nm can be achieved. I^5M, on the other hand, is a widefield technique that combines image interference microscopy (I^2M), the imaging of a sample by two opposing lenses on a single camera to create an interference pattern, and incoherent interference illumination (I^3), excitation of the fluorescent sample with axially varying illumination as a result of interference of the light from two juxtaposed lenses; both techniques result in modulation of axial sample frequencies and thus access to higher axial resolution information.

3.5 Super-resolution fluorescence microscopy

The far-field imaging methods described above push the boundaries of resolution that can be achieved by light microscopy. However, rather than truly breaking the diffraction barrier, they exploit the maximum possible NA of the system, or reduce the effective size of the PSF by minimising the excitation/emission focal volume within a sample. In the past two decades, fluorescence microscopy techniques capable of accessing previously unobtainable high frequency information within biological samples have grown explosively, revolutionising how cells can be visualised. The most popular of these techniques can be divided into two main categories: the first using patterned illumination, encompassing structured illumination microscopy (SIM) and stimulated emission depletion (STED) microscopy; and the second comprising single molecule localization microscopy (SMLM) techniques that activate subsets of individual fluorophores at different times, termed photoactivated localization microscopy (PALM) and stochastic optical reconstruction microscopy (STORM) (Huang, Babcock & Zhuang, 2010; Toomre & Bewersdorf, 2010).

3.5.1 Structured illumination microscopy

SIM refers to a collection of similar techniques that use periodic illumination to excite fluorophores within samples. Originally used as a method for optical sectioning (Neil, Juškaitis & Wilson, 1997), SIM is based upon standing-wave fluorescence microscopy which illuminates a sample plane with a pattern of alternating nodes and anti-nodes (Bailey *et al*., 1993). Soon after its development, 2D and 3D-SIM were introduced as techniques to enhance the lateral (Gustafsson, 2000) and axial resolution (Gustafsson *et al*., 2008) of the light microscope. For the purpose of this thesis, discussion of SIM shall largely be limited to the principles and applications of 2D and 3D-SIM. Practical use of the commercial Nikon-SIM (N-SIM) is detailed in Appendix C.

2D and 3D-SIM are widefield techniques that illuminate a whole sample at once, as for conventional fluorescence microscopy, the main difference being the addition of a grating that diffracts the excitation laser beam into several orders. The -1 and +1 diffraction orders (2D-SIM), or the -1, 0 and +1 orders (3D-SIM) interfere to produce a sinusoidal (2D periodic fringe) pattern of light (Figure 3.4). Illumination of a sample with this patterned light results in modulation of sample spatial frequencies, such that unobservable high frequency information

is brought into the observable range of the microscope. In order to produce a single 2D-SIM image, 9 frames are recorded, with the grating rotated 3 times through steps of 120° to gather information across the lateral image plane (Figure 3.6e) and frames acquired at 3 different grating phase shifts per rotation for correct image reconstruction (see below). A 3D-SIM image requires 15 frames, with 5 grating phase shifts per 3 rotations. The resulting images are a product of the sample structure and the excitation pattern. Image reconstruction is carried out with image processing software that uses an algorithm to return displaced information to its correct location in frequency space and convert the resulting frequency space image into a super-resolved real space image. Both 2D- and 3D-SIM are capable of doubling the lateral resolution from ~240nm to ~120nm; in addition, 3D-SIM doubles the axial resolution from ~700nm to ~300nm (Gustafsson, Agard & Sedat, 2000; Gustafsson *et al*., 2008). A more detailed explanation of the theory of resolution enhancement by SIM is given below in Section 3.5.1.1.

Despite yielding only a two-fold increase in resolution, SIM has many advantages over other super-resolution techniques: the choice of usable fluorophores is the same as for standard widefield fluorescence microscopy, no special sample preparation is required, and multicolour imaging can be performed; with the addition of the phase grating, SIM is compatible with conventional light microscopes; the use of structured illumination inherently yields optical sectioning (see below); and the relatively fast acquisition speed of images allows live-cell imaging with high temporal resolution. The main disadvantage of SIM is the propensity for artefacts in reconstructed images. However, these can be avoided by proper system calibration and image reconstruction (Ball *et al*., 2015; Demmerle *et al*., 2017) (see Appendix C). A direct comparison of the three main super-resolution techniques, SIM, STED and single molecule localization, is given in Section 3.5.4.

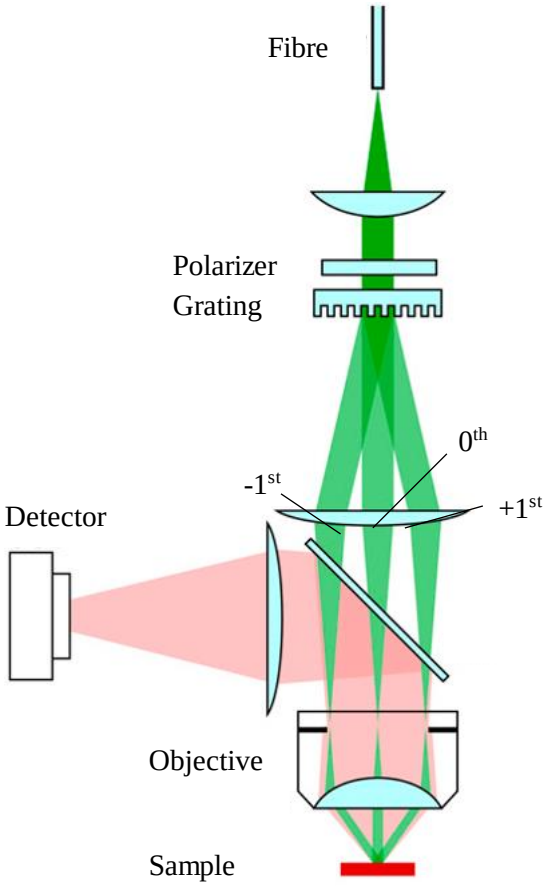

Figure 3.4 Simplified 3D-SIM setup. Excitation light from a multimode fibre is collimated and passed through a phase grating. The 0^{th} and $\pm1^{st}$ diffraction orders are focused though an objective lens and into a sample where they interfere to produce a sinusoidal pattern of light. Emission light from the sample is collected by the objective and detected using a camera. Image adapted from Gustafsson *et al.*, 2008.

3.5.1.1 Theory of resolution enhancement by SIM

The maths described below is not required by the user but is instead fundamental for image reconstruction by the image processing software.

To explain how SIM enhances image resolution, it is helpful to consider objects in Fourier space, also known as frequency, or *k* space. Objects are made up of information of varying frequencies: low frequency information varies in intensity in real space only over long distances, and high frequency information over much shorter distances (Figure 3.5). As explained in Section 3.2, object information above a certain spatial frequency cannot be resolved by a light microscope, as limited by the microscope PSF. Fourier transformation of the PSF yields the microscope optical transfer function (OTF), a measure of how well the

system conserves object contrast (Allen, Ross & Davidson, 2014). With increasingly high spatial frequencies, the magnitude of the OTF approaches zero, the equivalent of the microscope diffraction limit (Figure 3.5).

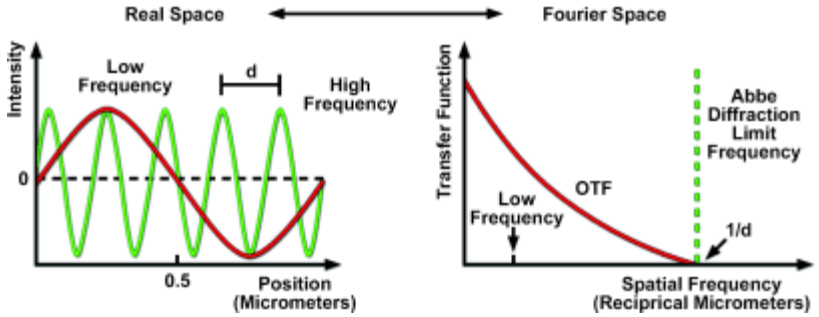

Figure 3.5 The diffraction limit in real and Fourier space. The graph on the left shows fluctuations in intensity of a fine (green) and coarse (red) sinusoidal pattern, where d is the period of the fine pattern. The fine pattern represents high frequency information within a sample that varies over short distances, whereas the coarse pattern depicts low frequency information that varies only over long distances. The graph on the right shows the locations of the frequencies of both patterns in Fourier space, with the fine frequency pattern at the lower limit of the OTF, corresponding to the Abbe diffraction limit frequency, 1/d. Image adapted from Allen, Ross & Davidson, 2014.

Resolvable object spatial frequencies are said to fall within the OTF support, which describes the set of sample frequencies that can be detected by the microscope and can be represented in the lateral dimensions by a circle (Figure 3.6b). The edge of the circle represents the maximum frequencies observable by the system (k_0), with low frequency information residing closer to the origin, and high frequency information nearer the edge.

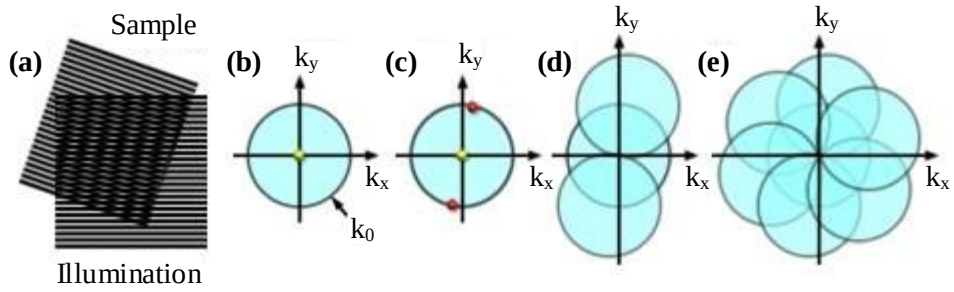

Figure 3.6 Principle of SIM for enhancement of lateral resolution. **(a)** Generation of Moiré fringes by superimposition of two patterns. In the case of SIM, one of the patterns corresponds to the sample, the other to periodically structured illumination. **(b)** Diagrammatic representation of the OTF support in the x and y dimensions. The highest frequencies resolvable by the system (k_0) are at the edge of the OTF support. **(c)** Illumination of the sample with a pattern of frequency k_0 results in the creation of frequency spectra centred at $k_0(\widetilde{D}(k+k_0))$ and $k_0(\widetilde{D}(k-k_0))$ (red circles). **(d)** Expansion of the OTF support region. Higher frequency information is made observable by the system. **(e)** Rotation of the illumination pattern results in an OTF support of approximately double the diameter of the original. Image adapted from Allen, Ross & Davidson, 2014.

SIM uses patterned illumination in order to expand the OTF support. Each attained image is a product of the real space position (r) of the object, $D(r)$, and the illumination pattern, $I(r)$, convolved ($\otimes$) with the microscope PSF, $PSF(r)$, to form the observed image, $E(r)$:

$$E(r) = [D(r)I(r)] \otimes PSF(r) \tag{3.5}$$

Applying a Fourier transform to Equation 3.5 yields:

$$\tilde{E}(k) = \left[\widetilde{D}(k) \otimes \tilde{I}(k)\right] OTF(k) \tag{3.6}$$

where ~ denotes the Fourier transform, k is the Fourier space position and $OTF(k)$ is the Fourier transform of $PSF(r)$ (Allen, Ross & Davidson, 2014).

Multiplication of the object and illumination pattern frequencies generates Moiré fringes, which represent modulated spatial frequencies (Figure 3.6a). If the patterned illumination has a frequency of k_1, then mixing with each object frequency k creates Moiré fringes at $k \pm k_1$. Hence, if the patterned illumination has a frequency of k_0, then mixing with each object frequency results in Moiré fringes at a maximum frequency of $\pm 2k_0$, thus doubling the OTF support in the lateral dimensions (Figure 3.6d). Three rotations of the illumination pattern expand the OTF support to approximately twice the diameter of the original (Figure 3.6e).

Sinusoidal patterned illumination is used:

$$I(r) = I_0[1 + cos(k_0 r + \phi)] \tag{3.7}$$

where $I(r)$ is the local illumination intensity, k_0 the illumination pattern frequency, and ϕ the illumination pattern phase (Gustafsson, Agard & Sedat, 2000). The Fourier transform of the illumination pattern contains three delta (frequency distribution) functions (Gustafsson, Agard & Sedat, 2000):

$$\tilde{\mathrm{I}}(k) = I_0\left[\delta(k) + \tfrac{1}{2}\delta(k + k_0)e^{i\phi} + \tfrac{1}{2}\delta(k - k_0)e^{-i\phi}\right] \tag{3.8}$$

Convolving $\tilde{\mathrm{I}}(k)$ with the object frequencies, $\widetilde{D}(k)$, from Equation 3.6 and the microscope OTF yields the detected frequency spectrum (Gustafsson, Agard & Sedat, 2000):

$$\tilde{\mathrm{E}}(k) = I_0\left[\widetilde{D}(k) + \tfrac{1}{2}\widetilde{D}(k + k_0)e^{i\phi} + \tfrac{1}{2}\widetilde{D}(k - k_0)e^{-i\phi}\right] OTF(k) \tag{3.9}$$

The first component of Equation 3.9 is the frequency spectrum of the sample detected using uniform illumination and centred at $\widetilde{D}(k)$ (Figure 3.6, yellow circle); the latter two components are the new sample frequency spectra shifted by $\pm k_0$ and centred at $(\widetilde{D}(k + k_0))$ and $(\widetilde{D}(k - k_0))$ respectively (Figure 3.6c, red circles). The resulting image is thus a sum of three terms, and it is unknown which image contribution comes from which term; the terms must therefore be recovered to reassign each set of sample frequencies to its correct location in Fourier space. The three terms can be separated using a 3x3 matrix by recording images with three different phases of the illumination pattern. The super-resolved spatial frequencies, $\tilde{\mathrm{E}}_{SR}(k)$, are then combined as follows:

$$\tilde{\mathrm{E}}_{SR}(k) = \frac{[OTF(k)D(k) + OTF(k+k_0)D_{k_0}(k+k_0) + OTF(k-k_0)D_{-k_0}(k-k_0)]}{[|OTF(k)|^2 + |OTF(k+k_0)|^2 + |OTF(k-k_0)|^2 + w^2]} \tag{3.10}$$

where w is the Wiener parameter, which supresses low signal-to-noise ratio (SNR) information (Allen, Ross & Davidson, 2014; Gustafsson, 2000). The inverse Fourier transform of $\tilde{\mathrm{E}}_{SR}(k)$ yields the real space super-resolution image.

Whilst 2D-SIM enhances lateral resolution by a factor of two, it does not improve axial resolution. In 2D-SIM and conventional widefield fluorescence microscopy, the OTF support in x-z is torus-shaped, with a missing cone of information along the z axis (Figure 3.7a-c). 3D-SIM uses interference of three beams to illuminate samples with a sinusoidal pattern that varies periodically in both the lateral and axial directions (Gustafsson *et al.*, 2008). Four new Fourier components are added along the z axis, which expand the OTF support such that the missing

cones are filled (Figure 3.7d-j), resulting in the detection of higher frequency information in z (Figure 3.7d, e) and an approximate two-fold increase in axial resolution (note that in 2D-SIM expansion of the OTF support occurs only in the x and y directions).

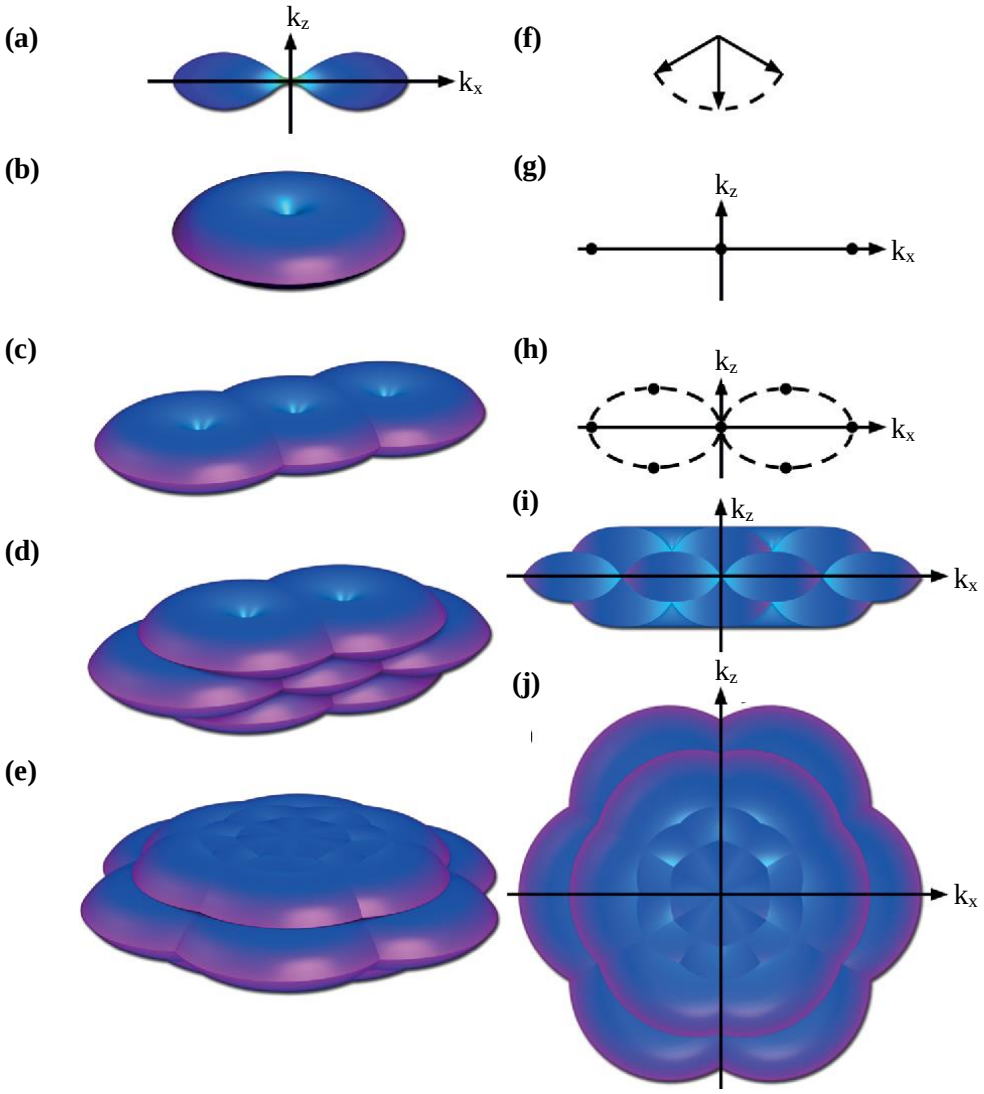

Figure 3.7 Enhancement of axial resolution by 3D-SIM. **(a)** OTF support with uniform illumination of the sample. The 'missing cone' is a result of the shape of the axial PSF. **(b)** 3D representation of the OTF support from (a). **(c)** Extended OTF support in 2D-SIM with one grating rotation. **(d)** Extended OTF support in 3D-SIM with seven harmonics with the missing cones of information filled. **(e)** Three rotations of the illumination pattern extend the OTF support in all directions. **(f)** The three illumination beam directions used for 3D-SIM. **(g)** The three spectral regions created in 2D-SIM along the k_x axis, and **(h)** the seven spectral regions in 3D-SIM. **(i)** lateral, and **(j)** top-down view of the extended 3D-SIM OTF support. Image adapted from Allen, Ross & Davidson, 2014.

Optical sectioning is an inherent feature of 3D-SIM: only light from the plane of the structured illumination is used to reconstruct the super-resolved image, thus eliminating any out-of-focus light above or below.

3.5.1.2 Variations on SIM

SIM was originally used to achieve confocal-like optical sectioning, a technique now known as optical sectioning SIM (OS-SIM) (Neil, Juškaitis & Wilson, 1997). However, OS-SIM uses a coarse illumination pattern (frequency of $k_0/2$) that does not allow for a substantial improvement in lateral resolution, and so shall not be discussed further.

Total internal reflection fluorescence (TIRF)-SIM restricts the excitation and detection of fluorophores to a thin (<100nm) volume between the specimen and glass coverslip, thus increasing the SNR (Chung, Kim & So, 2006). The resolution achievable by TIRF-SIM is enhanced by the fact that the standing evanescent wave has an effective wavelength of $\lambda/(2n\sin\theta)$, where λ is the wavelength of light, n is the refractive index of the high index medium and θ is the incident angle (Chung, Kim & So, 2006). By combining TIRF-SIM with a high NA objective, lateral resolution is improved to <100nm (Li *et al*., 2015b).

Further improvements to resolution can be achieved by exploiting the nonlinear emission response of fluorophores to excitation light. Nonlinear SIM (NL-SIM) can be achieved via two different methods: saturated SIM (SSIM), and the use of reversible photoswitchable probes. SSIM uses high intensity light to saturate the fluorophore excited state and introduce higher frequency spectral regions, thereby generating theoretically unlimited resolution (Gustafsson, 2005). In practise, background noise and photobleaching limits lateral resolution to ~50nm (Gustafsson, 2005; Li *et al*., 2015b). NL-SIM using photoswitchable fluorescent probes has been demonstrated with the fluorescent protein Dronpa, which decays from a fluorescent to a dark state under blue light (Rego *et al*., 2102). Illumination of the sample using structured light confines Dronpa molecules in the fluorescent state to the illumination intensity minima. By increasing the exposure time, the decay response can be saturated, further reducing the area of each fluorescent region. Photoswitchable fluorescent proteins are discussed in further detail in Section 3.5.3. NL-SIM requires a greater number of raw image frames than does 3D-SIM for image reconstruction due to the introduction of higher spectral components, and therefore is not ideal for live-cell imaging (Heintzmann & Huser, 2017).

Multifocal SIM (MSIM) (York *et al*., 2012) and Instant SIM (ISIM) (York *et al*., 2013) are both analogue implementations of 3D-SIM that offer distinct advantages for volumetric and live-cell imaging respectively. MSIM uses a digital micromirror device to generate a sparse 2D excitation pattern of multiple diffraction-limited spots, which is translated across a sample to illuminate the entire field of view. Fluorescence is captured with a camera, and a digital pinhole used to remove out-of-focus light. The resulting raw images are then digitally summed and deconvolved to yield the final super-resolution image (York *et al*., 2012). Resolution is doubled both laterally and axially, and imaging at depths greater than 45µm has been demonstrated (York *et al*, 2012). ISIM is similar to MSIM, but captures optically-sectioned images in a single frame by using a galvanometric mirror to translate the excitation pattern and sum fluorescence emissions prior to image collection with a camera, with resolution doubling post-deconvolution (York *et al*., 2013).

In order to both extend the spatial resolution of SIM and further increase image acquisition speed for live-cell imaging, high NA TIRF-SIM has been combined with a technique known as patterned-activation nonlinear SIM (PA NL-SIM), which uses photoswitchable proteins to generate patterned emission (Li *et al*., 2015b). In this study, the dynamics of clathrin-coated pits were investigated with sub-second image acquisition at a lateral resolution of 45 - 62nm over up to 40 time points.

3.5.1.3 Biological applications of 2D & 3D-SIM

The actin cytoskeleton is a convenient standard for measuring the lateral resolution obtainable by an imaging system, as individual filaments are typically separated by widths smaller than the resolution limit. Indeed, Gustafsson compared images of F-actin in HeLa cells taken using a conventional light microscope and SIM to demonstrate the improvement in resolution using structured illumination (Gustafsson, 2000). Beyond imaging the cellular cytoskeleton, multicolour 3D-SIM has been used to image individual nuclear pore complexes that colocalize with channels in the nuclear lamina, resolve distinct pore complex proteins and detect nuclear envelope invaginations associated with prophase previously observed only by EM (Schermelleh *et al*., 2008).

In addition to imaging of eukaryotic cells, 3D-SIM has been successfully applied to several microbiology studies. For example, parasites within malaria-infected red blood cells (RBCs) have been shown to communicate via exosome-like vesicles, which in turn promotes

differentiation of the parasites to reproductive forms (Regev-Rudzki *et al*., 2013). More recently, resolution doubling in both the lateral and axial directions by 3D-SIM has revealed distinct sites of peptidoglycan cell wall synthesis during bacterial cell division (Bisson-Filho *et al*., 2017).

Current diagnosis of nephrotic kidney disease by examination of the renal podocyte substructure is carried out using EM, which is both time-consuming and costly. However, a recent study has highlighted the potential use of SIM as an alternative and much faster means of diagnosis, both in terms of sample preparation and image acquisition (Pullman *et al*., 2016). In this study, control and minimal change disease (MCD) renal biopsies immunostained for podocin, a podocyte foot process protein, were imaged over a sample thickness of 5-10µm. 3D-SIM imaging of normal biopsies revealed glomeruli densely populated by curvilinear patterns of podocin, similar to those imaged by EM, whereas podocin staining of MCD biopsies was significantly sparser, again comparable to EM images. A second study used semi-automatized quantitative analysis to successfully differentiate between 3D-SIM images of normal and MCD podocyte foot processes, confirming the use of SIM as an appropriate tool for renal diagnostics (Siegerist *et al*., 2017) (see Chapter 5).

Several live-cell imaging studies have been carried out using 3D-SIM, though commercial systems are often too slow to capture fast cellular dynamics (Heintzmann & Huser, 2017). However, time-lapse two-colour imaging of HeLa cells has been shown to resolve movement of filopodia actin filaments and clathrin-coated vesicles (Fiolka *et al*., 2012). By using rolling shutter cameras, 2D-SIM has been demonstrated at speeds as high as 79 super-resolved frames per second, albeit in a limited field of view (Song *et al*., 2016).

3.5.2 Stimulated emission depletion microscopy

STED microscopy is a laser scanning technique that sharpens the PSF by using a second laser (STED laser) in addition to the excitation laser to supress the emission of fluorescence from fluorophores situated outside the centre of the excitation focus (Hell & Wichmann, 1994; Klar & Hell, 1999). An excitation laser pulse first excites fluorophores to S_1; a depletion pulse follows shortly after, which is red-shifted to match the emission spectrum of the fluorophore, thus quenching the excited fluorophores back to S_0 without emission of fluorescence (Figure 3.8a). The depletion pulse is shaped by a phase mask (Figure 3.8b) such that the centre of the beam has zero intensity, and fluorophores located at the focus of the excitation/depletion beam

fluoresce (Figure 3.8c). By raising the power of the STED laser, the region of fluorophore depletion expands, further reducing the size of the PSF (Figure 3.8c). The lateral resolution ($r_{x,y}$) achievable by STED is approximated by:

$$r_{x,y} = \frac{\lambda}{2NA\sqrt{1+I_{max}/I_S}} \tag{3.11}$$

where I_{max} is the maximum intensity of the depletion beam and I_S is the saturation intensity of the fluorophore (Hell, 2007). The lateral resolution using a commercial STED microscope is ~ 50nm (Wegel *et al*., 2016), though by increasing the intensity of the depletion beam, the lateral resolution is limited theoretically only by the size of the fluorophore. Axial enhancement of the PSF can be realized using a "bottle" depletion beam, which has two axially offset intensity maxima connected by a z-y ring of weaker intensity (Klar *et al*., 2000) (Figure 3.8d). Axial resolution using this beam is improved to 100nm, but can be further increased to 33nm using a STED setup in conjunction with 4Pi (Dyba & Hell, 2002).

STED can be performed using both pulsed and continuous wave (CW) depletion lasers (Willig *et al*., 2007). CW-STED is advantageous in that it does not require optimisation of the time delay between the excitation and depletion pulses, though higher laser powers are typically needed for efficient depletion. Gated STED improves resolution of CW-STED by filtering out photons from imperfectly depleted fluorophores based upon arrival time (Vicidomini *et al*., 2011).

No reconstruction or data processing is required for STED images. Traditional STED, however, can only be performed with two colours, though a 3-colour system using a single STED laser at different powers has been demonstrated (Sidenstein *et al*., 2016). Furthermore, the high laser intensities required can lead to both photobleaching, and in the case of live-cell imaging, phototoxicity. Reversible saturable/switchable optical fluorescence transitions (RESOLFT) represents an alternative technique that uses low light intensities to induce reversible transition of photoswitchable fluorescent proteins from a bright to a dark state (Hoffmann *et al*., 2005). As for STED, the centre of the depletion beam has zero intensity, such that fluorophores illuminated by the beam focus remain in the bright state. Tagging intracellular proteins with RESOLFT-compatible fluorescent proteins allows super-resolution live-cell imaging to be carried out at a lateral resolution of ~40nm without the need for high laser powers (Ratz *et al*., 2015).

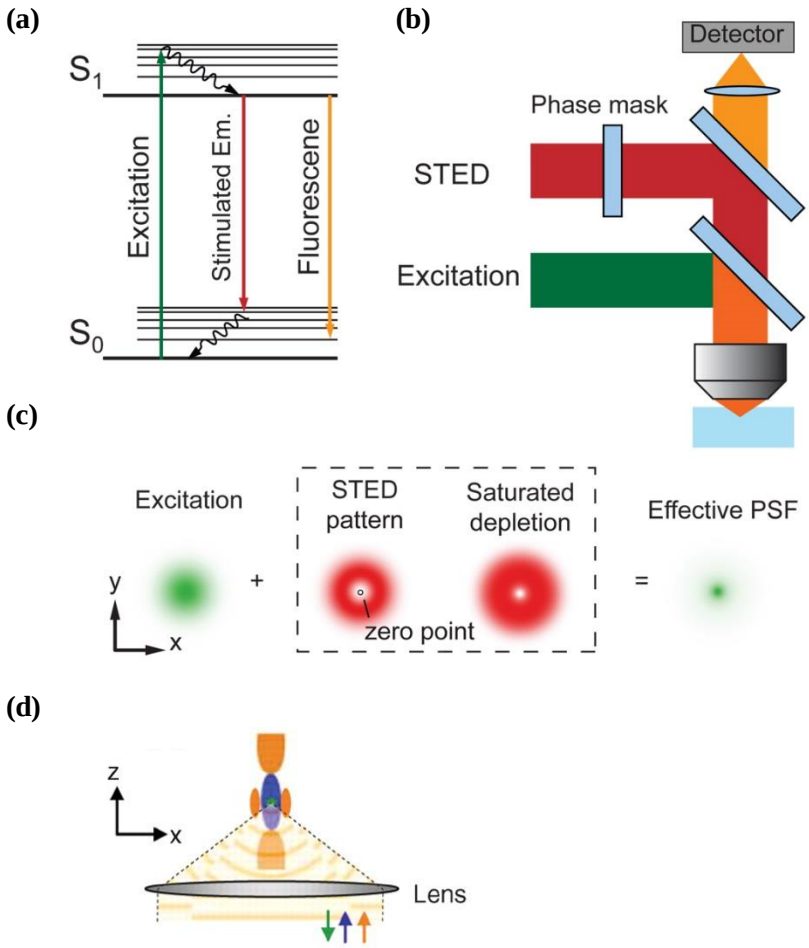

Figure 3.8 Principles of STED microscopy. **(a)** STED Jablonski diagram. Stimulated emission of an excited fluorophore is achieved by absorption of a photon with a wavelength corresponding to the energy difference between the ground and excited state. **(b)** STED microscope setup. The STED laser is shaped by a phase mask, and together with the excitation laser, focused through the microscope objective into the sample. **(c)** Reduction of the effective lateral PSF by the depletion beam. Fluorophores outside the zero-intensity centre of the beam are supressed. At high laser powers (saturated depletion), fluorescence close to the zero-point is also repressed, further reducing the size of the PSF. **(d)** Depletion beam for enhancement of the axial PSF, shown in orange; the blue focal spot represents the excitation beam, and the green arrow, detected fluorescence. Image adapted from Huang, Bates & Zhuang, 2009 and Hell, 2007.

Examples of biological applications of STED nanoscopy include the trafficking of synaptic vesicle trafficking in live neurons (Westphal *et al*., 2008), topological imaging of presynaptic protein architecture (Hua *et al*., 2011), and postsynaptic protein mapping (Nair *et al*., 2013). Recently, STED has revealed the protein ultrastructure organisation and cytoskeletal alignment at the nodes of Ranvier in the peripheral nervous system (D'Este *et al*., 2017).

3.5.3 Single molecule localization microscopy

A fluorophore can be precisely located within a sample if multiple photons are emitted from that fluorophore. When background noise is negligible, the error in the estimated position of a fluorophore in x and y is:

$$\sigma_{x,y} \approx \frac{s}{\sqrt{N}} \tag{3.12}$$

where s is the standard deviation of a Gaussian approximating the true PSF, and N is the number of photons detected from the fluorophore (Betzig *et al*., 2006). However, if two or more fluorophores overlap, then their exact localization becomes impossible. SMLM sequentially "switches on" subsets of fluorophores and computationally determines their individual position centres to build up a super-resolution image over many iterations (Figure 3.9).

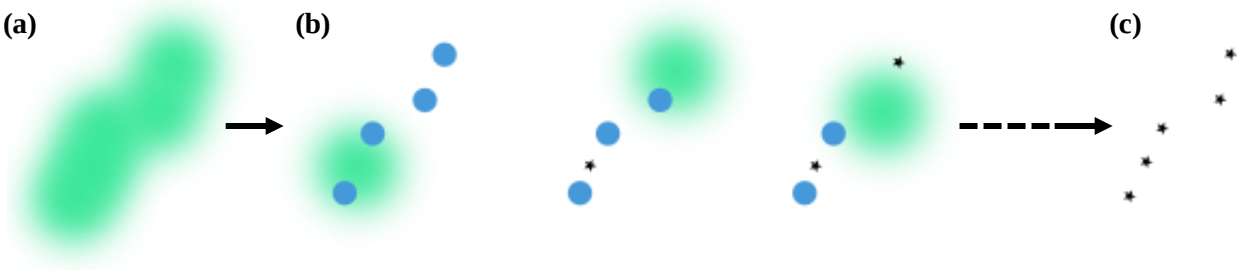

Figure 3.9 Principle of SMLM. **(a)** Fluorophores that are located too closely together such that their PSFs (green circles) overlap cannot be resolved using conventional fluorescence microscopy. **(b)** In SMLM, individual or subsets of fluorophores (blue circles) are activated at any one time, imaged as PSFs (green circles), and the PSF centres (black stars) precisely located. **(c)** Many iterations of fluorophore activation/deactivation and centre localization yield the super-resolution image.

PALM (Betzig *et al*., 2006; Hess, Girirajan & Mason, 2006) and STORM (Rust, Bates & Zhuang, 2006; Heilemann *et al*., 2008) were originally developed as separate SMLM methods, PALM using genetically expressed photoactivatable fluorescent proteins and STORM using organic photoswitchable fluorophores. However, both techniques now employ a wide range of photoswitchable and photoactivatable fluorescent probes. Under specific conditions, such as particular illumination wavelengths and aqueous buffers, photoswitchable fluorophores typically cycle between an "on", or bright state and "off", or dark state, before irreversibly

photobleaching (Sauer & Heilemann, 2017). Fluorescent proteins used in SMLM include photoactivatable GFP (Patterson & Lippincott-Schrwatz, 2002) and proteins that are converted from green to red fluorescent states under UV illumination (Wiedenmann *et al*., 2004).

The high lateral and axial resolution (~20nm) that can be achieved by PALM/STORM is undoubtedly the main advantage of SMLM. However, multicolour imaging is typically complex owing to the necessity for specific "switching" buffers, and to avoid crosstalk between different probes, a hybrid approach combining organic fluorophores with fluorescent proteins is often used (Sauer & Heilemann, 2017). Successful PALM/STORM relies on high molecular labelling density and low non-specific sample background. The requirement for high numbers (1000s) of frames per image is also a major limiting factor of SMLM for live imaging studies, and can readily induce fluorophore photobleaching in both fixed and live samples.

Point accumulation for imaging in nanoscale topography (PAINT) represents an elegant alternative to SMLM that detects transient binding of fluorophores to target molecules (Sharonov & Hochstrasser, 2006). The fluorophore is added at a low (nanomolar) concentration to the sample, and a TIRF objective used for imaging of individual binding events. PAINT is advantageous in that unlike SMLM, it does not require specific fluorophores or buffers. DNA PAINT is a derivative method that uses fluorescently-labelled oligonucleotides that transiently bind to complementary DNA strands, which are themselves linked to probes such as antibodies for protein targeting (Jungmann *et al*., 2010). Owing to the specificity and programmability of DNA molecules, multiplexed imaging has been demonstrated with 10-colour imaging of DNA nanostructures *in vitro* with sub-10nm lateral resolution (Jungmann *et al*., 2014).

PALM/STORM have been employed in a wide range of biological studies, from imaging plant cell microtubules with 20-40nm lateral resolution (Dong *et al*., 2015) to mapping pre- and post-synaptic proteins (Dani *et al*., 2010) and tracing rat hippocampal neurons (Lakadamyali *et al*., 2012). STORM has revealed the periodic suborganisation of actin, spectrin and other associated proteins in the axons of cultured neurons and within brain tissue slices (Xu, Zhong & Zhuang, 2013). SMLM has also been used to investigate the protein organisation of viruses e.g. herpes simplex virus type-1, and predict structural models (Laine *et al*., 2015).

3.5.4 Comparison of super-resolution fluorescence microscopy techniques for biological imaging

As discussed above, each of the three main super-resolution microscopy techniques, SIM, STED and PALM/STORM, have distinct advantages and disadvantages for fixed and live-cell imaging. The respective attributes of all three methods are summarised in Table 3.1.

3.5.5 Combining super-resolution techniques

Whilst STED and SMLM offer the greatest improvement in resolution, STED requires high laser intensities and SMLM, large numbers of frame iterations per single super-resolution image (Table 3.1). SIM, however, uses relatively minimal excitation power and few raw image frames per reconstructed image, and thus is arguably the most suitable of the three techniques for live-cell imaging.

To achieve maximum possible spatial and temporal imaging resolution, super-resolution modalities have been combined in various setups (Heintzmann & Huser, 2017). For example, SIM and SMLM have been combined in a single instrument to produce overlaid images of ~100nm resolution and with single molecule precision to identify imaging artefacts (Rossberger *et al*., 2013). A second similar setup used 3D-SIM to identify regions of interest in multicolour stained liver sinusoidal endothelial cells, followed by STORM to image these areas with further increased spatial resolution to investigate the cytoskeletal structure of transcellular pores (Mönkemöller *et al*., 2015).

PA NL-SIM has been combined with a technique known as lattice light sheet microscopy (LLSM) to achieve 3D volume super-resolution live-cell imaging (Li *et al*., 2015b). LLSM projects a thin sheet of light with the 2D periodic structure of an optical lattice through a sample plane-by-plane to build up an optically sectioned volume image. In the study by Li *et al*., photoactivatable fluorescent probes were activated and excited using a hexagonal lattice light sheet, and by stepping the light sheet in 9 equal fractions in x per plane and applying the algorithms of 3D-SIM, time-lapse 3D images with an xyz resolution of ~20nm by 20nm by 60nm were recorded (Li *et al*., 2015b). 3D super-resolution imaging at depth has also recently been demonstrated using a combination of DNA PAINT and spinning disk confocal microscopy, a method that uses a parallel array of pinholes on a rotating disk to achieve confocal sectioning of thick samples at fast acquisition and takes advantage of detection using

Microscopy technique	SIM	STED	PALM/STORM
Sample preparation	••• As for conventional widefield fluorescence microscopy (use of coverslips of accurate thickness)	•• Requires specific dyes	•• Requires specific dyes
Resolution improvement	• Lateral resolution ~ 100nm Axial resolution ~ 250nm	••• Lateral resolution <10nm Axial resolution ~ 30nm	••• Lateral resolution ~ 20nm Axial resolution ~ 20nm
Image acquisition speed	•• Widefield technique 3D SIM – 15 frames per image	• Laser scanning technique	• Widefield technique High number (5000-15,000) of frames required per image
Multicolour imaging	••• Up to 5 different colours with N-SIM	•• Conventional STED limited to 2 colours	•• Complex
Bleaching/phototoxicity	•• Dependent upon fluorophore and exposure time	• Requires high laser powers	• Imaging of multiple frames leads to photobleaching
Image reconstruction	• Image must be computationally reconstructed, possible introduction of artefacts	•• Image deconvolution required	•• Final image reconstructed from accumulated localizations
Ease of use	••• Easy to use system and software	• Complex	• Complex

Table 3.1 Comparison of SIM, STED and PALM/STORM for imaging of biological samples. • denotes the score for each system for a given attribute, where ••• is very good, •• is good and • is mediocre/poor.

charge-coupled device (CCD) cameras (Schueder *et al*., 2017). Imaging of mitochondrial proteins and DNA and RNA targets inside HeLa cells was carried out at sample depths up to ~10µm, with up to 20nm lateral and 80nm axial resolution.

3.6 Summary of super-resolution microscopy techniques

Compared to STED and SMLM, 3D-SIM offers only a modest improvement in lateral resolution. However, SIM is a user-friendly technique that requires no special sample preparation and is compatible with fluorophores used in standard fluorescent cell lines. In addition, the resolution achieved by SIM makes this super-resolution modality well-placed for examining the actin cytoskeleton, and so for the purposes of this thesis is an ideal choice of microscopy method (see Chapters 5 and 7). SIM is also a relatively fast super-resolution imaging technique and uses low light levels, making it arguably the best method for combination with an optical trapping system for live-cell imaging (see Chapter 6). Optical trapping is discussed below in Section 3.7.

3.7 Optical manipulation

As illustrated above, light has had a major influence on how we observe cells, especially in the past two decades with the arrival of super-resolution techniques. However, the application of light for scientific investigation is not restricted to passive visualisation; rather, because light carries momentum, it can also be used to hold and move microscopic objects.

In 1970, Ashkin demonstrated for the first time that micron-sized particles can be optically guided using a single weakly focused propagating laser beam (Ashkin, 1970). Particles were shown to be drawn into the beam focus and propelled along the beam axis. By counter-propagating two opposing weakly focused beams, a particle could be held, or "trapped" between them (Figure 3.10a). This dual beam setup was the first example of an optical trap. Following these original experiments, Ashkin developed the single-beam gradient force trap in which particles could be confined within the beam focus both laterally and axially (Ashkin *et al*., 1986) (Figure 3.10b). This 3D form of optical trap has since become known as "optical tweezers".

Soon after the invention of the single-beam trap, Ashkin demonstrated trapping of live yeast, bacteria and human red blood cells using infrared light with little optical damage (Ashkin,

Dziedzic & Yamane, 1987). Optical tweezers have since revolutionised the field of biophysics as a sterile and non-contact method for manipulating cells and single molecules. Major advancements, for example in our understanding of the dynamics of RNA transcription, are discussed in Section 3.7.2.

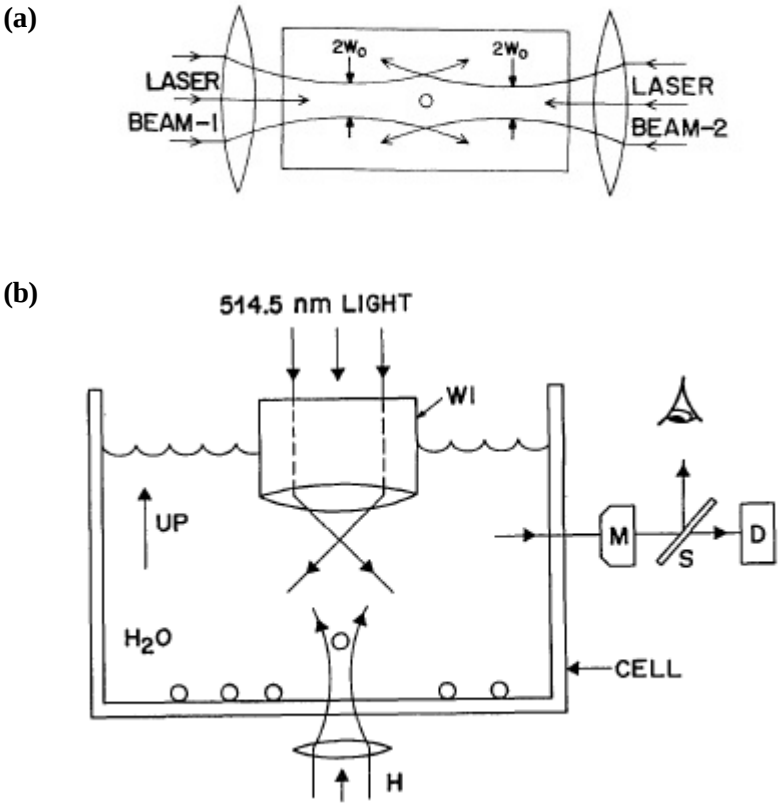

Figure 3.10 Original dual beam (a) and single beam (b) optical trap setups. **(a)** 2.68µm particles are stably trapped at the equilibrium position between two opposing argon laser beams with a radius w_0 = 6.2µm. **(b)** 514.5nm argon laser light is focused using a 1.25 NA water immersion (WI) objective lens into a water-filled glass cell. A vertically-directed holding beam (H) directs glass Mie particles into the focus of the laser beam where they are stably trapped by the trap axial gradient force. Rayleigh particles enter the trapping beam by Brownian motion. Trapped particles are observed using a microscope (M) off a beam splitter (S) or with a detector (D). Images adapted from Ashkin, 1970 and Ashkin *et al.*, 1986.

Advances in beam shaping and design of optical systems have pushed the boundaries of optical trapping beyond the single beam trap. By splitting the beam amplitude (Fällman & Axner, 1997) or using acousto-optic deflectors to share light between two sites (Visscher, Gross & Block, 1996), two adjacent traps, or double optical tweezers, can be created. Arrays of multiple

traps can be formed using spatial light modulators (SLMs) (Curtis, Koss & Grier, 2002). Optical tweezers use a high NA objective lens to generate a tightly focused laser beam for particle trapping. However, optical trapping can also be achieved using optical fibres. Originally, optical fibre traps consisted of two low NA counter-propagating fibres (Constable *et al*., 1993; Guck *et al*., 2001). High NA fibre traps have been developed, but suffer from impractically small working distances, on the order of only a few microns (Liu *et al*., 2006).

3.7.1 Forces within an optical trap

A transparent dielectric particle of refractive index n > medium near the focus of an optical trap experiences two main forces due to the transfer of momentum from the incident photons: the scattering force, F_s, and the gradient force, F_g (Neuman & Block, 2004). The scattering force is proportional to the optical intensity and acts in the direction of light propagation; the gradient force is proportional to the gradient of light intensity and acts in the direction of the light intensity gradient i.e. towards the region of highest light intensity, or the focus of the trapping beam. Thus, for an object to be stably trapped, the gradient force must be greater than the scattering force, necessitating a tightly focused laser beam.

If an object is displaced from an optical trap, the gradient restoring force brings it back to its equilibrium position. The gradient restoring force is proportional to the displacement of the object for short distances (~150nm) (Neuman & Block, 2004). Therefore, an optical trap can be thought of as a linear spring and obeys Hooke's law, $F = -kx$, where F is the trapping force, k is the trap stiffness, and x is the displacement of the trapped object. Methods for measuring the stiffness and force of an optical trap are discussed in Chapter 6.

When considering the forces within an optical trap, it is important to take into account the size of the trapped object. If the object has a diameter much smaller than the laser trapping wavelength, the Rayleigh regime is valid. If the object has a diameter much larger than the laser trapping wavelength, the Mie regime is valid (Dholakia, Reece & Gu, 2008). Objects with a diameter similar to the trap wavelength are said to fall within the Lorentz-Mie regime, which requires complex modelling (Dholakia, Reece & Gu, 2008) and so will not be discussed in this thesis. However, the Mie regime has been shown to be applicable for spheres with a radius as small as $r=10\lambda/\pi$ (van de Hulst, 1957). The scattering and gradient forces that act on a trapped particle in both the Rayleigh and Mie regime are illustrated in Figure 3.11 and described below.

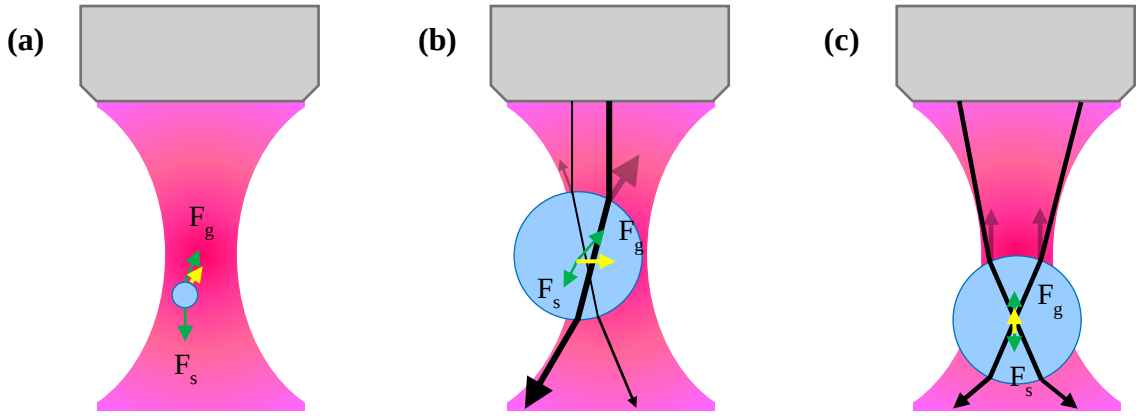

Figure 3.11 Illustration of optical forces acting on a trapped sphere of high refractive index in the Rayleigh and Mie regime. **(a)** A Rayleigh particle acts as a point dipole in an electric field gradient and experiences a net force towards the region of highest light intensity. **(b)** Refraction of incident rays through a laterally displaced Mie sphere imparts a force on the sphere towards the centre of the beam focus. **(c)** An axially displaced sphere below the beam focus experiences a net upwards force. F_s, scattering force; F_g, gradient force; black arrows, beam rays; dark pink arrows, reflected rays; green arrows, direction of gradient and scattering forces; yellow arrows, direction of total optical force. Image adapted from Dholakia, Reece & Gu, 2008.

3.7.1.1 Trapping in the Rayleigh regime

A trapped Rayleigh particle whose diameter is much smaller than the trapping wavelength can be considered a point dipole in an electric field gradient (Neuman & Block, 2004) (Figure 3.11a), and the overall optical force depends on the polarizability of the particle. For a sphere of radius r, the scattering force is:

$$F_s = \frac{I_0}{c}\frac{128\pi^5 r^6}{3\lambda^4}\left(\frac{m^2-1}{m^2+2}\right)^2 n_m \tag{3.13}$$

where I_0 is the light intensity, c is the speed of light, λ is the wavelength of the trapping beam, n_m is the refractive index of the trapping medium and m is the ratio of refractive index of the particle to the refractive index of the medium, n_p/n_m (Ashkin *et al.*, 1986). The gradient force is calculated as:

$$F_g = -\frac{{n_m}^3 r^3}{2}\left(\frac{m^2-1}{m^2-2}\right)\nabla E^2 \tag{3.14}$$

where ∇E^2 is the intensity gradient of the incident light electric field amplitude (Ashkin *et al.*, 1986). For $F_g/F_s > 1$ and trapping to occur, the particle must have a refractive index lower than

that of the surrounding medium, i.e. $m < 1$. If $m > 1$, both F_s and F_g switch signs and the particle is repelled away from the trap.

3.7.1.2 Trapping in the Mie regime

The Mie, or ray optics regime is valid for particles that are much larger than the trapping wavelength, and in this case, geometrical optics apply (Ashkin, 1992). The beam focus can be considered an infinitesimal point relative to the size of a Mie sphere, and the beam decomposed into individual rays that are reflected or refracted and can change polarization at the surface of the sphere according to the Fresnel equations, giving rise to the scattering and gradient forces.

A trapped sphere in the Mie regime that has a refractive index greater than that of the surrounding medium can be considered to act as a positive lens. When incident light hits the surface of the sphere, it refracts and undergoes a change in momentum. Owing to Newton's law of conservation of momentum, an equal and opposite change in momentum proportional to the light intensity is imparted on the sphere (Neuman & Block, 2004). For $m < 1$, the net force on the sphere is in the direction of the intensity gradient (Figure 3.11b, c). Light scattered from the surface of the sphere results in an additional force in the direction of light propagation, causing the trapping equilibrium position to be slightly below the focus of the trap.

The scattering and gradient forces can be calculated by considering a single ray of power P hitting a dielectric sphere at incident angle θ with incident momentum $n_m P/c$, giving rise to a reflected ray with power PR and an infinite number of refractive rays of decreasing power PT^2, PT^2R, $PT^2R^2 ... PT^2R^n$, where R and T are the Fresnel reflection and transmission coefficients of the surface at θ (Ashkin, 1992). The sum of these contributions from this single ray yields the force on the sphere: the scattering force is the sum of the reflected and refracted contributions that point in the direction of the incident ray; the gradient force is the sum of the contributions that are perpendicular to the incident ray. The scattering and gradient forces are given by:

$$F_s = \frac{n_m P}{c}\left\{1 + Rcos2\theta - \frac{T^2[cos(2\theta-2r)+Rcos2\theta]}{1+R^2+2Rcos2r}\right\} \quad (3.15)$$

$$F_g = \frac{n_m P}{c}\left\{Rsin2\theta - \frac{T^2[sin(2\theta-2r)+Rsin2\theta]}{1+R^2+2Rcos2r}\right\} \quad (3.16)$$

where θ and r are the angles of incidence and refraction respectively (Ashkin, 1992).

Methods for characterisation of optical traps are discussed later in Chapter 6.

3.7.2 Biological applications of optical trapping

The forces described above are on the order of piconewtons, and thus restricted to influencing the motion of objects only a few microns in diameter or smaller. However, this makes optical trapping an ideal tool for studies on the cellular and molecular level. Optical tweezers and dual beam traps have been used in multiple studies to trap both whole cells and microsphere "handles" that are attached to biomolecules of interest. Near-infrared beams are often used in biological optical trapping studies to reduce absorption by the sample and thus minimise optical damage (Dholakia, Reece & Gu, 2008). Examples of seminal and recent single molecule and whole cell optical trapping experiments are given below. Optical trapping on microscopy platforms for simultaneous trapping and imaging is also discussed.

3.7.2.1 Single molecule experiments

Calibration of optical tweezers allows measurements of forces produced by molecular motors, examples of which include kinesin which walks along microtubules, and RNA polymerase which progresses along a DNA template to generate complementary RNA. The movement of these proteins is often stepwise and driven by ATP hydrolysis. In single molecule optical trapping experiments, the molecular motors are not trapped directly, but rather the motor substrate, e.g. DNA, is attached to a trapped microsphere, or bead, using surface chemistry e.g. biotin-streptavidin links. Interaction of the substrate with a motor, e.g. RNA polymerase (RNAP), causes variations in the location of the bead within the trap which can be precisely monitored using a quadrant photodiode and used to calculate the force and movement of the motor.

Original single molecule optical trapping experiments were performed on kinesin and microtubules. Silica beads incubated with kinesin were captured in suspension with optical tweezers and moved to microtubules bound to a coverglass, to which they would spontaneously attach and move along (Block, Goldstein & Schnapp, 1990; Svoboda *et al*., 1993). Using a dual beam interferometer optical trap, a step size of ~8nm was measured, and hydrolysis of a single molecule of ATP observed per step (Svoboda *et al*., 1993). In a separate study, the movement of RNAP along a DNA template was examined using double optical tweezers (Abbondanzieri *et al*., 2005). DNA was attached to a polystyrene bead and held ~1µm above a coverglass with a strong optical trap, whilst a second bead attached to RNAP was held weakly

by a second adjacent trap but away from the trap focus, creating a "force clamp" (Figure 3.12). Discrete steps by RNAP of 3.7 ± 0.6Å were observed, corresponding to the mean rise per DNA base pair (Abbondanzieri *et al*., 2005). The trapping apparatus was enclosed in helium, which has a refractive index close to unity, in order to reduce beam wander and thus background noise due to turbulence. Similar optical tweezer setups have been used to further investigate DNA transcription by RNAP, for example to examine the effect of elongation factors on transcriptional pausing (Zhou *et al*., 2011).

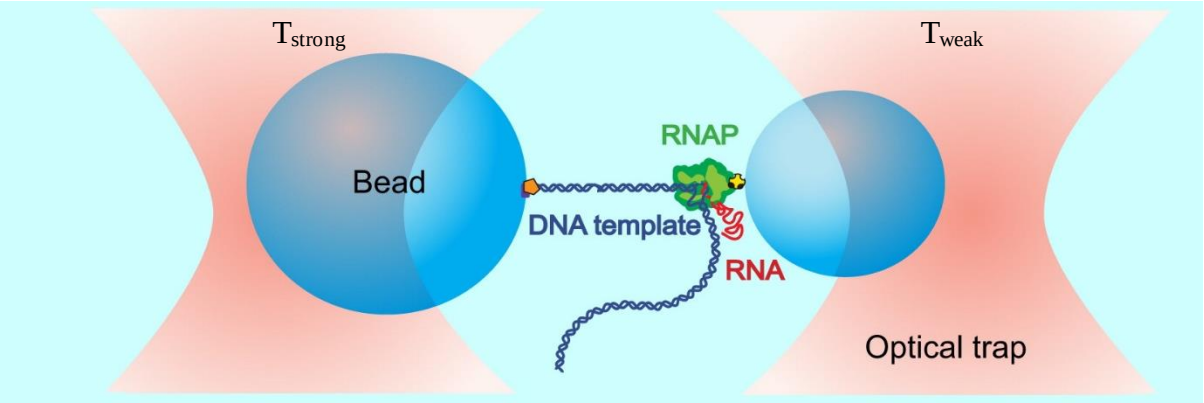

Figure 3.12 Cartoon of double optical tweezers geometry for molecular motor measurements. A single transcriptionally active RNAP molecule (green) is attached to a polystyrene bead held in a weak trap, T_{weak}, and tethered to a second larger bead held in a stable trap, T_{strong}, via a strand of template DNA (dark blue). During the course of transcription, the DNA tether lengthens, increasing the distance between the two beads. The right-hand bead is held away from the focus of the trap within a region of near-constant trapping force, whilst the left-hand bead is stably trapped. Only the right-hand bead moves, and it is for this bead that displacements are measured. Image adapted from Zhou *et al*., 2011. Drawing not to scale.

Nanoaperture optical tweezers have emerged as a powerful alternative to conventional optical tweezers for single molecule studies, allowing proteins and other molecules to be trapped directly using laser powers of ~3mW, without the need for tethers or microsphere handles (Al Balushi *et al*., 2015). The molecule of interest can therefore be studied in its native state, facilitating studies of single protein-protein and protein-DNA interactions. Other recent advances in single molecule optical trapping techniques have involved the hybridisation of optical tweezers and fluorescence microscopy, as discussed in Section 3.7.2.4.

3.7.2.2 Whole cell experiments

In addition to observing the mechanics of single molecules, optical tweezers can be used to manipulate and investigate the mechanical properties of whole cells. Multiple studies have utilised optical traps to position, transport, sort and even cut single cells (Zhang & Liu, 2008). For example, by employing an optical trap to capture single cells, six different species of bacteria could be identified and discriminated using Raman spectroscopy (Xie *et al*., 2005). More recently, the differentiation status of tumour cells was shown to be discernible by observing cell-cell adhesion: a single cell was trapped and placed near another, and the minimum time for adhesion to occur measured; a substantially higher minimum adhesion time was observed for tumour cells compared to neural progenitor stem cells, which was reversible upon tumour cell differentiation with retinoic acid (Pradhan *et al*., 2016). Optical tweezers can be used in conjunction with fluorescence-activated cell sorting (FACS): in microfluidic FACS, the detection of fluorescent cells triggers the switching on of either single or multiple traps and deflection of targeted cells to an output channel (Wang *et al*., 2005a). Using this setup, cells expressing a fused green-fluorescent protein were successfully separated from non-expressing cells. Single-fibre optical tweezers have been used to demonstrate enhanced axonal growth of neuronal cells irradiated with near-infrared laser light (Mohanty, Mohanty & Berns, 2008). By mode-locking the laser beam, the optical tweezers were transformed into optical scissors capable of cutting neuronal processes. In addition, cell stretching was achieved by trapping the neuronal cells in suspension, with cell elongation occurring along the direction of beam propagation (Mohanty, Mohanty & Berns, 2008).

Many of the studies that have used optical traps to deform cells have been carried out on RBCs owing to their malleable nature. By deforming a RBC using either force-calibrated double optical tweezers or a counter-propagating dual-beam trap, its shear modulus, or elasticity, can be measured. The shear modulus is a useful measure for comparing the state of individual RBCs, and can, for example, distinguish between those that are healthy and those that are infected with malaria parasites (Suresh *et al*., 2005). Trapping of RBCs has extended as far as trapping in living animals: tissue-penetrating infrared optical tweezers were used to trap RBCs in subdermal capillaries in live mice and perform a non-contact micro-operation, resulting in clearing of a blocked vessel (Zhong *et al*., 2013b).

Optical tweezers have, however, also been used to mechanically stimulate non-RBCs. In a 2005 study, for example, the authors applied beads coated with fibronectin, an extracellular

matrix protein that binds to integrins, to the membrane of human umbilical vein endothelial cells using single-beam optical tweezers (Wang *et al*., 2005b; Botvinick & Wang 2007). By pulling the adhered beads with the tweezers using controlled mechanical force (300pN), a local FRET response of a genetically-encoded Src reporter was stimulated around the beads, and a slower wave of signal propagation activated along the plasma membrane via the cytoskeleton.

Deformation of cells using the counter-propagating dual-beam trap configuration, or "cell-stretcher", is discussed below.

3.7.2.3 The optical stretcher

The optical stretcher is based upon two opposing optical fibres aligned such that the two beams counter-propagate one another (Guck *et al*., 2001). A dielectric, elastic object of refractive index greater than that of the surrounding medium placed and trapped between the two beams experiences additive surface forces such that the object is stretched along the axis of the beams (Figure 3.13). Since the light propagating from the fibres is confined and already has an intensity gradient, no focusing of the beams is required, thus minimising radiation damage to biological samples. Initial experiments using the optical stretcher were carried out on RBCs; however, suspended mouse fibroblasts were also successfully stretched. Subsequently, the optical stretcher has been used to distinguish between normal and malignant mouse fibroblasts and human breast epithelial cells by comparison of optical deformability (Guck *et al*., 2005).

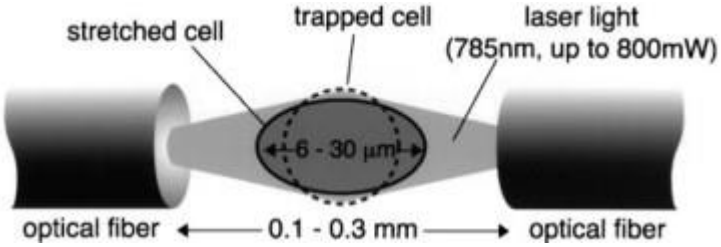

Figure 3.13 Schematic of a cell deformed by the optical stretcher. An elastic cell of refractive index higher than that of the surrounding medium is stably trapped between the two beams, and at sufficient laser power, stretched out along the laser beam axis due to momentum transfer from the photons to the cell surface. Drawing not to scale. Image from Guck *et al*., 2001.

More recently, the optical stretcher has been surpassed by real-time deformability cytometry (RT-DC), a method for continuous mechanical characterisation of large (>100,000) populations of cells (Otto *et al*., 2015). Instead of optical tweezers, RT-DC uses a microfluidic channel constriction to slow down and deform cells flowing through. Deformed cells are

illuminated using a pulsed LED and imaged using a high-speed camera, and analysis of cell deformation performed in real-time. RT-DC is sensitive to the actin cytoskeleton and can distinguish between cells in different stages of the cell cycle and differentiation (Otto *et al*., 2015). Cell populations within whole human blood can also be identified in a label-free manner.

3.7.2.4 Trapping on microscopy platforms

Trapping on a microscope platform allows simultaneous object manipulation and visualisation. Many of the above studies use basic microscopy setups to observe the trapped object. However, the advent of enhanced- and super-resolution light microscopy techniques means that objects can now be trapped and simultaneously imaged in greater detail than ever before. An early example is the combination of optical trapping and confocal microscopy (Hoffmann *et al*., 2000). In this study, 3D imaging of trapped chloroplasts in a vigorous cytoplasmic stream using a single objective was made possible by maintaining a fixed axial trapping position and moving the focal plane of the objective over ~15µm using fast-moving correctional optics. A separate study also combined confocal microscopy with optical trapping by using two objectives, one above and one below the sample, to decouple imaging from trapping (Vossen *et al*., 2004).

Holographic optical tweezers have recently been combined with the single-molecule localization microscopy technique STORM (Diekmann *et al*., 2016). An SLM shaped the trapping beam to create multiple, independent traps, which were used to hold freely diffusing bacterial cells in different orientations whilst imaging was carried out. 3D images of chromosomal DNA within *Escherichia coli* were obtained with <100nm resolution.

Physical space constraints are often an issue for combining optical tweezers and super-resolution microscopes, especially commercial systems, and therefore miniaturised traps are appealing. An example of a miniaturised trap on a super-resolution platform is the fibre-based gradient-index (GRIN) lens trap (Nylk *et al*., 2015). This miniaturised trapping apparatus was incorporated onto the N-SIM and used to trap mouse cells and induce formation of an immunological synapse, though imaging using the structured illumination capability of the microscope was not demonstrated (Nylk *et al*., 2015).

3.8 Concluding remarks

Since its inception, super-resolution microscopy has surpassed conventional fluorescence microscopy to become the method of choice for dissecting the fine ultrastructure of cells. However, in the case of live-cell imaging, there often exists a trade-off between temporal and spatial resolution. Recently, there has been a push for the development of systems that are capable of multimodal 3D super-resolution imaging in living samples. To this end, super-resolution modalities are being combined in order to exploit their unique benefits and meet imaging demands. Similarly, optical traps are being designed for super-resolution platforms for simultaneous high-performance imaging and micromanipulation. SIM offers double the resolution of conventional widefield fluorescence microscopy, along with ease of use, low light intensities and fast image acquisition, and is therefore an ideal choice for such an implementation. Recent studies also show promise for super-resolution microscopy and optical trapping replacing more traditional but slower methods such as EM for disease diagnosis in the near future.

Perhaps one of the most exciting developments in the realm of optical trapping is the idea that manipulation of objects by purely optical methods may have a significant impact in the advances of modern medicine. For example, the 'micro-surgery' performed by Zhong *et al*. (Zhong *et al*., 2013b) for clearing a blocked blood vessel in a living mouse may pave the way for optical trapping as one of a number of future methods for non-invasive surgical procedures. In addition, optical manipulation of whole cells has already shown great promise for disease diagnosis (Guck *et al*., 2005).

In this thesis, 3D-SIM is used to examine the effect of Willin expression on the actin cytoskeleton (Chapters 5 and 7) and investigate potential interactions between Willin and actin and Willin and AMOT (Chapter 7). In addition, the N-SIM is used as a platform for construction of a double optical trap with the aim of simultaneously stretching and imaging neuronal cells (Chapter 6).

4 Materials and methods

4.1 Plasmid preparation

4.1.1 Transformation of E. coli

DNA plasmids were obtained from Addgene/Clontech (see Table 4.1 for list of plasmids used). 1µl of DNA plasmid was added to 50µl of competent DH5α *E. coli* cells (New England Biolabs) and the combination mixed gently. Cells were incubated on ice for 30 mins then heat shocked at 42°C for 30 seconds and placed back on ice for 2 mins. 250µl of Super Optimal broth with Catabolite repression (SOC) medium (Sigma-Aldrich) was added to the cells and the mixture incubated in Bijou bottles at 37°C, shaking at 210 RPM for 1 hr. 200µl of transformed cells were streaked onto Luria broth (LB) (1% Tryptone, 0.5% yeast extract, 0.5% NaCl, 1.5% Agar; Sigma-Aldrich) agar plates containing 50µg/ml kanamycin, and the plates incubated at 37°C for 16 hrs.

4.1.2 Plasmid purification

A single transformed bacterial colony was transferred to 7ml of LB medium containing 50µg/ml kanamycin using a sterile loop and incubated at 37°C, shaking at 210 RPM overnight for 16 hrs. Plasmid DNA was then isolated using the QIAprep Spin Miniprep Kit (Qiagen) according to the manufacturer's protocol. Purified plasmid DNA was reconstituted in 50µl ultrapure Mili-Q® water and the concentration measured using the NanoDrop™ 2000 Spectrophotometer (Thermo Fisher Scientific) at 260nm absorbance. DNA sequencing was performed by DNA Sequencing & Services (University of Dundee, UK).

4.1.3 Generation of glycerol stocks

Glycerol stocks of bacterial cultures containing plasmid DNA were prepared by gently mixing 750µl of fresh overnight culture with 250µl of sterile 80% glycerol and stored at -80°C.

4.1.4 DNA maxiprep

Maxipreps of plasmid DNA were produced from overnight starter cultures. 500µl of bacterial culture was added to 200ml of LB medium containing 50µg/ml kanamycin and grown for 16 hrs at 37°C, shaking at 225 RPM. Purified plasmid DNA was obtained using the Endo-Free Plasmid Maxi Kit (Qiagen) according to the manufacturer's protocol and reconstituted in 200µl of ultrapure water. DNA concentrations were measured using the NanoDrop™ 2000 Spectrophotometer at 260nm absorbance and purified DNA stored at -20°C.

Table 4.1 Table of plasmids used

Plasmid	Expressed protein	Resistance	Company
pEGFP-C3-hYAP1	YAP-GFP	Kanamycin/neomycin	Addgene
pLifeAct tagRFP-T	Lifeact-RFP	Kanamycin/neomycin	Addgene
pmCherry-N1	Willin-mCherry	Kanamycin/neomycin	Clontech
pmCherry-C1	mCherry	Kanamycin/neomycin	Clontech

4.2 Cell culture

4.2.1 Cell lines

ShScr and shWillin SH-SY5Y cell lines were obtained from previously made cell stocks. ShScr-YAP-GFP, shWillin-YAP-GFP, shScr-Lifeact-RFP, shWillin-Lifeact-RFP and Willin-mCherry cell lines were generated via nucleofection and selection of shScr/shWillin/wild-type SH-SY5Y cells (see below).

4.2.2 Cell culture conditions

Cells were cultured in a humidified atmosphere of 5% CO_2 at 37°C. Cells were grown in Gibco™ Dulbecco's Modified Eagle Medium: Nutrient Mixture F-12 (DMEM/F-12) media (Thermo Fisher Scientific) supplemented with 10% FBS and 100 units/ml penicillin and 100µg/ml streptomycin (Thermo Fisher Scientific) and passaged at ~80% confluency using Gibco™ TrypLE™ Express (Thermo Fisher Scientific). Cell stocks were frozen in 90%

FBS/10% sterile-filtered DMSO (Sigma-Aldrich) cryoprotectant medium and stored in liquid Nitrogen.

The volumes of media and experimental number of cells used in various culture vessels are given in Table 4.2.

Table 4.2 Plating conditions for cell culture vessels

Cell culture vessel	Growth area (cm^2)	Volume of media (ml)	No. of cells
T25 flask	25	7	3×10^6 at 80% confluency
T75 flask	75	13	10×10^6 at 80% confluency
Single well of 6 well plate	9.6	2	1.22×10^5
35mm dish	10	3	1.76×10^5
10cm	56.7	10	1×10^6

4.2.3 Transfection

Cells were seeded on sterile coverslips in a 6 well plate and incubated for 16-24 hrs at 37°C, 5% CO_2. 1µg DNA and 6µl GeneJammer transfection reagent (Agilent) were separately added to 50µl of Gibco™ Opti-MEM™ I Reduced Serum Medium + GlutaMAX™-I Supplement (Thermo Fisher Scientific) and then mixed and incubated at room-temperature for 30 mins before being added dropwise to a single well. After 48 hrs, cells were fixed with 4% paraformaldehyde (PFA) (Thermo Fisher Scientific) for 15 minutes, and the coverslips mounted for examination (see Section 4.4.1).

4.2.4 Nucleofection

Cells were electroporated by nucleofection using the Cell Line Nucleofector™ Kit V (Lonza). 2×10^6 cells were harvested by trypsinization and centrifuged at 1200 RPM for 3 mins, and the pellet resuspended in 100µl Nucleofector™ solution. 2µg DNA was added to the cell suspension, and the mixture transferred to a Lonza cuvette. Cells were electroporated using the Amaxa™ Nucleofector™ II, programme A-023, then removed in 500µl pre-warmed culture media and immediately transferred to T25 flasks and incubated.

4.2.5 Selection and maintenance of cell lines

24 hrs after nucleofection, cell media was replenished, and cells were grown for a further 72 hrs. Culture media was then replaced with medium containing selective antibiotic (see Table 4.3) to select for successfully transfected cells. After selection was complete (7-14 days), cell lines were maintained with media containing a base level of antibiotic, which was subsequently removed during cell assays.

Table 4.3 Selective antibiotic concentrations for selection and maintenance of cell lines

Cell line	Selection G418 (µg/ml)	Maintenance G418 (µg/ml)	Maintenance puromycin (µg/ml)
shScr	-	-	1.5
shWillin	-	-	1.5
shScr-YAP-GFP	500	200	1.5
shWillin-YAP-GFP	500	200	1.5
shScr-Lifeact-RFP	500	200	1.5
shWillin-Lifeact-RFP	500	200	1.5
Willin-mCherry	500	200	-

4.2.6 Differentiation

10cm dishes and 22mm x 22mm 1.5 precision thickness (170µm ±5µm) coverslips (Thorlabs) in 6 well plates were coated with 20µg/ml poly-l-ornithine (Sigma-Aldrich) in sterile PBS and incubated for 1 hr at 37°C, 5% CO_2. Dishes and coverslips were then washed three times with PBS and incubated with 5µg/ml mouse laminin (Thermo Fisher Scientific) in PBS for 2 hrs at 37°C, 5% CO_2. The laminin was washed three times with PBS, and cells plated onto the coated dishes and coverslips and grown for 16-24 hrs. The next day (day 1), and on day 4, half of the media was removed and replaced with 1% FBS DMEM/F-12 media containing 20µM retinoic acid (RA) (Sigma-Aldrich). On day 8, cells were washed three times with 0% FBS media and incubated in 0% FBS media containing 50ng/ml brain-derived neurotrophic factor (BDNF) (Peprotech) for a following 3 days. Cell lysates were prepared from the 10cm dishes and immunocytochemistry carried out on cells grown on coverslips on days 1, 4, 8 and 11 prior to media changes (see below).

4.3 RNA and protein analysis

4.3.1 RNA extraction

Cells were plated on 10cm dishes and incubated at 37°C, 5% CO_2 for 24 hrs. The media was then removed and 1ml TRIzol® Reagent (Thermo Fisher Scientific) added to each dish for 5 mins. The resulting mixture was transferred to an Eppendorf tube and 0.2ml chloroform (Thermo Fisher Scientific) added. The mix was inverted until it turned an even shade of pink and incubated at room-temperature for 2-3 mins. Phase separation of the mixture was achieved by centrifugation at 12,000g at 4°C for 15 mins. The upper colourless RNA-containing phase was then transferred to a fresh RNA-ase free tube and diluted with an equal volume of 70% ethanol. RNA purification was performed using the Ambion® PureLink™ RNA Mini Kit (Thermo Fisher Scientific). Briefly, the sample was transferred to a spin cartridge to allow binding of RNA to the cartridge membrane, after which the RNA was washed and eluted. Purified RNA was dissolved in RNAase free water, and the concentration of the sample measured using the NanoDrop™ 2000 Spectrophotometer at 260nm absorbance. The final RNA product was stored at -80°C.

4.3.2 Reverse transcription

Reverse transcription of the extracted cellular RNA was carried out using the RevertAid First Strand cDNA Synthesis Kit (Thermo Fisher Scientific). RNA/primer mixtures were prepared by adding 1µg RNA, 1µl OligoDT or random hexamer primer, and nuclease-free water to a volume of 12µl to sterile nuclease-free Eppendorf tubes on ice. Reaction master mixtures were then prepared by adding 5x reaction buffer, 20 units RiboLock RNase inhibitor, dNTP mix (final concentration 1mM) and 200 units RevertAid reverse transcriptase to the RNA/primer mixtures for a total volume of 20µl per reaction mixture. The mixtures were centrifuged briefly and incubated at 25°C for 5 mins, followed by 42°C for 60 mins. The reaction was terminated by heat inactivation at 70°C for 5 mins. Reaction mixtures were incubated in a S1000 Thermal Cycler (Bio-Rad). cDNA products were stored at -20°C until use for Real-Time PCR.

4.3.3 Real-time polymerase chain reaction

Real-time polymerase chain reaction (RT-PCR), or quantitative PCR (qPCR), was carried out using the Brilliant III Ultra-Fast SYBR® Green QPCR Master Mix (Agilent) according to the manufacturer's protocol. RT-PCR reaction mixtures were prepared by combining 10µl 2X SYBR Green QPCR Master Mix, 1µl forward-primer, 1µl reverse-primer, and 7µl nuclease-free H_2O per reaction. RT-PCR primers were gene specific (for sequences see Appendix A). Reaction mixtures were aliquoted to PCR tubes, and 1µl cDNA, or nuclease-free H_2O in the case of no template controls, was added to each tube for a final reaction volume of 20µl. RT-PCR reactions were performed on the Rotor-Gene Q (QIAGEN) and dissociation curves analysed using the Rotor Gene Q Series Software. Melt curves were obtained to assess RT-PCR product purity. All measurements were performed in triplicate and standardised against β-actin, and relative levels of cDNA calculated using the $2^{-\Delta\Delta CT}$ method. The RT-PCR thermal cycle is shown in Table 4.4.

Table 4.4 RT-PCR thermal cycle conditions

Step	Temperature (°C)	Duration (s)	No. of cycles
Polymerase activation	95	180	1
Denaturation/annealing & elongation	95	10	40
	60	30	
Melt curve	55-95	30/0.5°C	1

4.3.4 Preparation of cell lysates

Cells were plated on 10cm dishes and incubated for 24 hrs at 37°C, 5% CO_2. Cells were then washed with 10ml ice-cold PBS and the excess PBS removed. 120µl of RIPA buffer (50mM Tris-HCl, pH 8.0, 150mM NaCl, 1.0% Triton X-100, 0.5% sodium deoxycholate, 0.1% sodium dodecyl sulphate (SDS) (all reagents purchased from Sigma-Aldrich)) with protease inhibitor (Pierce Protease Inhibitor Mini Tablets, EDTA-free) (Thermo Fisher Scientific) and in the case of investigation of phosphorylated proteins, phosphatase inhibitors (Sigma-Aldrich), was added to each dish, and the cells removed with a cell scraper and transferred into 1.5ml Eppendorf tubes. The cells were placed on ice for 30 mins, after which they were centrifuged at 13,000RPM for 10 mins to remove debris, and the clear lysates frozen and stored at -80°C.

4.3.5 BCA assay

Lysate protein concentrations were measured by carrying out a bicinchonic acid (BCA) assay. Briefly, 5µl of cell lysate and samples of known concentration of bovine serum albumin (BSA) (Thermo Fisher Scientific) diluted in RIPA buffer (0.0-2mg/ml) were added in duplicate to a 96-well plate and incubated with 100µl of BCA working reagent (Thermo Fisher Scientific) for 30 mins at 37°C. Endpoint absorbance of the purple reaction product was then measured at 562nm using the SpectraMax® M2^e spectrophotometer (Molecular Devices) and a standard curve of absorbance vs. protein concentration generated from the known BSA standards for determination of cell lysate protein concentrations.

4.3.6 SDS-PAGE

10% Tris-glycine gels were prepared for sodium dodecyl sulphate-polyacrylamide gel electrophoresis (SDS-PAGE) using 1.5ml spacer plates (Bio-Rad) by pouring and setting first the resolving gel (10% acrylamide (Thermo Fisher Scientific), 375mM Tris-HCl, pH 8.8, 0.1% SDS, 0.1% ammonium persulfate (Thermo Fisher Scientific), 0.1% TEMED (Thermo Fisher Scientific)) then the stacking gel (6% acrylamide, 125mM Tris-HCl, pH 6.8, 0.1% SDS, 0.1% ammonium persulfate, 0.1% TEMED); 12% Tris-glycine gels were used for resolving small proteins. Gels were placed in a Bio-Rad electrophoresis chamber and running buffer added (25mM Tris base, pH 8.3, 192mM glycine, 0.1% SDS (all reagents purchased from Sigma-Aldrich)). Protein samples were prepared with 20µg of protein lysate and 5x loading buffer (500mM dithiothreitol, 250mM Tris-HCl, pH 6.8, 50% glycerol, 10% SDS, 0.25% Bromophenol blue (all reagents purchased from Sigma-Aldrich)) and made up to final volume (20-35µl) with distilled water. Samples were boiled for 5 mins at 95°C and loaded into the gel wells alongside 5µl of protein marker (Blue Prestained Protein Standard, Broad Range 11-190kDa; New England Biolabs). Gels were run at 80V for 25 mins, after which the voltage was increased to 120V until the loading dye had reached the gel edge.

4.3.7 Western blotting

Protein lysates from the SDS-PAGE gel were transferred onto Immobilon™ FL polyvinylidene fluoride (PVDF) transfer membrane (EMD Millipore) using a Bio-Rad blotting module by blotting in transfer buffer (25mM Tris base, pH 8.3, 192mM glycine, 20% (v/v) methanol

(Thermo Fisher Scientific)) for 90-120 mins at 25V. The membrane was stained with Ponceau S solution (Sigma-Aldrich) to verify effective protein transfer, then washed with TBS-T (20mM Tris base, pH 7.6, 150mM NaCl, 0.1% Tween-20 (Sigma-Aldrich)). Membranes were blocked in either 5% skimmed dried milk (Marvel) in TBS-T or 5% BSA in TBS-T for 1 hr at room-temperature, before being incubated with primary antibody diluted in blocking solution overnight at 4°C (see Appendix B for blocking and primary and secondary antibody conditions). Membranes were then washed with TBS-T for 10 mins three times and incubated with horseradish peroxidase (HRP)-conjugated secondary antibody diluted in blocking solution for 1 hr at room-temperature. Membranes were washed with TBS-T for 15 mins three times, and protein bands detected by addition of 0.75ml Immobilon Western Chemiluminescent HRP Substrate (Merck Millipore) for 1 min. Bands were visualised with the LAS-3000 imaging system (Fujifilm) and analysed using FIJI.

4.3.8 Immunoprecipitation

Cells were grown to confluency on 10cm plates and lysed with 120µl Pierce™ immunoprecipitation (IP) lysis buffer (Thermo Fisher Scientific) containing protease inhibitor. Immunoprecipitation samples containing 1mg total protein were made up to a volume of 200µl with IP lysis buffer and stored on ice. 20µl protein A magnetic beads (New England Biolabs) were washed twice with 500µl IP lysis buffer using a magnetic separation rack (New England Biolabs). Immunoprecipitation samples were added to the pre-washed beads and incubated with rotation for 30 mins at room-temperature. The beads were then separated from the samples using the magnetic rack and discarded to remove any non-specifically bound proteins. 40µg pre-cleared lysate per sample was retained and stored at -80°C. Primary/isotype control antibody was added to the remaining immunoprecipitation sample, and the mix incubated with rotation overnight at 4°C to form the immunocomplex. After 16 hrs, the immunoprecipitation/antibody solution was transferred to a clean 1.5ml Eppendorf microcentrifuge tube containing 25µl pre-washed beads and incubated with rotation for 1 hr at 4°C. The beads were then pelleted using the magnetic rack and 40µl of the supernatant (unbound lysate) retained and stored on ice. The bead pellet was resuspended in 40µl 3x SDS sample loading buffer (187.5 mM Tris-HCl, pH 6.8, 6% (w/v) SDS, 30% glycerol, 150 mM DTT, 0.03% bromophenol blue, 2% β-mercaptoethanol; New England Biolabs) and incubated at 95°C for 5 mins. The beads were then pelleted, and the supernatant loaded onto a 10% SDS-PAGE gel alongside the pre-cleared and unbound lysate for procedure with Western blotting.

4.4 Cell assays

4.4.1 Immunocytochemistry

Cells were plated on 22mm x 22mm 1.5 precision thickness coverslips in 6 well plates and incubated at 37°C, 5% CO_2. After 16-24 hrs, the media was removed from the wells and cells washed with 2ml per well room-temperature PBS for 5 mins. The PBS was then removed, and the cells fixed with 2ml 4% PFA in PBS for 15 mins. Cells were washed twice with 0.05% Tween-20 in PBS and permeabilized with 2ml 0.1% Triton X-100 in PBS (PBS-T) for 3 mins. Cells were then blocked for 1 hr with 2ml 10% goat serum in PBS-T then incubated with primary antibody diluted in 200µl blocking solution overnight at 4°C. After 16 hrs, cells were washed with 0.05% Tween-20 in PBS for five mins three times and incubated with secondary antibody diluted in 200µl PBS for 1 hr at room-temperature in the dark. Cells were washed with 0.05% Tween-20 in PBS for 10 mins three times, and the coverslips mounted on slides using ProLong™ gold antifade mountant with DAPI (Thermo Fisher Scientific). Primary and secondary antibody conditions are given in Appendix B.

For visualisation of the actin cytoskeleton, cells were plated on coverslips and fixed as above. Cells were permeabilized with IGEPAL® CA-630 (Sigma-Aldrich) for 5 mins then washed three times with PBS and incubated with 1 unit (5µl) of Alexa Fluor™ 488 Phalloidin (Thermo Fisher Scientific) diluted in 200µl PBS per coverslip in the dark for 30 mins at room-temperature. Cells were washed three time with PBS and the coverslips dried and mounted as above.

Intracellular vesicle staining was carried out using Bodipy 495/503 (Thermo Fisher Scientific). 3µg/ml Bodipy in PBS was added to cells seeded on coverslips in 6 well plates, and the cells incubated overnight. After 16-24 hrs, the cells were washed three times with media and fixed with 4% PFA and mounted on slides as above.

4.4.2 Growth of cells on hydrogels

Chemically activated hydrogels of 0.5, 4 and 50kPa stiffness bound to 35mm polystyrene glass-bottomed (20mm diameter glass surface) dishes or 10cm dishes (Matrigen Softwell, Cell Guidance Systems) were coated with 5µg/ml laminin in sterile PBS and incubated at room-temperature. After 1hr, the solution was removed, and the dishes rinsed once in PBS and 1.76

x 10^5 or 1 x 10^6 cells added to each 35mm or 10cm dish respectively. Cells seeded on 35mm dishes were incubated at 37°C, 5% CO2 for 24 hrs before being fixed with 4% PFA in PBS for 15 mins then washed twice with PBS. Nuclei staining was carried out by incubating cells with 1µg/ml DAPI (Sigma-Aldrich) in PBS for 7 minutes at room-temperature. Cells were then washed once in PBS and examined under 20x magnification using SIM microscopy. Cells seeded on hydrogels bound to 10cm dishes were grown to confluency and trypsinized using 5ml TrypLE™ Express. Cell pellets were then washed once in ice-cold PBS and resuspended in 120µl RIPA buffer containing protease inhibitor. The cells were then placed on ice for 30 mins, after which they were centrifuged at 13,000RPM for 10 mins to remove debris and the clear lysates frozen and stored at -80°C.

4.5 Cell microscopy

4.5.1 Structured Illumination Microscopy (SIM)

Cells were grown on 22mm x 22mm 1.5 precision thickness coverslips and fixed as per above (Section 4.4.1). Coverslips were mounted on glass slides for examination using the N-SIM inverted microscope. SIM is a fluorescence imaging technique and so all cells imaged using SIM were either derived from fluorescent cell lines (see Section 4.2.1) or probed using fluorescent antibodies.

Prior to image acquisition, the N-SIM was calibrated for optimal image quality (see Appendix C for detailed calibration procedures). Images were acquired using the Nikon SIM imaging software: the sample was brought into focus live using z adjustment of the SIM objective (100x, Apo TIRF, NA 1.49, Nikon), and the illumination intensity of the SIM lasers set for each laser channel (405nm, 488nm and 561nm) to produce a fluorescent signal in the linear range of the camera (iXon 897, ANDOR) (signal between 10,000 and 13,000 arbitrary value). Images were then obtained as either single planes or z stacks for which the image volume was set around a middle z plane. Images could be acquired in standard widefield or 3D-SIM mode. Acquisition of 3D-SIM images required 15 individual image frames to create a raw image for a single z plane from which the final image was reconstructed using the Nikon imaging software (see Appendix C for image reconstruction parameters). Live-cell imaging was carried out using the stage top incubator (INUG2H-TIZSH, Tokai Hit) by first setting the laser illumination intensities as above and then the imaging time interval and duration.

4.5.2 Elastic Resonator Interference Stress Microscopy (ERISM)

Cells were seeded on either 0.5cm^2 or 1cm^2 collagen-coated microcavity sensors at a density of 6000 cells/cm^2 in a total volume of 400/800µl and incubated at 37°C, 5% CO_2 for 24 hrs. ERISM measurements were then carried out using an inverted Nikon Ti-S fluorescence microscope as follows: phase contrast images were taken to identify cells of interest, then reflectance images collected for a set of 201 illumination wavelengths at 550-750nm. For cells undergoing differentiation, measurements were taken on days 1 (pre-differentiation), 3, 6, 8 and 10, with half media changes (1% FBS DMEM/F-12 containing 20µM retinoic acid) carried out post-measurement on days 1, 3 and 6, and a full media change (0% FBS media containing 50ng/ml BDNF after washing the cells three times with 0% FBS media) on day 8. Long-term cell adhesion measurements were taken on days 1, 3, 6, 8 and 10, with half media changes post-measurement on days 3 and 8.

Analysis of reflectance images was carried out using the ERISM_Calc. programme. Briefly, resonance wavelengths were determined for each pixel and compared to a look-up-table of elastomer thickness vs. resonance wavelengths to obtain an elastomer thickness map. An elastomer deformation map was then created by subtracting the elastomer background thickness using the subtract_background programme. The volume of elastomer indentation was calculated for each cell in µm^3 by first determining the area of the cell for which the elastomer displacement was below -10nm for each pixel, calculating the average pixel displacement in this area and multiplying by the area as determined above. Fourier-filtered displacement maps were generated as follows: first the real space displacement map was transformed into a Fourier map of its frequency components and filtered to remove low frequency information; the resulting Fourier map was then transformed back into a real space displacement map that showed only high frequency elastomer deformations e.g. those produced by focal adhesions. All ERISM measurements were analysed using OriginPro. Post-measurements, cells were fixed using 4% PFA for 20 mins, and immunocytochemistry performed for proteins of interest as above. Fluorescence imaging was carried out under 40x magnification using the Nikon Ti-S microscope.

4.5.3 Image analysis

3D-SIM z-stacks of renal slices were analysed using FIJI (ImageJ). Briefly, a maximum intensity profile was created from each stack, and image regions manually defined using the area selection tool. Curvilinear structures were identified for each region using the Ridge Detection plugin, and the slit diaphragm density (SDD) calculated using Excel. For fully-automated image analysis, images were filtered for removal of background noise and thresholded to create an image mask of the region of interest; the mask was then multiplied with the original maximum intensity profile image, and the final image analysed using the Ridge detection plugin.

Lateral intensity profiles of the optical trapping beams were created in FIJI using the straight line and plot profile tools, and analysed in Excel.

5 Qualitative and quantitative studies using structured illumination microscopy

5.1 Introduction

Structured illumination microscopy (SIM) yields a theoretical two-fold increase in resolution over standard widefield fluorescence microscopy (Gustafsson, 2000) (see Chapter 3 for detailed explanation of SIM). Many cellular substructures such as actin filaments are just smaller in size than the diffraction limit of the conventional light microscope, and therefore ideally suited for examination by SIM. Here, the use of SIM is described for two separate studies, the first at the cellular level using the SH-SY5Y cell line, and the second at the clinical level. Practical considerations for use of the N-SIM are given in Appendix C.

The SH-SY5Y neuroblastoma cell line is a human-derived immortalized cell line commonly used as a neuronal cell model in place of primary mammalian neurons (Kovalevich & Langford, 2013). SH-SY5Y cells can be differentiated via chemical induction into a more neuron-like state. This chapter firstly defines the practical lateral resolution obtained by the commercial N-SIM at both 100x and 20x magnification using fixed SH-SY5Y cells, before examining the effect of Willin expression on SH-SY5Y differentiation. Quantitative analysis of renal biopsy SIM images towards a novel method for the clinical diagnosis of nephrotic syndrome is then described.

5.2 Lateral resolution of the N-SIM

According to the Abbe criterion, the theoretical lateral resolution obtained by a widefield microscope when imaging with an excitation wavelength of 488nm and a 1.49 NA objective lens is:

$$r_{x,y} = \frac{\lambda}{2NA} \tag{5.1}$$

$$r_{x,y} = \frac{488nm}{2.98} = 164nm \tag{5.2}$$

Under the same imaging parameters, the theoretical lateral resolution given by SIM is therefore ≈ 164nm /2 ≈ 82nm.

To determine the practical lateral resolution of the N-SIM and ascertain the quality of 3D-SIM compared to widefield images, fixed cell samples were imaged using both modes under 100x magnification. Comparative 3D-SIM and widefield images of SH-SY5Y cells stained with the actin marker Phalloidin-488 are shown below (Figure 5.1a, b). As illustrated in the zoomed in image selections, individual actin filaments appeared blurred in the widefield view compared to the 3D-SIM view. Line profiles through the rectangular selections showed a high level of background in the widefield image (Figure 5.1c), but separated peaks in the 3D-SIM image representing individually resolved actin filaments (Figure 5.1d). Lateral 3D-SIM resolution using the 100x objective was calculated from the full-width at half-maximum (FWHM) of the line profile peak from an individual actin filament as 129±32nm (Figure 5.1e).

Comparative 20x magnification 3D-SIM and widefield images of SH-SY5Y cells also stained for actin are shown in Figure 5.2. As for the 100x images, the zoomed in selections were blurry in the widefield view compared to the 3D-SIM view, with little or no resolution of individual actin filaments (Figure 5.2a, d). Individual actin strands were evident in the 60x image (Figure 5.2c) and in the zoomed in view of the 20x 3D-SIM image (Figure 5.2b, e). Lateral resolution was calculated from the FWHM of the line profile peak of the equivalent actin filament in the widefield and 3D-SIM images as 960±160nm and 480±160nm respectively (Figure 5.2f, g).

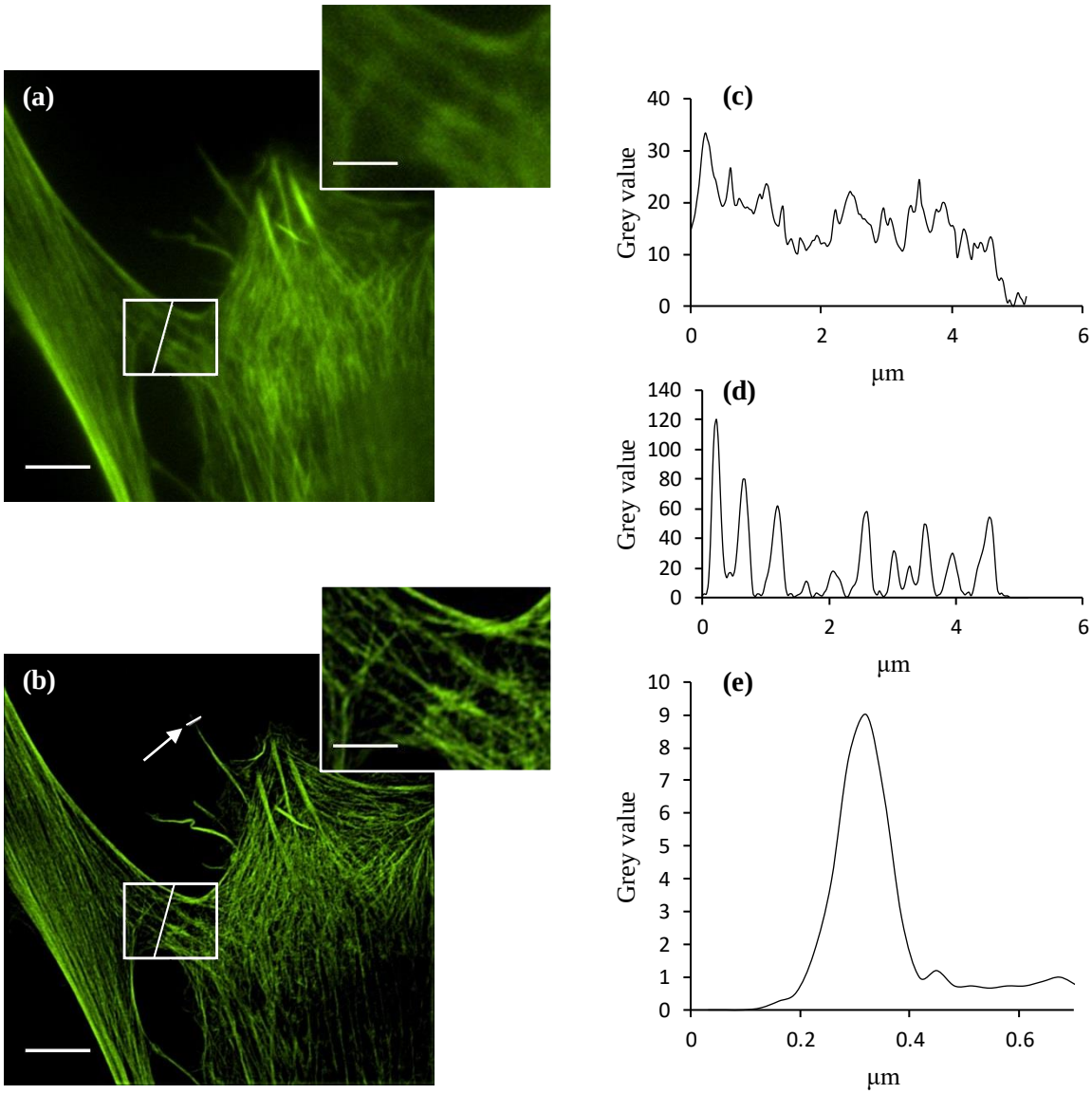

Figure 5.1 Comparison of widefield and 3D-SIM image resolution under 100x magnification. **(a)** Widefield image of actin in SH-SY5Y cells with zoomed in rectangular selection. **(b)** Comparative 3D-SIM image with zoomed in rectangular selection. **(c)** Background subtracted line profile through rectangular selection of (a). **(d)** Background subtracted line profile through rectangular selection of (b). **(e)** Background subtracted profile of actin filament in (b) (marked by arrow). Scale bar for original images, 5µm; scale bar for zoomed in images, 2µm.

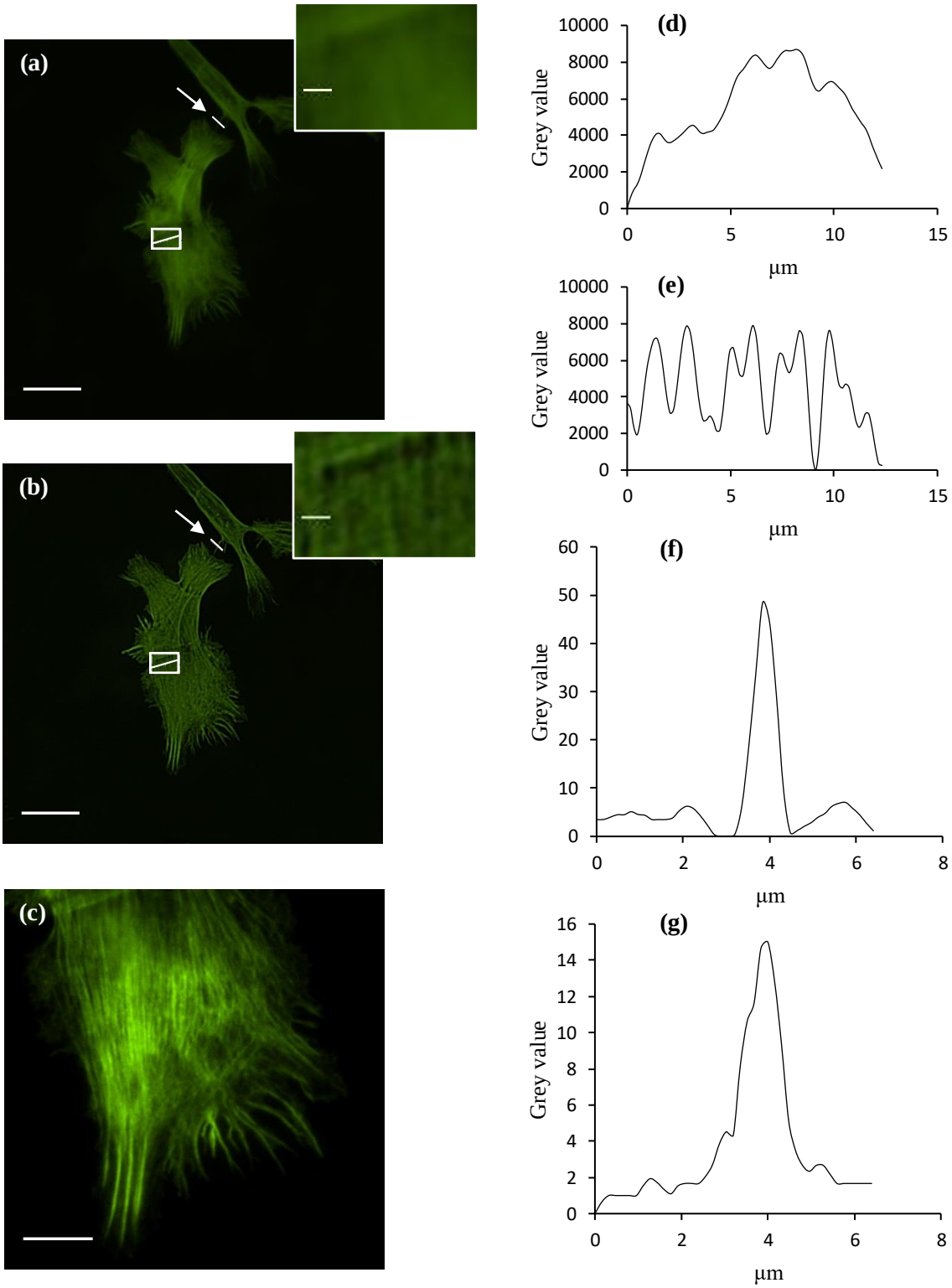

Figure 5.2 Comparison of widefield and 3D-SIM image resolution under 20x magnification. **(a)** Widefield image of actin in SH-SY5Y cells with zoomed in rectangular selection. **(b)** Comparative 3D-SIM image with zoomed in rectangular selection. **(c)** Comparative 60x widefield image. **(d)** Background subtracted line profile through rectangular selection of (a). **(e)** Background subtracted line profile through rectangular selection of (b). **(f)** Background subtracted profile of actin filament in (a) (marked by arrow). **(g)** Background subtracted profile of actin filament in (b) (marked by arrow). Scale bar for original 20x images, 25µm; scale bar for zoomed in images, 2µm; scale bar for 60x image, 10µm.

5.3 Investigation into Willin & SH-SY5Y differentiation using SIM

The Hippo pathway is a key regulator of organ growth, as previously discussed in Chapter 2. Hippo signalling, in addition to cell proliferation and apoptosis, also affects differentiation (Wang, Yu & Yu, 2017). For example, TAZ expression alters the osteogenic versus adipogenic potential of MSCs (Hong *et al*., 2005), and YAP activation diminishes neuronal differentiation (Cao, Pfaff & Gage, 2008). Cell differentiation is also modulated by cell shape, which is in turn determined by the actin cytoskeleton (Müller *et al*., 2013).

Willin has previously been shown to be an upstream member of the Hippo signalling pathway, with ectopic Willin expression increasing phosphorylation of core pathway components MST1/2, LATS1 and YAP (Angus *et al*., 2012). Given that Willin was discovered in the rat sciatic nerve, Willin may have a function in the nervous system and thus the role of Willin in the Hippo pathway in a neuronal context has been explored. The following sections examine whether Willin expression effects SH-SY5Y differentiation. During differentiation, the actin cytoskeleton and Willin localization were studied using 3D-SIM. In addition, TAZ localization has previously been shown to be altered during SH-SY5Y differentiation (Ahmed *et al*., 2015) and so was too investigated here as an indicator of differentiation status and Hippo pathway activity.

5.3.1 Validation of shScr and shWillin cell lines

SH-SY5Y cell lines expressing differing levels of Willin were previously produced using short-hairpin RNA (shRNA)-mediated knockdown. Cell lines were generated by transduction of wild-type SH-SY5Y cells with lentiviral vector constructs comprising shRNA targeting non-specific mRNA (scrambled shRNA, shScr, used as an shRNA control) or shRNA targeting Willin mRNA (shWillin) for Willin knockdown (Angus *et al*., 2012). Relative levels of Willin mRNA in shScr and shWillin cell lines were validated by qPCR (Figure 5.3). ShWillin cell mRNA was measured to be 29±6% that of shScr ($p<0.001$).

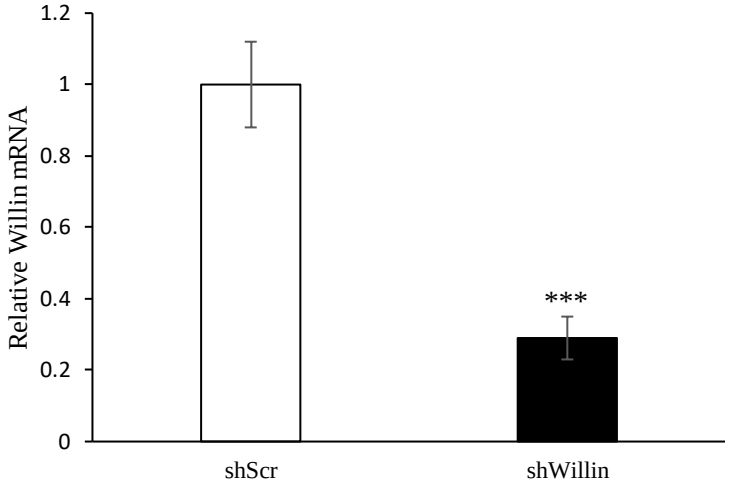

Figure 5.3 Relative levels of Willin mRNA in shScr and shWillin cells. n = 3 experimental repeats, error bars indicate standard deviation, *** $p<0.001$ as calculated using the two-tailed Student's t-test.

Relative expression of Willin protein in shScr and shWillin cell lines was confirmed by Western blot (Figure 5.4). ShWillin cell Willin protein expression was 17±2% that of shScr cells ($p<0.05$). The difference in relative levels of Willin protein versus mRNA in the shWillin and shScr cell lines was not unexpected, since not all mRNA transcribed from DNA is translated into protein owing to cytoplasmic mRNA degradation (Schoenberg & Maquat, 2012).

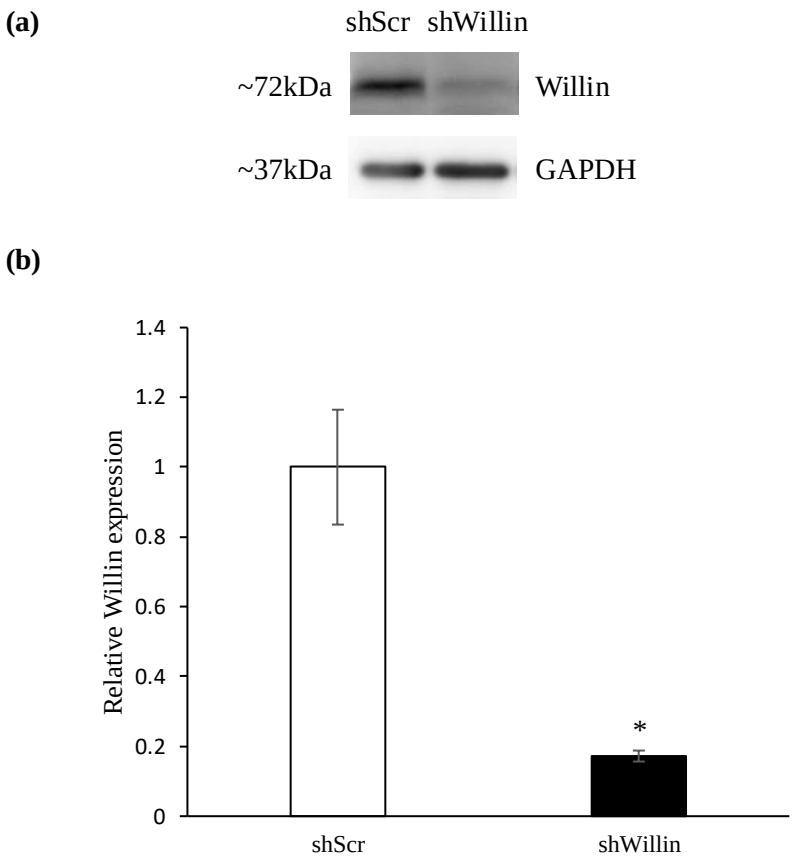

Figure 5.4 Relative Willin protein expression in shScr and shWillin cells. **(a)** Representative Western blot Willin protein bands of shScr and shWillin lysate samples. GAPDH served as a loading control. **(b)** Quantification of Willin protein expression in shScr and shWillin cell lines. Willin expression in shWillin cells was measured relative to that of shScr cells (n = 3 experimental repeats, error bars indicate standard deviation, * $p<0.05$ as calculated using the two-tailed Student's t-test).

5.3.2 Willin knockdown induces morphological changes in SH-SY5Y cells

Having confirmed knockdown of Willin in shWillin cells, the effect of reduced Willin expression on SH-SY5Y morphology was next investigated. Under brightfield illumination, shWillin cells appeared more elongated and spindle-like in shape compared to shScr cells. To further investigate their morphology, shScr and shWillin cells were labelled with the actin marker Phalloidin-488 and imaged under 20x magnification using 3D-SIM (Figure 5.5). Neurite-like projections of actin extending from the cell edge and up to twice the length of the cell body (~75μm) were observed in shWillin cells that were not present in shScr cells.

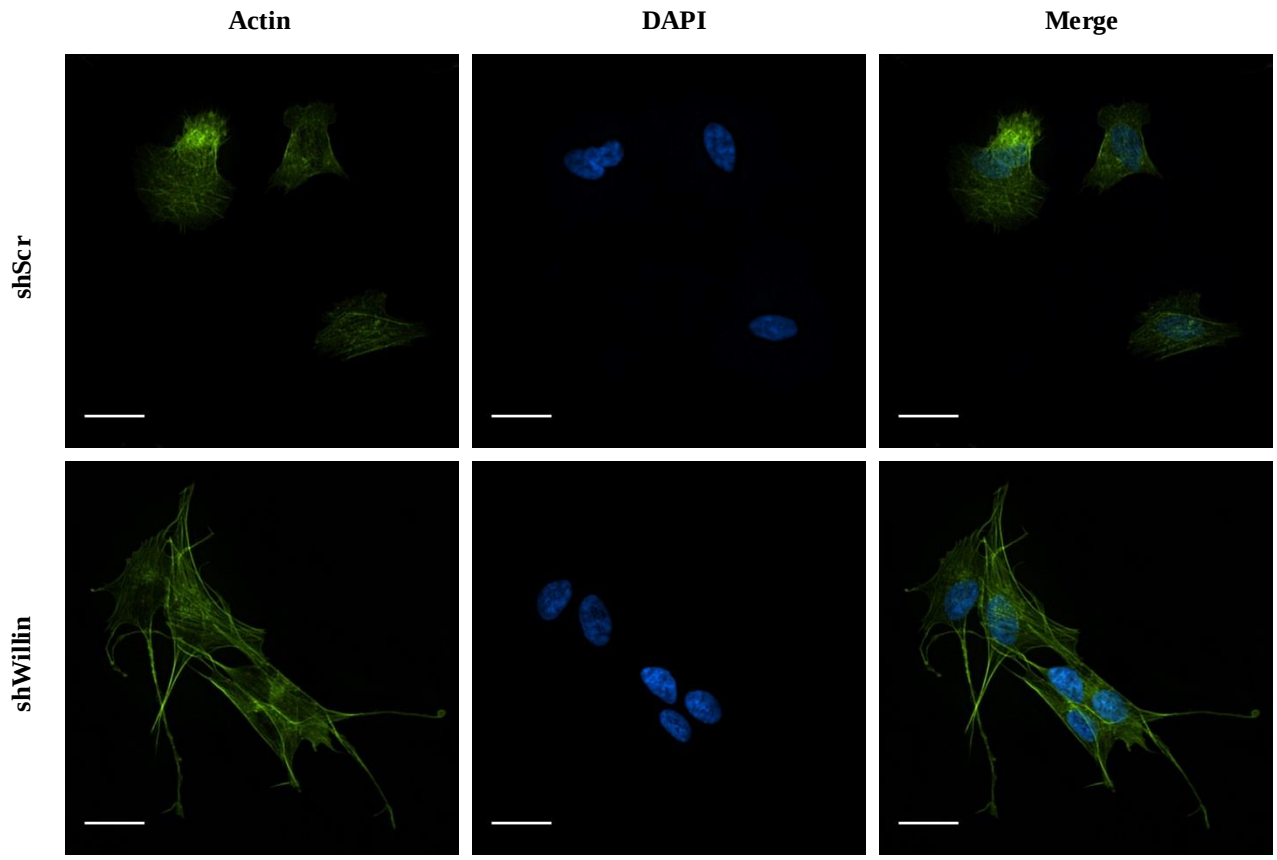

Figure 5.5 3D-SIM images of shScr and shWillin cells labelled with Phalloidin-488 under 20x magnification. Upper row, shScr cells; lower row, shWillin cells. Left column, actin (green); middle column, DAPI (blue); right column, merged image. Scale bar, 25μm.

5.3.3 Willin expression levels modulate SH-SY5Y differentiation

The presence of neurite-like projections in the shWillin cells suggested that expression levels of Willin may affect differentiation of SH-SY5Y cells. ShScr and shWillin cells were therefore treated with retinoic acid (RA) and brain-derived neurotrophic factor (BDNF) as described in Chapter 4. Cells were imaged under brightfield illumination prior to differentiation (day 1) and following treatments with RA (days 4 and 8) and BDNF (day 11) (Figure 5.6). As described above, prior to treatment, shWillin cells appeared elongated, with neurite-like processes already present in some cells. After addition of RA, these neurite-like projections lengthened and began to form networks. Following treatment with BDNF, cell bodies shrank, and complex morphological networks of thin processes formed between cells. In comparison, shScr cells grew shorter neurites after the addition of RA, and developed only limited networks after treatment with BDNF (Figure 5.6).

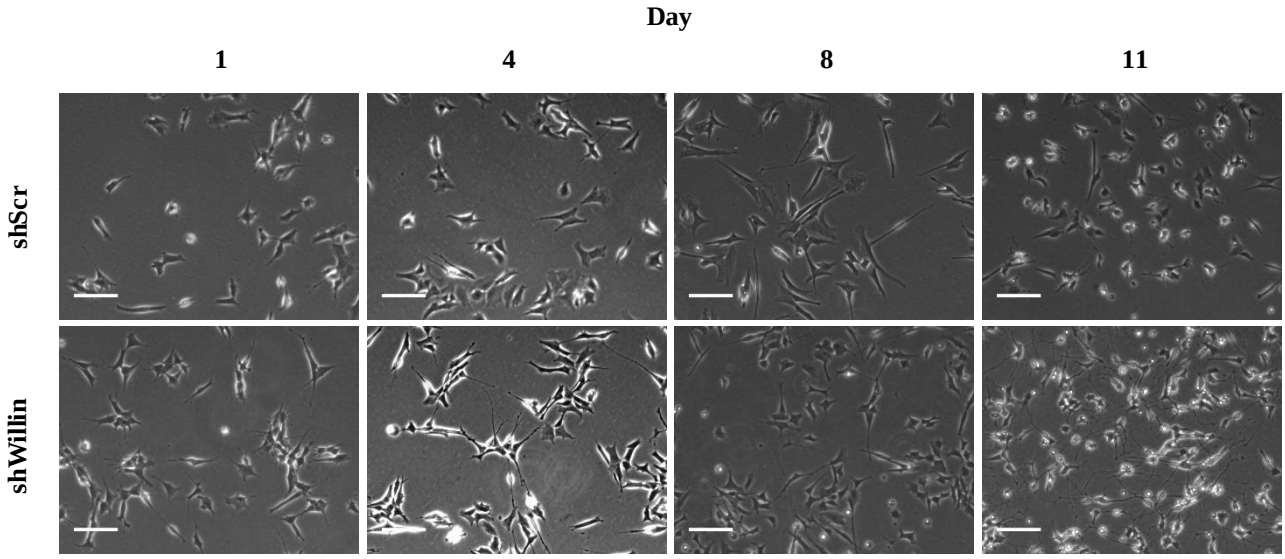

Figure 5.6 Brightfield phase contrast images of shScr and shWillin cells during differentiation under 10x magnification. Upper row, shScr cells; lower row, shWillin cells. Day 1, undifferentiated cells; day 4, post-treatment with RA; day 8, post-second treatment with RA; day 11, post-treatment with BDNF. Scale bar, 50μm.

Untreated and differentiated cells were labelled with the neuron-specific marker Beta-III tubulin (Figures 5.7 & 5.8). Beta-III tubulin was present in the cytoplasm of both untreated shScr and shWillin cells. However, Beta-III tubulin became concentrated in the neurites and neuronal networks of the shWillin cells after RA/BDNF treatment (Figure 5.8).

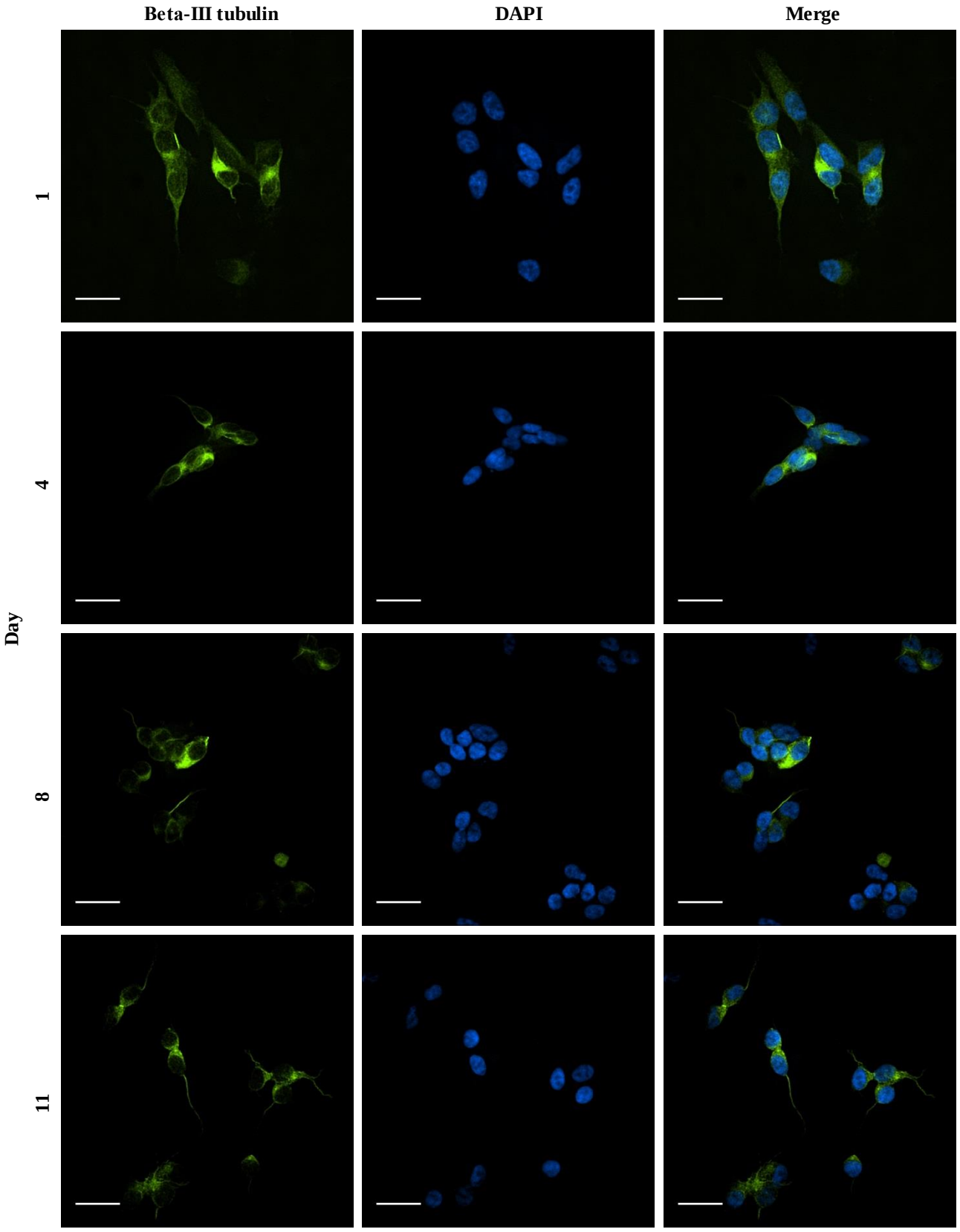

Figure 5.7 3D-SIM images of untreated and RA/BDNF-treated shScr cells labelled with Beta-III tubulin-488 under 20x magnification. Left column, Beta-III tubulin (green); middle column, DAPI (blue); right column, merged image. Upper row, day 1 of differentiation; second row, day 4 of differentiation; third row, day 8 of differentiation; lower row, day 11 of differentiation. Scale bar, 25μm.

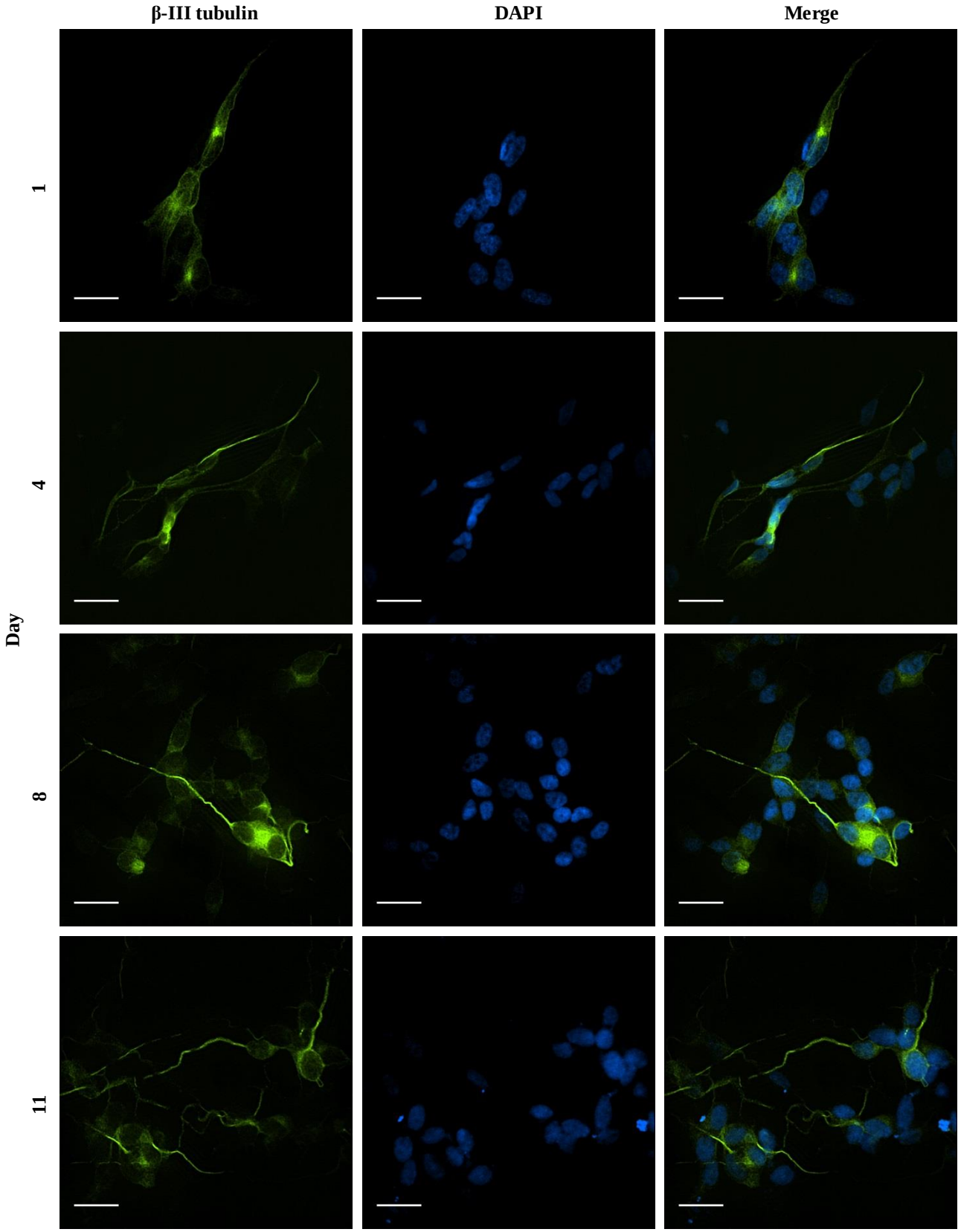

Figure 5.8 3D-SIM images of untreated and RA/BDNF-treated shWillin cells labelled with Beta-III tubulin-488 under 20x magnification. Left column, Beta-III tubulin (green); middle column, DAPI (blue); right column, merged image. Upper row, day 1 of differentiation; second row, day 4 of differentiation; third row, day 8 of differentiation; lower row, day 11 of differentiation. Scale bar, 25μm.

5.3.4 The actin cytoskeleton is remodelled during differentiation of shWillin SH-SY5Y cells

The formation of neurites, or neuritogenesis, requires rearrangement of the actin cytoskeleton (Santos Da Silva & Dotti, 2002). In order to investigate any changes in actin organisation during differentiation, untreated and RA/BDNF-treated shScr and shWillin cells were labelled with Phalloidin-488 and examined using 3D-SIM (Figures 5.9 & 5.10). Both untreated and RA-treated shScr cells contained prominent actin stress fibres arranged in a parallel fashion, with no significant changes to the actin cytoskeleton after BDNF treatment (Figure 5.9). Stress fibres were also visible in untreated and RA-treated shWillin cells. After addition of BDNF to shWillin cells, however, the actin cytoskeleton appeared disassembled within the cell body, with disruption to the previously ordered nature of the filament pattern, indicating morphological differentiation of shWillin cells (Figure 5.10).

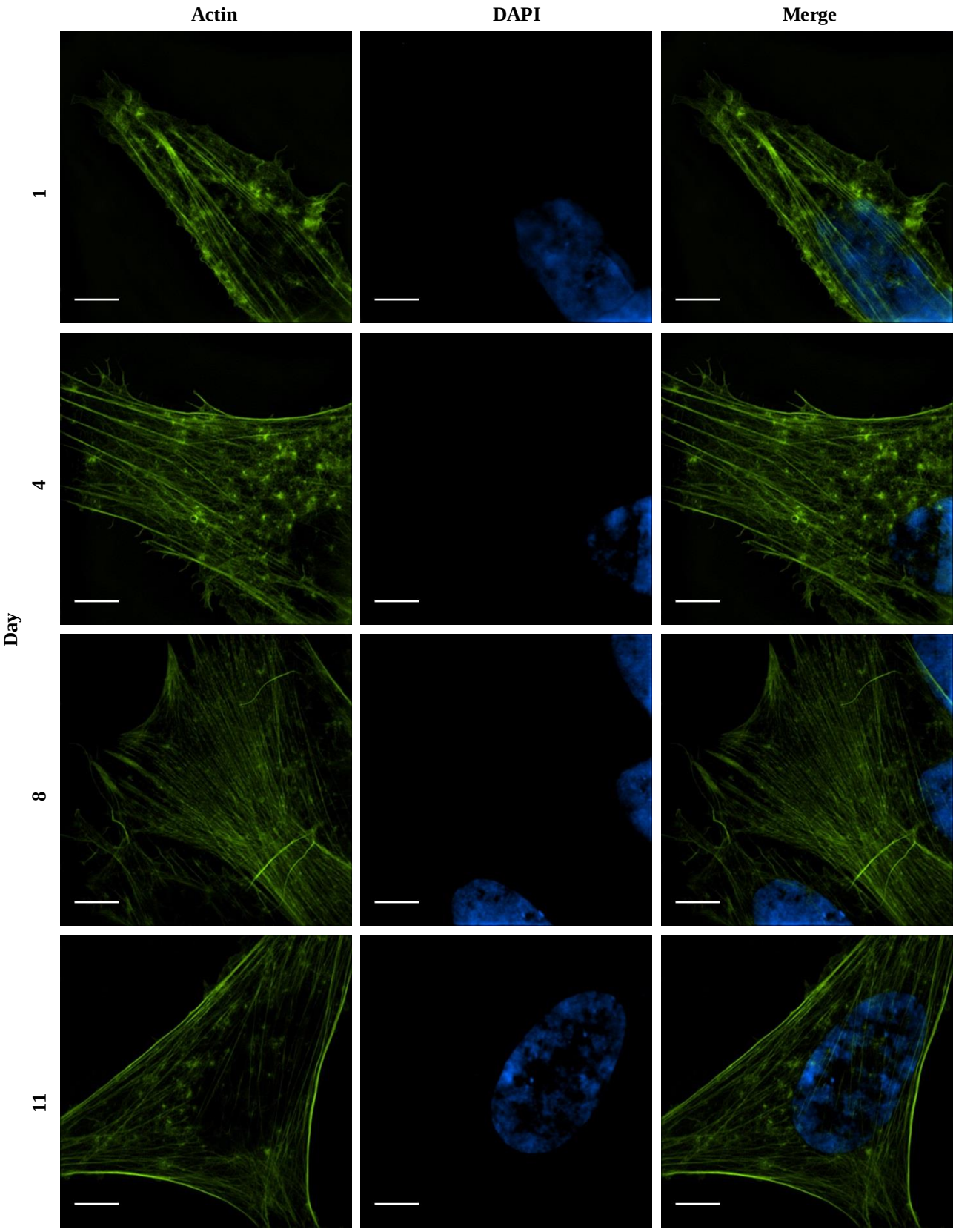

Figure 5.9 3D-SIM images of untreated and RA/BDNF-treated shScr cells labelled with Phalloidin-488 under 100x magnification. Left column, actin (green); middle column, DAPI (blue); right column, merged image. Upper row, day 1 of differentiation; second row, day 4 of differentiation; third row, day 8 of differentiation; lower row, day 11 of differentiation. Scale bar, 5μm.

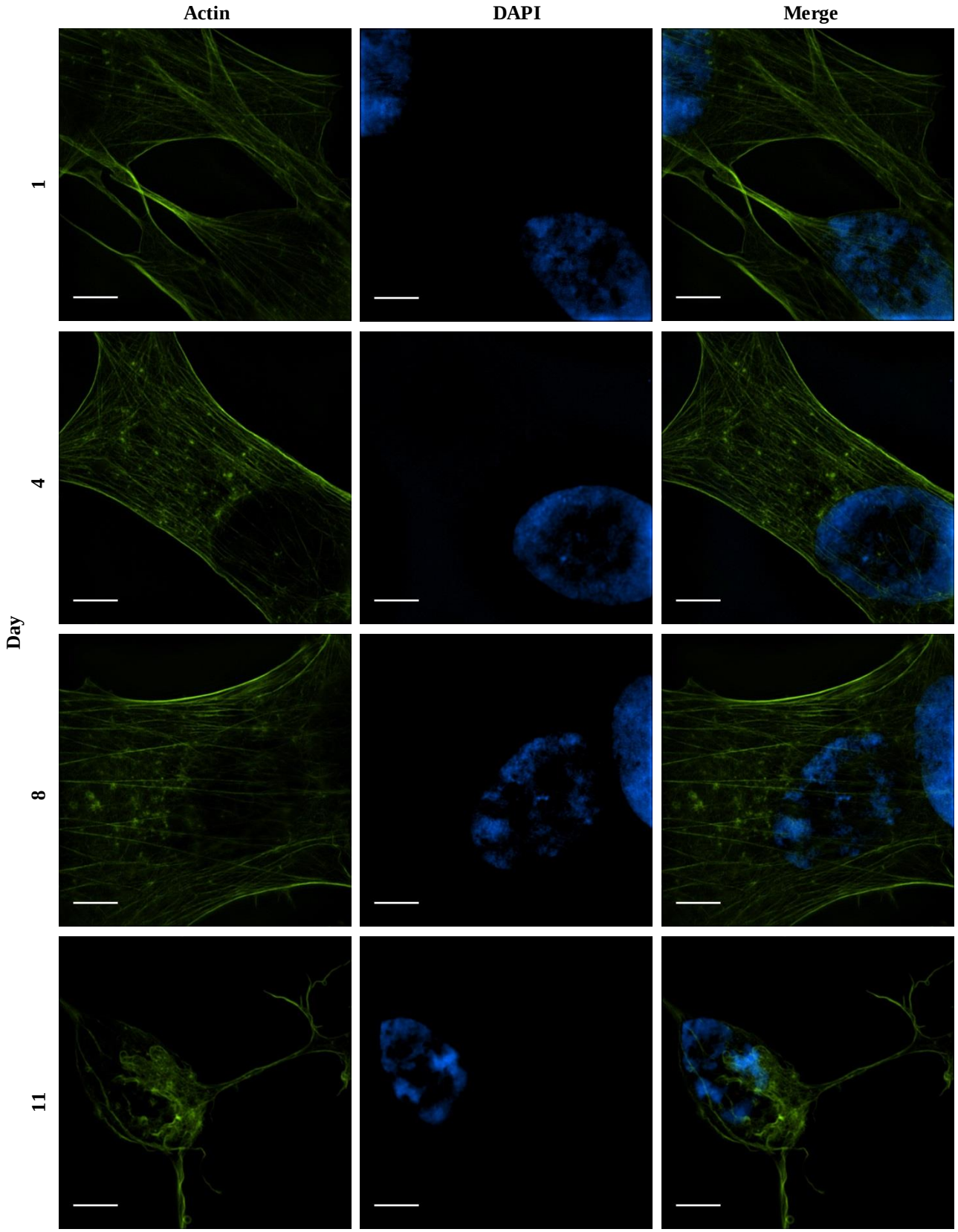

Figure 5.10 3D-SIM images of untreated and RA/BDNF-treated shWillin cells labelled with Phalloidin-488 under 100x magnification. Left column, actin (green); middle column, DAPI (blue); right column, merged image. Upper row, day 1 of differentiation; second row, day 4 of differentiation; third row, day 8 of differentiation; lower row, day 11 of differentiation. Scale bar, 5μm.

5.3.5 Willin expression does not affect expression of TAZ

As Willin is an upstream component of the Hippo pathway (Angus *et al*., 2012), Hippo signalling effectors YAP and TAZ weres investigated in shScr and shWillin cells. TAZ expression was similar in shScr and shWillin cells, with shWillin cells expressing 101±25% that of shScr (Figure 5.11a, b). YAP protein bands, however, were not detectable by Western blot (Figure 5.11c)

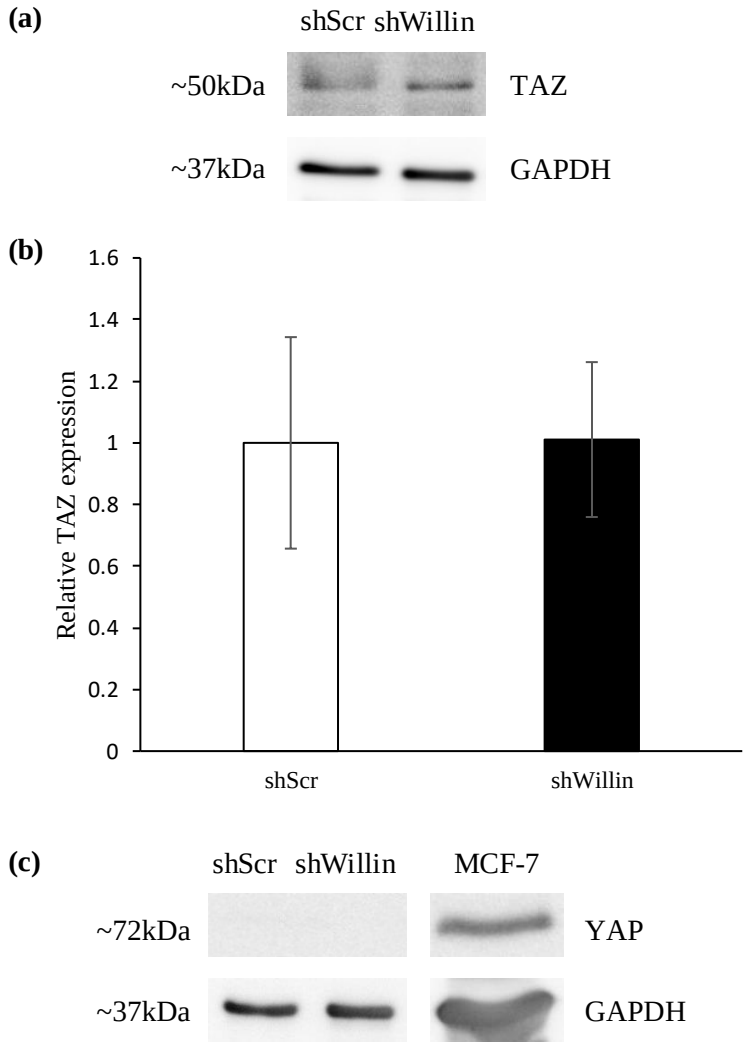

Figure 5.11 Expression of YAP and TAZ in shScr and shWillin cells. **(a)** Representative Western blot TAZ protein bands of shScr and shWillin lysate samples. GAPDH served as a loading control. **(b)** Quantification of TAZ protein expression in shScr and shWillin cell lines. TAZ expression in shWillin cells was measured relative to that of shScr cells (n = 3 experimental repeats, error bars indicate standard deviation, * $p<0.05$ as calculated using the two-tailed Student's t-test). **(c)** Western blot YAP protein bands of shScr and shWillin lysates samples. MCF-7 cell lysate served as a positive control.

5.3.6 TAZ expression is increased upon differentiation of shWillin SH-SY5Y cells with BDNF

YAP/TAZ expression has previously shown to be altered during neuronal differentiation (Ahmed *et al*., 2015; Hindley *et al*., 2016). Since YAP expression in shScr and shWillin cell lines was shown to be negligible, expression of TAZ was investigated during differentiation of shScr and shWillin cells (Figure 5.12). Levels of TAZ were shown to decrease during differentiation of shScr cells, with BDNF-treated cells expressing 53% that of untreated cells. A marked increase in TAZ expression occurred after addition of BDNF to shWillin cells, with levels 5.5-fold than of untreated cells.

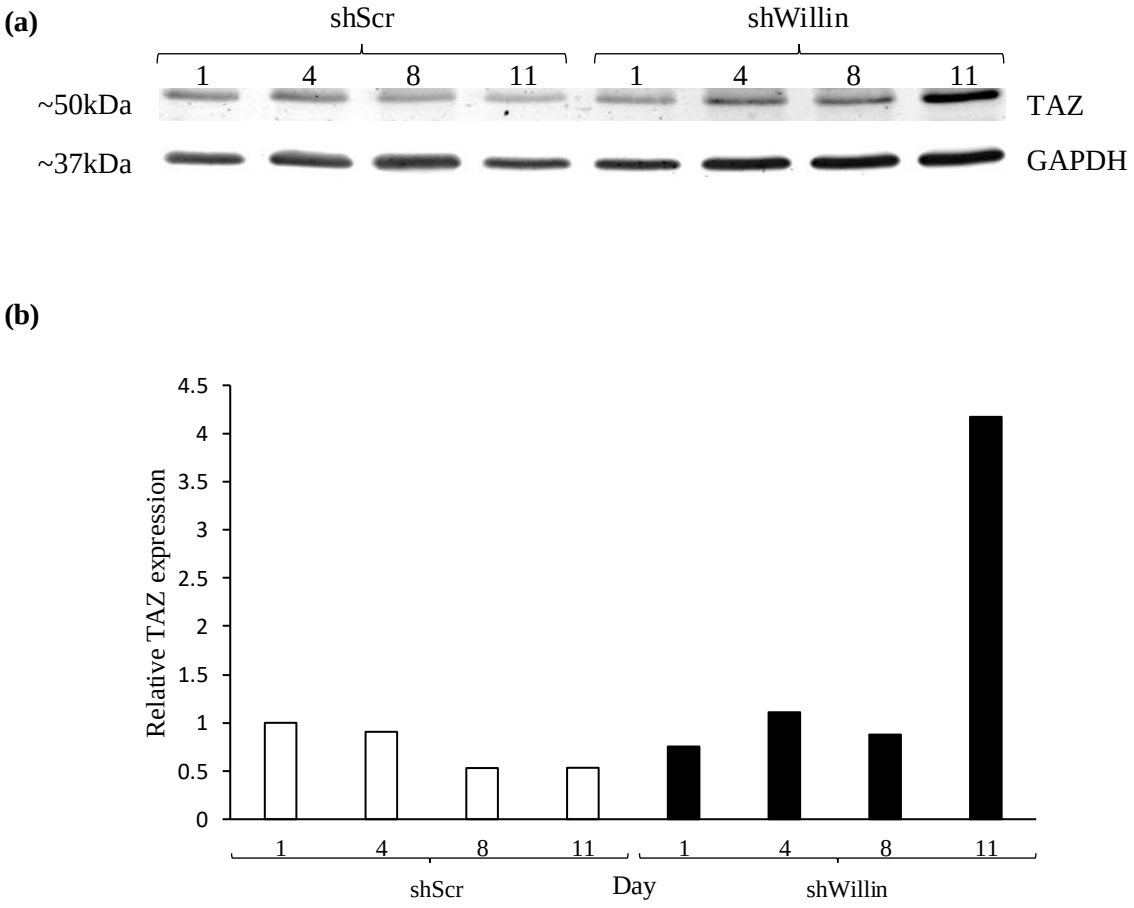

Figure 5.12 Expression of TAZ during differentiation of shScr and shWillin cells. **(a)** Western blot TAZ protein bands of shScr and shWillin lysate samples collected on day 1, 4, 8 and 11 of differentiation. GAPDH served as a loading control. **(b)** Quantification of TAZ protein expression (n = 1).

5.3.7 SH-SY5Y differentiation induces a nucleoplasmic shift in TAZ localization

TAZ activity is determined by its localization: TAZ is transcriptionally inactive in the cytoplasm and active in the nucleus, where it acts as a transcriptional co-activator of several genes that promote cell proliferation (Yu, Zhao & Guan, 2015). Therefore the localization of TAZ was investigated during differentiaion of shScr and shWillin cells. Untreated and RA/BDNF-treated cells were labelled with TAZ-488 and examined under 20x magnification (see Section 4.4.1 for immunocytochemistry methods) (Figures 5.13 & 5.14). TAZ remained largely nuclear in shScr cells throughout differentiation, with some shift to the cytoplasm occuring by day 8 (Figure 5.13). A more marked nucleocytoplasmic shift occurred during differentiation of shWillin cells, with the majority of TAZ localized to the cytoplasm after addition of BDNF (Figure 5.14).

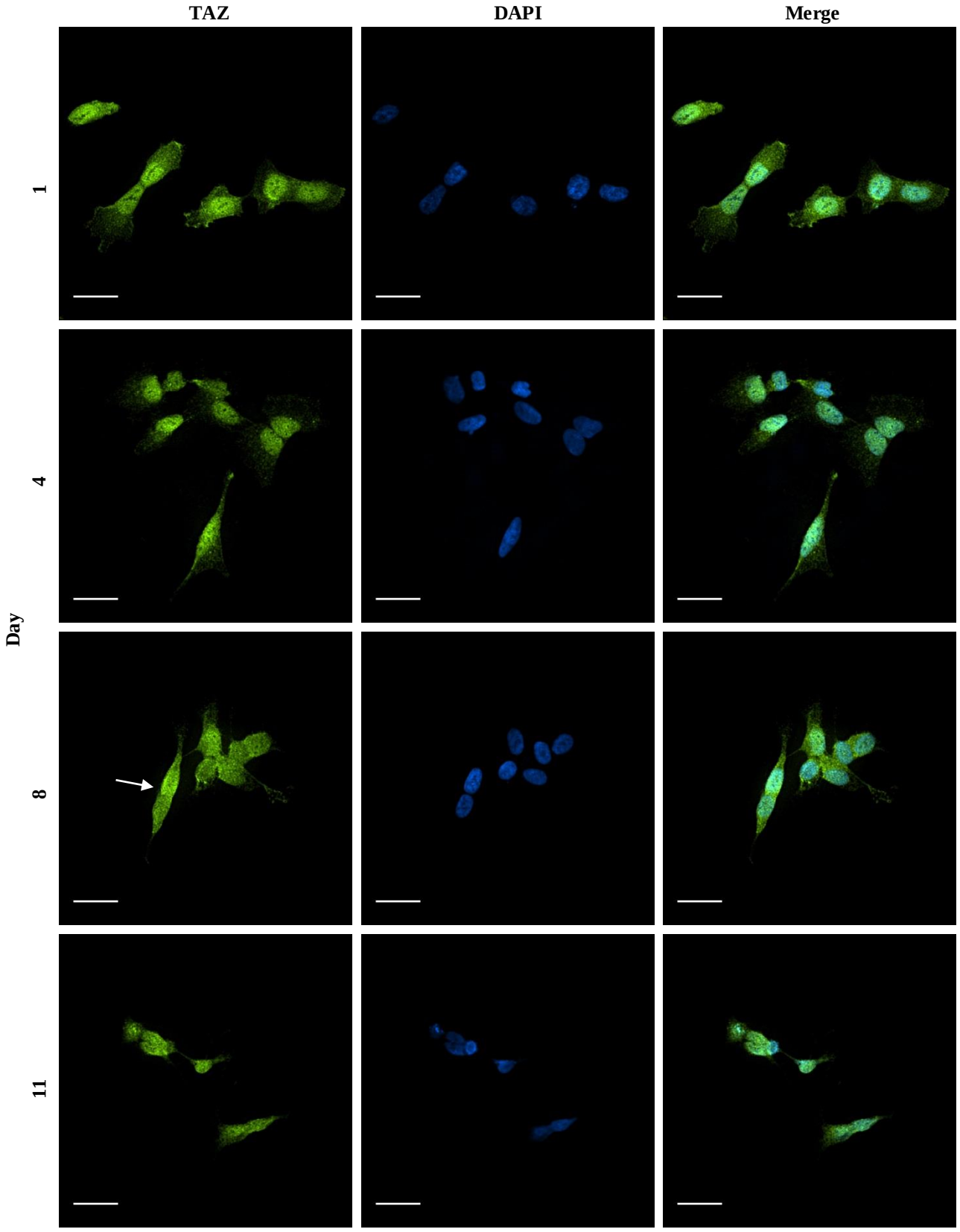

Figure 5.13 3D-SIM images of untreated and RA/BDNF-treated shScr cells labelled with TAZ-488 under 20x magnification. Left column, TAZ (green); middle column, DAPI (blue); right column, merged image. Upper row, day 1 of differentiation; second row, day 4 of differentiation; third row, day 8 of differentiation; lower row, day 11 of differentiation. Arrow marks cytoplasmic TAZ. Scale bar, 25μm.

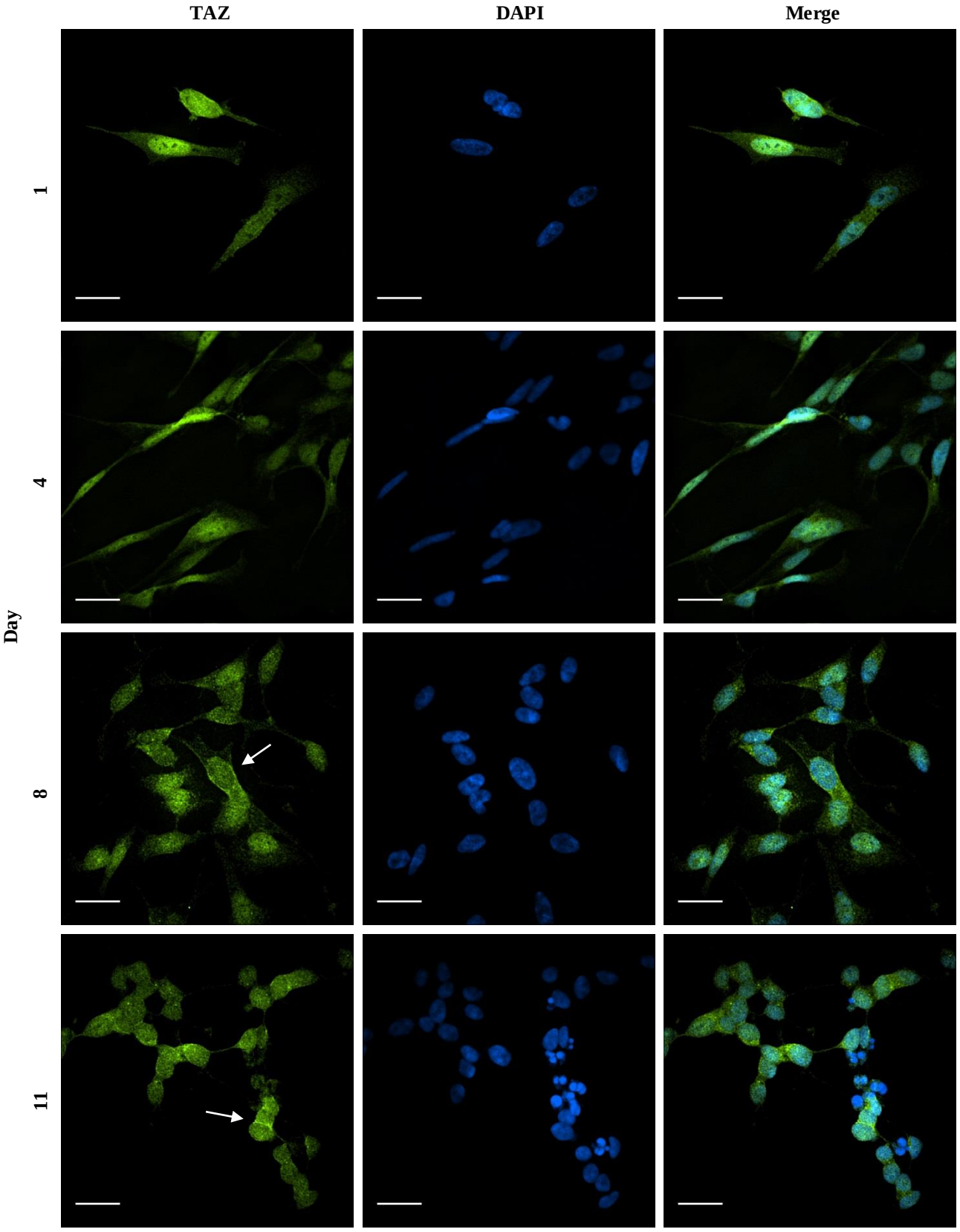

Figure 5.14 3D-SIM images of untreated and RA/BDNF-treated shWillin cells labelled with TAZ-488 under 20x magnification. Left column, TAZ (green); middle column, DAPI (blue); right column, merged image. Upper row, day 1 of differentiation; second row, day 4 of differentiation; third row, day 8 of differentiation; lower row, day 11 of differentiation. Arrows mark cytoplasmic TAZ. Scale bar, 25μm.

5.3.8 Willin expression is increased during SH-SY5Y differentiation

To investigate whether Willin expression is changed during neuronal differentiation, wild-type SH-SY5Y cells were differentiated as per shScr and shWillin cells by treatment with RA/BDNF, and Willin expression examined by Western blot (Figure 5.15). After 7 days of treatment with RA, the level of Willin expression was 2.1-fold that of untreated cells ($p<0.05$), whilst after RA treatment followed by addition of BDNF, Willin protein expression was 2.65-fold that of untreated cells ($p<0.01$).

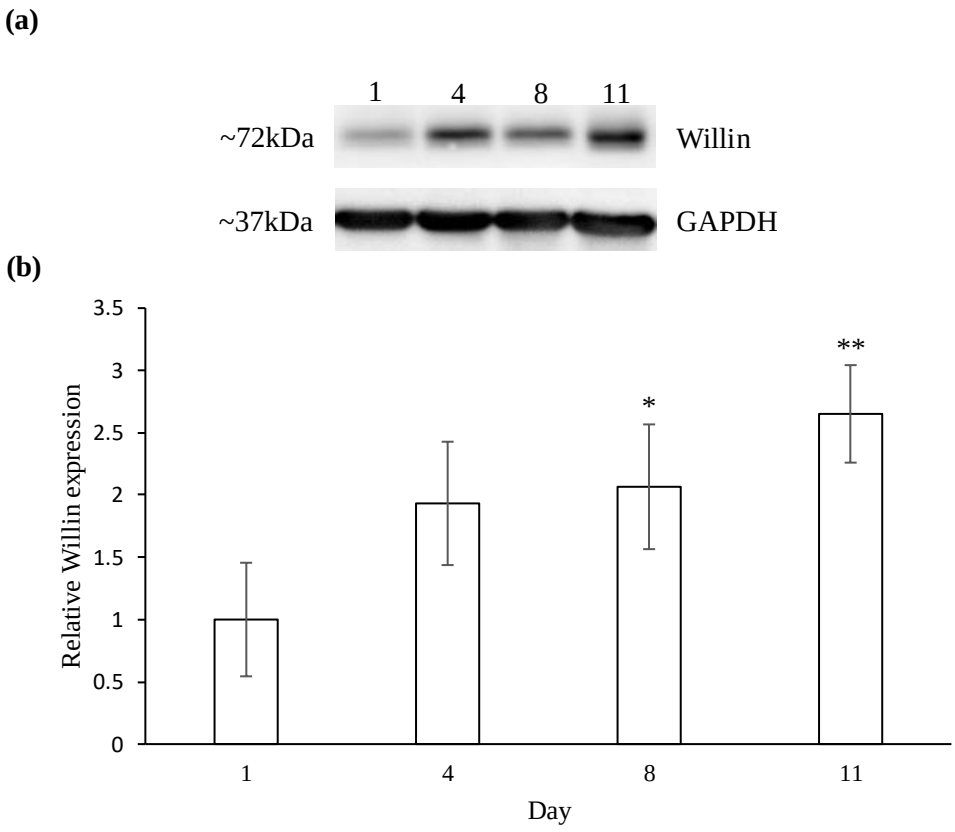

Figure 5.15 Expression of Willin during differentiation of wild-type SH-SY5Y cells. **(a)** Representative Western blot Willin protein bands of lysate samples collected on day 1, 4, 8 and 11 of differentiation. GAPDH served as a loading control. **(b)** Quantification of Willin protein expression ($n = 3$ experimental repeats, error bars indicate standard deviation, * day 8>day 1, $p<0.05$, ** day 11>day 1, $p<0.01$ as calculated using the two-tailed Student's t-test).

5.3.9 Willin localizes to neurites of differentiated SH-SY5Y cells

To identify the localization of Willin in differentiated SH-SY5Y cells, Willin-mCherry cells were treated with RA alone or RA followed by BDNF and fixed for examination by 3D-SIM (see Chapter 7 for production of Willin-mCherry cell line). After both treatments, Willin-mCherry was observed to localize in a punctate manner to cell neurites, suggesting that Willin may have a role in neuritogenesis during neuronal differentiation (Figure 5.16).

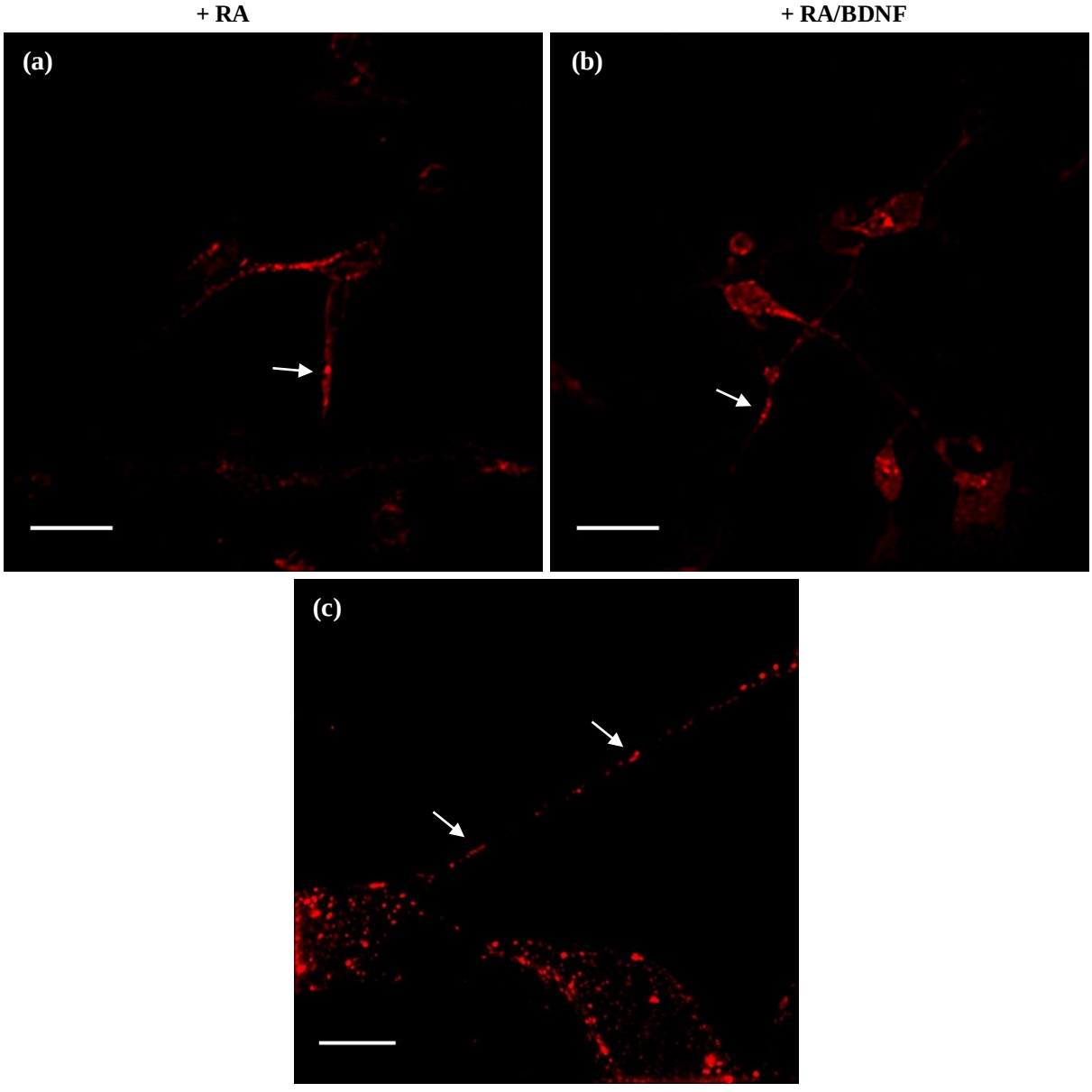

Figure 5.16 3D-SIM images of differentiated Willin-mCherry cells. **(a)** Willin-mCherry cells treated with RA for 7 days under 20x magnification. **(b)** Willin-mCherry cells treated with RA for 7 days followed by BDNF for 3 days under 20x magnification. **(c)** 100x magnification maximum intensity profile of 10µm image stack of Willin-mCherry cells treated with RA for 7 days. Arrows mark presence of Willin-mCherry in neurites. Scale bar for (a) and (b), 25µm; scale bar for (c), 5µm.

5.3.10 Summary

Willin knockdown was shown to induce morphological changes in neuronal model SH-SY5Y cells and direct them towards a more differentiated phenotype after activation with RA/BDNF, concurrent with work previously carried out by Dr Andrew Lunel. Differentiation of shWillin SH-SY5Y cells was accompanied by disassembly of the actin cytoskeleton, as investigated using SIM, and a nucleocytoplasmic shift in Hippo pathway effector TAZ. Willin-mCherry was also shown to localize to the neurites of differentiated Willin-mCherry SH-SY5Y cells.

Below is described a separate study, out of the scope of this thesis, but that nevertheless demonstrates SIM at the tissue level and highlights its potential as an aid for disease diagnosis.

5.4 SIM as a diganostic tool in nephrotic disease

In addition to being used for imaging single cells, SIM can be performed at the tissue level, with promise for clinical research. Recently, for example, SIM was used as an imaging tool for distinguishing between renal biopsies from healthy subjects and subjects with nephrotic disease (Pullman *et al*., 2016).

One of the key roles of the kidney is to retain proteins in the blood during urine filtration. Impairment of this ability leads to nephrotic syndrome, which comprises a group of disorders of varying severity, some of which can be fatal (Mundel & Reiser, 2010). The glomerulus acts as the major kidney filtration apparatus, each consisting of a coil of capillaries that are covered in cells known as podocytes. Podocyte foot processes attach to the exterior of the capillaries and connect to one another via thin intercellular slit diaphragms to help form the filtration barrier. Loss of these foot processes (effacement) and disappearance of the slit diaphragms are two of the structural changes that are associated with protein leakage and nephrotic syndrome and are therefore used as disease markers (Pullman *et al*., 2016).

Podocyte foot processes are between 250 and 700nm in width, and the slit diaphragms that separate them ~40nm, and are therefore unable to be visualised using a standard light microscope. These structures are instead observed typically using electron microscopy, which has become the gold standard for diagnosis of nephrotic syndrome over the last few decades. The recent SIM study examined the podocyte substructure of renal biopsy sections from both healthy subjects and subjects diagnosed with Minimal Change Disease (MCD), one of the leading causes of nephrotic syndrome (Pullman *et al*., 2016). Sections were fluorescently

stained for podocin, a protein located at the perimeter of the foot process, and sample volumes comprising glomeruli imaged using 3D-SIM. This study showed that SIM was able to successfully resolve the podocyte substructure and differentiate between healthy and MCD samples.

More recently, a separate second study implemented semi-automated quantification of 3D-SIM image stacks taken of healthy and MCD renal biopsy samples stained for the slit diaphragm protein nephrin (Siegerist *et al*., 2017). The slit diaphragm density (SDD) (slit length per glomerular capillary surface area) was used as a means to quantify podocyte effacement and calculated using a custom-made FIJI plugin that includes the Ridge Detection algorithm for detection of curvilinear structures within images (see below). Samples from a total of 8 healthy and 13 MCD subjects were analysed to yield a mean SDD of $3.10\pm0.27\mu m^{-1}$ and $1.83\pm0.49\mu m^{-1}$ for healthy and MCD samples respectively ($p<0.001$).

Here, SDD analysis was replicated for image stacks obtained from the Pullman *et al*. 2016 study as a means of method validation, and the results described below. In addition, fully-automated image quantification was performed using an adjusted FIJI plugin.

5.4.1 Quantitative analysis of renal samples

As was carried out in the Siegerist 2017 study, regions of the image stack maximum intensity profiles were manually selected in FIJI and curvilinear structures detected and highlighted using the Ridge Detection plugin (Figure 5.17). The individual lengths of all detected lines and the total area of the selected region were given in Excel format, from which the SDD for each region was calculated.

Sample images from 3 healthy (n=8) and 3 MCD (n=9) subjects were analysed to produce a mean SDD of $2.34\pm0.21\mu m^{-1}$ and $1.37\pm0.27\mu m^{-1}$ for healthy and MCD samples respectively ($p<0.0001$ as calculated using the two-tailed student's t-test).

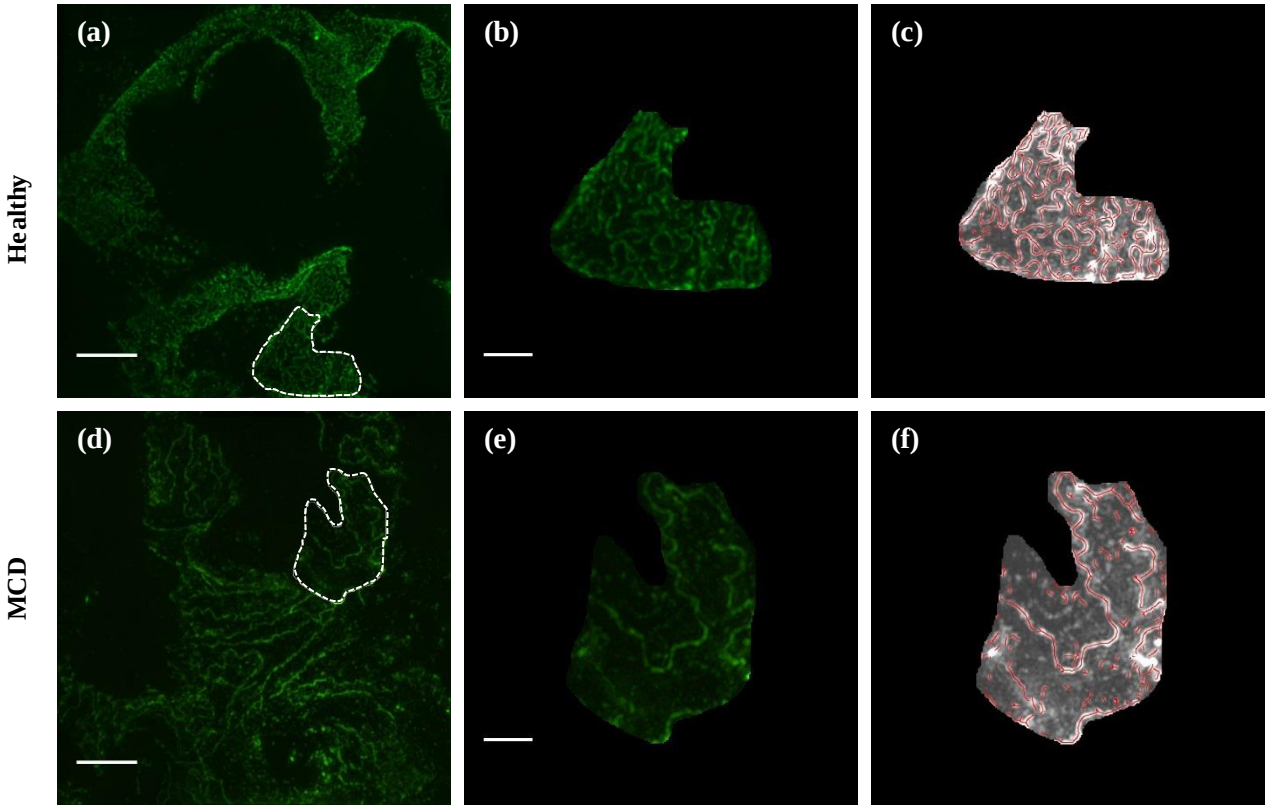

Figure 5.17 Semi-automated quantification of SDD for healthy and MCD renal biopsy sample 3D-SIM image stacks. **(a)** and **(d)** selection of region of maximum intensity profile of representative healthy and MCD sample image stacks. **(b)** and **(e)** manually selected regions of (a) and (d). **(c)** and **(f)** detection of slit diaphragm (shown in red) in selected regions using Ridge Detection plugin. Scale bar for (a) and (d), 5μm; scale bar for (b) and (e), 2μm.

The same sample images were then analysed using a fully-automated approach: a low pass filter was firstly performed on the maximum intensity profile of the image stack for removal of background noise, and the subsequent image thresholded to find the edge of the capillary region (Figure 5.18a-c); the resulting image mask was then multiplied with the original maximum intensity profile image, and the final image analysed using the Ridge Detection plugin (Figure 5.18d-f).

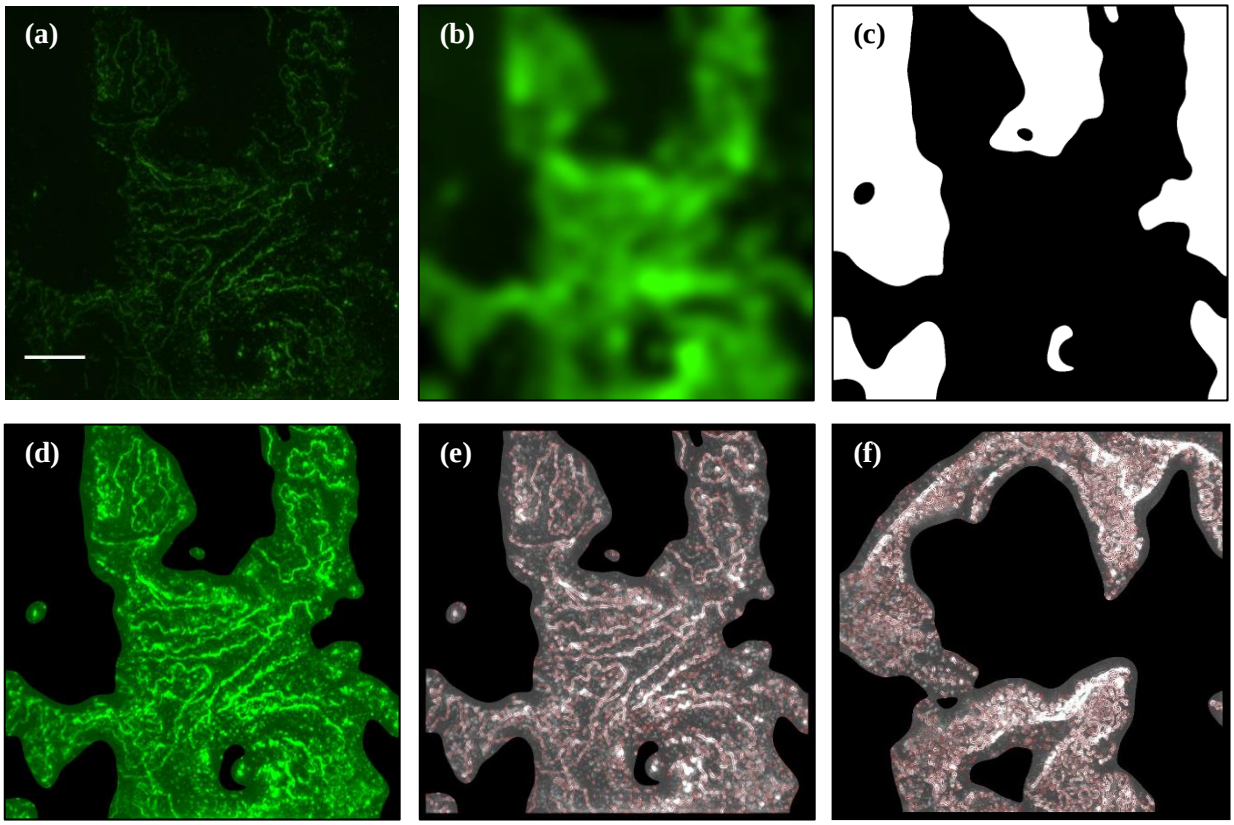

Figure 5.18 Fully-automated quantification of SDD for healthy and MCD renal biopsy sample 3D-SIM image stacks. **(a)** Maximum intensity profile of representative MCD sample image stack. **(b)** Low pass filter of (a). **(c)** Thresholded image mask. **(d)** Multiplication of original projected image (a) and image mask (c). **(e)** Detection of slit diaphragm (shown in red) using Ridge Detection plugin. **(f)** Slit diaphragm detection in representative healthy sample image stack. Scale bar, 5μm.

This fully-automated method yielded a mean SDD of 1.79±0.25μm^{-1} and 0.99±0.27μm^{-1} for healthy and MCD samples respectively ($p<0.0001$ as calculated using the two-tailed student's t-test).

In conclusion, successful differentiation of healthy and MCD renal tissue samples was achieved by both semi- and fully-automated quantification of 3D-SIM images.

5.5 Discussion & future work

SIM is one of the most commonly utilised forms of super-resolution microscopy due to its ease of use and relatively simple system requirements. The consensus lateral resolution of SIM for biological samples is ~120nm (Hayashi & Okada, 2015). In this study I was able to show that the lateral resolution of the N-SIM, as measured using cells labelled for actin with Phalloidin-488, approximately reaches this limit, at 129nm. More notable perhaps is the resolution of

individual actin stress fibres in the 3D-SIM compared to widefield view. Though SIM is not designed for a 20x objective (NA = 0.5), it is nevertheless compatible, and at this magnification provides double the lateral resolution of the equivalent widefield image. This may be due to interference of the excitation beam diffraction orders close to the focus of the sample plane to produce patterned illumination and subsequent generation of Moiré fringes in the detected emission fluorescence. The stress fibres visible under 60x magnification indicate that the enhanced resolution of the 3D-SIM 20x image was not merely a result of reconstruction artefacts. This chapter described two separate studies that employed SIM, both of which are discussed below.

3D-SIM was used to investigate the morphology of shScr and shWillin SH-SY5Y cells to examine the effect of reduced Willin expression in a neuronal cell model. The changes that occurred in the morphology of shWillin cells towards a more elongated and morphologically differentiated phenotype are suggestive of a role for Willin in assembly of the actin cytoskeleton and/or neuronal differentiation. A previous study has shown that the acquisition of a neuron-like morphology of bone marrow stromal cells by addition of chemical induction medium is due to retraction of the cytoplasm at the cell edge and disruption of actin stress fibres and can be mimicked by treatment with DMSO alone or actin-depolymerising factors (Neuhuber *et al*., 2004). The long processes observed in undifferentiated shWillin SH-SY5Y cells may therefore be due to the formation of less well developed stress fibres and subsequent retraction of the cytoplasm as a result of reduced Willin expression.

Treatment of SH-SY5Y cells with RA induces extension of neurite-like processes and induces expression of the BDNF receptor TrkB (Encinas *et al*., 2000). BDNF is a neurotrophic growth factor, which when added to RA-treated SH-SY5Y cells, promotes their survival. ShWillin cells were shown to be much more responsive than shScr cells to RA/BDNF treatment. This may be due to the shWillin cells being 'primed' for differentiation owing to their altered morphology, or an independent cause.

Since Willin functions upstream of the Hippo signalling pathway, it was logical to infer that the enhancement of SH-SY5Y differentiation by Willin knockdown may have been a result of altered YAP or TAZ activity. YAP has previously been shown to be negatively regulated during neuronal differentiation of retinal progenitors, for example, with nuclear activity associated with maintaining progenitor cells in a proliferative state (Zhang *et al*., 2012). Less is known about the role of TAZ in neuronal differentiation, although its localization has

recently been shown to play an important role in determining the fate of primed pluripotent stem cells, with TAZ nuclear translocation promoting their differentiation (Zhou *et al*., 2017). Willin expression has been shown to increase phosphorylation of YAP in HEK-293 cells (Angus *et al*, 2012). However, the effect of Willin on TAZ activity is unknown.

Levels of YAP and TAZ present in undifferentiated shScr and shWillin cells were therefore first examined. YAP was undetectable by Western blot in shScr and shWillin cells but evident in MCF-7 cells. TAZ, however, was present in both cell lines at similar expression levels. This is concurrent with previous reports that SH-SY5Y cells express much higher levels of TAZ than they do YAP (Ahmed *et al*., 2015; The Human Protein Atlas). TAZ was also nuclear in undifferentiated shScr and shWillin cells, indicative of similar activity in both cell lines. TAZ expression was markedly increased in RA/BDNF-treated shWillin cells, yet cytoplasmic in localization, concomitant with another study in which differentiation of SH-SY5Y cells by treatment with the protein kinase C activator *12-O-Tetradecanoylphorbol-13-acetate* (TPA) led to increased expression but decreased activity of TAZ via the upstream Hippo component FAT1 (Ahmed *et al*., 2015).

Disassembly of the actin cytoskeleton was shown using 3D-SIM to occur after addition of BDNF to RA-treated shWillin cells, along with shrinkage of the cell body and the formation of networks of the extended neurites. This dissociation of actin stress fibres correlated with the cytoplasmic localization of TAZ, which corresponds with the mechanical model of the Hippo pathway described in Chapter 2.

Although the neuronal marker Beta-III tubulin was observed in the neurite networks of differentiated shWillin cells, it was undetermined if the cells were truly differentiated into cells with neuronal activity or rather just morphologically differentiated, as was suggested in the Neuhuber 2004 study for similar *in vitro* differentiation of bone marrow stromal cells. Indeed, RA treatment alone has been shown to be insufficient for biochemical differentiation of SH-SY5Y cells, with addition of insulin-like growth factor 1 required for optimal differentiation (Dwane, Durack & Kiely, 2013) To verify whether RA/BDNF chemical induction causes true neuronal differentiation, treated cells could be probed for synaptic markers, the expression level of Beta-III tubulin measured during differentiation, or live-cell imaging of induced cells performed to determine if neurite outgrowth is a result of growth cone extension or cytoplasmic retraction. In the future, the effect of Willin expression on neuronal differentiation could be

examined using a more robust model, such as neural differentiation of human induced pluripotent stem cells.

Willin expression and localization were also examined during SH-SY5Y differentiation. The presence of Willin along the neurites of differentiated cells, and the increase in Willin expression after RA/BDNF treatment are both indicative of a potential role for Willin in neuronal function that could be explored in the future. For example, knockdown of Willin in functional neuronal networks and measurement of synaptic output would provide ground-breaking results as to whether Willin has a function in neuronal synaptic activity.

Quantitative analysis of renal biopsy 3D-SIM images was performed as a separate study for investigation into alternative methods for diagnosis of nephrotic syndrome. The Ridge Detection plugin, as used in the Siegerist 2017 study, was applied to previously obtained images of healthy and MCD renal biopsy sections stained for the podocyte slit diaphragm protein podocin. Podocin staining appeared much denser for healthy than for MCD subject sections, and a correspondingly higher SDD was calculated. The highly significantly different mean SDDs of $2.34\pm0.21\mu m^{-1}$ and $1.37\pm0.27\mu m^{-1}$ for healthy versus MCD subjects showed a similar trend to those measured in the original study of $3.10\pm0.27\mu m^{-1}$ and $1.83\pm0.49\mu m^{-1}$. The slightly lower SDDs measured here may have been due to differences in sample preparation, for example staining of podocin as opposed to nephrin.

The method of image quantification used in the Siegerist study and validated above relies on manual selection of parts of capillary areas, which could introduce results bias. Therefore, a fully automated method was tested that calculated the SDD based upon the entire capillary area of the image, without the need for manual selection. Using this method, SDD results were slightly lower, $1.79\pm0.25\mu m^{-1}$ and $0.99\pm0.27\mu m^{-1}$ for healthy versus MCD subjects, which was likely due to detection of a slightly larger capillary area than was present, but still highly significantly different. Further validation of this approach requires a greater number of images and more subjects. However, the image quality and initial quantitative results obtained using 3D-SIM are highly promising. The currently used method of diagnosis, electron microscopy, is both costly and time-consuming. SIM is advantageous in that it uses standard immunohistological techniques and produces comparatively rapid results. The combination of extended-resolution non-linear implementations of SIM alongside reliable methods of image quantification should see SIM lead the way for future ultrastructure-based clinical diagnosis.

5.6 Chapter acknowledgements

The sequence for specific shRNA knockdown of Willin was designed by Dr Susana Moleirinho and ShScr and shWillin SH-SY5Y cell lines generated by Dr Andrew Lunel. The MCF-7 cell lysate was kindly donated by Peter Mullen. All qPCR, Western blots and imaging with exception of the renal biopsy sections was performed by the author. SH-SY5Y differentiation was carried out in conjunction with Dr Andrew Lunel. Renal biopsy images were obtained from Professor Jim Pullman and Dr Jonathan Nylk and analysed by the author. Adjustment of the Ridge Detection plugin for fully-automated analysis was performed by Dr Jonathan Nylk.

6 Design and characterisation of a double optical trap for integration with a structured illumination microscope

6.1 Introduction

Examination of the mechanical control of the Hippo signalling pathway has thus far been limited to cell populations (Dupont *et al*., 2011; Aragona *et al*., 2013; Furukawa *et al*., 2017). Whilst these studies have provided invaluable insight into the role of factors such as the extracellular matrix, the actin cytoskeleton and cellular stretch in Hippo regulation, they have been unable to capture the real-time intracellular dynamics that occur during mechanical Hippo signalling in individual cells.

Optical trapping on a microscopy platform is ideal for biomechanical investigation at the single cell level, simultaneously allowing both non-contact physical handling and passive visualisation of a cell. A major advantage of optical trapping for mechanical studies is calibration of the applied force (usually on the order of pN) by various characterisation methods. Cell stretching is one example of manipulation that can be performed using optical trapping. Optical stretching methods include the dual beam cell stretcher (Guck *et al*., 2001) and optical tweezers that use beads as cell handles (Lim *et al*., 2004) (Figure 6.1). Double optical tweezers are advantageous in that they can be more readily combined with pre-existing microscopy platforms. In addition, the user has the choice of bead refractive index for trapping, and thus more control over the strength of the optical traps (Figure 6.2).

Optical trapping is typically carried out on a conventional light microscope using a high NA imaging objective. Recently, optical traps have been adapted for super-resolution fluorescence microscopy systems (Heller *et al*., 2013; Diekmann *et al*., 2016). Previously, a fibre-based GRIN lens 2D trap was demonstrated on the commercial N-SIM (Nylk *et al*., 2015). However, optical trapping has so far not been combined with super-resolution structured-illumination modality.

The aim of this chapter was to construct a double optical trap on the N-SIM to stretch fluorescent cells and examine live changes in Hippo pathway components YAP and/or the actin cytoskeleton using 3D-SIM. Successful stretching would then be followed up by investigation

of the effect of Willin expression on the behaviour of YAP/actin stress fibres during cell stretching, since there is evidence to suggest that Willin, as the proposed mammalian homologue of the *Drosophila* protein Ex, may play a mechanical role in the regulation of the Hippo pathway (Fernández *et al*., 2011; Gaspar *et al*., 2015) (see Chapter 2).

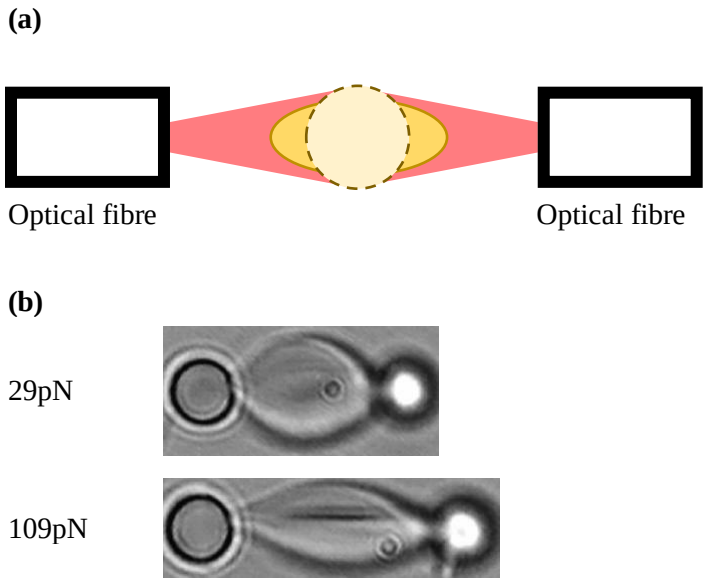

Figure 6.1 Optical methods for cell stretching. **(a)** Dual beam fibre trap cell stretcher. A cell (light pink) is stably trapped between two counter-propagating laser beams (red). Owing to transfer of momentum to the cell surface from the incident rays due to refractive index mismatch between the cell and surrounding medium, at a certain laser power the cell is stretched out along the beam axis (yellow). **(b)** Stretching a red blood cell using bead handles. Two beads are attached to either end of a red blood cell; one bead is attached to a glass surface and the other trapped by optical tweezers. By moving the glass surface relative to the optical tweezers, the red blood cell is deformed. A larger deformation is achieved using a greater trapping force (109pN compared to 29pN). Images adapted from Guck *et al.*, 2001 and Zhang & Liu, 2008.

There are a couple of major advantages in combining optical trapping with SIM, in particular for live-cell manipulation: firstly, SIM image acquisition is fast compared to other super-resolution techniques, therefore allowing high temporal resolution live-cell imaging; and secondly, SIM uses relatively low light intensities, thus reducing issues of photobleaching and phototoxicity.

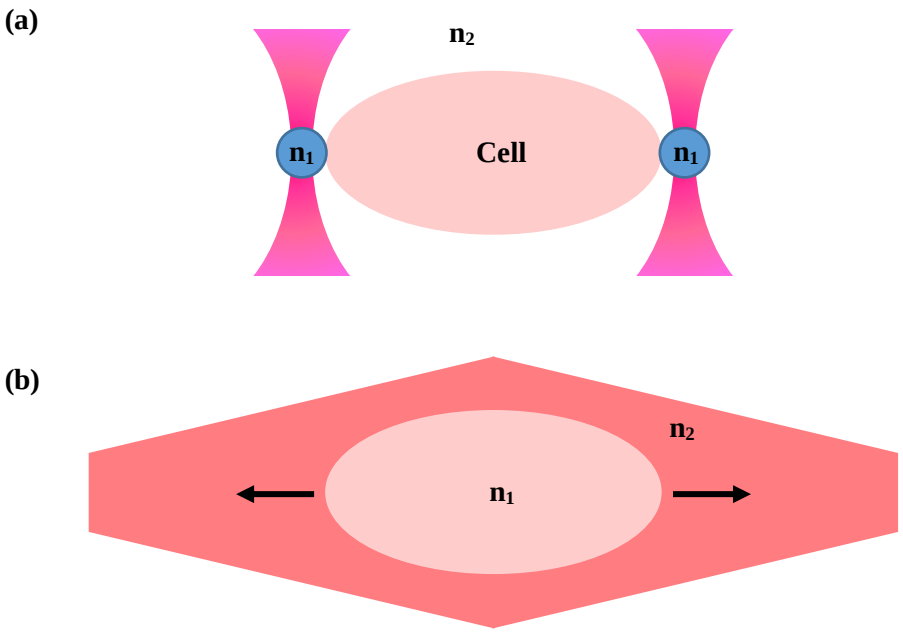

Figure 6.2 Double optical tweezers vs. optical stretcher. **(a)** Double optical tweezers (dark pink) are used to trap microspheres (blue) that are then attached to the cell membrane and used as 'optical handles'. The gradient force of the optical traps is proportional to the difference in the refractive index of the trapped particle (n_1, in the case of polystyrene microspheres ≈ 1.59) and that of the surrounding medium (n_2, for cell media ≈ 1.33) (Spesyvtseva & Dholakia, 2016), and also varies with the size of the trapped object. The strength of the optical traps is therefore dependent upon the microspheres used and so is tuneable. **(b)** The forces that act upon the cell in the optical stretcher causing it to stretch out along the beam axis arise from the difference between n_1 and n_2, which cause a change in momentum of light rays as they enter and leave the cell (Guck *et al.*, 2001). The refractive index mismatch is less than that of (a), since the refractive index of a cell (n_1) is approximately 1.35-1.40 (Liang *et al.*, 2007), and is not tuneable. Black arrows, direction of cell stretch. Cell shown in light pink, beams in dark pink.

This chapter first illustrates the various methods used to characterise optical traps, before describing the construction and characterisation of two different double optical tweezer traps (as represented by Figure 6.2a) integrated with the N-SIM.

6.2 Characterisation of optical traps

An optical trap can be thought of as a microscopic Hookean spring, i.e. for small displacements of a trapped particle, the gradient restoring force is proportional to the particle displacement:

$$F = -kx \tag{6.1}$$

where F is the trapping force, k is the trap stiffness and x is the particle displacement. Several methods exist to characterise the performance of an optical trap by measuring trap stiffness. Here, three of the most commonly used methods are described: the viscous drag force method, the power spectral density (PSD) method, and the equipartition theorem method.

In addition, the Q value is often used as a measure of trap quality independent of the trapping beam power. Equations 3.15 and 3.16 from Chapter 3 that describe the scattering (F_s) and gradient (F_g) forces can be re-expressed as:

$$F_s = Q_s \frac{n_m P}{c} \tag{6.2}$$

$$F_g = Q_g \frac{n_m P}{c} \tag{6.3}$$

where Q_s and Q_g are dimensionless factors that are proportional to F_s and F_g respectively. The total force acting on the sphere is:

$$F = Q \frac{n_m P}{c} \tag{6.4}$$

where Q is $(Q_s^2+Q_g^2)^{1/2}$, n_m is the refractive index of the trapping medium, P is the trap power and c is the speed of light. The Q value can be determined using the viscous drag force method as described below. The maximum theoretical value of Q is 2, though in practice Q values of <0.30 are typical (Ashkin, 1992).

6.2.1 Viscous drag force method

The viscous drag force method measures the displacement of a trapped particle from its equilibrium position by establishing a fluid flow around the particle, thus imparting a Stokes' drag force (Sarshar, Wong & Anvari, 2014). To induce a fluid flow, either the trap or particle sample chamber is moved using a motorised stage at known velocity whilst the other remains fixed.

The Stokes' drag coefficient γ_0 is given by:

$$\gamma_0 = 6\pi\eta r \tag{6.5}$$

where η is the fluid viscosity and r is the particle radius (Neuman & Block, 2004). For small displacements up to ~110nm of the particle from the trap centre (Perkins, 2009), the trapping force is equal to the drag force F_{drag} (F from Equation 6.1) such that from Equation 6.1:

$$k = -\frac{F_{drag}}{x} = -\frac{\gamma_0 \, v_{flow}}{x} \tag{6.6}$$

where $v\,flow$ is the fluid flow velocity relative to the trapped particle. The particle displacement x is determined using a CCD camera.

Trapping is typically performed close to the surface of a glass coverslip, where the Stokes' drag increases dramatically and the trapped particle experiences an increased effective fluid viscosity. Faxen's correction must therefore be applied (Faxen, 1922). The modified Stokes' drag coefficient γ is given by:

$$\gamma = \frac{\gamma_0}{1 - \frac{9}{16}\left(\frac{r}{h}\right) + \frac{1}{8}\left(\frac{r}{h}\right)^3 - \frac{45}{256}\left(\frac{r}{h}\right)^4 - \frac{1}{16}\left(\frac{r}{h}\right)^5} \tag{6.7}$$

where h is the height of the particle from the surface (Neuman & Block, 2004).

The Q value can be obtained independently of knowledge of x. If the stage velocity is increased such that the Stokes' drag force just overcomes the trapping force, the particle is freed from the trap. At this escape velocity v_{escape}, the drag force and trapping force F can be equated, and Equation 6.4 solved for Q:

$$F_{drag} = 6\pi\eta r v_{escape} \tag{6.8}$$

$$Q = \frac{cF}{n_m P} \tag{6.9}$$

The viscous drag force method involves a simple setup, requiring only a motorised stage and CCD camera. However, it fails to consider the Brownian motion of the trapped particle and so often does not provide a reliable value of trap stiffness. The Q value, however, though less frequently used, is a useful indicator of trapping efficiency.

6.2.2 Power spectral density method

A trapped particle moves randomly within an optical trap due to Brownian motion. The PSD method uses frequency domain analysis to determine the trap stiffness for a particle of known

size (Berg-Sørensen & Flyvbjerg, 2004). The position of the trapped particle is recorded over time using a CCD camera or quadrant photodiode (QPD). A Fourier transform of bead position yields a one-sided power spectrum:

$$S(f) = \frac{k_B T}{\pi^2 \gamma_0 ({f_0}^2 + f^2)} \tag{6.10}$$

where $S(f)$ is the PSD in units of displacement^2/Hz, k_B is Boltzmann's constant, T is the absolute temperature, f_0 is the roll-off frequency of the optical trap and f represents the frequency (Neuman & Block, 2004). The drag coefficient γ_0 may be substituted by γ (Equation 6.7) for particles trapped close to the coverslip surface. The trap stiffness k is determined from f_0 by:

$$k = f_0(2\pi\gamma_0) \tag{6.11}$$

The PSD method is the most commonly used approach to determine trap stiffness and has been used to calibrate optical tweezers with less than 1% error (Berg-Sørensen & Flyvbjerg, 2004). However, it assumes that the trap is a harmonic potential and requires a sufficiently high bandwidth for accurate particle tracking.

6.2.3 Equipartition theorem method

The equipartition method estimates the trap stiffness by analysing the thermally driven position fluctuations of a trapped particle (Florin *et al*., 1998). The equipartition theorem states that for a particle trapped in a harmonic potential of stiffness k, each particle degree of freedom has $\frac{1}{2}k_B T$ of energy:

$$\frac{1}{2}k_B T = \frac{1}{2}k\sigma^2 \tag{6.12}$$

where σ^2 is the position variance of the trapped particle in relation to the centre of the trap (Neuman & Block, 2004). The movement of the trapped particle is tracked using a CCD camera or QPD, and a histogram of particle positions in x and y dimensions produced and the trap stiffness determined from the position variance:

$$k_{x,y} = \frac{k_B T}{{\sigma^2}_{x,y}} \tag{6.13}$$

where $k_{x,y}$is the trap stiffness in x or y, and ${\sigma^2}_{x,y}$ the position variance in x or y. Equipartition is a relatively simple method for obtaining trap stiffness, since it does not require knowledge of the Stokes' drag coefficient. However, the equipartition method does not account for trap

or particle drift, which broadens the width of the position histogram, and as for the PSD method requires sufficient detector bandwidth for accurate particle tracking. The equipartition theorem also assumes that the movement of the trapped particle is due only to thermal fluctuations.

6.3 Optical trapping using an aspheric lens

The N-SIM is an inverted microscope, with the objective lens positioned below the sample. As the N-SIM is a commercial system, it was advantageous to design an optical trapping setup that was decoupled from the microscope, and to therefore trap from above the SIM objective and sample. To reduce the optical damage of live cells, an infrared (IR) cw Ytterbium fibre 1064nm laser (YLR-10-1064-LP-SF, IPG Laser GmbH, maximum output power 10W, M^2 <1.10) provided the trapping beam.

In order to trap from above the sample, a compact trapping apparatus was required to accommodate the spatial restraints of the N-SIM and for mechanical stability. Rather than using a second objective lens, a miniaturised aspheric lens designed to work in water and with a theoretical NA of 0.77 was selected for trapping (Geltech moulded aspheric lens, LightPath Technologies). 2μm carboxylated polystyrene beads were chosen for trap characterisation as these have previously been used as handles for optical trapping of neuronal CATH.a cells (Saxena, 2003).

6.3.1 Characterisation of the aspheric lens

To determine the focusing ability and practical NA of the aspheric lens, a single beam trap and imaging system was constructed (Figure 6.3). The aspheric lens was fixed at the end of a custom-made conical holder and suspended above a 35mm glass-bottomed dish (fluorodish, World Precision Instruments, FD35-100) filled with water, supported in a vertical cage system. The 1064nm laser was directed to the single beam aspheric lens trap using a polarizing beamsplitter (PBS) cube (PBS253, Thorlabs) for adjustment of laser power and doubled in width using a Keplerian telescope to fill the back-aperture of the aspheric lens. The power of the beam was controllable by a half-wave plate (HWP) (WPH10M-1064, Thorlabs). The beam was focused in water by the aspheric lens (focal length 3.10mm) and imaged using a 60x objective lens (NA 0.80, Nikon) and CCD camera (piA640-210gm, Basler). The height of the objective lens was adjusted using a z-axis translation mount (SM1Z, Thorlabs). A short-pass

IR filter (FF01-950/SP-25, Brightline, Semrock) was placed before the CCD camera to reduce camera saturation by the trapping beam.

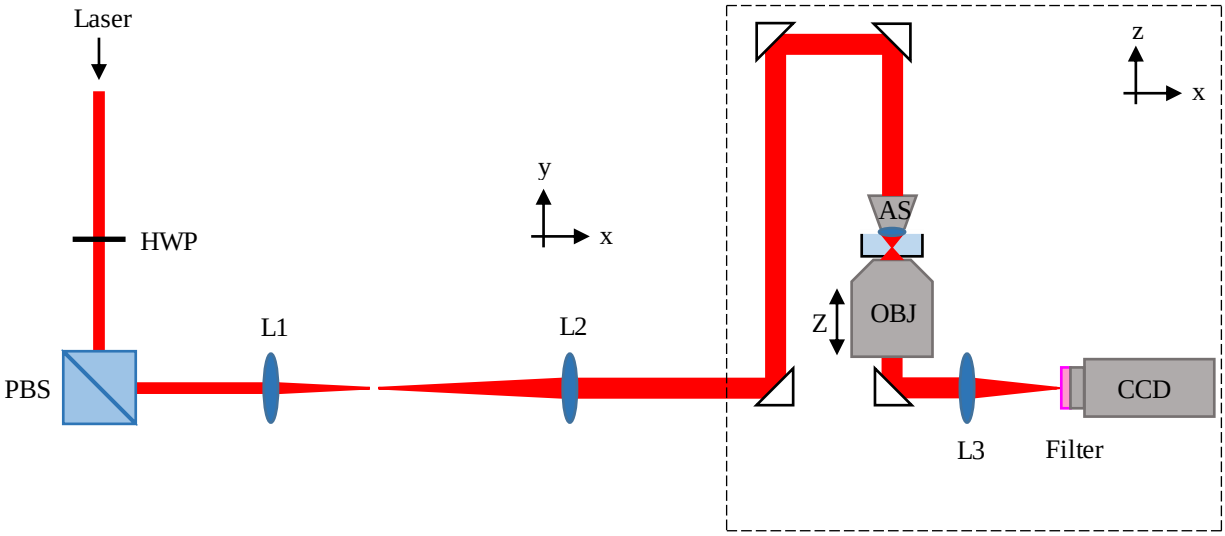

Figure 6.3 Aspheric lens trap imaging setup. HWP, half-wave plate; PBS, polarizing beamsplitter; L1-L3, lenses 1-3; AS, aspheric lens; OBJ, objective lens; Z, z-translation mount; CCD, camera; white triangles, mirrors; 1064nm laser beam shown in red. Lens focal lengths: L1, 100mm; L2, 200mm; L3, 200mm. Critical distances: L1-L2, 300mm; OBJ-L3, 200mm; L3-CCD, 200mm. Image not to scale.

Prior to measuring the NA of the aspheric lens, the magnification of the 60x objective/CCD camera imaging system was calculated as 72±2x by imaging twenty 4μm polystyrene beads (Polysciences) in a sample dish of water and measuring their diameter using FIJI. The expanded beam Airy disk was then imaged, and the FWHM of the beam focus measured as 1345±104nm (Figure 6.4). From $r_{x,y} = \lambda/2NA$, where $r_{x,y}$ is the lateral beam radius and λ the beam wavelength, the NA of the aspheric lens was calculated as 0.40.

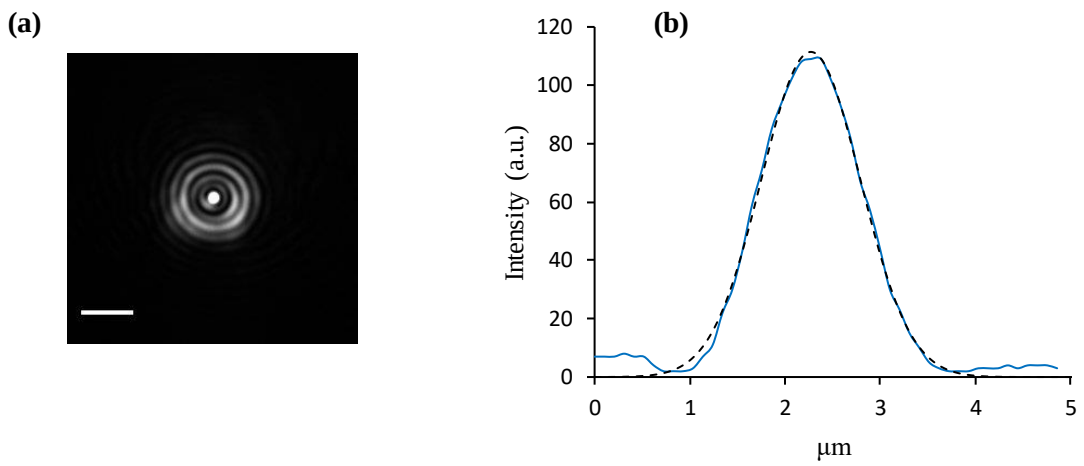

Figure 6.4 Aspheric lens lateral beam profile. **(a)** Expanded Airy disk. Scale bar, 5µm. **(b)** Lateral intensity profile of the beam focus determined using FIJI (solid blue). The profile was fitted with a Gaussian model (dashed black) using MATLAB.

6.3.2 Construction of an aspheric lens double optical trap on the N-SIM

A double optical trap was designed for the N-SIM based upon the Fällman and Axner system for steerable dual-trap optical tweezers (Fällman & Axner, 1997) (Figure 6.5). This setup was chosen for its compact geometry, and as a simple method to allow independent x/y control of each trapping beam as well as z control for one of the traps relative to the other.

The 1064nm laser beam described above was split into two orthogonally polarized beams (henceforth referred to as the reflected and transmitted beams) using a PBS (PBS1, PBS253, Thorlabs), and steering mirrors placed in the arm of each beam. The beams were recombined into a common path using a second PBS (PBS2) and expanded to fill the back aperture of the aspheric lens using a 1.67x Keplerian telescope. The power of each beam was controlled using the HWP placed before PBS1. The aspheric trapping lens was fixed at the end of the conical holder in a vertical cage attached to the microscope condenser mount such that both beams were focused into a fluorodish positioned on an incubation stage above the microscope objective. The condenser mount positioning screws allowed for adjustment of position of the aspheric lens in x, y and z.

Fine adjustments of the x and y positions of the traps in the sample dish could be made using the steering mirrors (SM1 and SM2) at conjugate planes to the back aperture of the aspheric lens. A small tilt of SM1/SM2 around its nominal position resulted in a change in the direction of the beam at the back aperture of the aspheric lens and a change in the x and y position of the

trap focus in the sample plane. For matching of the z position of the trapping plane for both beams, an afocal lens cage system was placed in the reflected beam arm such that movement of one of the lenses relative to the other along the cage produced a slightly more divergent or convergent beam and the focus of the trap in z was changed in the sample plane. For instance, movement of L1 away from L2 towards PBS1 produced a more divergent reflected beam that shifted the focus of the trap in the sample downwards in z.

For trap stiffness measurements (see below), the beams were imaged with the pylon Viewer software using the Basler CCD camera attached to the camera port of the microscope. The short-pass IR filter was placed in the microscope filter turret to reduce camera saturation. White light for imaging trapped beads was provided by a fibre illuminator (OSL1-EC, Thorlabs) positioned above the final mirror.

2.19μm carboxylated polystyrene beads (PC05N, 10095, Bangs Laboratories) have previously been shown to attach to the membrane of neuronal cells (Saxena, 2003) and so were used as trapping particles. For trapping, a 1% bead suspension was diluted in 2ml of deionized water and added to a fluorodish, and the sample placed on the stage above the microscope objective with the aspheric lens raised above the dish. Using the fibre illuminator as a light source, beads that had settled just above the base of the dish were brought into focus by adjusting the height of the objective and located using the CCD camera. To match the trapping plane with the bead sample plane, the fibre illuminator was switched off and the aspheric lens slowly lowered into the sample dish. As the trap was brought into focus, the IR filter was selected to reduce camera saturation. In order to trap a bead, the beam focus was moved close to a bead exhibiting Brownian motion using the appropriate steering mirror to allow the bead to be pulled into the trap. Beads were trapped at a distance of 1.6mm from the surface of the aspheric lens.

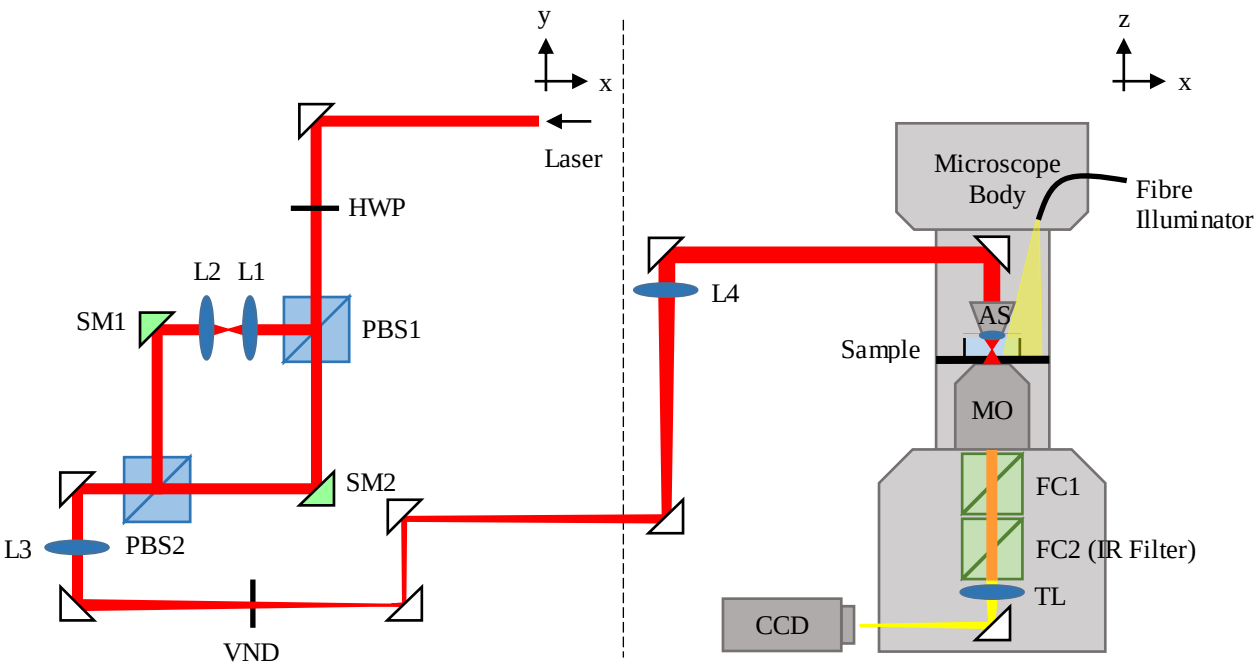

Figure 6.5 Schematic of aspheric lens double optical trap setup on SIM. HWP, half-wave plate; PBS, polarizing beamsplitter; L1-L4, lenses 1-4; SM, steering mirror; VND, variable ND filter; AS, aspheric lens; MO, microscope objective; FC, filter cube; TL, tube lens; CCD, camera; white triangles, mirrors; 1064nm laser beam shown in red. Lens focal lengths: L1, 35mm; L2, 35mm; L3, 300mm; L4, 500mm. Critical distances: L1-L2, 70mm; SM1-L3, 300mm; SM2-L3, 300mm; L3-L4, 800mm; L4-AS, 500mm. Image not to scale.

Prior to carrying out trap stiffness measurements, the practical NA of the aspheric lens for both the reflected and transmitted beams was measured using the 100x SIM objective (Apo TIRF, NA 1.49, Nikon). The magnification of the 100x objective imaged using the CCD camera was calculated as 107±2x by measuring the diameter of twenty 4μm polystyrene beads as described above. The expanded Airy disk of each beam was then imaged, and the lateral FWHM of the reflected and transmitted beam focus measured using FIJI as 1597±69nm (error of ± 1 pixel) and 1250±69nm respectively, corresponding to an effective lens NA of 0.34 and 0.43 (Figure 6.6).

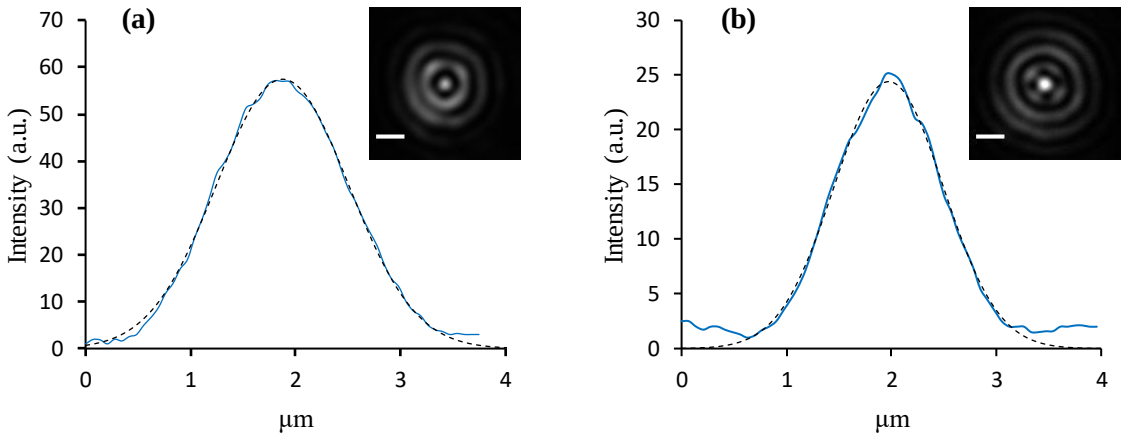

Figure 6.6 Double trap lateral beam profiles. Lateral profile (solid blue) and expanded Airy disk of reflected beam **(a)** and transmitted beam **(b)**. The profiles were fitted with a Gaussian model (dashed black). Scale bar, 2µm.

6.3.3 Characterisation of the aspheric lens double optical trap

Trap stiffness for the transmitted beam was measured using the equipartition method (see Section 6.2.3). 100 second videos of individually trapped 2.19µm carboxylated polystyrene beads were recorded using the pylon Viewer software at 400 frames per second and with an exposure time of 123ms. Trapped beads were imaged using the 100x objective and the fibre illuminator as the light source. Videos were recorded for a transmitted power of 20-200mW every 10mW, with 5 videos recorded per power, and analysed using MATLAB.

Trap stiffness in the x and y dimensions was determined for each video using three different MATLAB codes: "imfindcircles", "centre-of-mass" and "filtered centre-of-mass". The purpose of each code was to track the position variance of the trapped bead in x and y over time. "imfindcircles" traced the outline of the bead as a circle; "centre-of-mass" identified the centre of the bead from a thresholded image frame; and "filtered centre-of-mass" identified the centre of the bead in each image frame that had been filtered for noise removal. From the position variance, the trap stiffnesses k_x and k_y in pN µm^{-1} were calculated from Equation 6.13. Example output results for k_x from MATLAB using the "imfindcircles" code are shown in Figure 6.7. Frequency histograms of bead positions in x and y displayed Gaussian profiles.

(a) **(b)** **(c)**

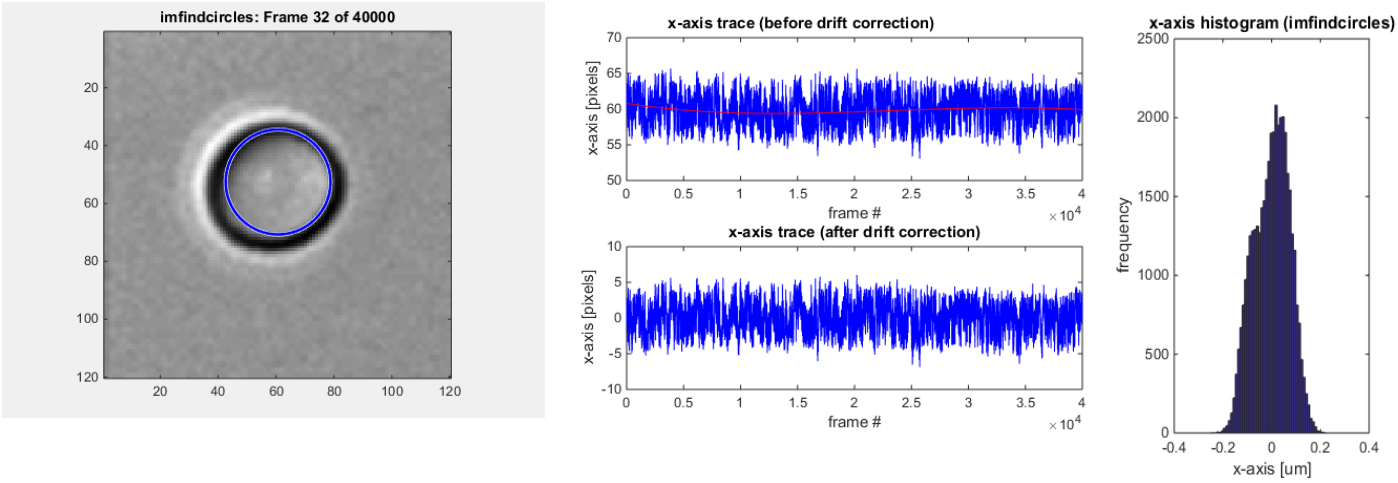

Figure 6.7 MATLAB output data for k_x using "imfindcircles" from a video of a bead trapped at 200mW. **(a)** Identification of the bead as a circle in a 120x120 pixel image frame. **(b)** Trace of circle fitted to bead in x in 4000 image frames before and after drift correction. **(c)** Histogram of frequency of bead position in x.

Results for k_x and k_y calculated using all three codes are shown below in Figure 6.8; k_x' and k_y' were determined from the line of the graphs in pN μm^{-1} mW^{-1}. The greatest measured k_x' value was 0.0167pN μm^{-1} mW^{-1} using the "centre-of-mass" code, an order of magnitude lower than reported for other optical trap setups. For example, a k_x' value of 0.63pN μm^{-1} mW^{-1} was measured for 3µm diameter polystyrene beads trapped by a beam of NA 0.30 (Nylk *et al.*, 2015). Attempts to optimise the three codes, including by principal component analysis (PCA, see Section 6.5.3) to minimise background noise and image artefacts as performed by Nylk *et al*. (2015), resulted in negligible changes in the calculated k_x and k_y values (data not shown). As illustrated by the graphs of k_x and k_y versus beam power, equipartition results were also extremely disparate and displayed weak linear trends. Equipartition experients for the reflected beam were not carried out owing to the poor results of the transmitted beam. Inherent mechanical instability of the double trap optical setup may have contributed to the low trap stiffness results. A new design for a double optical trap for the N-SIM was therefore conceived.

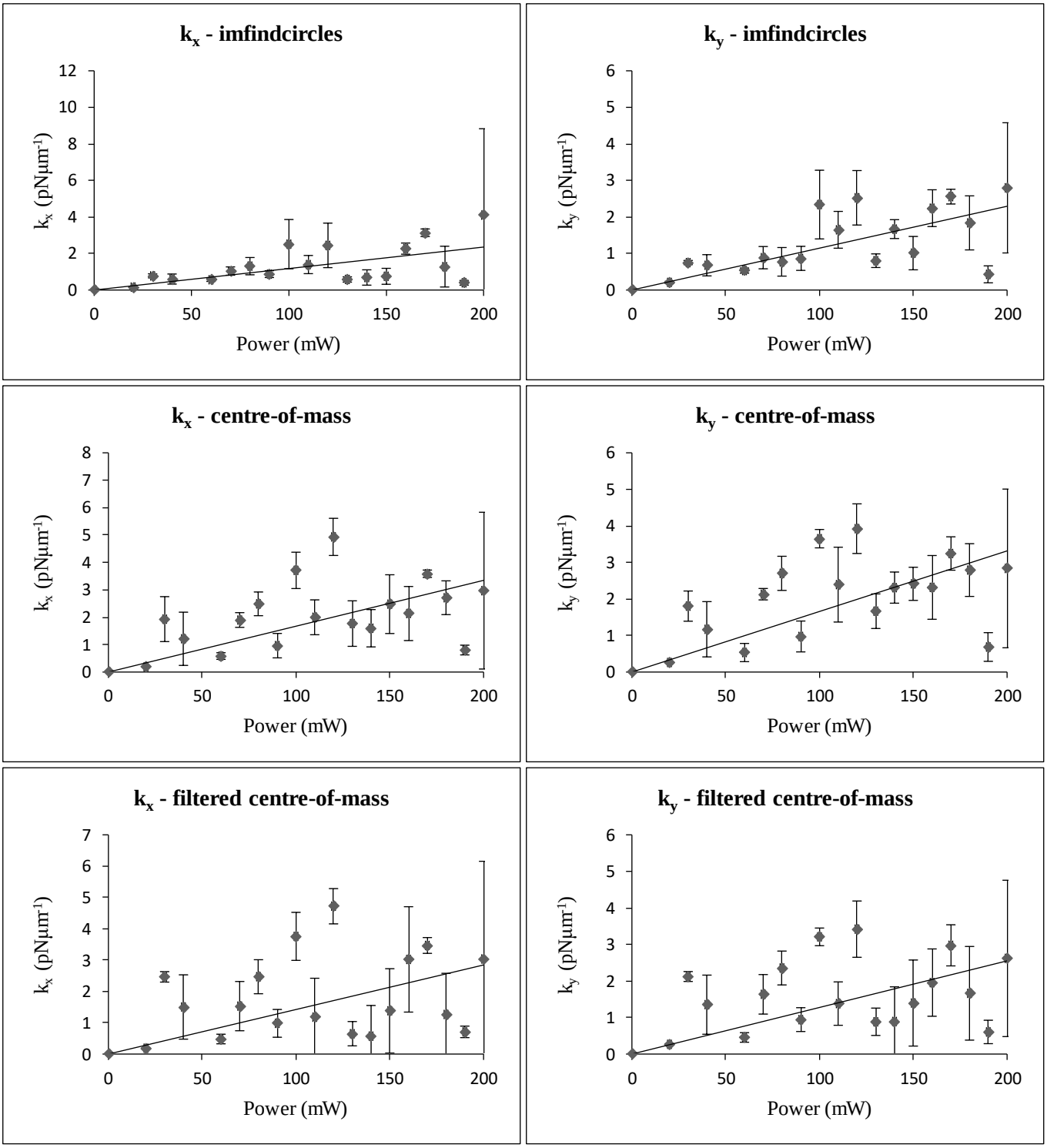

Figure 6.8 Graphs of k_x (left) and k_y (right) versus power for the transmitted beam. Dark grey circles, mean k_x and k_y values; error bars, standard deviation.

Previously, a single beam GRIN lens optical fibre trap was successfully integrated with the N-SIM (Nylk *et al*., 2015). This system had the advantage of being more compact than the above setup for the aspheric lens and being fibre-based, negated the requirement for continuous whole-system alignment and so was incorporated into a new design for a double optical trap.

Described below are the characterisation of a single-beam GRIN lens trap using a basic microscope setup and construction of a fibre-based double GRIN lens optical trap on the N-SIM.

6.4 Optical trapping using a gradient-index lens

6.4.1 Viscous drag force Q value measurements for a single beam GRIN lens optical fibre trap

To determine the quality of the GRIN lens for trapping, a basic microscope was constructed as a means for determining the Q value (trapping efficiency) of a single beam GRIN lens trap using the drag force method (see Section 6.2.1) (Figure 6.9a, b). Although this microscope could also have been used to determine trap stiffness as above, Q value measurements were advantageous in that they are comparatively simpler and less time-intensive than equipartition measurements.

The trapping probe consisted of a commercially-available GRIN microlens (GT-MO-080-018-810, GRINTECH) (Figure 6.9c) positioned 200μm from the distal end of a single mode (SM) optical fibre (780HP-custom, NA 0.13, design wavelength 780-960nm, SMA-SMA connected, Thorlabs) using a custom-made SMA adaptor (Figure 6.9a). A 785nm laser (TA 100, TuiOptics, maximum power output 300mW) was coupled into the SM fibre via a fibre collimator lens (F220SMA-780, Thorlabs) using two steering mirrors (SM1 and SM2). The beam power was adjusted using a variable neutral density (ND) filter (NDC-50C-2-B, Thorlabs).

The microscope comprised a fluorodish sample stage on an xyz mount (M-562-XYZ-LH ULTRAlign™, Newport), below which the 60x objective lens was positioned. The trapping probe was fixed on a second xyz mount on top of the sample stage. White light from the fibre illuminator was collimated using L2 and directed through the objective and into the sample via a PBS cube (PBS251, Thorlabs) and mirror. The 785nm beam and polarized white light reflected from the sample were detected by the CCD camera. A short-pass IR filter (FESH0700, Thorlabs) positioned before the camera was used to block the trapping beam.

Polarized light was used to image the beads in order that light reflected by the GRIN lens was not detected by the camera: S-polarized light was reflected by the PBS towards the sample dish, and P-polarized light transmitted by the PBS to the camera; therefore, only light that had

changed from S-polarized to P-polarized by reflection off the round surface of the beads contributed to the detected image.

With an input beam of NA 0.18, the theoretical NA of the GRIN lens is 0.8 (Figure 6.9c). However, the SM fibre used in this system had an NA of ~0.13, restricting the GRIN lens NA to ~0.58. The FWHM of the beam was measured as 1035±104nm, equivalent to an NA of 0.38 (Figure 6.10a).

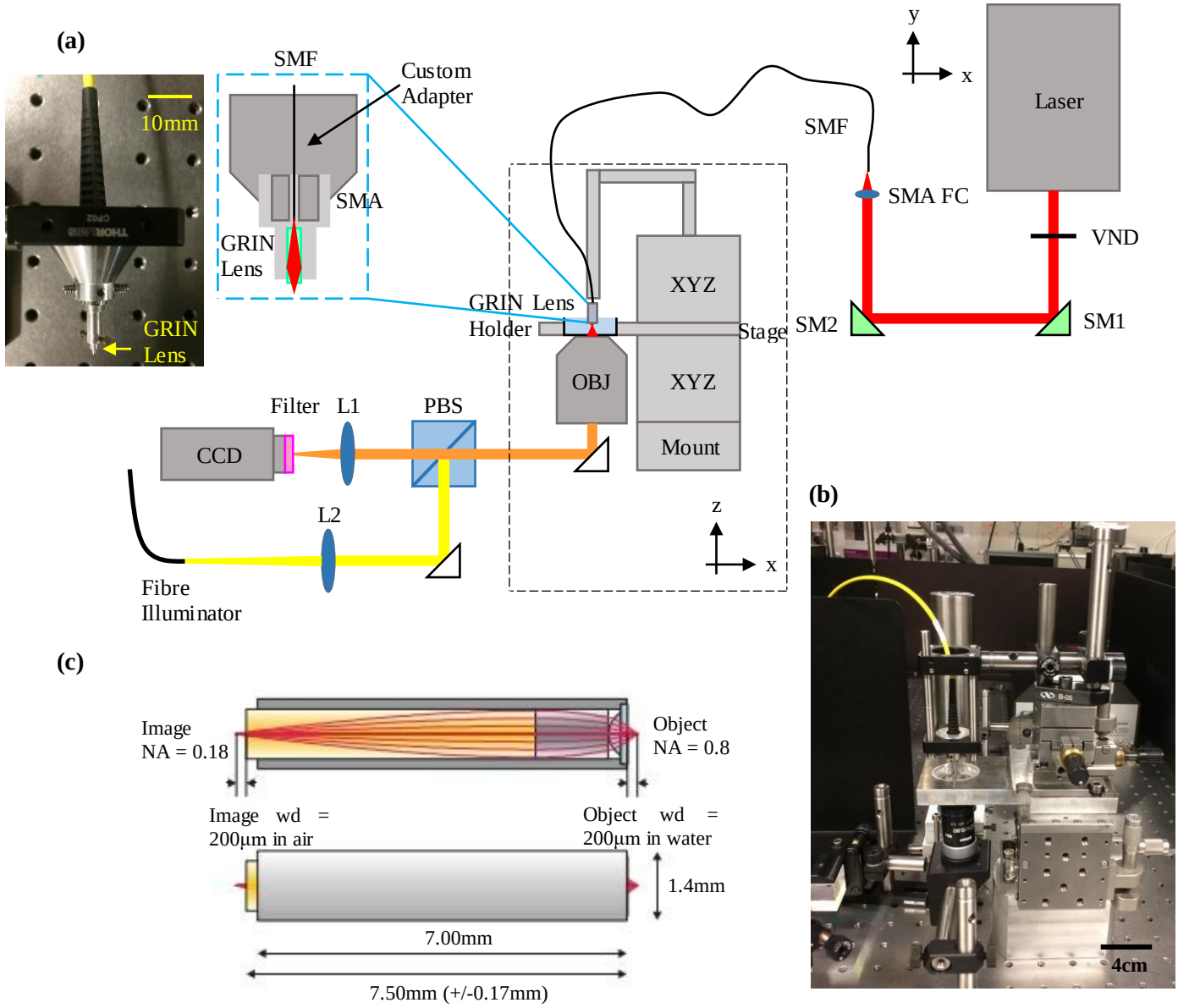

Figure 6.9 GRIN lens fibre optical trap and imaging system for drag force measurements. **(a)** Schematic of optical trap and microscope setup. The custom adaptor for mounting the GRIN lens to the end of the SM fibre is shown in the photograph. VND, variable ND filter; SM, steering mirror; SMA, subminiature version A connector; SMA FC, SMA fibre collimator; SMF, single mode fibre; XYZ, xyz translation stage; OBJ, 60x objective lens; white triangles, mirrors; PBS, polarizing beamsplitter; L1 & L2, lenses 1 & 2; CCD, camera; 785nm laser beam shown in red; white light shown in yellow; 785nm beam and white light shown in orange. Lens focal lengths: L1, 200mm; L2, 50mm. Critical distances: OBJ-L1, 200mm; L1-CCD, 200mm. Image not to scale. **(b)** Photograph of SM fibre/GRIN lens single beam trap mounted on an xyz stage above the sample dish and 60x objective. **(c)** GRIN lens dimensions, working distances (wd) and NA. The GRIN lens is comprised of two smaller lenses (yellow and purple) of graded refractive index mounted in a stainless steel holder (light and dark grey). Beam rays are shown in red.

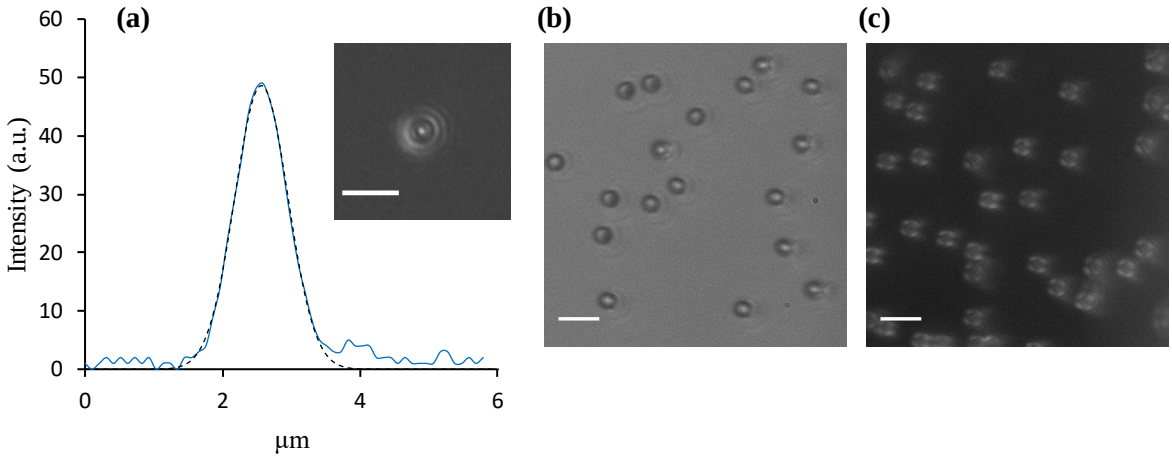

Figure 6.10 Lateral trap profile and beads imaged using the GRIN lens trap 60x objective imaging system. **(a)** Lateral profile (solid blue) and expanded Airy disk of the 785nm trap in water. The profile was fitted with a Gaussian model (dashed black). **(b)** 2.19µm carboxylated polystyrene beads imaged using brightfield light. **(c)** 2.19µm carboxylated polystyrene beads imaged using polarized light. Scale bars, 5µm.

Q values were calculated from viscous drag force measurements for four sets of polystyrene beads (1, 2 and 5µm uncoated polystyrene beads and 2.19µm carboxylated beads) in both the x and y dimensions at three different powers (2.5, 4 and 5mW) and five individual beads per power (Table 6.1). The 785nm laser was coupled from free space to the end of the GRIN lens with an efficiency of 25%, with the majority of power loss occurring after coupling of the collimated beam into the SM fibre. Bead trapping samples were made up in fluorodishes in water such that approximately 4 beads were present in the field of view. A representative image of the 2.19µm carboxylated beads imaged under polarized light is shown in Figure 6.10c. Beads appeared similar to those imaged using a conventional polarization microscope (Yang *et al*., 2003). Once a bead was stably trapped in the lateral direction, the trapping probe was moved, in one step, 40µm in the x or y directions at a specified velocity (maximum 0.4mm s^{-1}) using a motorised actuator attached to the trap xyz translation stage (ESP300, Newport). Beads were trapped at a distance of 200µm from the surface of the GRIN lens. The velocity at which the bead escaped the trap (v_{escape}) was recorded and used to determine Q from Equations 6.8 and 6.9. As trapping was carried out near (~250nm from) the surface of the fluorodish, Faxen's correction was applied for the calculation of the drag coefficient γ (Equation 6.7) (Neuman & Block, 2004). Results for Q_x and Q_y are given in Table 6.1.

Table 6.1 Average Q_x and Q_y values for various polystyrene beads**.** Q values were calculated for 2.19μm carboxylated polystyrene beads and 1, 2 and 5μm uncoated polystyrene beads.

Bead diameter (μm)	**Q_x**	**Q_y**
1	0.08 +/- 0.01	0.05 +/- 0.01
2	0.21 +/- 0.01	0.19 +/- 0.01
Non-fluorescent 2.19 (carboxylated)	0.27 +/- 0.01	0.22 +/- 0.06
5	0.30 +/- 0.01	0.25 +/- 0.02

The calculated Q values were shown to be within the upper range of those described in the literature (Table 6.2). The relatively high Q values obtained with a trap of relatively low NA (0.38) could be explained by the fact that the GRIN lens operated in water, thus minimising spherical aberrations that would otherwise arise with oil-immersion objectives. In addition, the flow of water around the trapped particle may have been extremely low, owing to the proximity (200μm) of the particle to the surface of the GRIN lens in the sample dish. This may have resulted in hydrodynamic trapping effects on the particle (Karimi, Yazdi & Ardekani, 2013). Relatively high Q values have previously been reported for low NA traps, e.g. Q_x values of ~0.2 were measured for an optical trap of NA 0.6 (Lei *et al*., 2013).

Table 6.2 Q values described in the literature. Q values for biological samples are typically lower than for polystyrene/silica microspheres, which can be attributed to the lower refractive index contrast between the cells/organelles and the surrounding media.

Sample	Optical trap	Q value	Reference
Polystyrene microsphere, 4.5μm diameter	1064nm single beam trap, 100x 1.4NA oil objective	0.14	Khatibzadeh *et al.*, 2014
Polystyrene microsphere, 10μm diameter		0.19	
Polystyrene microsphere, 15μm diameter		0.23	
Isolated mammalian chromosome		0.01-0.019	
Silicon sphere, 1.28μm diameter	800nm cw/femtosecond single beam optical tweezer, 100x objective	0.13	Agate *et al.*, 2004
Latex sphere, 3μm diameter	cw 1064nm single beam trap, 100x 1.3NA oil objective	0.21	Felgner, Müller & Schliwa, 1995
Glass sphere, 1.49μm diameter		0.14	
Glass sphere, 4.26μm diameter		0.33	
Silica sphere, 2μm diameter	532nm single beam trap, 100x oil objective	0.068	O'Neil & Padgett, 2001
Silica sphere, 5μm diameter		0.12	

6.4.2 Characterisation of a GRIN lens double optical trap

In order to create a double optical trap for cell stretching, two beams were required to be focused through the GRIN lens such that the traps were far enough apart to be at opposite ends of a cell but still have a small enough beam radius for trapping. To test that this was the case, the single beam GRIN lens fibre optical trap constructed for measuring Q values was adapted to steer the beam into the lens at different angles such that the trap could be imaged at different positions in x and y within the sample (Figure 6.11).

In order to achieve a GRIN lens trap of NA 0.8, the beam entering the GRIN lens was required to have an NA of 0.18 (see Figure 6.9c). To fulfill this requirement, the 785nm beam was

expanded four-fold using a Keplerian telescope to ~10mm in diameter and focused through a 25mm focal length lens into the GRIN lens. A relay lens system was placed such that the steering mirror was conjugate to the back focal plane of L5 and any tilt of the SM around its nominal position resulted in a change in direction of the beam at L5 and entering the GRIN lens and thus a change in the lateral position of the trap in the sample plane.

The trap was imaged at increasing distances from the central trap position using the 60x objective. The FWHM of the beam was within one standard deviation error for a distance of ~35μm in the x dimension and 30μm in the y dimension (Figure 6.12b, c).

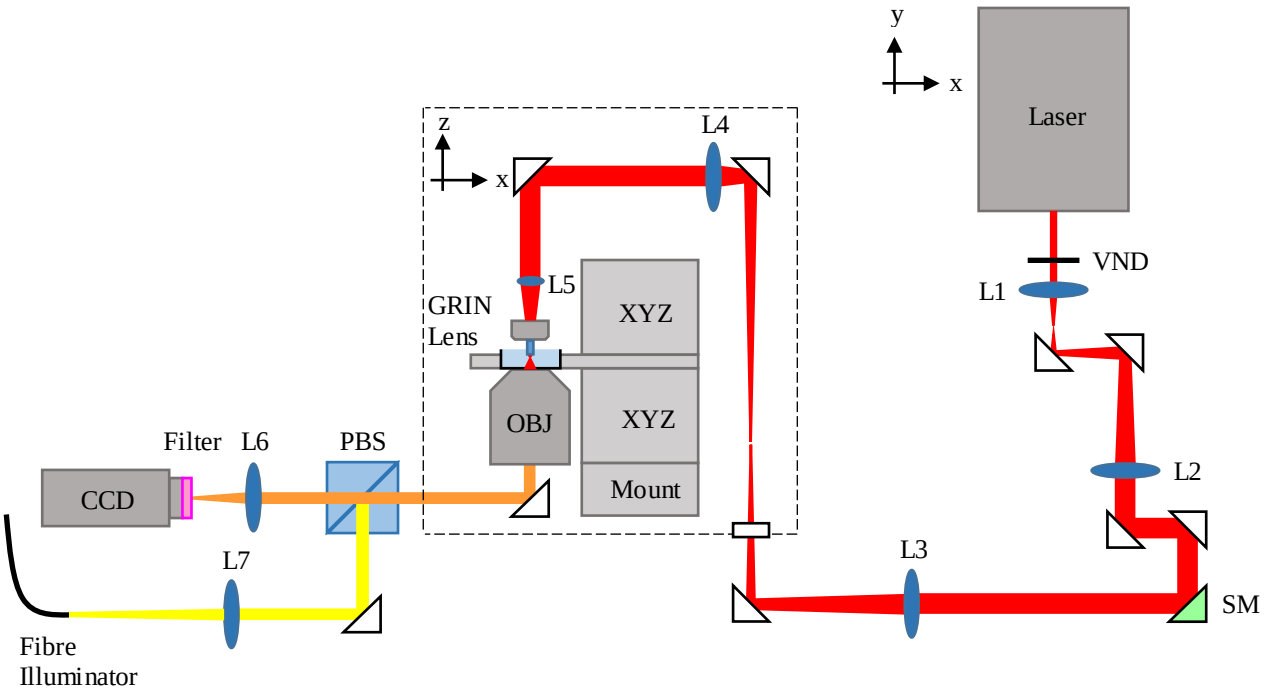

Figure 6.11 Schematic of optical setup for steering the GRIN lens trap. VND, variable ND filter; L1-L7, lenses 1-7; white triangles, mirrors; SM, steering mirror; XYZ, xyz translation stage; OBJ, 60x objective lens; PBS, polarizing beamsplitter; CCD, camera; 785nm laser beam shown in red; white light shown in yellow; 785nm beam and white light shown in orange. Lens focal lengths: L1, 50mm; L2, 200mm; L3, 200mm; L4, 200mm; L5, 25mm; L6, 200mm; L7, 50mm. Critical distances: L1-L2, 250mm; SM-L3, 200mm; L3-L4, 400mm; L4-L5, 225mm; L5-GRIN lens, 25.2mm; OBJ-L6, 200mm; L6-CCD, 200mm.

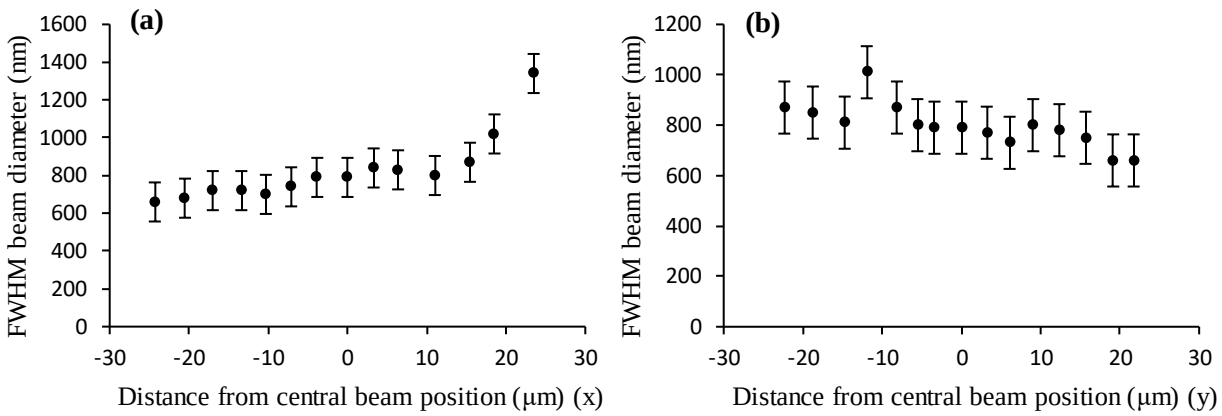

Figure 6.12 Beam profile at different lateral positions in the trapping plane. FWHM of beam profiles in x **(a)** and y **(b)** at increasing distances from the original trapping position. Error bars indicate ± 1 pixel error.

6.4.3 Design and characterisation of a GRIN lens double optical fibre-based trap for integration with the N-SIM

To transition easily from the optical bench to the SIM, a more flexible system than that of the aspheric lens N-SIM trap (Figure 6.5) was required. Therefore, rather than using a cage system as previously, a double optical fibre-hybrid trap was designed. An optical fibre system was also advantageous in that it negated the requirement for alignment of the beams in free space using multiple mirrors. The 785nm laser was split into two orthogonally polarized beams using a PBS (PBS252, Thorlabs) and each beam coupled into an SM fibre via an SMA fibre collimator using two steering mirrors (Figure 6.13a). A variable ND filter allowed for tuning of the laser power, and an HWP for control of the power of the two individual beams. The two SM fibres were connected to the double optical trapping probe attached to the microscope condenser mount above the sample stage.

Two key considerations for design of the double optical trapping probe were: 1) the available space between the condenser mount and microscope stage; and 2) maintaining the maximum NA of the two traps. To fulfil both requirements, a system of miniature aspheric lenses with focal lengths on the order of mms was constructed in a vertical cage system (Figure 6.13). The probe consisted of a vertical lens system and an orthogonal system for the second SM fibre. The fibre output beams were collimated in free space using two SMA fibre collimators (F240-SMA780), and the two beams expanded using a 2x telescope comprising two aspheric lenses.

The beams were then recombined into a common light-path using a 5mm x 5mm PBS (PBS052) and focused into the GRIN lens using lens C240TME-B (Thorlabs). The system was designed to expand each beam from the fibre output diameter 1.5mm to 2.99mm, such that when the beams were focused using C240TME-B, they had a theoretical NA of 0.18 to match that of the GRIN lens.

All optical components were mounted in Thorlabs SM cage plates, except for the PBS which was mounted in a custom-made steel holder that was also used to attach the side component of the probe, and the GRIN lens that was positioned in a thin custom-made steel cage plate. A kinematic mounting adaptor allowed for steering of the side trap relative to the other. The microscope incubator stage (INUG2H-TIZSH, Tokai Hit) was adapted to accommodate the double optical trapping probe.

The z positions of the trapping probe aspheric lenses were adjusted such that both traps were in the same z plane in the sample, then the height of the GRIN lens corrected to achieve the optimal focus of both traps. Figure 6.14 shows the lateral beam profiles of the reflected and transmitted traps imaged using the 60x objective and CCD camera. The FWHM of each beam was 618±104nm, corresponding to an NA of 0.64.

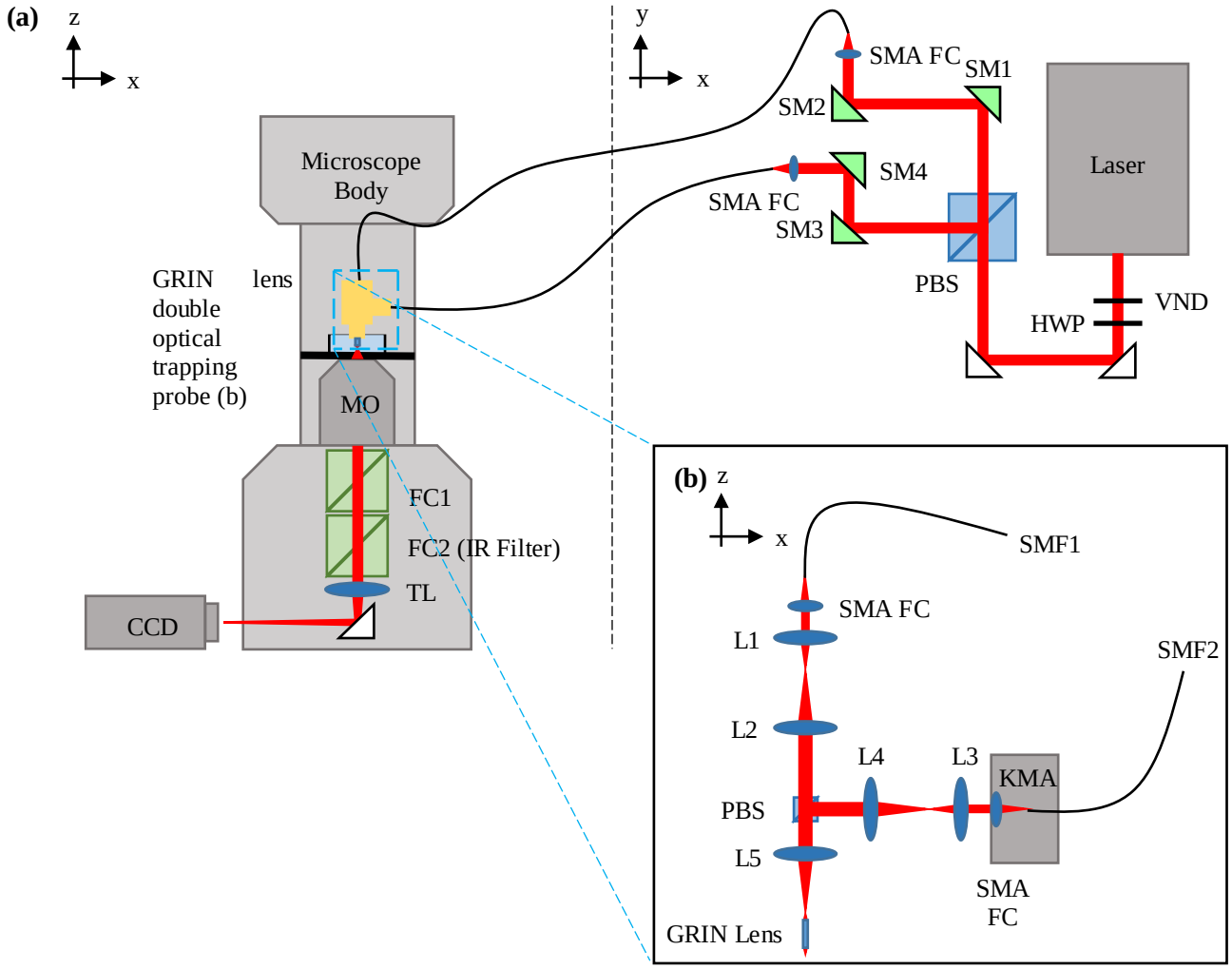

Figure 6.13 GRIN lens double optical trap setup on the N-SIM. **(a)** Overall system design. VND, variable ND filter; HWP, half-wave plate; PBS, polarizing beamsplitter; SM1-4, steering mirrors 1-4; SMA FC, SMA fibre collimator; MO, microscope objective; FC, filter cube; TL, tube lens; CCD, camera. Image not to scale. **(b)** Optical components of GRIN lens double optical trapping probe. SMF, single mode fibre; KMA, kinematic mounting adaptor; SMA FC, SMA fibre collimator; L1-L5, lenses 1-5; PBS, polarizing beamsplitter. Image not to scale.

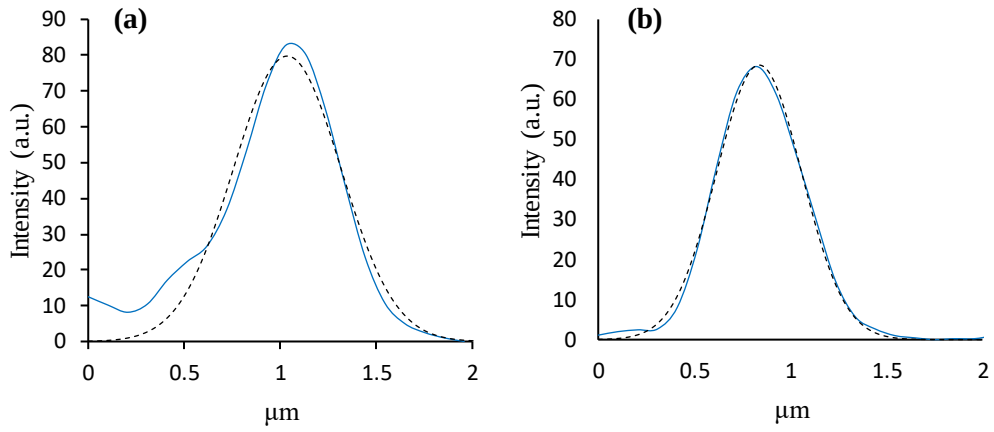

Figure 6.14 GRIN lens double optical trap lateral beam profiles. Lateral profiles (solid blue) of the transmitted **(a)** and reflected **(b)** beam. The profiles were fitted with a Gaussian model (dashed black).

Characterisation of both traps was carried out using the equipartition method as for the aspheric lens trap. The transmission efficiency of each trap from free space was 15% using maximum power directed into each SM fibre. Trapping videos were recorded for 6 different trap powers, from 5-30mW in 5mW steps, with 5 videos recorded per power. The microscope mercury lamp (C-HGFI Intensilight, Nikon) was used as the light source and was directed to the sample using a half mirror placed in the epifluorescence filter turret. Figure 6.15 shows the equipartition results for the reflected and transmitted beams for videos of trapped 2.19µm carboxylated beads that were filtered for noise using PCA (Nylk *et al*., 2015). Both k_x and k_y were higher for the reflected beam than for the transmitted beam (Table 6.3), with the latter showing greater data variability at higher trapping powers (Figure 6.15b).

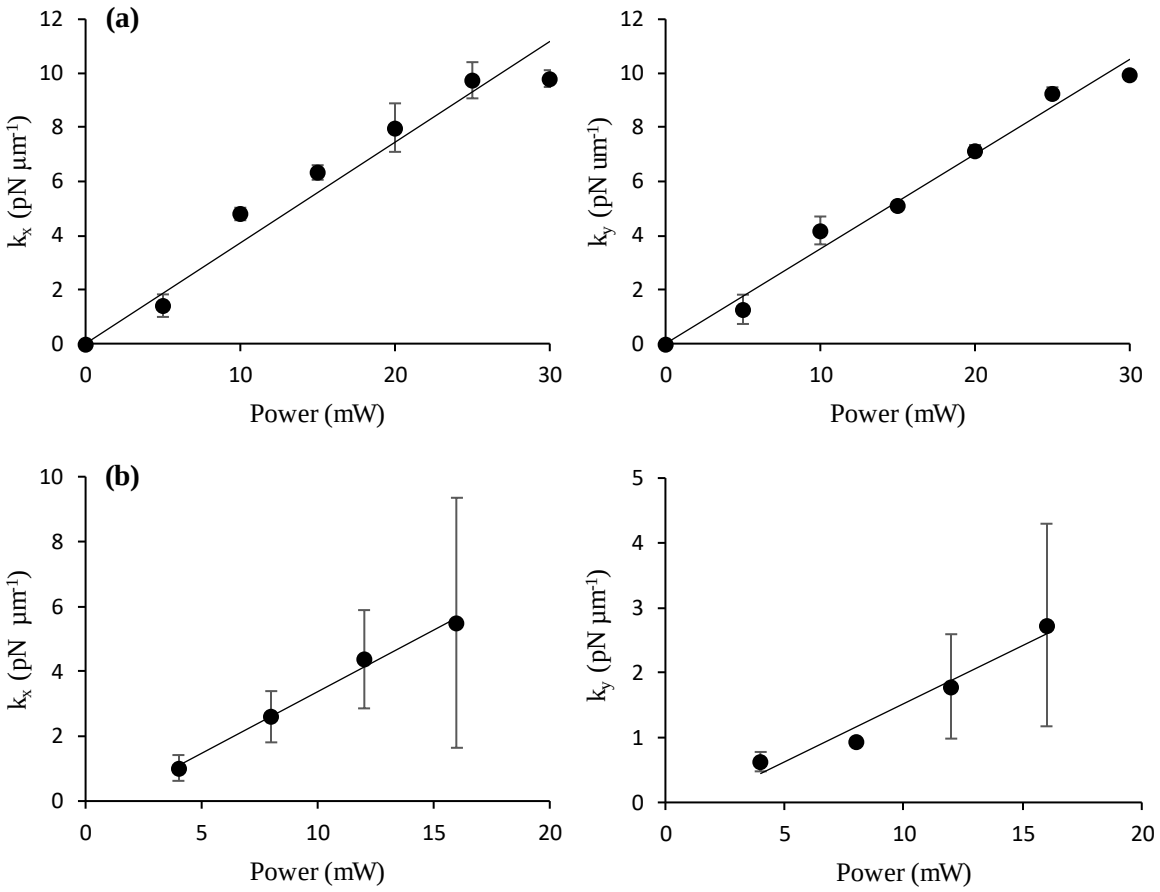

Figure 6.15 Graphs of trap stiffness vs power. k_x and k_y were calculated for **(a)** the reflected beam and **(b)** the transmitted beam of the double optical trap using MATLAB code "filtered centre-of-mass" from videos that were PCA-filtered using principal components 2-5.

Under visible light and imaged using the N-SIM electron multiplying CCD (EMCCD) camera (iXon 897, ANDOR), the carboxylated beads were not detectable. Fluorescent beads were therefore required for trapping with cells. Equipartition of 2µm carboxylated green fluorescent polystyrene beads (Fluoresbrite YG microspheres, 09847-5, Polysciences) was carried out for comparison with the non-fluorescent beads at 3 different powers with 3 videos recorded per power, and the results shown in Figure 6.16.

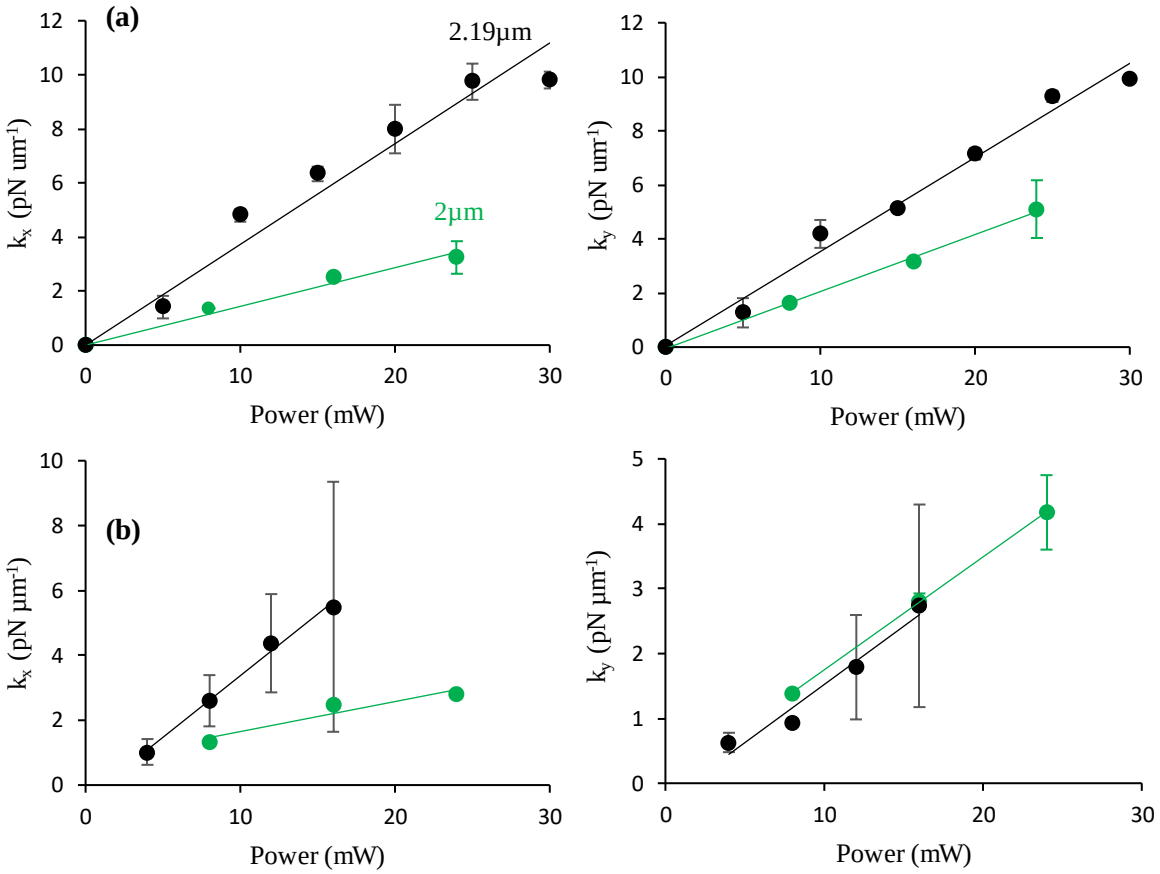

Figure 6.16 Trap stiffness graphs for fluorescent vs non-fluorescent beads. k_x and k_y were calculated for **(a)** the reflected beam and **(b)** the transmitted beam using MATLAB code "filtered centre-of-mass" from videos that were PCA-filtered using principal components 2-5. Trap stiffness results for the fluorescent beads are shown in green, and for the non-fluorescent beads, in black.

Trap stiffness results for both beams are shown below in Table 6.3.

Table 6.3 Equipartition trap stiffness results for fluorescent and non-fluorescent carboxylated beads for the GRIN lens double optical trap reflected and transmitted beams.

Bead	**Reflected beam**		**Transmitted beam**	
	k_x' (pN µm^{-1} mW^{-1})	**k_y' (pN µm^{-1} mW^{-1})**	**k_x' (pN µm^{-1} mW^{-1})**	**k_y' (pN µm^{-1} mW^{-1})**
Non-fluorescent 2.19µm	0.38±0.08	0.34±0.07	0.32±0.14	0.15±0.06
Fluorescent 2µm	0.15±0.02	0.20±0.02	0.15±0.02	0.17±0.01

Trap stiffness for fluorescent beads was much lower than that for non-fluorescent beads. This may have been due to differences in bead material/refractive index, or else the subtle difference

in size between the fluorescent (2µm) and non-fluorescent (2.19µm) beads. Indeed, the trap stiffnesses as shown above in Table 6.3 reflect the Q values as measured for the GRIN lens single-beam trap (Table 6.2): Q_x and Q_y for the 2.19µm non-fluorescent carboxylated beads were measured as 0.27 and 0.22 respectively; and Q_x and Q_y for the 2µm fluorescent beads as 0.21 and 0.19 respectively; Q_x and Q_y for larger 5µm beads were 0.30 and 0.25 respectively.

To test the double optical trap system using live cells, fluorescent shWillin-Lifeact-RFP cells were cultured in fluorodishes and incubated with the Fluoresbrite green 2µm carboxylated polystyrene beads. Once the beads had settled, cells were identified using the 561nm N-SIM filter cube. The trapping probe was then lowered into the sample dish and the trap moved into the ANDOR camera field of view. For trapping, IR filters were placed into the epifluorescence filter turret in order to block the beam entering the camera. Figure 6.17 shows an shWillin Lifeact-RFP cell alongside two trapped beads.

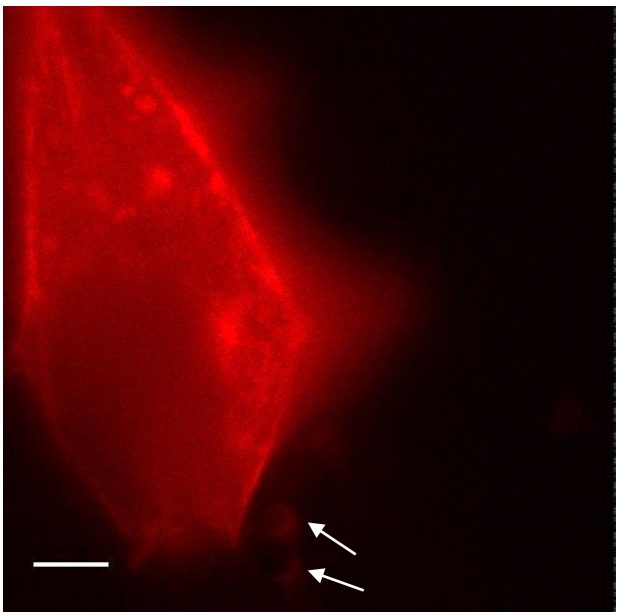

Figure 6.17 Widefield image of shWillin-Lifeact-RFP cell and 2µm fluorescent beads under 100x magnification. White arrows mark beads. Scale bar, 5µm.

A major issue encountered when trapping the fluorescent beads with cells was the sticking of the beads to the surface of the fluorodish after trapping, such that any further manipulation was not possible. This sticking was shown to be a result of the cell media, as with media alone, the beads stuck, but with water as the trapping medium instead of media, the beads did not stick. Using serum-free media and Tyrode's solution in place of DMEM/F12 media did not solve this issue.

This adherence of trapped beads to the glass surface of the fluorodish was thought to be due to the salt present in the media, required for the osmotic balance of the cells. Salt decreases the length of the electrical double layer at the interface between the trapping liquid medium and the glass surface; this double layer acts as a repulsive screen between a trapped bead and the glass, counteracting attractive Van der Waals forces. With increasing salt concentrations, the double layer length has previously been shown to diminish, and at high salt concentrations, beads to jump into contact with the glass surface and become immobilised shortly afterwards (Schäffer, Nørrelykke & Howard, 2007). Here, attempts to block the glass surface from bead contact by coating fluorodishes with the siliconizing reagent SigmaCote, 1% bovine serum albumin and pluronic F127 proved ineffective.

6.5 Discussion & future work

The aim of this chapter was to integrate a double optical trap with the commercial N-SIM for simultaneous optical manipulation and live-cell imaging to study the effect of Willin expression on mechanical control of YAP. Two double optical traps were designed and implemented: the first using a miniaturised aspheric lens, and the second, a GRIN micro-lens. Characterisation of both traps was performed using equipartition, and in addition, Q values of a single beam GRIN lens trap were measured on a custom-built microscope using the drag force method. Trap stiffness results of the original aspheric lens double trap were poor (k_x' = 0.0167pN μm^{-1} mW^{-1}), possibly due to mechanical instability of the trapping apparatus or the low effective NA of the traps (0.34 and 0.43 for the reflected and transmitted beams respectively). Trap stiffness results for the GRIN lens trap, however, were much improved, with k_x' and k_y' for the reflected beam determined as 0.38 pN μm^{-1} mW^{-1} and 0.34 pN μm^{-1} mW^{-1} respectively; for the transmitted beam, k_x' and k_y' were measured as 0.32 pN μm^{-1} mW^{-1} and 0.15 pN μm^{-1} mW^{-1} respectively. Q values for the GRIN lens single beam trap were also high: for 2μm polystyrene beads, Q_x was 0.21, and Q_y, 0.19. It should be noted that the two traps constructed on the N-SIM used different wavelengths, the aspheric lens trap, 1064nm, and the GRIN lens trap, 785nm, which may have led to different levels of sample heating for each trap and could have affected trap stiffness measurements.

In summary, a double optical trap was successfully implemented on the N-SIM, with full control of one of the traps in the x, y and z dimensions. The adsorption of trapped polystyrene beads to the fluorodish surface in the presence of cell media, however, was a major impediment

for cell manipulation. This may have been prevented if the trap was 3D, such that the bead was trapped axially as well as laterally, or if the trapping beam was directed from below the sample, rather than from above, as the radiation pressure of the beam may have contributed to the overall downwards force acting on the trapped beads. Trapping from below the sample could be implemented using the SIM 100x oil immersion objective lens, the NA of which (1.49) would be ideal for trapping. Figure 6.18 shows the potential path that the beam could take from the optics bench to through the SIM objective.

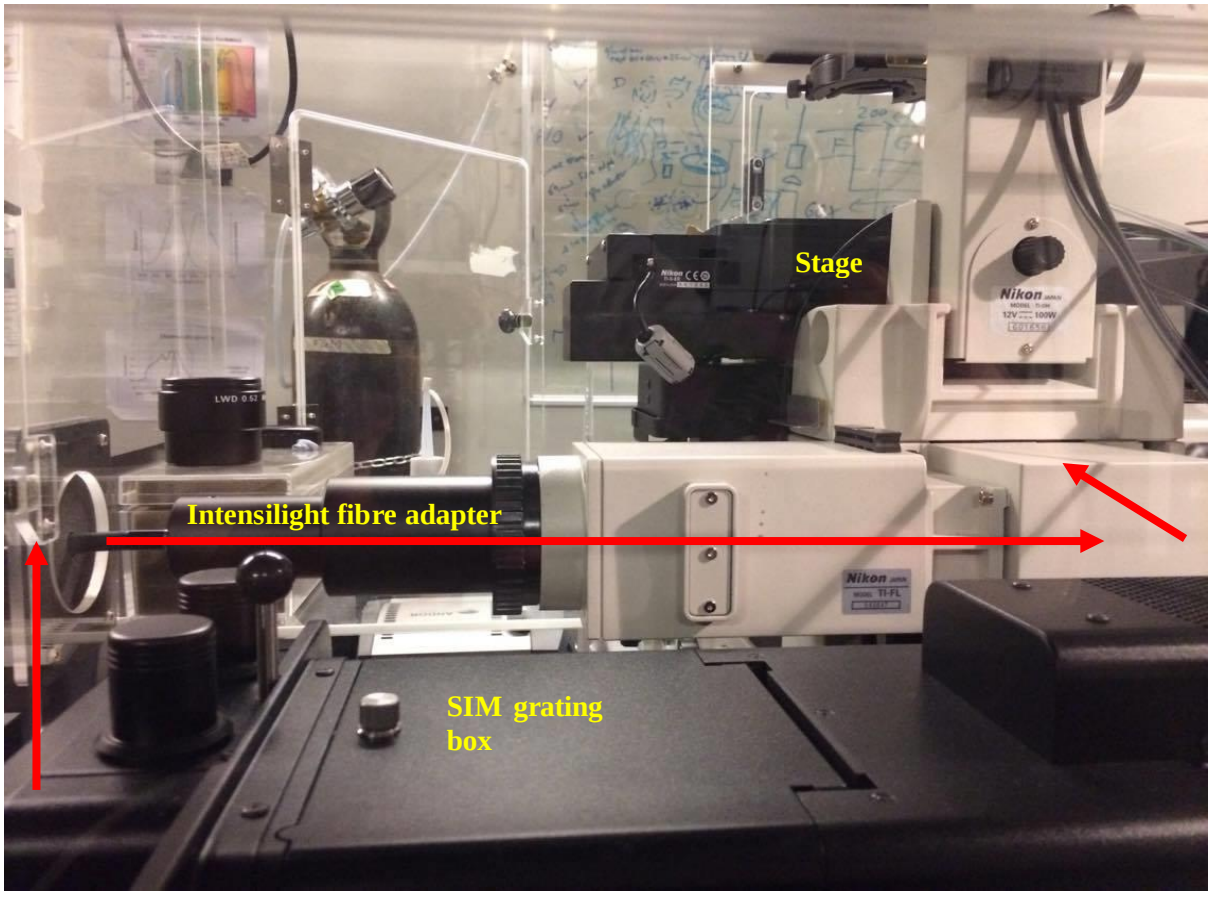

Figure 6.18 Light path for optical trapping through the N-SIM 100x objective lens. Red arrows denote the beam path from the optics bench and through the Intensilight fibre illuminator apparatus to the microscope objective lens.

As an alternative to stretching cells by pulling on beads adhered to the cell surface as was attempted in this study, beads could instead be dropped onto the cell surface to bring about an actin response. Since beads were occasionally phagocytosed by cells, internalised beads could also be manipulated by optical tweezers to generate internal forces. Optical traps have previously been used, for example, to manipulate particles internalised in living cells and attach them to molecular motors to study their dynamics (Norregaard *et al*., 2014).

The integration of an optical trap with a commercial microscope such as the N-SIM brings added complexities to the system design, namely spatial constraints and potential interference with the existing microscope optics. A more practical alternative may be the combination of an optical trap with a custom-built widefield microscope, for which the novel technique super-resolution radial fluctuations (SRRF) could be applied (Gustafsson *et al*., 2016). SRRF enables the acquisition of SIM-like images from standard widefield images and circumvents the requirement of the SIM grating. The construction of a custom microscope would also allow simpler implementation of an incubation chamber for control of temperature, humidity and CO_2 for long-term live-cell manipulation and imaging.

The question of whether optical trapping was the optimal method for stretching of adherent cells remained unanswered in this study. However, since the cytoskeleton enables the cell to resist deformation (Fletcher & Mullins, 2010), the optical trapping force would have to supersede the internal forces of the cell to enable cell stretching. The forces generated by optical traps are on the order of pN (Neuman & Block, 2004); meanwhile, the force generated by a single myosin molecule is ~3-4pN (Finer, Mehta & Spudich, 1995), whilst the native tension in contractile stress fibres of adherent cells has been shown to be on the order of 1-10nN (Labouesse *et al*., 2016; Harris, Jreij & Fletcher, 2018). Multiple studies have used optical tweezers to deform red blood cells (RBCs) (Lim *et al*., 2004; Mills *et al*., 2004; Suresh *et al*., 2005); however, RBCs are especially malleable since they lack a nucleus, and rather than actin-myosin stress fibres, the cytoskeleton instead consists of a flexible two-dimensional network of spectrin proteins beneath the plasma membrane (Li *et al*., 2007).

In light of the above, other methods may be better suited than optical trapping for stretching/manipulating adherent cells that could too potentially be combined with super-resolution microscopy. Several types of cell stretching device have been developed that are based on deformation of a thin, flexible and transparent membrane on which cells can be cultured (Kamble *et al*., 2016). This deformation is achieved by different means of actuation, e.g. pneumatic or dielectric. An advantage of using cell stretching membrane devices over optical tweezers for cell stretching is the ability to directly deform multiple adherent cells at once with repeatable delivery of strain (Tremblay *et al*., 2014; Imsirovic *et al*., 2015). Combination of these devices with an inverted microscope allows real-time live-cell imaging of deformed cells (Imsirovic *et al*., 2015; Poulin *et al*., 2016; Sigaut *et al*., 2018). A constraint for high- or super-resolution real-time imaging is the thickness of the membrane (on the order of ~ 0.1mm) and thus distance between the cells and objective lens, which limits the use of

high NA objectives that typically have very short working distances. However, devices have been fabricated that have enabled imaging with a long working-distance 60x objective lens (Poulin *et al*., 2018), for example, and with a 63x oil immersion objective for simultaneous cell stretching and FRET (Sim *et al*., 2012). Recently, an equibiaxial silicon membrane stretching device was combined with a confocal microscope for live-cell imaging using a high NA 63x water immersion objective (Sigaut *et al*., 2018). In this study, mechanical strain was shown to induce focal adhesion growth and translocation of zyxin to actin stress fibres. In the future, long working distance 100x objective lenses could be employed for implementation of these devices with SRRF, SIM or other super-resolution microscopy techniques.

In the context of this investigation, a cell-stretching membrane device could be combined with the N-SIM for stretching of Willin-mCherry cells; any changes in Willin-mCherry localization would suggest a direct mechanosensing role for Willin.

6.6 Chapter Acknowledgements

YAP-GFP cell lines were generated and characterised by the author. Optical system design was advised by Dr Jonathan Nylk; optical trapping systems were built and characterised by the author. Custom optomechanical parts were produced by the physics workshop. Equipartition and PCA MATLAB codes were written by Dr Jonathan Nylk.

7 Investigation of the association of Willin with the actin cytoskeleton

7.1 Introduction

The actin cytoskeleton is a highly dynamic structure that extends throughout the cell, defining the cell edge and forming the cellular framework (Pollard & Copper, 2009). This network of actin filaments is regulated by multiple proteins, including actin capping proteins and polymerising factors (see Chapter 2). In turn, the actin cytoskeleton plays a key role in the control of important cell signalling pathways, both by providing mechanosensory input from the external environment and generating internal forces (Ohashi, Fujiwara & Mizuno, 2017). The Hippo pathway is one such example of a signalling pathway regulated by the actin cytoskeleton machinery. An intact actin cytoskeleton is essential for YAP/TAZ activity (Dupont *et al*., 2011), and F-actin depolymerising factors act as potent inhibitors of YAP/TAZ (Aragona *et al*., 2013). Actin stress fibres are influenced by substrate stiffness, which in turn modifies Hippo signalling (Dupont *et al*., 2011). In addition, several cell polarity proteins that function upstream of the canonical Hippo pathway have been shown to be mediated by F-actin and/or Myosin II (Dai *et al*., 2013; Rauskolb *et al*., 2014; Mana-Capelli *et al*., 2014).

Here, the question of whether Willin plays a mechanical role in the regulation of the Hippo pathway is explored by investigating the relationship between Willin and the actin cytoskeleton. Experimentally, actin is traditionally visualised using the phallotoxin phalloidin (Dancker *et al*., 1975). Recently, a small peptide probe, 'Lifeact' has become popular as a versatile maker for F-actin, including in a genetically-expressed fluorescently-tagged form for live-cell tracking (Riedl *et al*., 2008). Previously, the effect of Willin knockdown was briefly investigated by Dr Andrew Lunel in SH-SY5Y cells expressing Lifeact-RFP. Swirls of actin, referred to in this chapter as actin bundles, were prominent within these cells, which are here examined using 3D-SIM. In addition, the localization of Willin in the cell with respect to the actin cytoskeleton is studied using cells stably expressing Willin-mCherry, and the potential interaction of Willin and the cytoskeletal protein AMOT considered. Finally, the effect of substrate elasticity on Willin localization and expression is explored.

7.2 Investigation into the behaviour of Willin-mCherry

In order to study the association of Willin with actin, the intracellular localization of Willin was first investigated. Attempts to probe for Willin using immunocytochemistry were non-specific, and therefore a cell line expressing an mCherry-tagged form of exogenous Willin protein was generated.

7.2.1 Production of Willin-mCherry cell line

The Willin-mCherry plasmid was previously constructed using a pmCherry-N1 vector (Clontech). Wild-type SH-SY5Y cells were transfected by nucleofection as described in Chapter 4 and selected for using G418. Stable expression of Willin-mCherry was confirmed by fluorescence microscopy (see below) and Western blot (Figure 7.1). The observed band at ~100kDa in the Willin-mCherry cell lysate sample was approximately the equivalent of the sum of Willin (~72kDa) and mCherry protein (~28.8kDa).

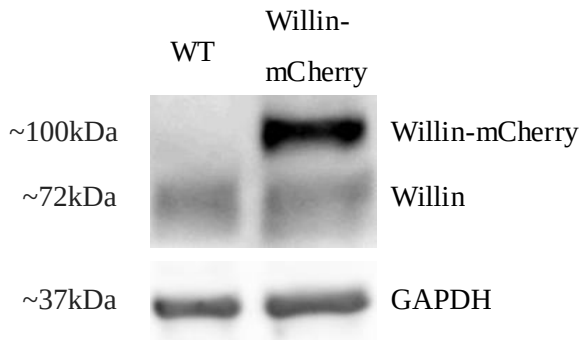

Figure 7.1 Validation of Willin-mCherry cell line. Representative Western blot Willin protein bands of wild-type and Willin-mCherry lysate samples. The additional Willin-mCherry band of the created cell line had an approximate molecular weight of 100kDa. GAPDH served as a loading control.

Fixed Willin-mCherry cells were observed under 20x magnification using 3D-SIM (Figure 7.2). Willin-mCherry appeared concentrated at cell junctions and punctate throughout the cell, though particularly surrounding the nucleus. Willin has previously been shown to localize to the cell membrane, cell junctions and throughout the cytosol (Gunn-Moore *et al*., 2005).

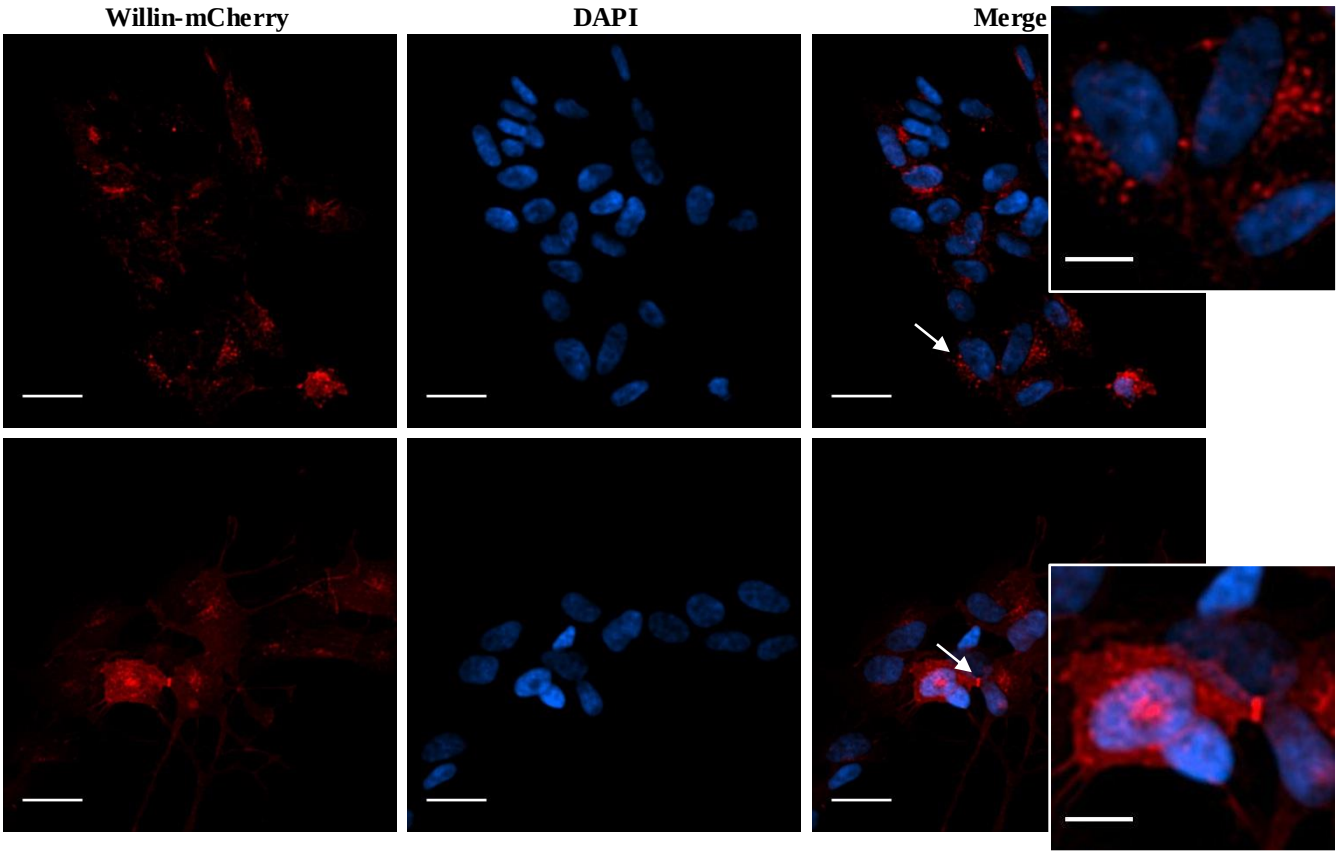

Figure 7.2 3D-SIM images of Willin-mCherry cells under 20x magnification. Left column, Willin-mCherry (red); middle column, DAPI (blue); right column, merged image. White arrows mark punctate perinuclear Willin-mCherry (upper row) and Willin-mCherry at cell junction (lower row). Scale bar for panel images, 25µm; scale bar for inserts, 10µm.

To determine whether Willin localization was dependent upon cell density, Willin-mCherry cells were fixed and stained with phalloidin as a marker of the cell edge. Willin-mCherry appeared punctate and perinuclear in both sparsely-populated and relatively confluent cells (Figure 7.3). In addition, Willin-mCherry was observed at the cell edges in some confluent cells.

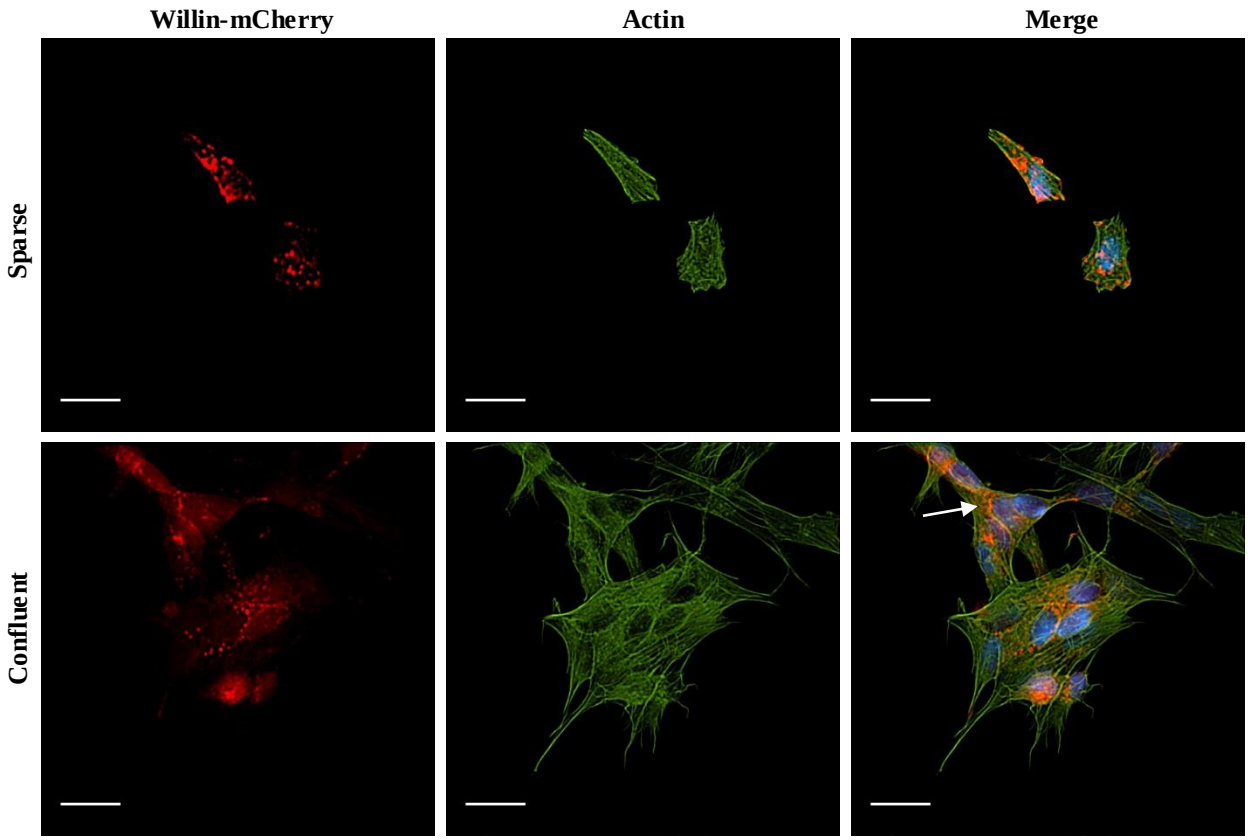

Figure 7.3 3D-SIM images of sparse and comparatively confluent Willin-mCherry cells under 20x magnification. Left column, Willin-mCherry (red); middle column, actin (green); right column, merged image with DAPI (blue). Upper row, sparse cells; lower row, confluent cells. White arrow marks Willin-mCherry at cell boundary. Scale bar, 25µm.

7.2.2 Willin-mCherry partially colocalizes with actin stress fibres

To investigate the potential interaction of Willin with actin, Willin-mCherry cells were fixed and stained with phalloidin for examination with 3D-SIM (Figure 7.4). Two different forms of Willin-mCherry were observed using the N-SIM: larger and spherical vesicle-like structures with a diameter range of 0.3-0.8µm, and much smaller structures with a diameter range of 130-270nm (below the diffraction limit of light), previously unobserved using conventional fluorescence microscopy, that interestingly colocalized with actin stress fibres, suggesting a potential role for Willin in the regulation or functioning of the actin cytoskeleton.

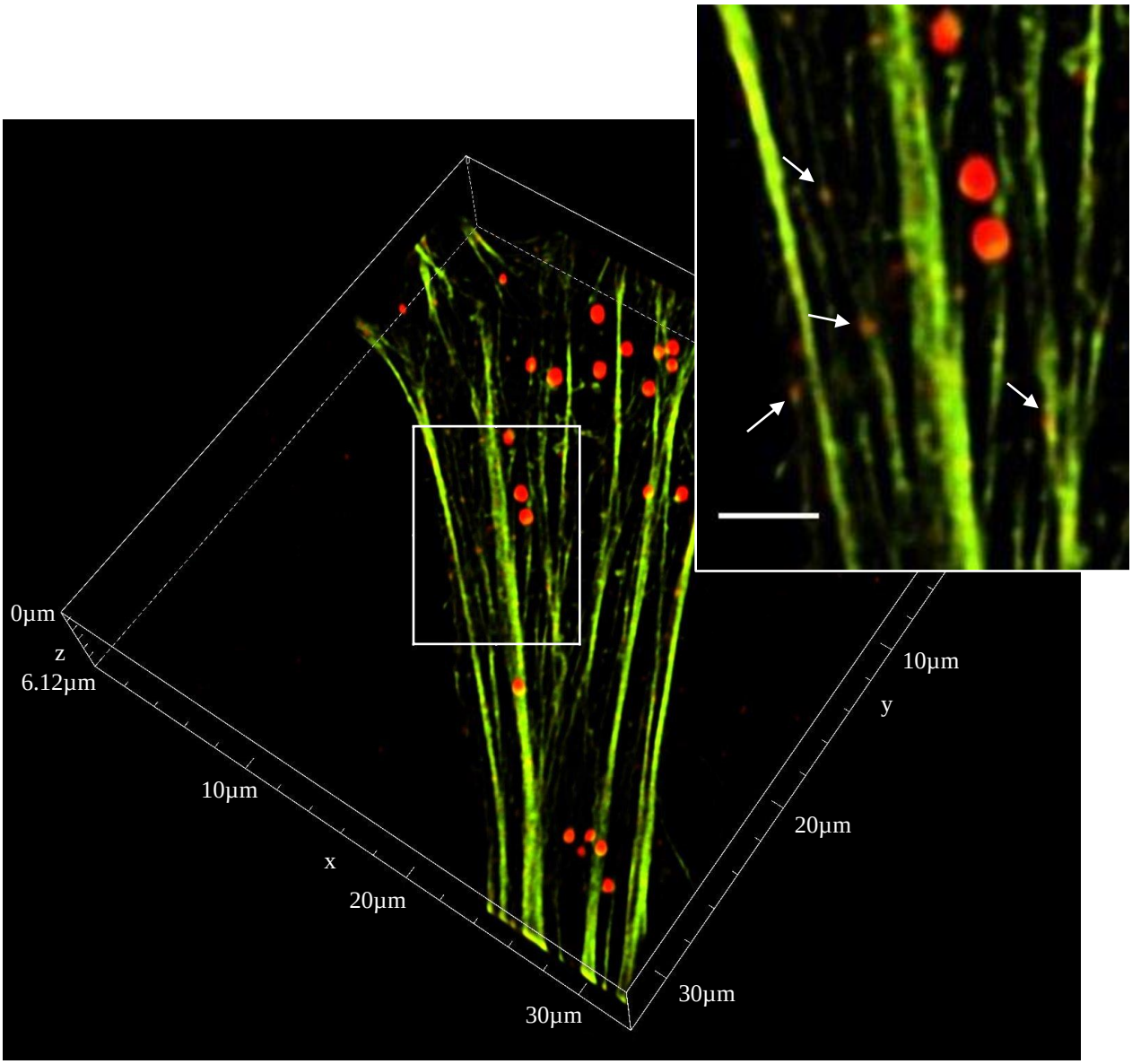

Figure 7.4 3D-SIM volume view of Willin-mCherry and actin under 100x magnification. Actin was stained using phalloidin-488. White arrows mark colocalization of Willin-mCherry and actin stress fibres. Zoomed in selection scale bar, 2µm.

7.2.3 Willin-mCherry is partially vesicular

To further study the larger spherical structures of Willin-mCherry as shown above, Willin-mCherry cells were stained with the lipophilic dye Bodipy, a probe for intracellular lipid-rich structures such as vesicles. Many of the Willin-mCherry structures colocalized with the Bodipy dye, suggesting that they may be vesicular (Figure 7.5). Transfection of wild-type SH-

SY5Y cells with mCherry DNA resulted in diffuse staining of the cell, confirming that it was not the mCherry tag causing the Willin to colocalize with Bodipy.

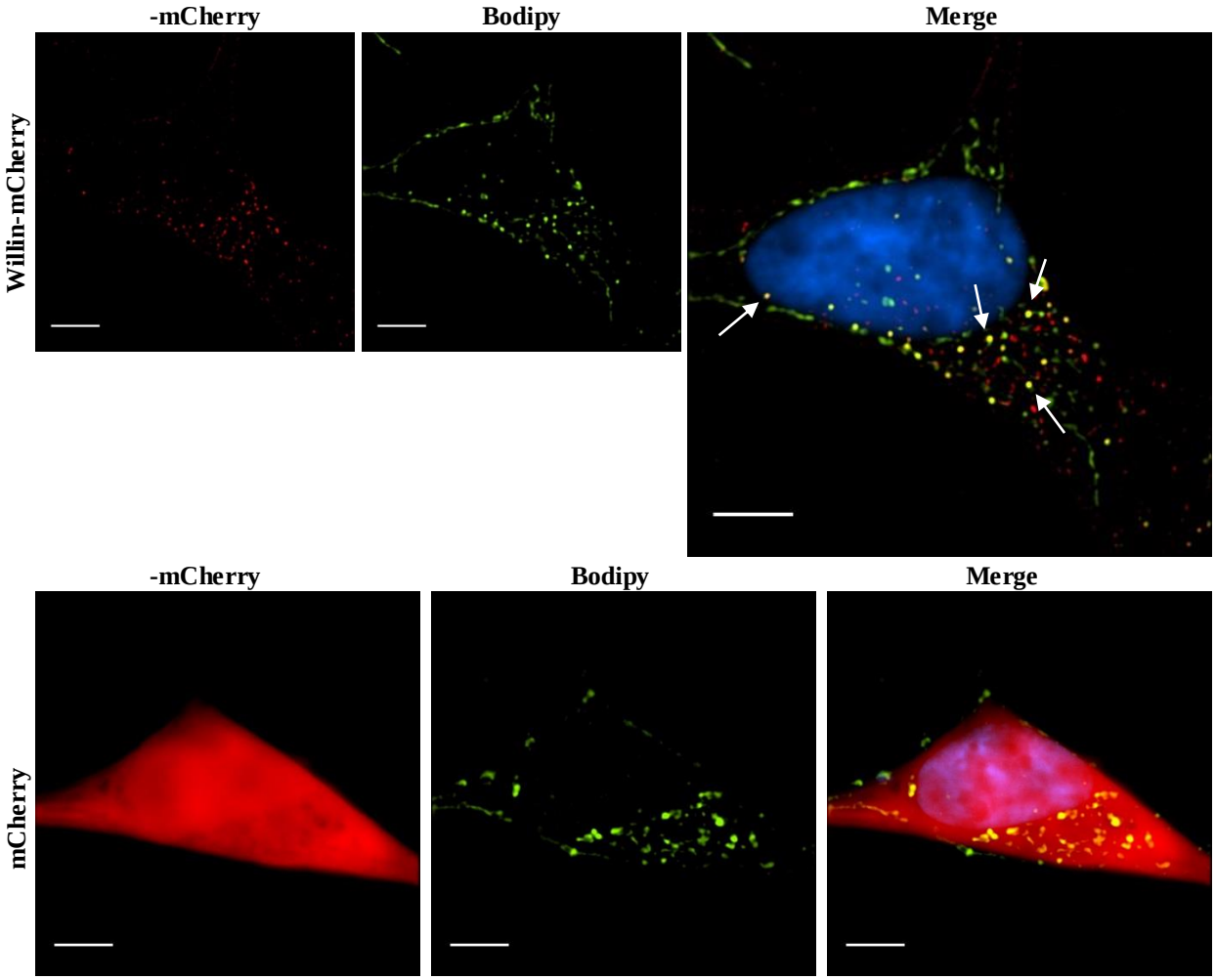

Figure 7.5 3D-SIM images of Willin-mCherry and Bodipy 495/503 under 100x magnification. Left column, Willin-mCherry (red); middle column, Bodipy 495/503 (green); right column, merged image with DAPI (blue). Upper row, Willin-mCherry cell line; lower row, mCherry-transfected cell. White arrows mark colocalization of Willin-mCherry and Bodipy. Scale bar, 5µm.

Live Willin-mCherry cells were visualised under epifluorescence using the N-SIM (Figure 7.6). Time lapse imaging revealed that the vesicle-like foci of Willin-mCherry shown in Figures 7.4 and 7.5 were highly mobile, moving at a speed of approximately 1-2µm s^{-1}. This result is consistent with the speed of intracellular vesicle transport as reported in the literature (Lodish *et al*., 2000).

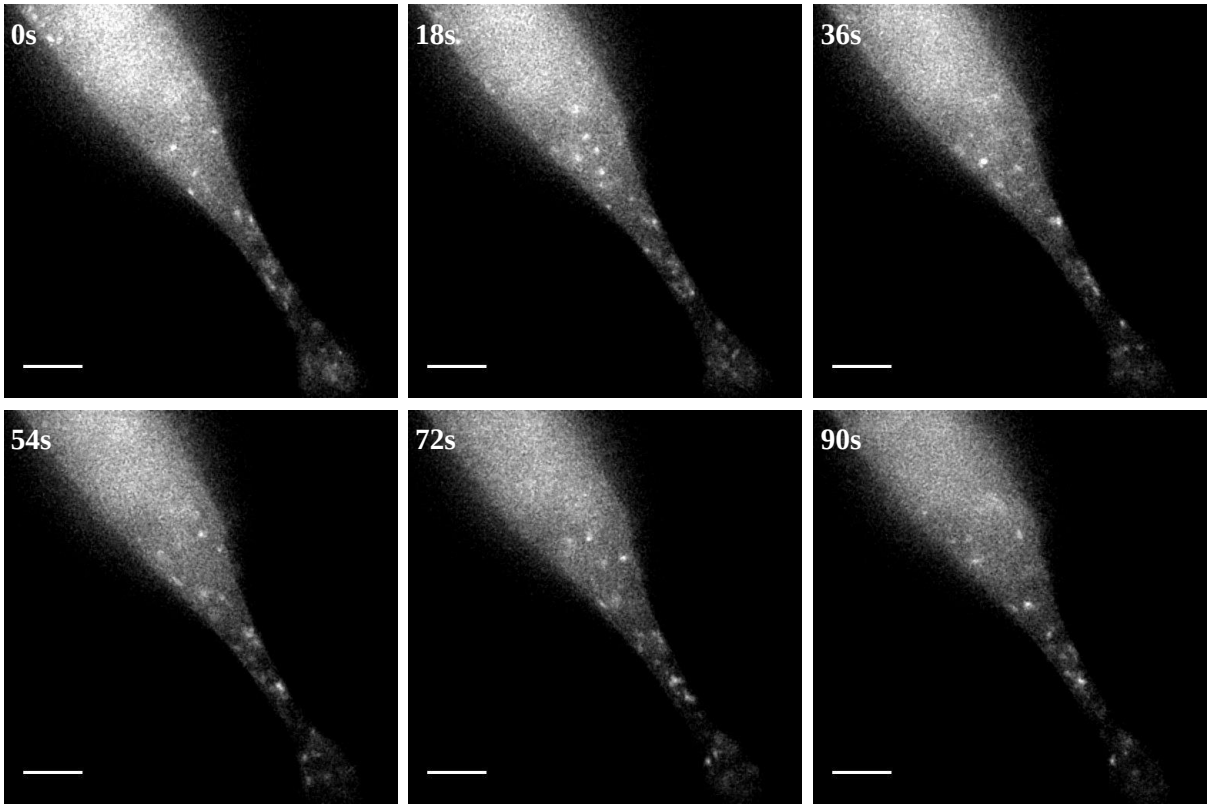

Figure 7.6 Time lapse widefield epifluorescence images of live Willin-mCherry cells under 100x magnification. Exposure time, 102ms; scale bar, 5µm.

To further investigate the potential vesicular localization of Willin, fractions of wild-type SH-SY5Y cells produced by Dr Luke Thompson as per the fractionation protocol detailed in Thompson *et al*., 2018 were probed for Willin protein by Western blotting (Figure 7.7). Briefly, cells were Dounce-homogenized, and the nuclei (N) pelleted at 300 g for 5 mins; the supernatant was then centrifuged at 16,100 g (16.1k pellet) and the resulting supernatant centrifuged at 100,000 g (100k pellet) for 1hr; the remaining supernatant (S) was retained for analysis. The 100k g pellet has been shown to contain lighter membranous structures such as vesicles (de Duve, 1971; Huber, Pfaller & Vietor, 2003). Quantification of the Western blot bands revealed that the majority (71%) of the detected intracellular Willin was present in the cytosolic S fraction, with 6% present in the nuclear fraction, 10% in the 16.1k fraction and 12% in the 100k fraction. These results contrast with those shown in Figure 7.4 in which it appears that Willin is largely in vesicle-like structures, with the remaining Willin localized on actin in the cytosol.

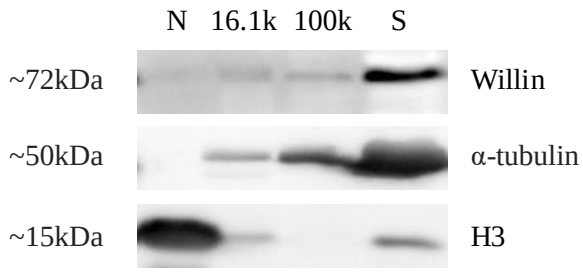

Figure 7.7 Willin expression in cell fractions. Representative Western blot Willin protein bands of nuclear (N), heavy cytoplasmic (16K g), light cytoplasmic (100k g) and supernatant (S) fractions of wild-type SH-SY5Y cells. α-tubulin was used as a cytoplasmic/cytosolic marker, and Histone H3 as a nuclear marker.

7.3 Investigation into the effect of Willin expression on the actin cytoskeleton

Previously, unpublished data showed that Willin knockdown resulted in large actin swirls in SH-SY5Y cells expressing Lifeact-RFP. To further investigate this observation, control (shScr-) and Willin knockdown (shWillin-) Lifeact-RFP cell lines were re-generated and examined using 3D-SIM.

7.3.1 Knockdown of Willin causes bundling of actin stress fibres

ShScr and shWillin cells were transfected with Lifeact-RFP DNA and selected for using G418 as described in Chapter 4. Willin expression levels of shWillin-Lifeact-RFP cells were validated by Western blot to be 29±14% of shScr-Lifeact-RFP cells ($p<0.05$) (Figure 7.8). ShScr- and shWillin-Lifeact-RFP cells were then visualised using 3D-SIM. Figure 7.9 shows the maximum intensity projection of a z-stack image of representative shWillin-Lifeact-RFP cells. The actin swirl present in the cell on the right of the image was shown to be a bundle of several actin stress fibres that wound through the cell parallel to the intracellular F-actin. This bundling of actin stress fibres was not apparent in shScr-Lifeact-RFP cells.

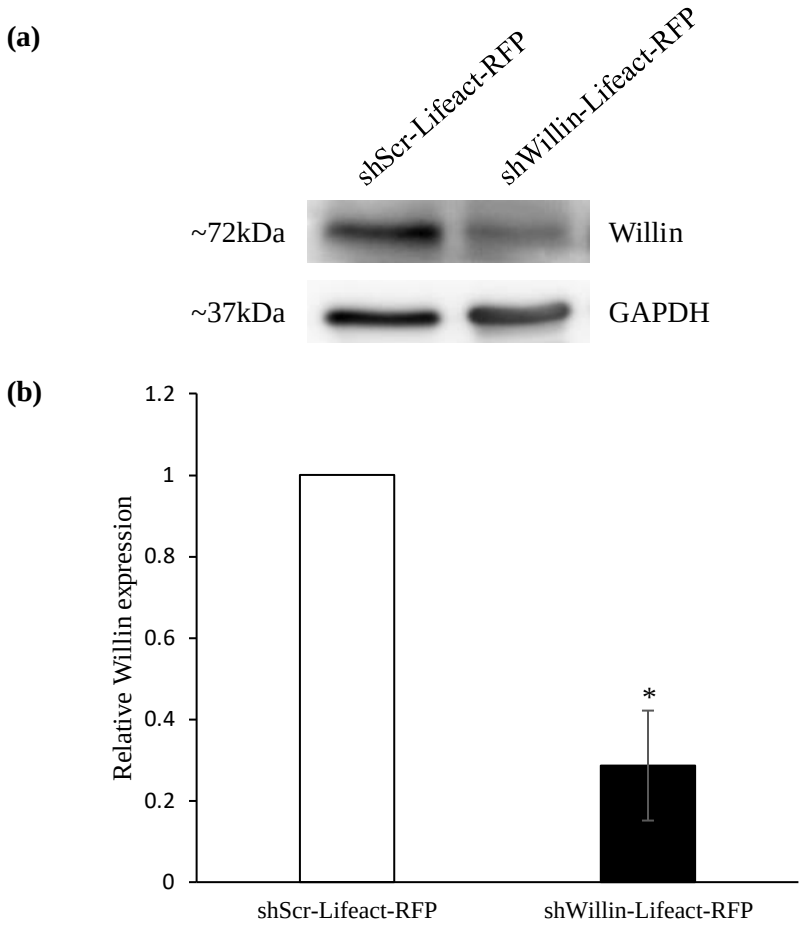

Figure 7.8 Relative Willin expression in shScr-Lifeact-RFP and shWillin-Lifeact-RFP cell lines. **(a)** Representative Western blot Willin protein bands of shScr- and shWillin-Lifeact-RFP lysate samples. GAPDH served as a loading control. **(b)** Quantification of Willin protein expression in shScr- and shWillin-Lifeact-RFP cell lines from (a). Willin expression in shWillin-Lifeact-RFP cells was measured relative to that of shScr-Lifeact-RFP cells (n = 3 experimental repeats, error bars indicate standard deviation, * $p<0.05$ as calculated using the two-tailed Student's t-test).

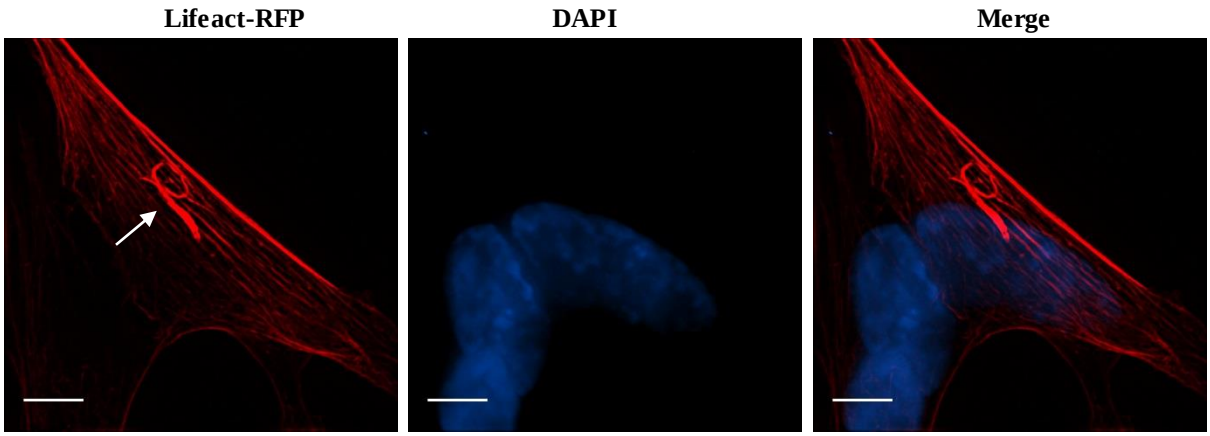

Figure 7.9 Maximum intensity projection of 3D-SIM z-stack of shWillin-Lifeact-RFP cells under 100x magnification. Left column, Lifeact-RFP (red); middle column, DAPI (blue); right column, merged image. White arrow marks bundling of actin stress fibres. Volume, 9µm; scale bar, 5µm.

To confirm that this actin bundling was not an artefact, Lifeact-RFP cells were fixed and stained with the actin-marker phalloidin-488. Figure 7.10 shows 2D views of shScr- and shWillin-Lifeact-RFP cells imaged using both 3D-SIM and widefield epifluorescence. The shWillin-Lifeact-RFP actin stress fibre bundles, in this case perpendicular to the intracellular F-actin, were evident under both the 488 and RFP channel, confirming that the previously observed Lifeact-RFP swirls were indeed composed of F-actin, though were less apparent when imaged with 3D-SIM than with standard widefield. In addition, non-Lifeact expressing shScr and shWillin cells were stained with phalloidin to confirm that it was not the expression of Lifeact-RFP that was causing the actin bundling (Figure 7.11). Actin stress fibre bundles were observed in shWillin cells stained with both phalloidin-488 and phalloidin-568, verifying that the actin bundling was a result of Willin knockdown.

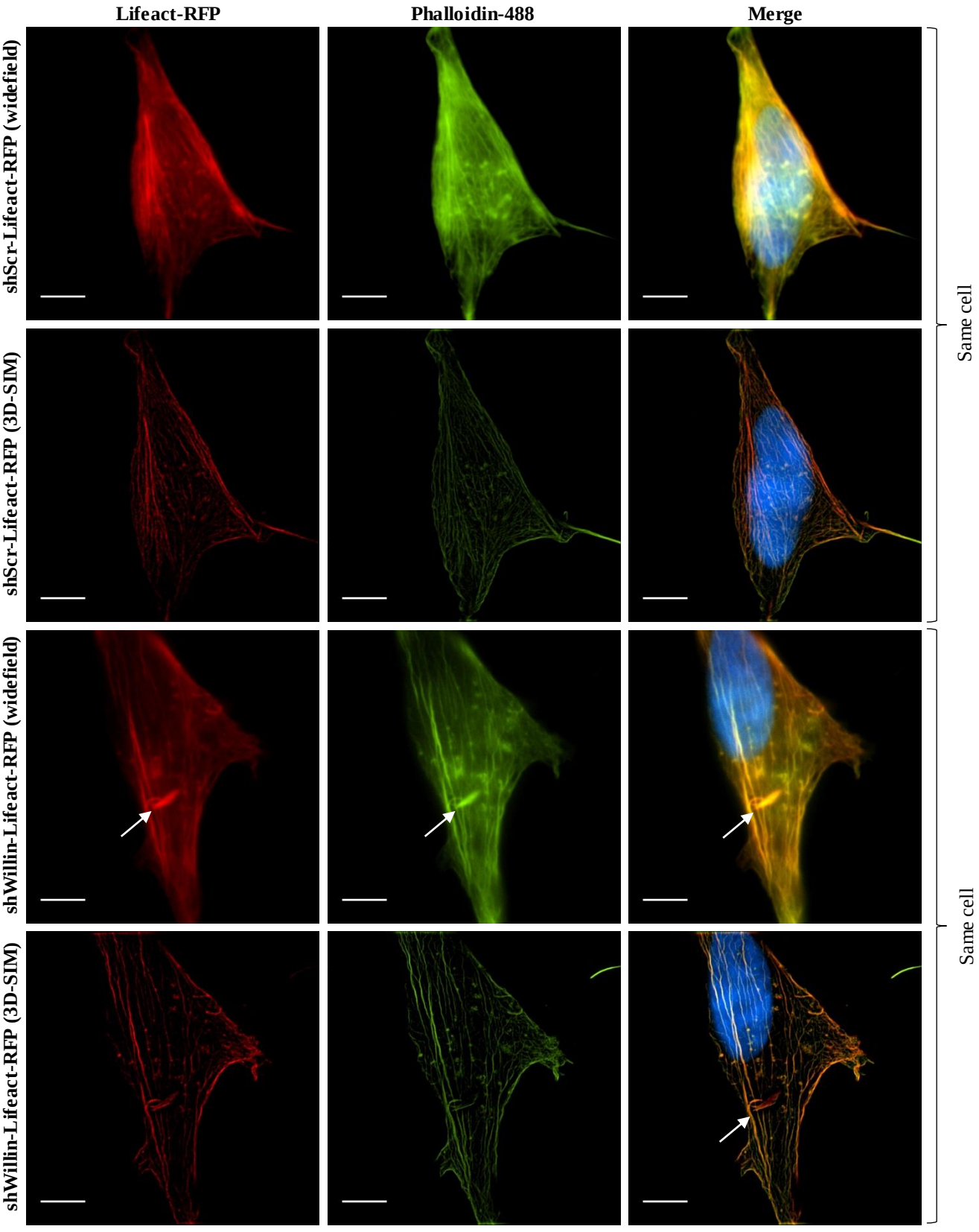

Figure 7.10 3D-SIM and widefield images of shScr- and shWillin-Lifeact-RFP cells stained with phalloidin-488 under 100x magnification. Left column, Lifeact-RFP (red); middle column, actin stained with phalloidin-488 (green); right column, merged image with DAPI (blue). White arrows mark actin stress fibre bundles. Scale bar, 5µm.

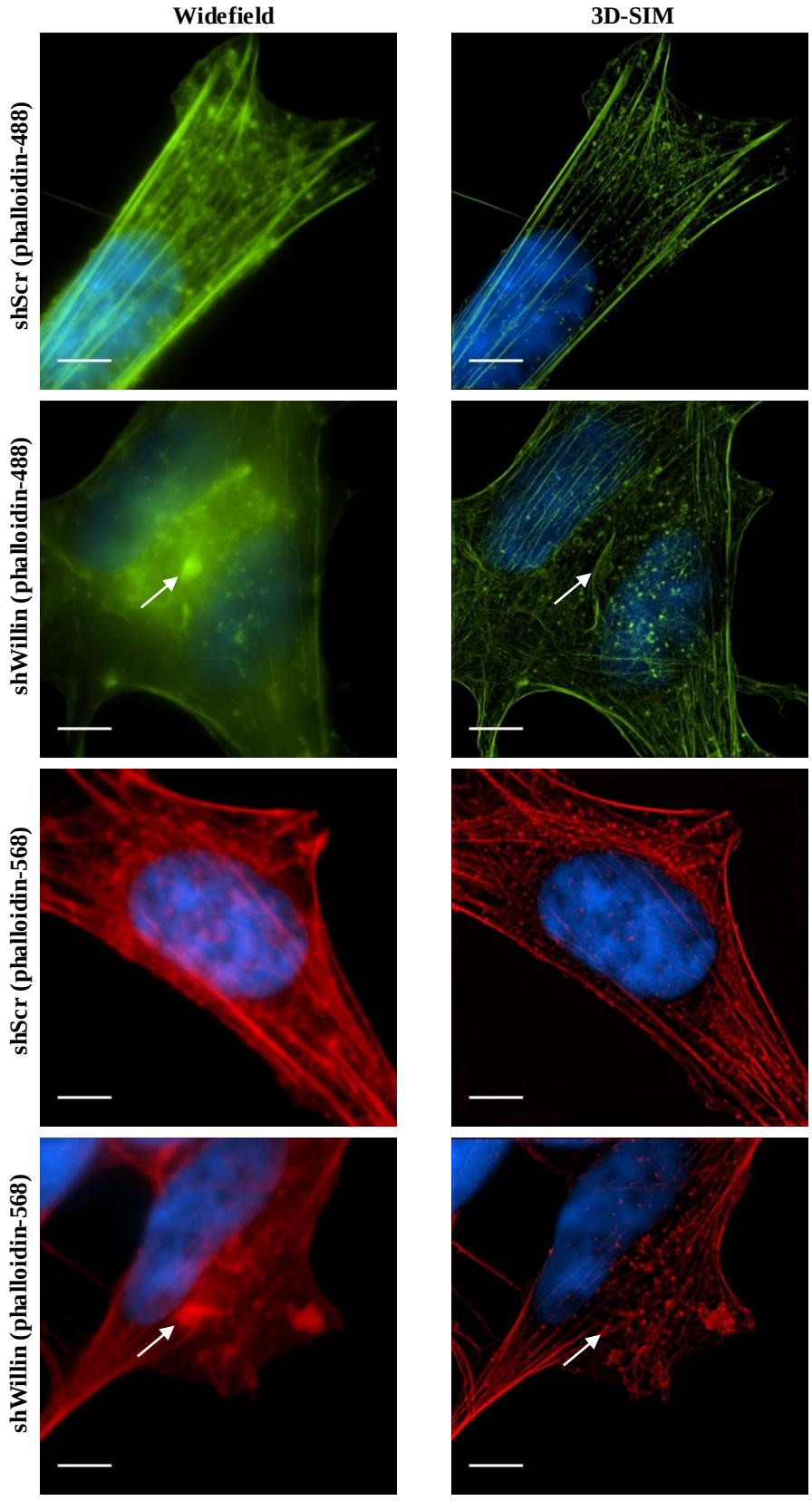

Figure 7.11 3D-SIM and widefield images of shScr and shWillin cells stained with phalloidin-488 and 568 under 100x magnification. Left column, widefield image; right column, 3D-SIM image. Actin stress fibre bundles (marked by white arrows) were less noticeable when imaged with 3D-SIM than with widefield microscopy. Scale bar, 5µm.

7.3.2 Willin expression does not affect expression of actin capping protein

An unpublished mass spectroscopy immunoprecipitation assay performed by Dr Andrew Lunel revealed actin-capping protein as a potential binding partner of Willin. Actin capping protein is a heterodimer composed of two subunits, α and β, which regulates actin polymerisation by capping the fast-growing barbed end of growing actin filaments (Edwards *et al*., 2014). A potential mechanism for the occurrence of actin bundles in shWillin cells may therefore have been the up- or down-regulation of actin capping protein as a result of Willin knockdown. To examine this hypothesis, expression of actin capping protein subunit β was tested in shScr and shWillin cells by Western blot (Figure 7.12). There was no significant difference between shScr and shWillin cell actin capping protein β expression (shWillin expression 112±18% that of shScr, p = 0.37).

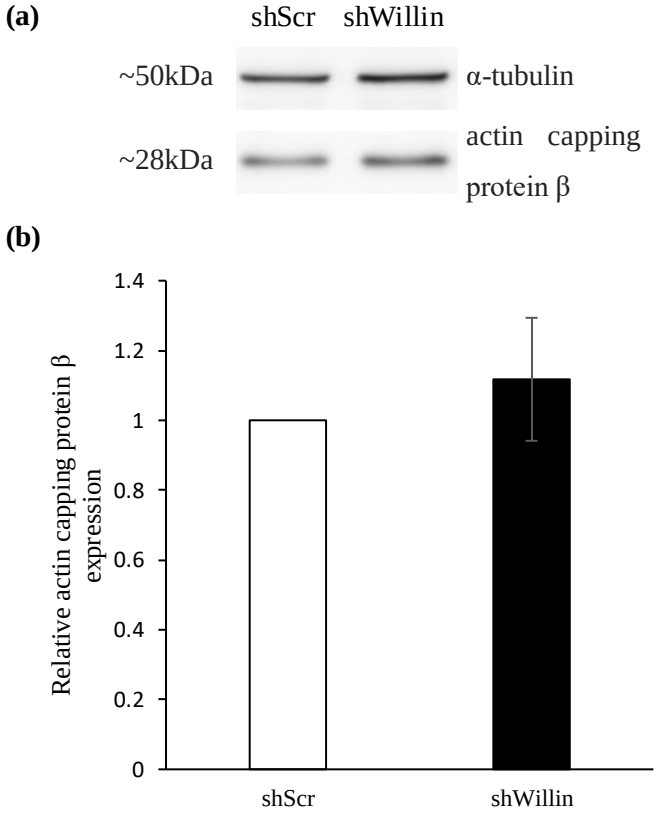

Figure 7.12 Relative actin capping protein β expression in shScr and shWillin cells. **(a)** Representative Western blot actin capping protein β protein bands of shScr and shWillin lysate samples. α-tubulin served as a loading control. **(b)** Quantification of actin capping protein β protein expression in shScr and shWillin cell lines. Actin capping protein β expression in shWillin cells was measured relative to that of shScr cells (n = 3 experimental repeats, error bars indicate standard deviation, p = 0.37 as calculated using the two-tailed Student's t-test).

7.3.3 Willin knockdown induces over-expression of AMOT

Previously, it has been proposed that Willin and AMOT, a polarity protein and key regulator of YAP/TAZ (see Sections 2.5.1.2.4 and 2.5.2.1.3 and Figure 2.6), may share a common evolutionary ancestor, Ex (see Section 2.5.1.1.2). Therefore, research of the role of AMOT in the Hippo pathway was carried out. A literature search revealed that the F-actin bundling as described above in the shWillin and shWillin-Lifeact-RFP cells had been formerly observed in cells overexpressing the long isoform of AMOT, AMOT-p130 (Dai *et al*., 2013; Mana-Capelli *et al*., 2014). Expression of AMOT-p130 and the short isoform of AMOT, AMOT-p80, was examined in shScr- and shWillin-Lifeact-RFP cells by Western blot (Figure 7.13). AMOT-p80 expression in shWillin-Lifeact-RFP cells was 2-fold that in shScr-Lifeact-RFP cells ($p<0.05$), and AMOT-p130 expression nearly 3-fold ($p = 0.099$). HEK-293 cell lysate was used as a positive control for AMOT (data not shown).

To confirm that the increase in AMOT expression was a result of Willin knockdown, levels of AMOT-p80 and -p130 protein were also examined in shScr and shWillin cells (Figure 7.14). Results were similar to the above, with AMOT-p80 and -p130 expression 2.6-fold ($p<0.01$) and 3.1-fold ($p<0.05$) higher respectively in shWillin cells compared to shScr cells. It is feasible to suggest therefore that AMOT may have compensated for the decreased presence of Willin, and that the two proteins may share a collective role within the cell. As next steps to investigate this hypothesis, both the relative localization and potential physical interaction of Willin and AMOT were explored, as described below.

(a)

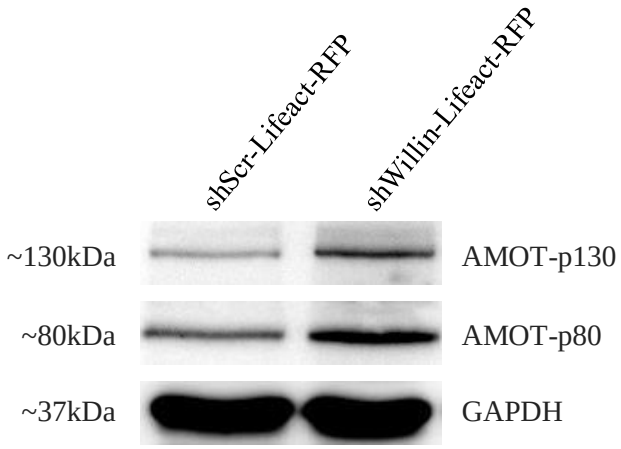

(b)

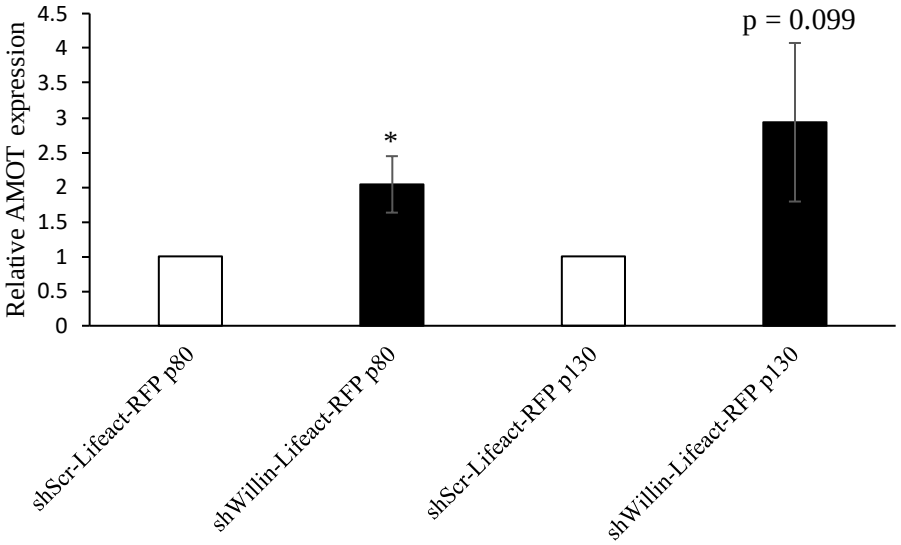

Figure 7.13 Relative AMOT expression in shScr- and shWillin-Lifeact-RFP cells. **(a)** Representative Western blot AMOT protein bands of shScr- and shWillin-Lifeact-RFP lysate samples. GAPDH served as a loading control. **(b)** Quantification of AMOT-p80 and -p130 expression. AMOT- p80 and -p130 expression in shWillin-Lifeact-RFP cells was measured relative to that of shScr-Lifeact-RFP cells (n = 3 experimental repeats, error bars indicate standard deviation, * $p<0.05$ for shScr- and shWillin-Lifeact-RFP AMOT-p80, $p = 0.099$ for shScr- and shWillin-Lifeact-RFP AMOT-p130 expression as calculated using the two-tailed Student's t-test).

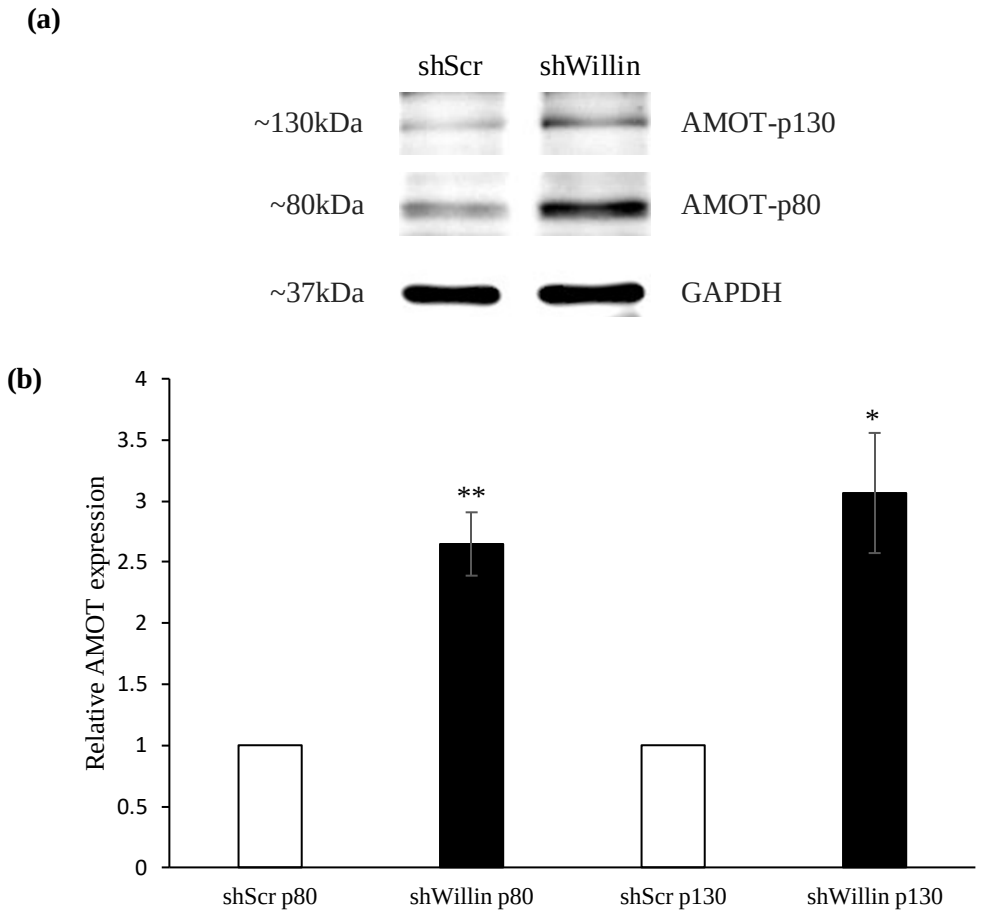

Figure 7.14 Relative AMOT expression in shScr and shWillin cells. **(a)** Representative Western blot AMOT protein bands of shScr and shWillin lysate samples. GAPDH served as a loading control. **(b)** Quantification of AMOT-p80 and -p130 expression. AMOT-p80 and -p130 expression in shWillin cells was measured relative to that of shScr cells (n = 3 experimental repeats, error bars indicate standard deviation, ** $p<0.01$ for shScr and shWillin AMOT-p80, * $p<0.05$ for shScr and shWillin AMOT-p130 expression as calculated using the two-tailed Student's t-test).

7.4 Investigation into a potential interaction of Willin and AMOT

It has been predicted that the *Drosophila* protein Ex, in the evolution of the Hippo pathway, was split into two separate proteins, Willin and AMOT: Willin shares high homology with the N-terminal domain of Ex, whilst AMOT contains two PPxY motifs that are found in the C-terminal domain of Ex but which Willin lacks (Moleirinho *et al.*, 2013a); in addition, the sum of the molecular weights of Willin (~72kDa) and the short isoform of AMOT (~85kDa) are approximately equal to the molecular weight of Ex (154kDa). The possibility of a potential

physical interaction between these two proteins was therefore investigated by examining their localization and by immunoprecipitation.

7.4.1 AMOT partially colocalizes with Willin-mCherry

Willin-mCherry cells were fixed and probed for AMOT by immunocytochemistry. Partial colocalization was observed, with multiple foci containing both Willin-mCherry and AMOT, suggesting that Willin and AMOT may interact (Figure 7.15).

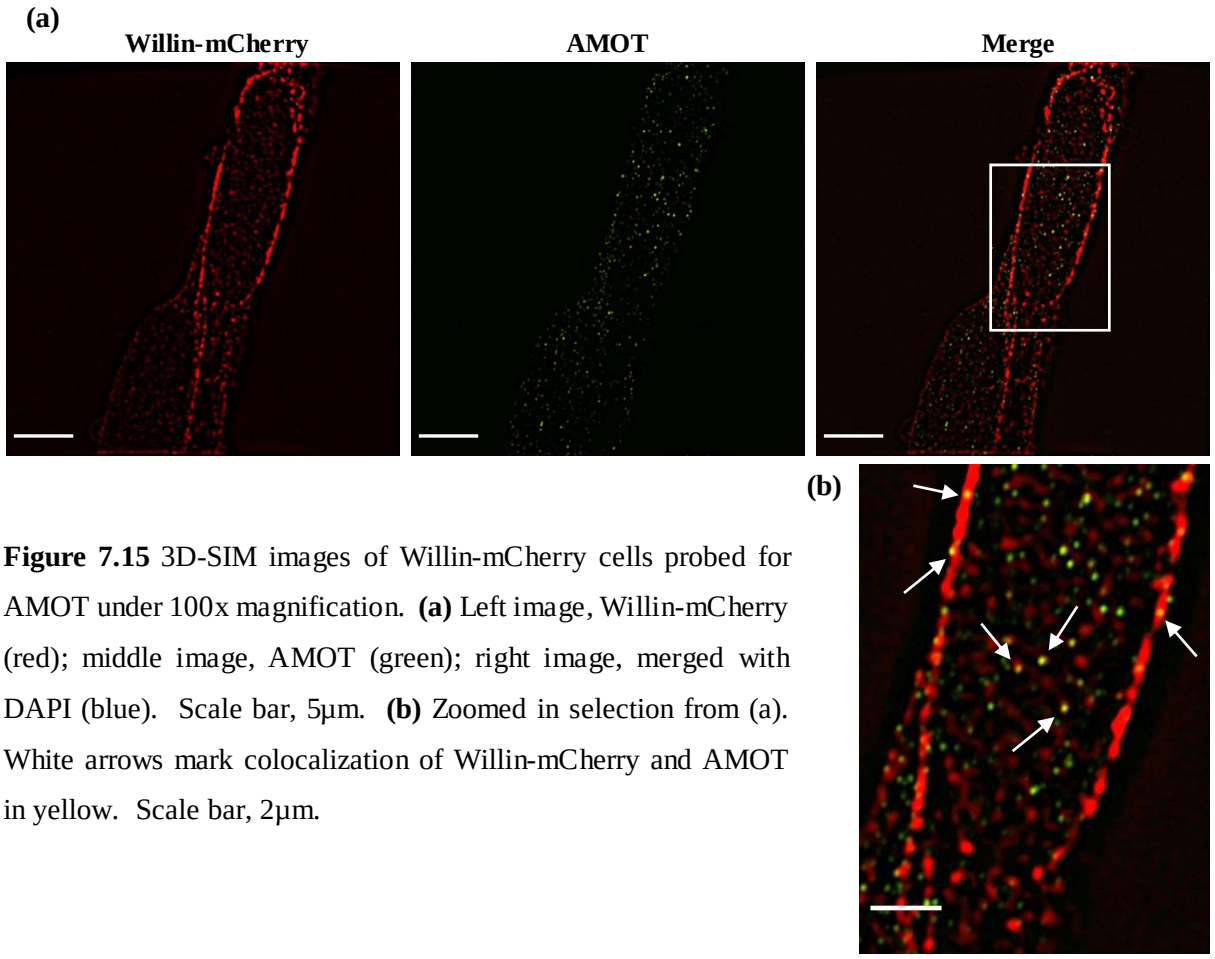

Figure 7.15 3D-SIM images of Willin-mCherry cells probed for AMOT under 100x magnification. **(a)** Left image, Willin-mCherry (red); middle image, AMOT (green); right image, merged with DAPI (blue). Scale bar, 5µm. **(b)** Zoomed in selection from (a). White arrows mark colocalization of Willin-mCherry and AMOT in yellow. Scale bar, 2µm.

7.4.2 Immunoprecipitation of Willin by AMOT

Immunoprecipitation of AMOT in wild-type SH-SY5Y cells was performed as described in Section 4.3.8. Immunoprecipitation is a technique that precipitates a particular protein out of a cell lysate solution using an antibody that binds specifically to that protein. In the case of this study, AMOT was immunoprecipitated from SH-SY5Y lysate samples to determine whether Willin is pulled down alongside AMOT and thus establish whether AMOT and Willin are binding partners. Briefly, cell lysate samples containing 1mg of total protein were incubated with protein A magnetic beads and either isotype control or anti-AMOT antibody overnight. The pre-cleared lysate (PC, containing proteins that had bound non-specifically to the beads), immunoprecipitation elute (IP, containing proteins that had bound to the antibody-bead complex) and unbound protein supernatant (UB, containing proteins in solution that had not bound to the antibody-bead complex) were loaded onto an electrophoresis gel for detection of endogenous AMOT and Willin protein by Western blot. Using the anti-AMOT antibody, AMOT-p80 and -p130 were successfully pulled down (Figure 7.16). A faint Willin signal was visible from the anti-AMOT IP elute, indicating that Willin and AMOT may physically interact.

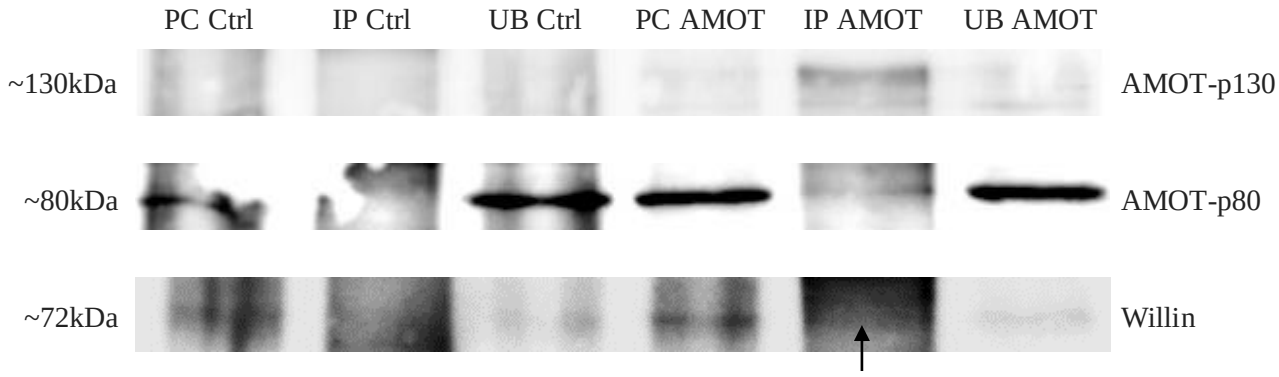

Figure 7.16 Immunoprecipitation of endogenous Willin by endogenous AMOT. PC, pre-cleared lysate; IP, immunoprecipitation; UB, unbound sample; Ctrl, isotype control antibody; AMOT, anti-AMOT antibody. Black arrow marks Willin band in AMOT IP lane.

7.5 Investigation into the effect of substrate elasticity on Willin expression and localization

The elasticity of the extracellular matrix is a key regulator of the actin cytoskeleton and Hippo pathway activity (Dupont *et al*., 2011; Aragona *et al*., 2013). Therefore, the effect of cell substrate stiffness was examined with respect to Willin in SH-SY5Y cells.

7.5.1 Substrate elasticity does not affect Willin localization

In order to investigate the effect of substrate elasticity on Willin localization, Willin-mCherry cells were grown on hydrogels of varying stiffness. Hydrogels of 0.5, 4 and 50kPa (Cell Guidance Systems) were chosen as SH-SY5Y cells grown on substrates of the same order of these elasticities have been shown to have significantly different morphologies (Lam *et al*., 2010). In addition, these stiffnesses fall within the physiological range of human tissue (Bao & Suresh, 2003).

Cells were fixed and stained with phalloidin-488 to mark the actin cytoskeleton and cell edge. Cell morphology was markedly changed on the three different stiffness substrates: on the 0.5kPa hydrogels, cells appeared largely rounded with few actin stress fibres and processes; on the 4kPa hydrogels, cells had a slightly differentiated morphology, with visible actin stress fibres; and on the 50kPa hydrogels, cells often grew in clusters, and displayed organised stress fibres and long extended processes, as observed by Lam *et al*. Willin-mCherry localization, however, was similar on all three hydrogels, with 3D-SIM revealing punctate localization around the nucleus, the cell edge and at the junction of dividing cells (Figure 7.17).

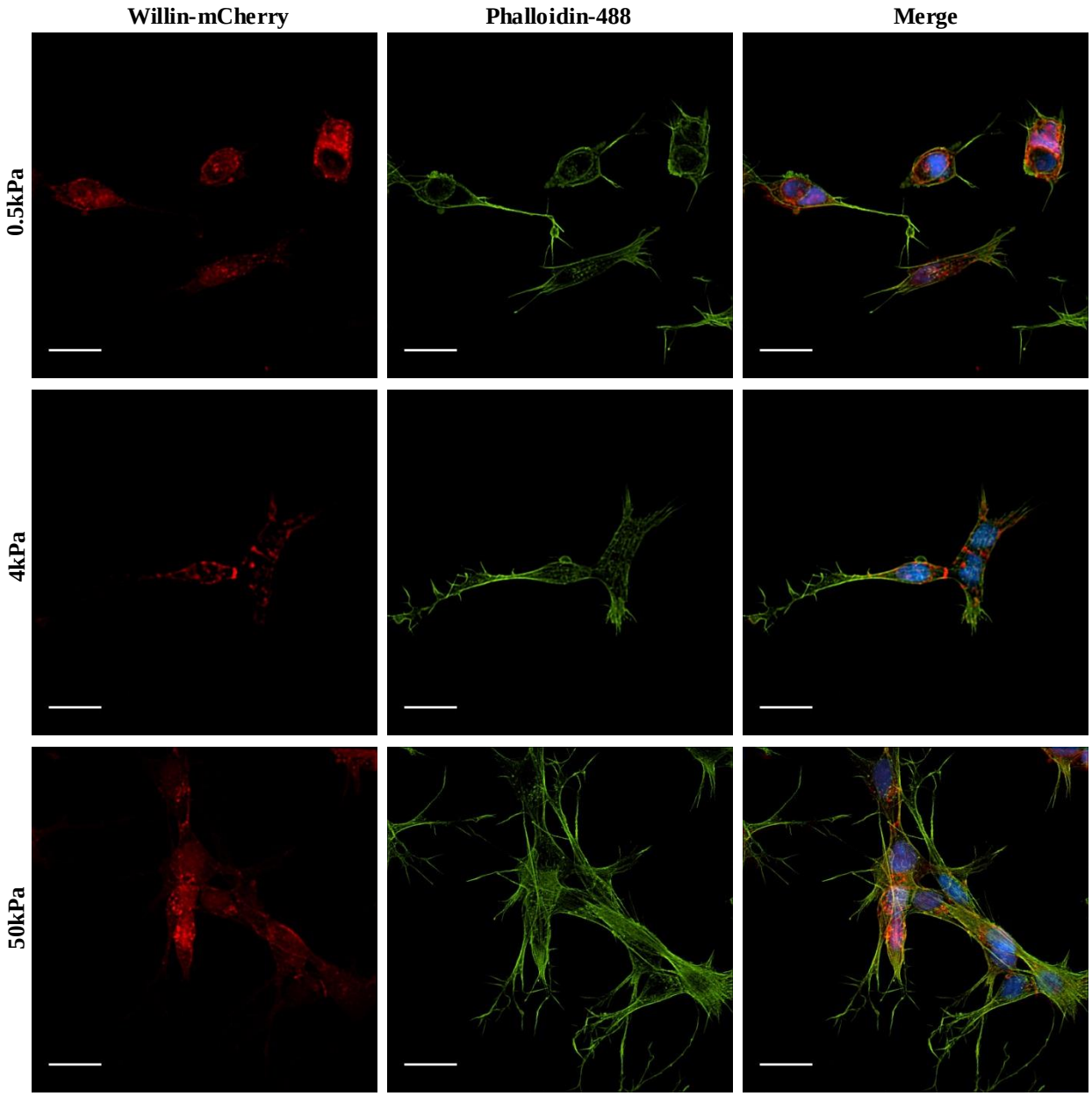

Figure 7.17 3D-SIM images of Willin-mCherry cells grown on hydrogels of varying stiffness under 20x magnification. Left column, Willin-mCherry (red); middle column, actin (green); right column, merged image with DAPI (blue). Upper row, 0.5kPa hydrogel; middle row, 4kPa hydrogel; lower row, 50kPa hydrogel. Scale bar, 25µm.

7.5.2 Substrate elasticity affects Willin expression

To investigate the effect of substrate elasticity on Willin expression, wild-type SH-SY5Y cells were grown on 10cm dishes coated with hydrogels of stiffnesses 0.5, 4 and 50kPa, and lysates collected for probing of Willin protein by Western blot. Willin expression in cells grown on

hydrogels of 4kPa stiffness was 2.75-fold and ~3.5-fold higher than in cells grown on hydrogels of 0.5kPa and 50kPa stiffness respectively (Figure 7.18). A one-way analysis of variance (ANOVA) of the quantified bands revealed that Willin expression was significantly different on the three hydrogel stiffnesses ($p<0.01$).

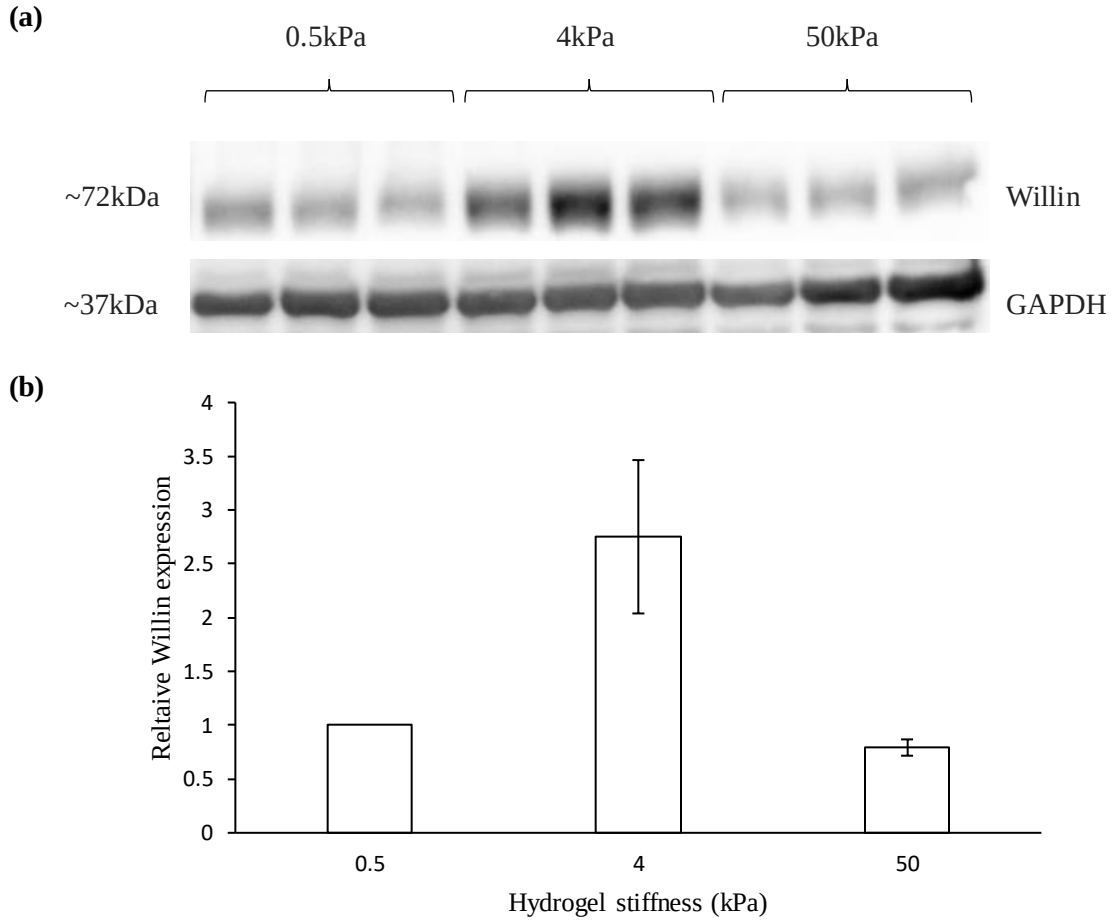

Figure 7.18 Relative Willin expression in wild-type SH-SY5Y cells grown on hydrogels of varying stiffness. **(a)** Triplicate Western blot Willin protein bands of SH-SY5Y cells grown on 0.5, 4 and 50kPa hydrogels. GAPDH served as a loading control. **(b)** Quantification of Willin expression. Willin expression was measured relative to that of cells grown on 0.5kPa hydrogels (n = 3 experimental repeats, error bars indicate standard deviation, $p<0.01$ as calculated using a one way ANOVA).

7.6 Discussion & future work

The actin cytoskeleton is a complex and dynamic mechanical structure that feeds into many signalling pathways, including the Hippo pathway. Here, the association of Willin with the actin cytoskeleton was explored using 3D-SIM, protein assays and hydrogels as cell substrates. Due to the low signal-to-noise ratio of Willin-mCherry, laser illumination was required for

both live and fixed-cell imaging. The N-SIM was therefore an ideal tool for the visualization of intracellular Willin. 3D-SIM revealed that Willin-mCherry partially colocalizes with the lipid dye Bodipy. The movement of Willin-mCherry foci around the cell at a speed of 1-2µm s^{-1} (similar to that of intracellular vesicular transport) as detected using the N-SIM lasers suggests that Willin may be contained within vesicles. In addition to the larger vesicle-like structures of Willin-mCherry, smaller foci were detected that colocalize with F-actin, indicating a potential split intracellular localization of Willin, with some transported around the cell in vesicles, and some along actin stress fibres (Figure 7.4). SH-SY5Y cell fractions that had been previously generated were probed by Western blot to investigate the intracellular localization of Willin (Figure 7.7). The results obtained from this study, in which the majority of Willin was found in the cytosolic fraction, contrasted with those described above. The relative lack of Willin found in the light cytoplasmic (vesicular) fraction, however, may have been due to the fractionation protocol or Western blot technique used in this experiment.

The actin bundling that had previously been observed in shWillin-Lifeact-RFP cells was verified in a newly-generated cell line and confirmed using both phalloidin-488 and in shWillin cells without expression of Lifeact-RFP. After a literature search, it was found that this actin bundling has been recorded before in cells overexpressing the actin-binding protein AMOT (Dai *et al*., 2013; Mana-Capelli *et al*., 2014). Willin-knockdown cells were found to express significantly more of both the long and short isoform of AMOT than the Willin-control cells. However, in this study, it was inconclusive as to whether it was the increase in expression of AMOT, the knockdown of Willin, or another, indirect mechanism that was causing the bundling of F-actin in the shWillin cells. To determine which of these explanations is correct, shWillin-Lifeact-RFP cells could be transfected with an expression plasmid containing Willin or siRNA targeting AMOT for knockdown, and examined for rescue of control-cell phenotype.

The increase in AMOT expression in shWillin cells may have been due to a change in Hippo pathway activity as a result of decreased Willin expression, or due to compensation for the decrease in Willin expression, which would indicate a potential functional interaction between AMOT and Willin. 3D-SIM of Willin-mCherry cells stained for AMOT revealed that AMOT and Willin-mCherry partially colocalize. Additionally, a weak Willin band was detected by immunoprecipitation of AMOT in SH-SY5Y cells. To verify whether Willin is pulled down by AMOT and thus confirm a physical interaction between the two proteins, further immunoprecipitation assays could be carried out in cells over-expressing Willin or AMOT or using HEK-293 cells which express higher levels of endogenous AMOT.

The localization of Willin-mCherry in cells on hydrogels of varying stiffness appeared unchanged and similar to in cells grown on glass coverslips (Figure 7.2), suggesting that Willin may not have a role in the detection or signalling of ECM stiffness. Willin expression, however, was significantly altered by substrate elasticity; YAP/TAZ activity has previously shown to be affected by cell substrate stiffness (Dupont *et al*., 2011), and may potentially, like CRB3 expression (Mao *et al*., 2017), modify transcription of Willin mRNA.

Future investigations into the association of Willin with actin would include investigating the interaction of Willin and actin capping protein and the focal-adhesion protein zyxin, both of which are indicated to be involved in the regulation of Hippo signalling in *Drosophila* by the Willin homologue Ex (Fernández *et al*., 2011; Gaspar *et al*., 2015). Moving forward, it would be interesting to examine whether Willin is an upstream regulator of RhoA signalling, which is involved in the assembly of actin stress fibres and cross-talk with the Hippo pathway (Sit & Manser, 2011; Ohgushi, Minaguchi & Sasai, 2015; Liu *et al*., 2017; Shi *et al*., 2017). Levels of total and phospho-RhoA could be compared in shScr and shWillin cells by Western blot. In addition, shWillin cells could be treated with a RhoA positive plasmid, and shScr cells with a RhoA negative plasmid; recovery of the reverse phenotype would indicate that Willin may act upstream of RhoA to control actin stress fibre formation.

7.7 Chapter acknowledgements

Cell line production, Western blots and imaging were carried out by the author. The Bodipy dye and cell fractionation samples were kindly provided by Dr Luke Thompson.

8 Investigation of the effect of Willin expression on SH-SY5Y cell forces using elastic resonator interference stress microscopy

The work in this chapter was carried out in collaboration with Dr Nils Kronenberg.

8.1 Introduction

The actin cytoskeleton, as discussed in Chapters 2 and 7, is a central regulator of the Hippo pathway. Integrin-based focal adhesions that link actin stress fibres to the ECM are key sensors and transmitters of mechanical forces between the cell and cell substrate, and as such too have an important role in Hippo signalling. For instance, adhesion to the ECM protein fibronectin regulates the Hippo pathway via the focal adhesion component FAK (Kim & Gumbiner, 2015), and detachment of cells from the ECM leads to YAP phosphorylation and inhibition through cytoskeleton rearrangement (Zhao *et al*., 2012). Recently, forces transmitted from focal adhesions to the nucleus via the cytoskeleton have been shown to increase YAP nuclear import by inducing nuclear flattening and stretching of nuclear pores (Elosegui-Artola *et al*., 2017). In addition, cell adhesion is tightly coupled with actin organisation and sensing the mechanical nature of the environment, both of which in turn are key for the mechanoregulation of YAP/TAZ (Geiger, Spatz & Bershadsky, 2009; Parsons, Horwitz & Schwartz, 2010).

Several methods exist that are capable of quantifying cell forces (Polacheck & Chen, 2016). The most widely-used methods to measure cell forces are currently traction force microscopy (TFM) (Sabass *et al*., 2008) and the use of micropillar arrays (Tan *et al*., 2003). Both of these methods are indirect, relying on tracking displacement of fluorescent particles by cells and zero-force reference images, and the latter of which requires the cells to be removed from the substrate thus making them unavailable for further investigation. Furthermore, TFM and micropillar arrays have limited sensitivity to vertical forces from cells (Kronenberg *et al*., 2017).

Elastic resonator interference stress microscopy (ERISM) is a novel technique that measures forces exerted by cells by detecting cell-induced deformations of an elastic micro-cavity (Kronenberg *et al*., 2017). Vertical deformations are calculated with exceptionally high

accuracy (2nm displacement resolution). ERISM is a widefield technique and so avoids the use of high light intensities, minimising phototoxic effects. Additionally, it requires no zero-force reference, enabling long-term measurements and further investigation of cells, e.g. by immunocytochemistry. The technique of ERISM is described below.

This chapter investigates the effect of Willin expression on the forces exerted by SH-SY5Y cells using ERISM. Cell morphology, focal adhesions, TAZ localization and the organisation of the actin cytoskeleton are examined. Collectively, the results indicate that Willin expression has a significant effect upon the cytoskeletal machinery and forces exerted by SH-SY5Y cells.

8.1.1 ERISM concept

Cells are grown on the surface of a protein-coated elastic optical micro-resonator consisting of an elastomer of stiffness 1.3kPa sandwiched between two thin and semi-transparent gold mirrors (Figure 8.1a, b). Cells of interest are identified by phase-contrast microscopy (Figure 8.1c). Reflectance images of the micro-cavity are then obtained using monochromatic light at 201 different wavelengths between 550 and 750nm from a tuneable light source. Deformation of the microcavity, e.g. by a cell, produces a fringe pattern (Figure 8.1d). For each pixel of the field of view, reflectance is yielded as a function of wavelength, and the local resonance wavelengths calculated (Figure 8.1e). Resonance occurs at elastomer thicknesses, L:

$$L = \frac{\lambda}{2n} m \tag{8.1}$$

where λ is the monochromatic light wavelength, n is the refractive index of the elastomer and m is the mode number. The resonance wavelengths are then fitted to an optical model to compute the actual elastomer thickness and deformation for each pixel from a look-up table. This process is then repeated for every pixel in the field of view to generate a deformation map (Figure 8.1f).

Here, elastomer indentation volume rather than force was quantified to allow both lateral and vertical cellular forces to be taken into account.

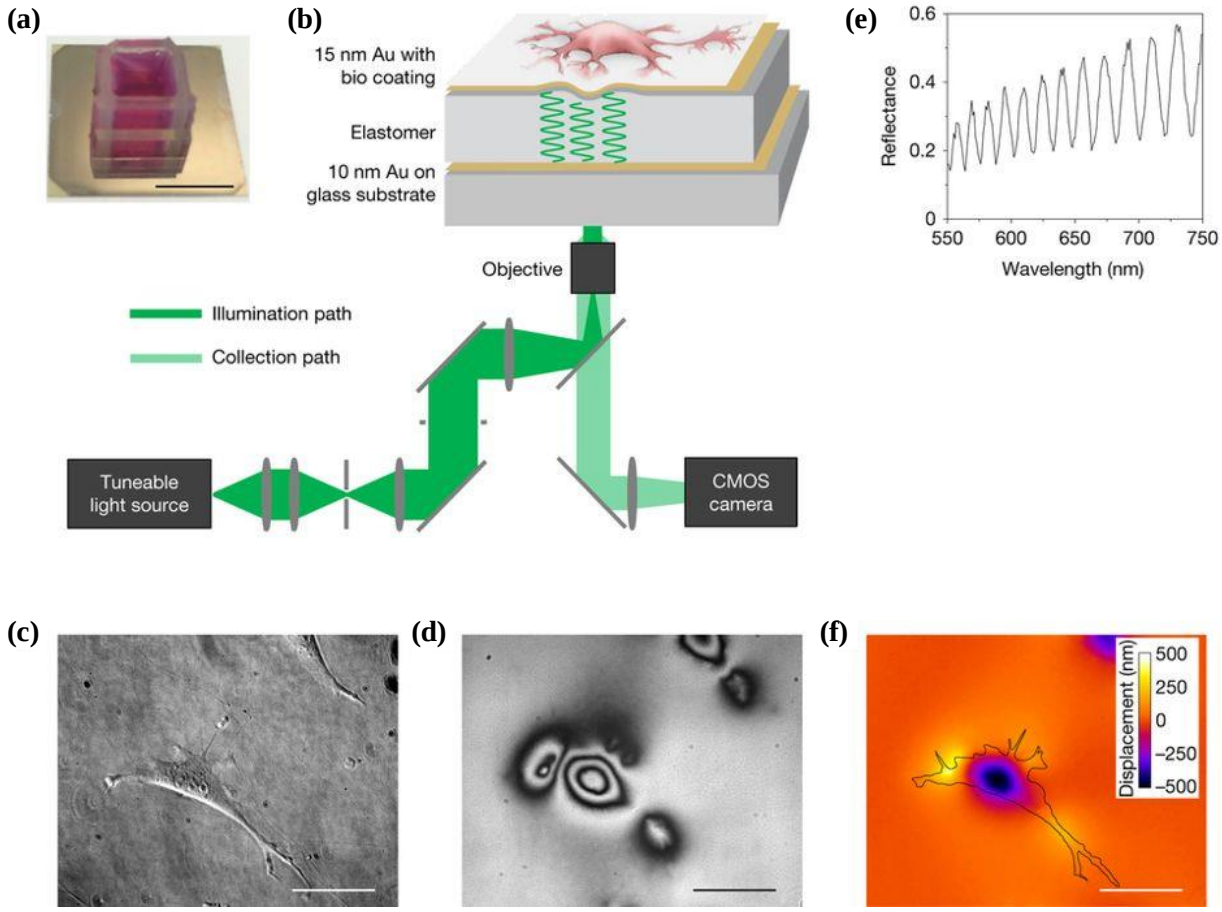

Figure 8.1 Elastic resonator interference stress microscopy. **(a)** Photograph of silicone chamber micro-cavity filled with cell medium. **(b)** Schematic of microcavity structure with an elastomer layer between two gold mirrors, and illumination and detection light paths. **(c)** Phase-contrast image of cell attached to micro-cavity bio coating. **(d)** Reflectance image of micro-cavity at 655nm illumination wavelength. **(e)** Reflectance between illumination wavelengths 550-750nm for one representative pixel within the field of view. **(f)** ERISM displacement map showing deformation by cell in (c). The cell outline is shown in black. Scale bar for (a), 1cm; for (c), (d), (f), 50µm. Figure adapted from Kronenberg *et al.*, 2017.

8.2 Willin knockdown reduces cellular forces

During cell passaging, it was observed that shWillin cells were removed from the flask surface using TrypLE™ far more easily than shScr cells, inferring that Willin knockdown may have an effect on cell adhesion. The forces exerted by shScr and shWillin cells were therefore examined using ERISM. Representative displacement maps that show displacement of the elastomer in nm are displayed in Figure 8.2 (note the difference in scale between the shScr and

shWillin displacement maps). Areas where the cell is pulling the elastomer up are shown in yellow, and pushing down on the elastomer, in purple. Fourier-filtered displacement maps (see Section 4.5.2) are also given that depict high frequency elastomer deformations that represent cell focal adhesions. The median elastomer indented volume was calculated from displacement maps as 78.51 and 16.21μm^3 for shScr and shWillin cells respectively ($U < 0.0001$) (Figure 8.2b).

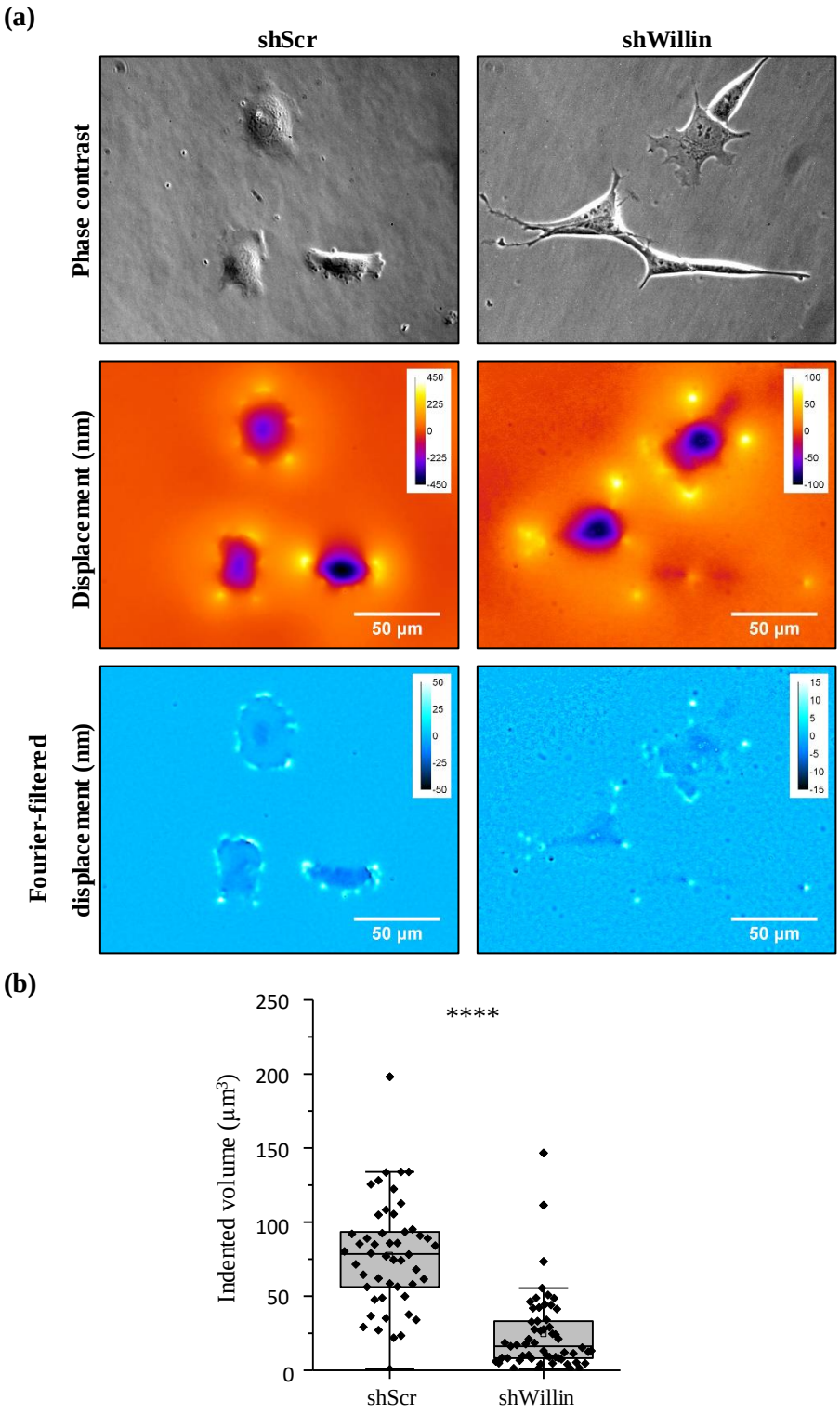

Figure 8.2 ERISM measurements for shScr and shWillin cells. **(a)** Representative phase-contrast images, and displacement and Fourier-filtered displacement maps of shScr and shWillin cells. Scale bar, 50µm. Displacement map scale for shScr cells, -450 – 450nm; for shWillin cells, -100 – 100nm. **(b)** Box plots of calculated displacement volumes for shScr and shWillin cells (shScr n = 50 cells, shWillin n =57 cells, **** U < 0.0001 as calculated using the Mann-Whitney test). Grey box, interquartile range; middle line in grey box, median value; lower and upper edges of grey box, lower and upper quartiles; lower and upper whiskers, minimum and maximum values within 1.5 times the interquartile range below the lower quartile and above the upper quartile; outer values, outliers.

8.3 Willin knockdown alters cell morphology

The difference in morphology between shScr and shWillin cells as previously described in Chapter 5 was quantified from phase contrast images taken on the ERISM setup using FIJI. The median area of shWillin cells was significantly less than that of shScr cells (558μm^2 compared to 855μm^2, U < 0.001) (Figure 8.3a). Cell elongation was also quantified using the formula (1-a/b), where a is the length of the cell orthogonal to the longest length of the cell, b. ShWillin cells were significantly more elongated than shScr cells, with a median elongation of 0.71 compared to 0.48 (U < 0.01) (Figure 8.3b).

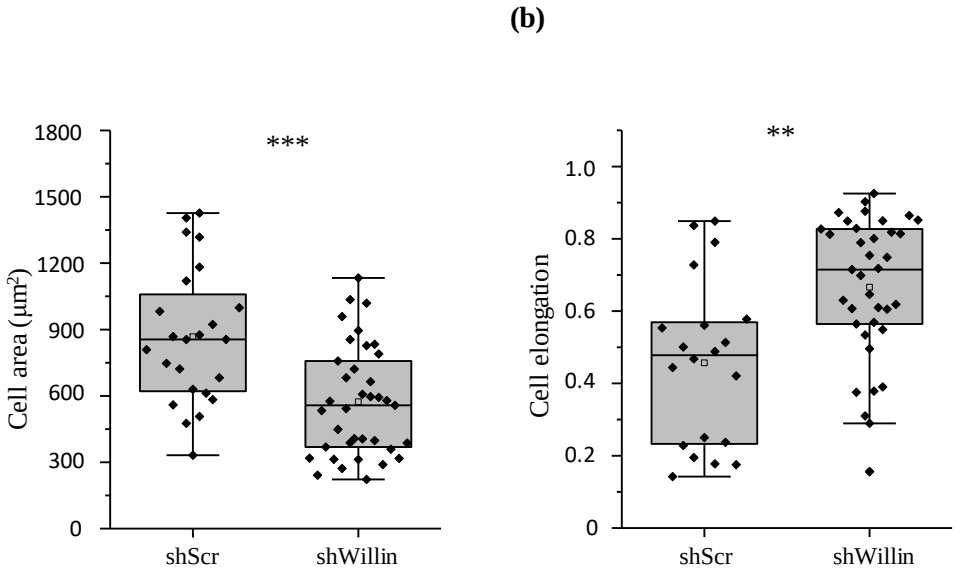

Figure 8.3 Quantification of shScr and shWillin cell morphology. **(a)** Box plots of shScr and shWillin cell area (shScr n = 24, shWillin n = 37, *** U < 0.001 as calculated using the Mann-Whitney test). **(b)** Box plots of shScr and shWillin cell elongation (shScr n = 20 cells, shWillin n = 37 cells, ** U < 0.01 as calculated using the Mann-Whitney test).

8.4 Willin knockdown reduces vinculin expression and formation of focal adhesions

The main sites of cell adhesion to the substrate are focal adhesions, and it is at these sites that forces are transmitted from the cell to the substrate (Balaban *et al*., 2001). Focal adhesions of shScr and shWillin cells were therefore examined to determine any differences in their characterisation. The focal adhesion component vinculin, which regulates force transmission between the cell and ECM (Dumbauld *et al*., 2013), was used as a focal adhesion marker.

Levels of vinculin protein expression in shScr and shWillin cells were firstly compared by Western blot. Vinculin expression in shWillin cells was measured as 64% that of shScr cells ($p < 0.05$) (Figure 8.4).

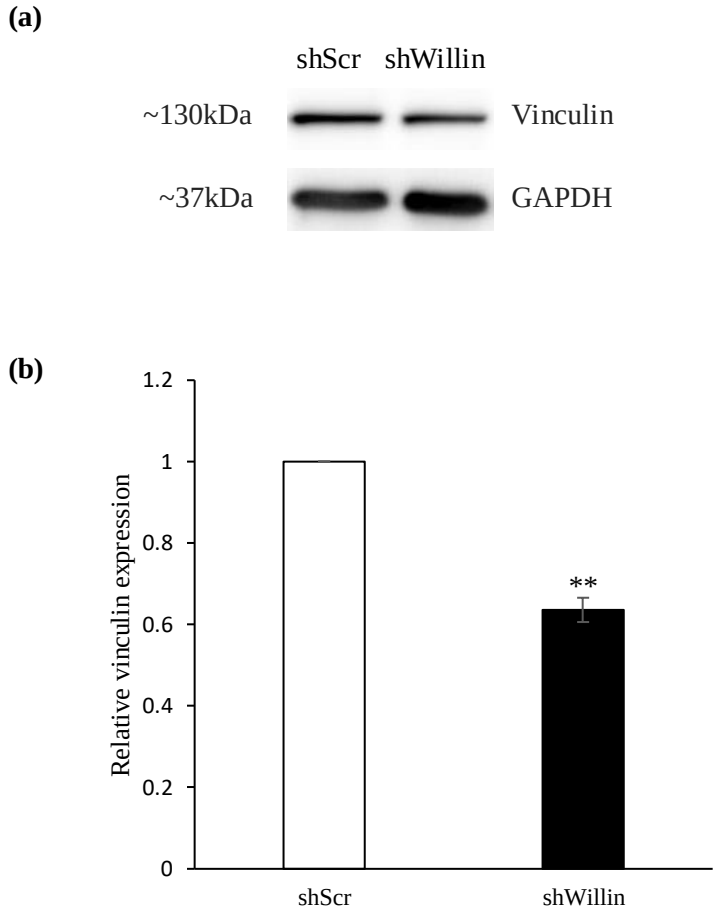

Figure 8.4 Relative vinculin expression in shScr and shWillin cell lines. **(a)** Representative Western blot vinculin protein bands of shScr and shWillin lysate samples. GAPDH served as a loading control. **(b)** Quantification of vinculin protein expression in shScr and shWillin cell lines. Vinculin expression in shWillin cells was measured relative to that of shScr cells (n = 3 experimental repeats, error bars indicate standard deviation, ** $p<0.01$ as calculated using the two-tailed Student's t-test).

Post-ERISM measurements, cells were fixed and stained for vinculin (see Figure 8.7a). The number of focal adhesions per cell and average focal adhesion area for shScr and shWillin cells were determined using FIJI. The median average focal adhesion area for shWillin cells was significantly lower than for shScr cells (1.29μm^2 compared to 1.78μm^2, $U < 0.001$) (Figure 8.5a). The median number of focal adhesions per cell was also lower for shWillin cells (11) compared to shScr cells (23) ($U < 0.001$) (Figure 8.5b).

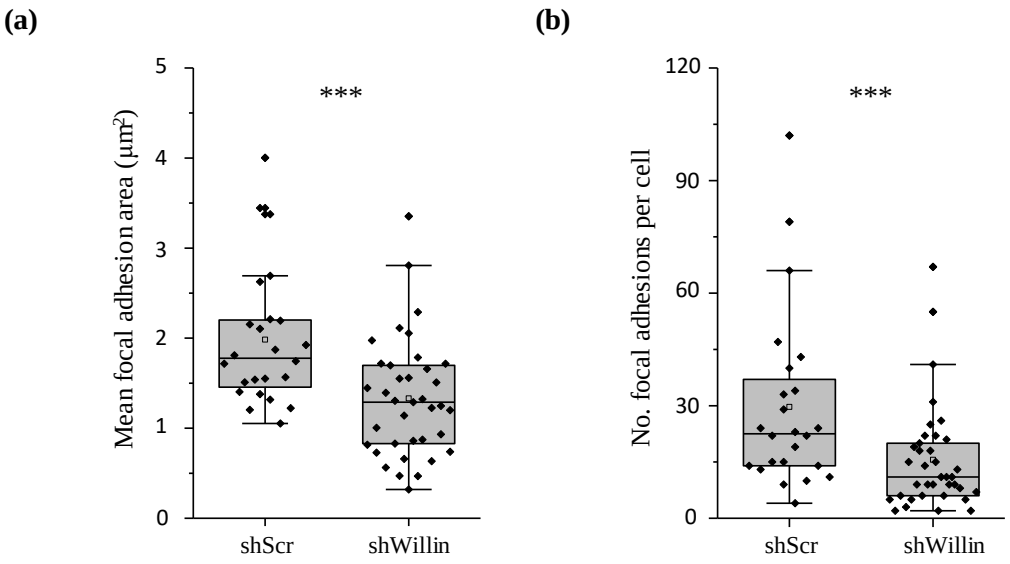

Figure 8.5 Focal adhesion characterisation in shScr and shWillin cells. **(a)** Box plots of mean focal adhesion area for shScr and shWillin cells (shScr n = 24, shWillin n = 37, *** $U < 0.001$ as calculated using the Mann-Whitney test). **(b)** Box plots of number of focal adhesions per cell for shScr and shWillin cells (shScr n = 24 cells, shWillin n = 37 cells, *** $U < 0.001$ as calculated using the Mann-Whitney test).

Collectively, this data implies that Willin knockdown in SH-SY5Y cells results in fewer and smaller focal adhesions.

8.5 Willin knockdown alters localization of TAZ

Hippo pathway effectors and transcriptional-coactivators YAP and TAZ are both mechanosensitive (Dupont *et al*., 2011). As previously determined, SH-SY5Y cells express much higher levels of TAZ than they do YAP (see Chapter 5). The localization of TAZ in shScr and shWillin cells was therefore examined by immunocytochemistry post-ERISM as a means of inferring TAZ activity in the two cell lines (see Figure 8.7a). The median ratio of nuclear: cytoplasmic TAZ in shWillin cells was found to be lower than in shScr cells (1.1 compared to 1.2, $U < 0.001$) (Figure 8.6), implying that TAZ is more nuclear and therefore potentially more transcriptionally active in shScr cells than in shWillin cells.

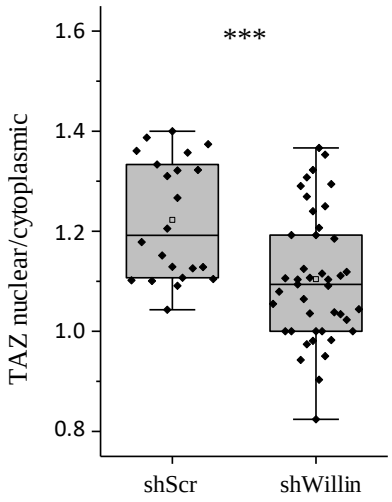

Figure 8.6 TAZ localization in shScr and shWillin cells. Box plots of nuclear: cytoplasmic TAZ in shScr and shWillin cells (shScr n = 22 cells, shWillin n = 43 cells, *** $U < 0.001$ as calculated using the Mann-Whitney test).

8.6 Cell forces and focal adhesion formation correlate with TAZ localization in shScr and shWillin cells

TAZ localization was plotted against ERISM indented volume and the number of focal adhesions per cell for shScr and shWillin cells to determine if there was a correlation between Hippo pathway activity and cell forces and focal adhesion formation (Figure 8.7b, c). Data points were obtained from cells that had been probed using ERISM and then fixed and stained for vinculin, actin and TAZ (Figure 8.7a). The scatter plots show that both cell forces and focal adhesion formation were positively correlated with TAZ nuclear localization, and in addition highlight the difference in these features between the shScr and shWillin cells.

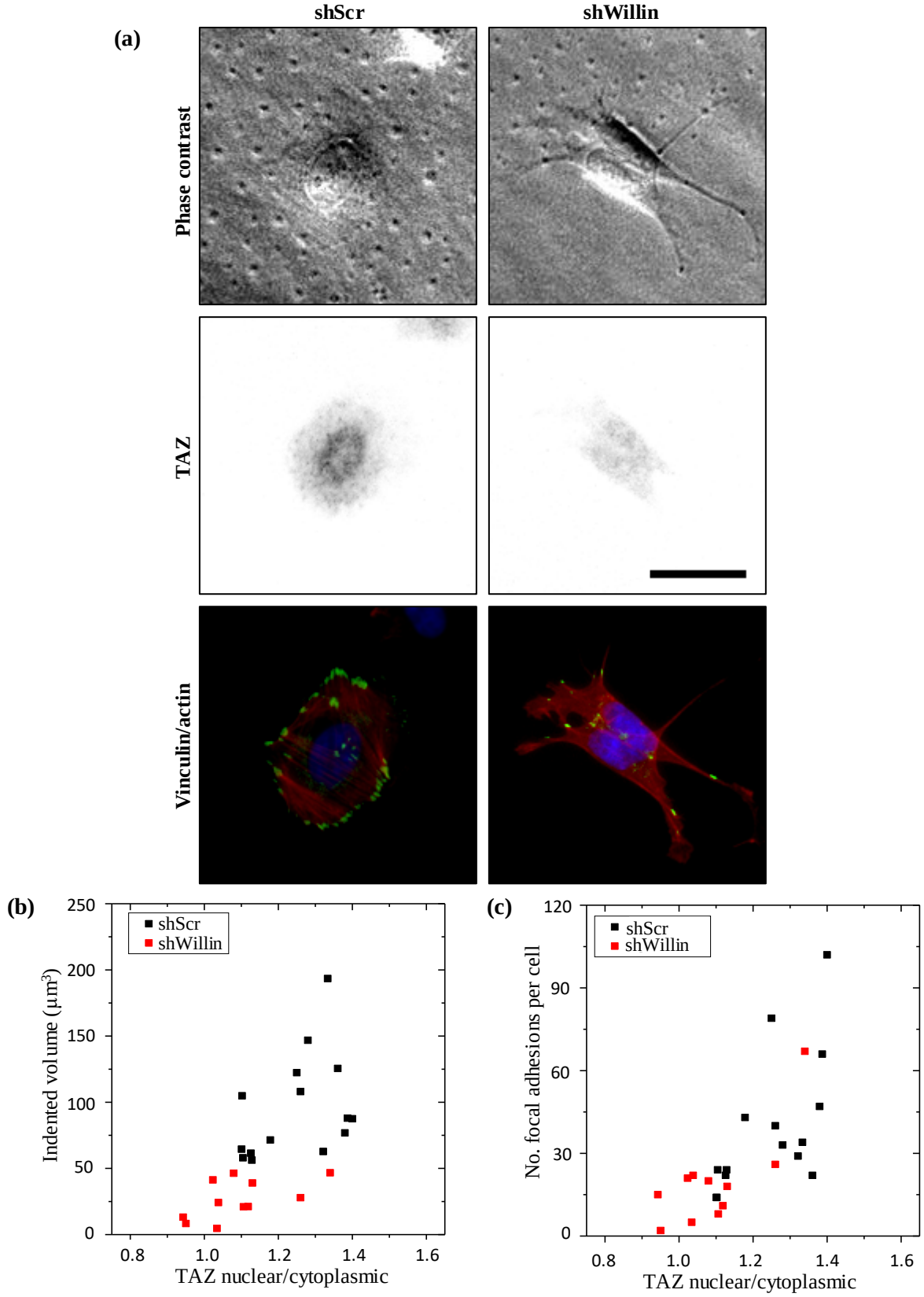

Figure 8.7 Correlation of TAZ localization and cell force and focal adhesion formation in shScr and shWillin cells. **(a)** Representative images of shScr and shWillin cells stained for TAZ (grey-scale) and vinculin (green) and actin (red). Scale bar, 50μm. **(b)** Scatter plot of ratio of nuclear: cytoplasmic TAZ vs. indented volume (shScr, black; shWillin, red). **(c)** Scatter plot of ratio of nuclear: cytoplasmic TAZ vs. number of focal adhesions per cell (shScr, black; shWillin, red) for the same cells as in (b).

8.7 Willin knockdown reduces actin stress fibre formation

The actin cytoskeleton is a major transducer of forces within cells and to the ECM via focal adhesions (Schwarz & Gardel, 2012). Actin stress fibres were therefore examined in shScr and shWillin cells by staining fixed cells post-ERISM with phalloidin-568. A difference in phenotype was immediately noticeable between the two cell lines, with thicker, organised and parallel stress fibres present in shScr cells, and thinner, less organised and fewer stress fibres present in shWillin cells (Figure 8.8).

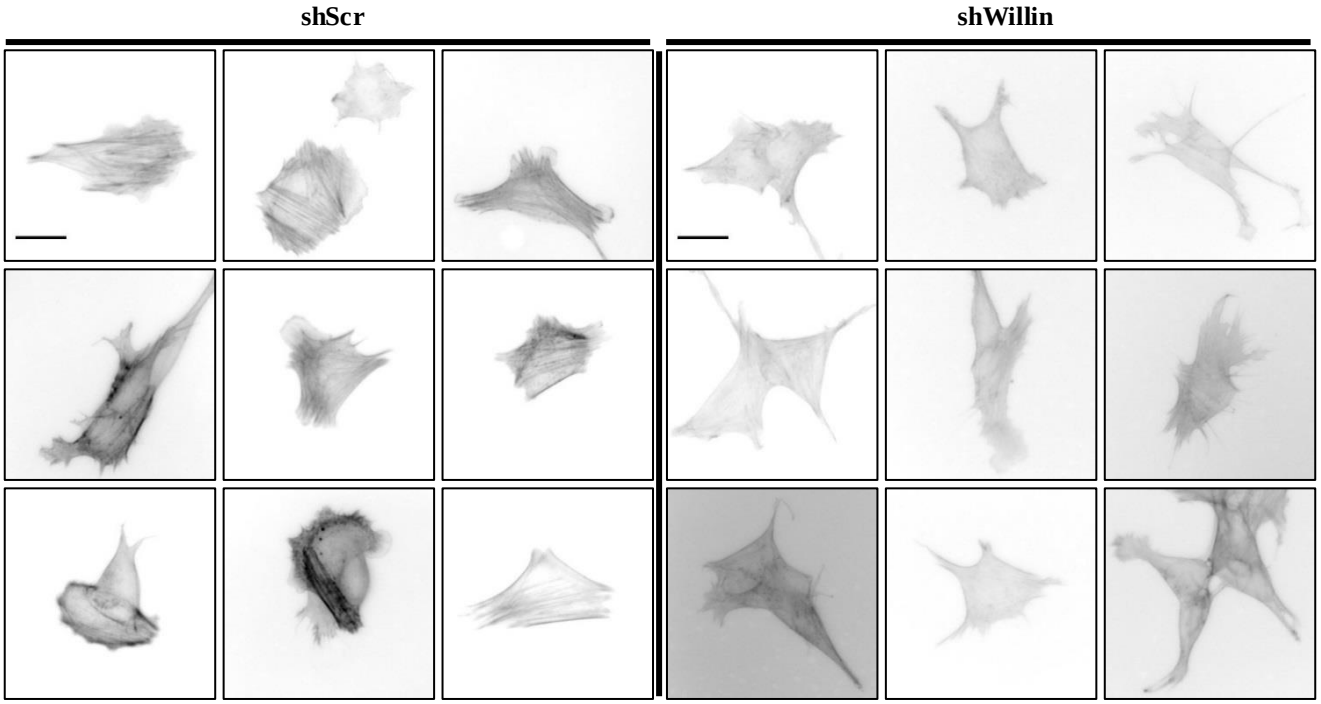

Figure 8.8 Organisation of actin stress fibres in shScr and shWillin cells**.** Representative images of shScr (left 3 x 3 panel) and shWillin (right 3 x 3 panel) cells stained for actin using phalloidin-568. Scale bar, 20μm.

8.8 Differentiation of shScr and shWillin cells reduces cell forces

As described in Chapter 5, Willin knockdown results in enhanced neuronal differentiation of SH-SY5Y cells. To explore a potential link between Willin expression, cell force and neuronal differentiation, cell force was examined during differentiation of shScr and shWillin cells by the same RA/BDNF differentiation method (see Section 4.2.6). ShScr and shWillin cells were seeded in separate ERISM sensors and on day 1, prior to chemical induction by RA, were selected for ERISM measurements and their positions recorded. Cells were grown in media

containing only 1% FBS to prevent cell division. The same cells were then examined by ERISM after addition of RA on days 3, 6 and 8, and after addition of BDNF on day 10. Between measurements, cells were incubated in a humidified atmosphere of 5% CO_2 at 37°C. As previously observed, shWillin cells showed enhanced neuronal differentiation compared to shScr cells. For both shScr and shWillin cells, differentiation resulted in overall reduced cell forces (Figure 8.9a). During differentiation, cellular forces showed a biphasic pattern, with an increase in cell force on day 6 for both cell lines. ERISM was also carried out on shScr and shWillin cells growing under normal conditions on the sensors for 10 days. Interestingly, shScr cells showed a large decrease in cellular forces over the experiment, whereas shWillin cells showed a small increase (Figure 8.9b). By overlaying the cellular forces measured during shScr differentiation (green) with the long-term growth measurements (red and blue), it was observed that differentiation of shScr cells results in cell forces similar to that of undifferentiated shWillin cells.

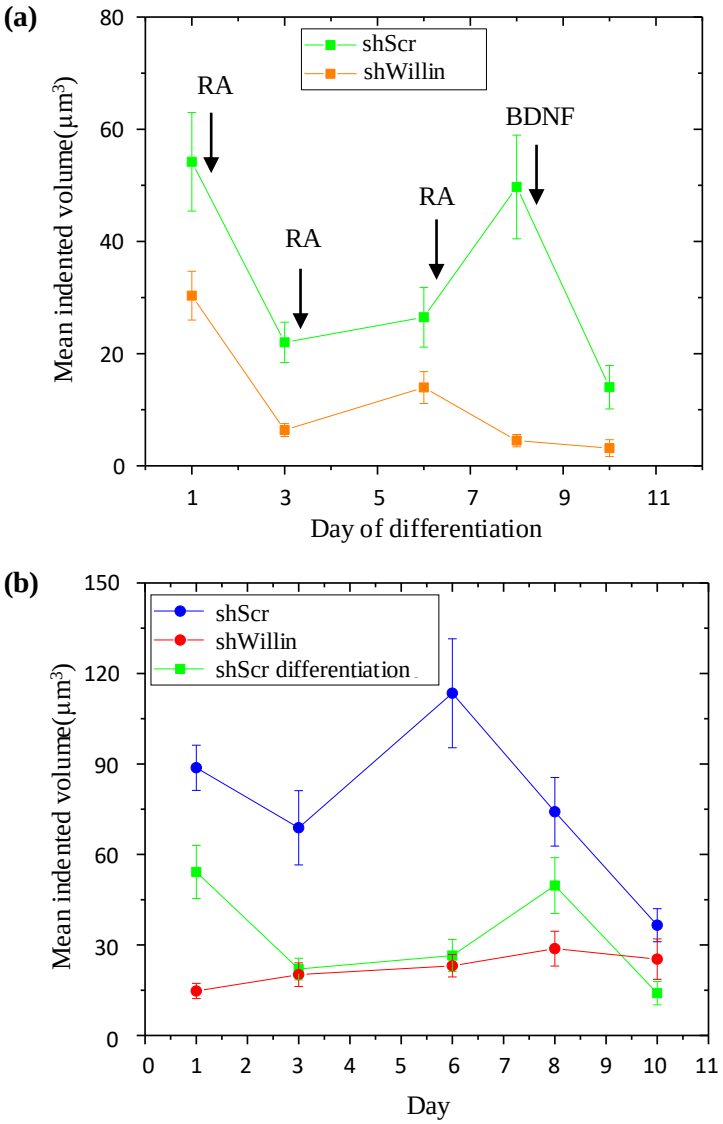

Figure 8.9 ERISM measurements during differentiation and long-term growth of shScr and shWillin cells. **(a)** Cell forces as measured for days 0, 3, 6, 8 and 10 of differentiation (shScr differentiation, green; shWillin differentiation, orange; error bars indicate standard error of the mean). Cells were treated with RA post day 0 ERISM, and with BDNF post day 8. **(b)** Cell forces as measured for long-term growth of shScr and shWillin cells, and for shScr cells during differentiation (as per (a)). Measurements were taken on days 1, 3, 6, 8 and 10 of growth (shScr growth, blue; shWillin growth, red; shScr differentiation, green; error bars indicate standard error of the mean).

8.9 Discussion & future work

The development of ERISM has allowed for the accurate detection of cell forces in a range of different cell types, as described in the technical proof-of-concept publication (Kronenberg *et*

al., 2017). Here, it has been used to reveal the reduction of SH-SY5Y cell forces as a result of Willin knockdown. The ability of ERISM to detect very small changes in elastomer thickness by cell indentation enabled measurements of cells that exerted only very weak forces, e.g. differentiated cells. The direct and non-phototoxic methodology of this technique allowed not only long-term (10 day) cell force studies, but also visualisation of proteins of interest in those cells probed by ERISM using immunocytochemistry.

Together, the data described above consistently infer that Willin knockdown alters the forces exerted by and cytoskeletal machinery of SH-SY5Y cells. Firstly, Willin knockdown significantly reduced cell forces as measured by indentation of an elastomer substrate using ERISM. Secondly, Willin knockdown reduced cell area and altered cell shape toward a more elongated phenotype. Thirdly, Willin knockdown decreased expression of a key focal adhesion component, vinculin, and reduced the number and size of focal adhesions present in the cell. This alteration in specific sites of cell adhesion is also apparent in the Fourier-filtered elastomer displacement maps that display the high frequency changes in elastomer indentation (Figure 8.2a). Fourthly, Willin expression altered the localization of a mechanosensitive protein, TAZ, which correlated with both the ERISM indented volume measurements and the number of focal adhesions per cell. And finally, Willin knockdown resulted in disassembly of the actin cytoskeleton.

How Willin affects cell forces remains unexplored. The adhesome, or network of proteins that make up focal adhesions or are connected to focal adhesions via signalling events, is vast, containing nearly 700 links, with the integrin adhesome consisting of ~160 components alone (Geiger, Spatz & Bershadsky, 2009). Furthermore, there is much crosstalk between focal adhesions and the forces at play within the actin cytoskeleton that arise from actin polymerisation and actomyosin contraction (Geiger, Spatz & Bershadsky, 2009). Thus Willin may affect cell forces via focal adhesions directly, the actin cytoskeleton, or an indirect signalling pathway as part of the adhesome network. The direct involvement of Willin at focal adhesions is perhaps unlikely, since Willin-mCherry did not colocalize with the focal adhesion component vinculin (data not shown), suggesting that Willin acts either via actin (as potentially indicated by colocalization of Willin-mCherry and F-actin, see Figure 7.4) or an indirect signalling pathway to modify cell forces. To determine if the reduction in cell force as a result of Willin knockdown is due to disassembly of the actin cytoskeleton, shWillin cells could be treated with the actin-specific reagent jasplakinolide that promotes actin polymerisation

(Holzinger, 2009) to ascertain whether the shScr phenotype, including stress fibre and focal adhesion formation, force exertion and TAZ localization, can be rescued.

Interestingly, the binding of AMOT-p130 to F-actin is thought to stabilise actin stress fibres (Ernkvist *et al*., 2006), and phosphorylation of AMOT-p130 by LATS1/2 disrupts its interaction with F-actin, which is correlated with the presence of reduced F-actin stress fibres and focal adhesions (Dai *et al*., 2013). A potential hypothesis, therefore, is that Willin enhances the binding of ability of AMOT-p130 to F-actin, possibly by preventing its phosphorylation by LATS1/2, and in turn leads to increased actin stress fibre and focal adhesion formation (Figure 9.1). Concurrently, phosphorylation of AMOT-p130 also inhibits endothelial cell migration (Dai *et al*., 2013), whilst expression of Willin induces quicker migration of peripheral nerve fibroblasts (Moleirinho *et al*., 2013b).

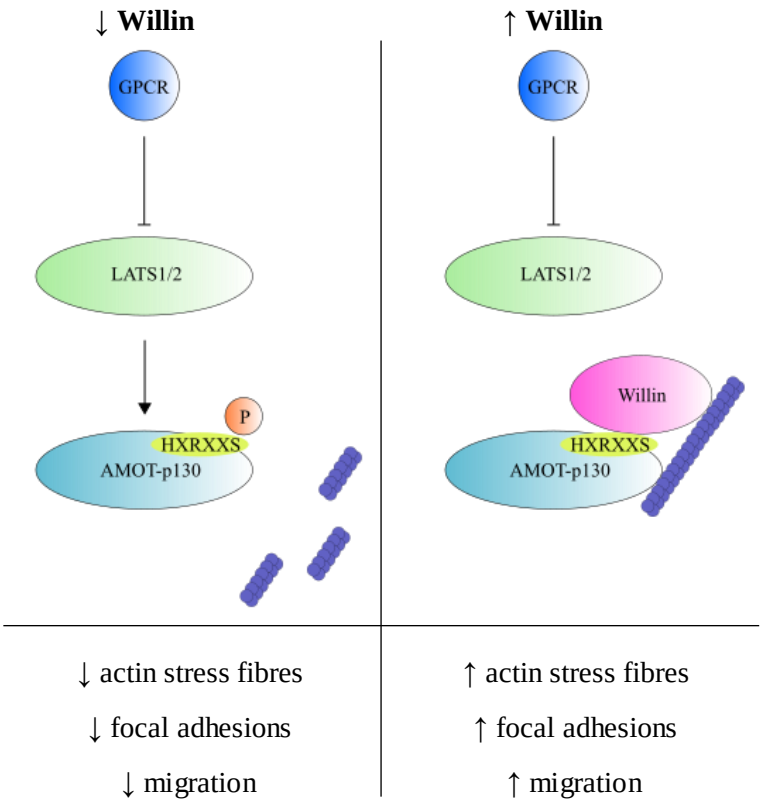

Figure 8.10 Hypothesis model of AMOT-p130 regulation by Willin. Left panel: phosphorylation of AMOT-p130 residue S175 by LATS1/2 downstream of GPCR signalling disrupts AMOT interaction with F-actin (dark blue) and correlates with reduced stress fibre and focal adhesion formation and cell migration (Dai *et al*., 2013). Right panel: Willin may interact with AMOT-p130 to prevent phosphorylation by LATS1/2 and enhance binding of AMOT to F-actin.

The fact that Willin colocalizes with both AMOT and actin stress fibres, as shown using 3D-SIM (see Chapter 7), lends itself as evidence to this hypothesis. Future work would be required to confirm the interaction between AMOT and Willin, and whether Willin binding to AMOT prevents phosphorylation by LATS1/2 and enhances AMOT binding to F-actin. Both the localization (actin-bound/cytoplasmic) and phosphorylation status of AMOT could also be investigated in Willin-knockdown and Willin-overexpressing cells.

An alternative explanation for the effect of Willin expression on SH-SY5Y cellular force is that Willin knockdown drives SH-SY5Y cells into differentiation. The effect of Willin expression on SH-SY5Y neuronal differentiation using the RA/BDNF method was investigated in Chapter 5: Willin knockdown resulted in the formation of pre-neurites in undifferentiated cells, and escalated differentiation upon the addition of RA/BDNF to cells. Here, differentiation of shScr and shWillin SH-SY5Y cells was shown to reduce cell force. Furthermore, differentiation of shScr cells decreased cellular forces to a similar level to that of untreated shWillin cells; this suggests that the reduced cell forces observed for shWillin cells may have been due to them having assumed a differentiated phenotype in the absence of chemical activation. Interestingly, shScr and shWillin cell forces were similar after 10 days of growth without differentiation (Figure 8.9b). However, long-term adhesion measurements were carried out in a single experiment, and repeats are required to determine whether this result is an anomaly or a real phenomenon.

The relationship between TAZ localization and focal adhesions/ forces exerted by SH-SY5Y cells may be one- or two-way: vinculin is necessary for nuclear localization of YAP/TAZ on rigid surfaces (Kuroda *et al*., 2017), and thus the reduction in focal adhesions in shWillin cells may have caused TAZ to be more cytoplasmic; secondly, or possibly in addition, like YAP-(Nardone *et al*., 2017), nuclear TAZ may drive the formation of focal adhesions in SH-SY5Y cells. To explore the above, TAZ/vinculin knockdown could be performed in shScr and shWillin cells using shRNA, and the cells examined for focal adhesions and TAZ localization respectively.

The reduction in cell area of shWillin cells compared to shScr cells may have also affected TAZ localization. The localization of YAP, for instance, has been shown to be controlled by cell area regardless of focal adhesion formation, with a smaller area resulting in less nuclear YAP (Nardone *et al*., 2017). To determine if this was the case, shScr cells could be grown on

micropatterns to restrict cell spreading and examined for TAZ localization as well as focal adhesions.

Willin has previously been shown to activate the Hippo signalling pathway in HEK-293 cells: increased Willin expression led to phosphorylation of MST1/2, LATS1 and YAP (Angus *et al*., 2012). However, here it was conversely shown that in SH-SY5Y cells, a decrease in Willin expression led to a small but significant increase in cytoplasmic localization of TAZ (Figure 8.6), inferring that decreased Willin expression led to activation of the Hippo pathway.

Other regulators of the Hippo pathway have been demonstrated to have opposing effects in different cell types. For example, the diacylglycerol analogue TPA induces via activation of protein kinase C (PKC), YAP dephosphorylation and nuclear translocation in HEK-293 cells, but phosphorylation and cytoplasmic localization of YAP in MEF cells (Gong *et al*., 2015). This was shown to be due to activation of different PKC isoforms in the two different cell types. Willin may therefore act through an upstream regulator of the Hippo pathway such as PKC that has different isoforms expressed in cell types that have opposing roles in YAP/TAZ activation. AMOT has also been shown to exert different effects on Hippo signalling in different cells and tissues: in MDCK epithelial cells and HEK-293 cells, AMOT inhibits YAP-dependent transcription, but in hepatocarcinoma and breast cancer cells, AMOT induces transcription of TEAD-target genes (Chan *et al*., 2011; Zhao *et al*., 2011; Yi *et al*., 2013; Lv *et al*., 2015).

Another possible explanation for the observation that Willin has a different effect on YAP and TAZ in HEK-293 and SH-SY5Y cells respectively is that Willin may regulate YAP and TAZ in an opposite manner. There is evidence to suggest that YAP and TAZ are not entirely redundant, as crystal structures of the YAP-TEAD and TAZ-TEAD complexes have revealed distinct interactions (Kaan *et al*., 2017), and YAP and TAZ have recently been shown to have slightly different transcriptional profiles (Plouffe *et al*., 2018). Further work, however, is required to investigate the effect of Willin expression on the phosphorylation state and transcriptional activity of TAZ (and YAP) in SH-SY5Y cells. As Willin was originally shown to act upstream of YAP in HEK-293 cells, it would also be interesting to determine whether Willin has a role in regulation of the actin cytoskeleton and AMOT in this cell line (see above), especially since AMOT has been specifically shown to regulate YAP activity via actin (Mana-Capelli *et al*., 2014). It may be that Willin, like many other upstream members of the Hippo

pathway, regulates Hippo signalling via more than one mechanism, both as part of the canonical pathway, and via the actin cytoskeleton.

It was interesting to observe that the previously recorded actin bundling in shWillin cells (Figure 7.9) was not evident in this study (Figure 8.8). This may have been due to the fact that here, images were recorded in only a single plane; often, actin bundling was observed in a plane that was different from that of the majority of actin stress fibres. Another explanation could be that this actin bundling only occurs in shWillin cells grown on a stiff substrate e.g. glass. The elastomer stiffness used for ERISM (1.3kPa), was much lower than that of glass (>1000kPa).

In this study, ERISM was carried out using a collagen substrate. In the future, it would be interesting to observe the forces exerted by shScr and shWillin cells on different substrates, such as laminin or fibronectin, to determine if the effect of Willin expression on cell adhesion is substrate-dependent and Willin acts through a signalling pathway that is associated with the ECM.

8.10 Chapter acknowledgements

Preparation of ERISM chips was carried out by Dr Nils Kronenberg, and culturing and differentiation of cells for ERISM by the author. ERISM was performed by both Dr Nils Kronenberg and the author. All Western blotting and immunostaining was performed by the author. Deformation analysis and fluorescence imaging was completed by Dr Nils Kronenberg. Cell morphology and focal adhesion analysis was carried out by the author, and TAZ analysis by Dr Nils Kronenberg. Figures were produced by Dr Nils Kronenberg.

9 Final conclusions

This thesis examined the question of whether Willin has a mechanical role to play in the mammalian Hippo signalling pathway. Optical techniques SIM and ERISM were employed to aid in this investigation, and a double optical trap was developed for integration with the commercial N-SIM. The main outcomes of this thesis are summarised below.

9.1 Development of a double optical trap on the N-SIM

A major aim of this thesis was to develop a double optical trap on the N-SIM for the purpose of cell-stretching and simultaneous super-resolution imaging of fluorescent cells (Chapter 6). Initial design of the double trap used an aspheric lens, which was characterised as having an NA of 0.40. The trap design was based on the system by Fällman and Axner (Fällman & Axner, 1997), which enabled steering of both traps in the x and y dimensions, and of one of the traps in the z dimension. Characterisation of the double trap was carried out using equipartition. However, equipartition results for the transmitted beam were poor, with k_x measured as 0.0167pN μm^{-1} mW^{-1}. A new double trap design was therefore conceived that used a GRIN microlens as the trapping lens.

Prior to integration of the GRIN lens double trap on the N-SIM, the GRIN lens was characterised by drag-force measurements using a custom-built polarization microscope. Q_x and Q_y for trapping caboxylated 2.19μm beads were relatively high (0.27 and 0.22 respectively) considering that the trap had an NA of 0.38. This system was then adjusted to determine that beams entering the GRIN lens at different angles could still produce a trap with a sufficiently small spot size for trapping, and thus that the GRIN lens could allow for two traps to be positioned at different points of a cell for stretching.

A double optical fibre-based GRIN lens trap was designed and constructed on the N-SIM. Both traps were characterised using equipartition, with k_x and k_y for the reflected beam measured as 0.38pN μm^{-1} mW^{-1} and 0.34pN μm^{-1} mW^{-1} respectively, and k_x and k_y for the transmitted beam as 0.32pN μm^{-1} mW^{-1} and 0.15pN μm^{-1} mW^{-1}. However, on trapping with live cells, trapped beads were immobilized on the sample dish, and therefore their attachment to cells for manipulation was not possible. This was due to the presence of cell media, which was required for maintaining cell viability.

9.2 Biophysical studies of Willin

Investigation into the effect of Willin expression on SH-SY5Y differentiation by chemical induction with RA/BDNF revealed that Willin knockdown resulted in enhanced neuronal differentiation (Chapter 5). This morphological differentiation was accompanied by actin stress fibre dissaembly and nucleocytoplasmic translocation of Hippo pathway effector TAZ. Willin was also shown using 3D-SIM to localize to the neurites of differentiated cells, and to increase in expression during SH-SY5Y differentiation.

A Willin-mCherrry SH-SY5Y cell line was produced in order to study Willin localization and behaviour (Chapter 7). Willin-mCherry was shown using 3D-SIM to localize both on actin stress fibres and within larger vesicle-like structures. These structures were highly mobile, and co-localized with the lipid dye Bodipy, suggesting that they may have been intracellular vesicles. Willin-mCherry was also shown to partially co-localize with the Hippo pathway and polarity protein, AMOT, and a potential interaction between Willin and AMOT was explored by immunoprecipitation. Substrate elasticity was shown to have no effect on Willin-mCherry localization, but did significantly affect Willin expression in SH-SY5Y cells.

Previously observed 'actin swirls' in shWillin cells were imaged using 3D-SIM and shown to be a result of stress fibre bundling (Chapter 7). A literature search revealed that this actin bundling had been previously observed as a result of overexpression of AMOT-p130 (Mana-Capelli *et al*., 2014). AMOT expression in shScr and shWillin cells was therefore examined by Western blot and found to be significantly higher in shWillin cells.

Willin-knockdown was shown to have a significant effect on cell forces, as investigated using ERISM (Chapter 8). Compared to shSCr cells, shWillin cells exerted lower forces and had a more elongated shape, overall fewer actin stress fibres and fewer and smaller focal adhesions. TAZ was also less nuclear in shWillin cells compared to in shScr cells. Cell forces were shown to decrease during differentiation of shScr and shWillin cells.

9.3 Concluding remarks

Given the effect of Willin expression on the actin cytoskeleton in SH-SY5Y cells, it is likely that Willin plays a mechanical role in the regulation of the mammalian Hippo pathway. This role may occur via the RhoA signalling pathway, or via the cell polarity protein AMOT. Further work as outlined in this thesis will help to elucidate a more precise mechanism of how

Willin regulates the actin cytoskeleton and YAP/TAZ activity. The use of optical techniques SIM and ERISM has been fundamental to this thesis. Cell stretching to study the behaviour of Willin under mechanical strain in real-time and using super-resolution microscopy would in the future give further insight into a more direct role for Willin in mechanosensing, both upstream of Hippo signalling and in other cellular processes.

Bibliography

Abbe, E., 1873. Beiträge zur Theorie des Mikroskops und der mikroskopischen Wahrnehmung. *Archiv für mikroskopische Anatomie* **9** (1), pp.413-418.

Abbondanzieri, E.A., Greenleaf, W.J., Shaevitz, J.W., Landick, R. and Block, S.M., 2005. Direct observation of base-pair stepping by RNA polymerase. *Nature* **438** (7067), pp.460-465.

Aerne, B.L., Gailite, I., Sims, D. and Tapon, N., 2015. Hippo stabilises its adaptor salvador by antagonising the HECT ubiquitin ligase Herc4. *PLoS One* **10** (6), e0131113.

Agate, B., Brown, C.T.A., Sibbett, W. and Dholakia, K., 2004. Femtosecond optical tweezers for in-situ control of two-photon fluorescence. *Optics Express* **12** (13), pp.3011-3017.

Ahmed, A.F., de Bock, C.E., Lincz, L.F., Pundavela, J., Zouikr, I., Sontag, E., Hondermarck, H. and Thorne, R.F., 2015. FAT1 cadherin acts upstream of Hippo signalling through TAZ to regulate neuronal differentiation. *Cellular and Molecular Life Sciences* **72** (23), pp.4653-4669.

Al Balushi, A.A., Kotnala, A., Wheaton, S., Gelfand, R.M., Rajashekara, Y. and Gordon, R., 2015. Label-free free-solution nanoaperture optical tweezers for single molecule protein studies. *Analyst* **140** (14), pp.4760-4778.

Alenghat, F.J. and Ingber, D.E., 2002. Mechanotransduction: all signals point to cytoskeleton, matrix, and integrins. *Science Signaling* **2002** (119), p.e6.

Allen, J.R., Ross, S.T. and Davidson, M.W., 2014. Structured illumination microscopy for superresolution. *ChemPhysChem* **15** (4), pp.566-576.

Angus, L., Moleirinho, S., Herron, L., Sinha, A., Zhang, X., Niestrata, M., Dholakia, K., Prystowsky, M.B., Harvey, K.F., Reynolds, P.A. and Gunn-Moore, F.J., 2012. Willin/FRMD6 expression activates the Hippo signaling pathway kinases in mammals and antagonizes oncogenic YAP. *Oncogene* **31** (2) pp.238-250.

Aragona, M., Panciera, T., Manfrin, A., Giulitti, S., Michielin, F., Elvassore, N., Dupont, S. and Piccolo, S., 2013. A mechanical checkpoint controls multicellular growth through YAP/TAZ regulation by actin-processing factors. *Cell* **154** (5), pp.1047-1059.

Archibald, A., Al-Masri, M., Liew-Spilger, A. and McCaffrey, L., 2015. Atypical protein kinase C induces cell transformation by disrupting Hippo/Yap signaling. *Molecular Biology of the Cell* **26** (20), pp.3578-3595.

Ash, E.A. and Nicholls, G., 1972. Super-resolution aperture scanning microscope. *Nature* **237** (5357), pp.510-512.

Ashkin, A., 1970. Acceleration and trapping of particles by radiation pressure. *Physical Review Letters* **24** (4), pp.156-159.

Ashkin, A., Dziedzic, J.M., Bjorkholm, J.E. and Chu, S., 1986. Observation of a single-beam gradient force optical trap for dielectric particles. *Optics Letters* **11** (5), pp.288-290.

Ashkin, A., Dziedzic, J.M. and Yamane, T., 1987. Optical trapping and manipulation of single cells using infrared laser beams. *Nature* **330** (6150), pp.769-771.

Ashkin, A., 1992. Forces of a single-beam gradient laser trap on a dielectric sphere in the ray optics regime. *Biophysical Journal* **61** (2), pp.569-582.

Badouel, C., Gardano, L., Amin, N., Garg, A., Rosenfeld, R., Le Bihan, T. and McNeill, H., 2009. The FERM-domain protein Expanded regulates Hippo pathway activity via direct interactions with the transcriptional activator Yorkie. *Developmental Cell* **16** (3), pp.411-420.

Bai, H., Gayyed, M.F., Lam-Himlin, D.M., Klein, A.P., Nayar, S.K., Xu, Y., Khan, M., Argani, P., Pan, D. and Anders, R.A., 2012. Expression of Yes-associated protein modulates Survivin expression in primary liver malignancies. *Human Pathology* **43** (9), pp.1376-1385.

Bailey, B., Farkas, D.L., Taylor, D.L. and Lanni, F., 1993. Enhancement of axial resolution in fluorescence microscopy by standing-wave excitation. *Nature* 366 (6450), pp.44-48.

Balaban, N.Q., Schwarz, U.S., Riveline, D., Goichberg, P., Tzur, G., Sabanay, I., Mahalu, D., Safran, S., Bershadsky, A., Addadi, L. and Geiger, B., 2001. Force and focal adhesion assembly: a close relationship studied using elastic micropatterned substrates. *Nature Cell Biology* **3** (5), pp.466-472.

Ball, G., Demmerle, J., Kaufmann, R., Davis, I., Dobbie, I.M. and Schermelleh, L., 2015. SIMcheck: a toolbox for successful super-resolution structured illumination microscopy. *Scientific Reports* **5**, 15915.

Bao, G. and Suresh, S., 2003. Cell and molecular mechanics of biological materials. *Nature Materials* **2** (11), pp.715-725.

Basu, S., Totty, N.F., Irwin, M.S., Sudol, M. and Downward, J., 2003. Akt phosphorylates the Yes-associated protein, YAP, to induce interaction with 14-3-3 and attenuation of p73-mediated apoptosis. *Molecular cell* **11** (1), pp.11-23.

Baumgartner, R., Poernbacher, I., Buser, N., Hafen, E. and Stocker, H., 2010. The WW domain protein Kibra acts upstream of Hippo in Drosophila. *Developmental Cell* **18** (2), pp.309-316.

Benhamouche, S., Curto, M., Saotome, I., Gladden, A.B., Liu, C.H., Giovannini, M. and McClatchey, A.I., 2010. Nf2/Merlin controls progenitor homeostasis and tumorigenesis in the liver. *Genes & Development* **24** (16), pp1718-1730.

Bennett, F.C. and Harvey, K.F., 2006. Fat cadherin modulates organ size in Drosophila via the Salvador/Warts/Hippo signaling pathway. *Current Biology* **16** (21), pp.2101-2110.

Berg-Sørensen, K. and Flyvbjerg, H., 2004. Power spectrum analysis for optical tweezers. *Review of Scientific Instruments* **75** (3), pp.594-612.

Betzig, E., Lewis, A., Harootunian, A., Isaacson, M. and Kratschmer, E., 1986. Near field scanning optical microscopy (NSOM): development and biophysical applications. *Biophysical Journal* **49** (1), pp.269-279.

Betzig, E., Patterson, G.H., Sougrat, R., Lindwasser, O.W., Olenych, S., Bonifacino, J.S., Davidson, M.W., Lippincott-Schwartz, J. and Hess, H.F., 2006. Imaging intracellular fluorescent proteins at nanometer resolution. *Science* **313** (5793), pp.1642-1645.

Bisson-Filho, A.W., Hsu, Y.P., Squyres, G.R., Kuru, E., Wu, F., Jukes, C., Sun, Y., Dekker, C., Holden, S., VanNieuwenhze, M.S. and Brun, Y.V., 2017. Treadmilling by FtsZ filaments drives peptidoglycan synthesis and bacterial cell division. *Science* **355** (6326), pp.739-743.

Block, S.M., Goldstein, L.S. and Schnapp, B.J., 1990. Bead movement by single kinesin molecules studied with optical tweezers. *Nature* **348** (6299), pp.348-352.

Boggiano, J.C., Vanderzalm, P.J. and Fehon, R.G., 2011. Tao-1 phosphorylates Hippo/MST kinases to regulate the Hippo-Salvador-Warts tumor suppressor pathway. *Developmental Cell* **21** (5), pp.888-895.

Bosanquet, D.C., Ye, L., Harding, K.G. and Jiang, W.G., 2014. FERM family proteins and their importance in cellular movements and wound healing. *International Journal of Molecular Medicine* **34** (1), pp.3-12.

Botvinick, E.L. and Wang, Y., 2007. Laser tweezers in the study of mechanobiology in live cells. *Methods in Cell Biology* **82**, pp.497-523.

Bretscher, A., Edwards, K. and Fehon, R.G., 2002. ERM proteins and merlin: integrators at the cell cortex. *Nature Reviews Molecular Cell Biology* **3** (8), pp.5865-99.

Burridge, K. and Wittchen, E.S., 2013. The tension mounts: stress fibers as force-generating mechanotransducers. *The Journal of Cell Biology* **200** (1), pp.9-19.

Butcher, D.T., Alliston, T. and Weaver, V.M., 2009. A tense situation: forcing tumour progression. *Nature Reviews Cancer* **9** (2), pp.108-122.

Cai, J., Zhang, N., Zheng, Y., de Wilde, R.F., Maitra, A. and Pan, D., 2010. The Hippo signaling pathway restricts the oncogenic potential of an intestinal regeneration program. *Genes & Development* **24** (21), pp.2383-2388.

Callus, B.A., Verhagen, A.M. and Vaux, D.L., 2006. Association of mammalian sterile twenty kinases, Mst1 and Mst2, with hSalvador via C-terminal coiled-coil domains, leads to its stabilization and phosphorylation. *The FEBS Journal* **273** (18), pp.4264-4276.

Camargo, F.D., Gokhale, S., Johnnidis, J.B., Fu, D., Bell, G.W., Jaenisch, R. and Brummelkamp, T.R., 2007. YAP1 increases organ size and expands undifferentiated progenitor cells. *Current Biology* **17** (23), pp.2054-2060.

Cao, X., Pfaff, S.L. and Gage, F.H., 2008. YAP regulates neural progenitor cell number via the TEA domain transcription factor. *Genes & Development* **22** (23), pp.3320-3334.

Chachisvilis, M., Zhang, Y.L. and Frangos, J.A., 2006. G protein-coupled receptors sense fluid shear stress in endothelial cells. *Proceedings of the National Academy of Sciences* **103** (42), pp.15463-15468.

Chakraborty, S., Lakshmanan, M., Swa, H.L., Chen, J., Zhang, X., Ong, Y.S., Loo, L.S., Akıncılar, S.C., Gunaratne, J., Tergaonkar, V. and Hui, K.M., 2015. An oncogenic role of Agrin in regulating focal adhesion integrity in hepatocellular carcinoma. *Nature Communications* **6**, 6184.

Chakraborty, S., Njah, K., Pobbati, A.V., Lim, Y.B., Raju, A., Lakshmanan, M., Tergaonkar, V., Lim, C.T. and Hong, W., 2017. Agrin as a mechanotransduction signal regulating YAP through the Hippo pathway. *Cell Reports* **18** (10), pp.2464-2479.

Chalfie, M., 2009. Neurosensory mechanotransduction. *Nature reviews Molecular Cell Biology* **10** (1), pp.44-52.

Chan, E.H., Nousiainen, M., Chalamalasetty, R.B., Schäfer, A., Nigg, E.A. and Sillje, H.H., 2005. The Ste20-like kinase Mst2 activates the human large tumor suppressor kinase Lats1. *Oncogene* **24** (12), pp.2076-2086.

Chan, S.W., Lim, C.J., Loo, L.S., Chong, Y.F., Huang, C. and Hong, W., 2009. TEADs mediate nuclear retention of TAZ to promote oncogenic transformation. *Journal of Biological Chemistry* **284** (21), pp.14347-14358.

Chan, S.W., Lim, C.J., Chong, Y.F., Pobbati, A.V., Huang, C. and Hong, W., 2011. Hippo pathway-independent restriction of TAZ and YAP by angiomotin. *Journal of Biological Chemistry* **286** (9), pp.7018-7026.

Chen, C.L., Gajewski, K.M., Hamaratoglu, F., Bossuyt, W., Sansores-Garcia, L., Tao, C. and Halder, G., 2010. The apical-basal cell polarity determinant Crumbs regulates Hippo signaling in Drosophila. *Proceedings of the National Academy of Sciences* **107** (36), pp.15810-15815.

Chen, D., Sun, Y., Wei, Y., Zhang, P., Rezaeian, A.H., Teruya-Feldstein, J., Gupta, S., Liang, H., Lin, H.K., Hung, M.C. and Ma, L., 2012. LIFR is a breast cancer metastasis suppressor upstream of the Hippo-YAP pathway and a prognostic marker. *Nature Medicine* **18** (10), p.1511-1517.

Chishti, A.H., Kim, A.C., Marfatia, S.M., Lutchman, M., Hanspal, M., Jindal, H., Liu, S.C., Low, P.S., Rouleau, G.A., Mohandas, N. and Chasis, J.A., 1998. The FERM domain: a unique module involved in the linkage of cytoplasmic proteins to the membrane. *Trends in Biochemical Sciences* **23** (8), pp.281-282.

Cho, S., Irianto, J. and Discher, D.E., 2017. Mechanosensing by the nucleus: From pathways to scaling relationships. *The Journal of Cell Biology* **216** (2), pp.305-315.

Chung, E., Kim, D. and So, P.T., 2006. Extended resolution wide-field optical imaging: objective-launched standing-wave total internal reflection fluorescence microscopy. *Optics Letters* **31** (7), pp.945-947.

Clattenburg, L., Wigerius, M., Qi, J., Rainey, J.K., Rourke, J.L., Muruganandan, S., Sinal, C.J. and Fawcett, J.P., 2015. NOS1AP functionally associates with YAP to regulate Hippo signaling. *Molecular and Cellular Biology* **35** (13), pp.2265-2277.

Codelia, V.A., Sun, G. and Irvine, K.D., 2014. Regulation of YAP by mechanical strain through Jnk and Hippo signaling. *Current Biology* **24** (17), pp.2012-2017.

Colin-York, H., Eggeling, C. and Fritzsche, M., 2017. Dissection of mechanical force in living cells by super-resolved traction force microscopy. *Nature Protocols* **12** (4), p.783-796.

Constable, A., Kim, J., Mervis, J., Zarinetchi, F. and Prentiss, M., 1993. Demonstration of a fiber-optical light-force trap. *Optics Letters* **18** (21), pp.1867-1869.

Coons, A.H., 1951. Fluorescent antibodies as histochemical tools. *Federation Proceedings* **10** (2), pp.558-559.

Cordenonsi, M., Zanconato, F., Azzolin, L., Forcato, M., Rosato, A., Frasson, C., Inui, M., Montagner, M., Parenti, A.R., Poletti, A. and Daidone, M.G., 2011. The Hippo transducer TAZ confers cancer stem cell-related traits on breast cancer cells. *Cell* **147** (4), pp.759-772.

Cui, Y., Hameed, F.M., Yang, B., Lee, K., Pan, C.Q., Park, S. and Sheetz, M., 2015. Cyclic stretching of soft substrates induces spreading and growth. *Nature Communications* **6**, 6333.

Curtis, J.E., Koss, B.A. and Grier, D.G., 2002. Dynamic holographic optical tweezers. *Optics Communications* **207** (1-6), pp.169-175.

Curto, M., Cole, B.K., Lallemand, D., Liu, C.H. and McClatchey, A.I., 2007. Contact-dependent inhibition of EGFR signaling by Nf2/Merlin. *The Journal of Cell Biology* **177** (5), pp.893-903.

D'Este, E., Kamin, D., Balzarotti, F. and Hell, S.W., 2017. Ultrastructural anatomy of nodes of Ranvier in the peripheral nervous system as revealed by STED microscopy. *Proceedings of the National Academy of Sciences* **114** (2), E191-E199.

Da Silva, J.S. and Dotti, C.G., 2002. Breaking the neuronal sphere: regulation of the actin cytoskeleton in neuritogenesis. *Nature Reviews Neuroscience* **3** (9), pp.694-704.

Dai, X., She, P., Chi, F., Feng, Y., Liu, H., Jin, D., Zhao, Y., Guo, X., Jiang, D., Guan, K.L. and Zhong, T.P., 2013. Phosphorylation of angiomotin by Lats1/2 kinases inhibits F-actin

binding, cell migration and angiogenesis. *Journal of Biological Chemistry* **288** (47), pp.34041-34051.

Dancker, P., Löw, I., Hasselbach, W. and Wieland, T., 1975. Interaction of actin with phalloidin: Polymerization and stabilization of F-actin. *Biochimica et Biophysica Acta (BBA)-Protein Structure* **400** (2), pp.407-414.

Dani, A., Huang, B., Bergan, J., Dulac, C. and Zhuang, X., 2010. Superresolution imaging of chemical synapses in the brain. *Neuron* **68** (5), pp.843-856.

Das, T., Safferling, K., Rausch, S., Grabe, N., Boehm, H. and Spatz, J.P., 2015. A molecular mechanotransduction pathway regulates collective migration of epithelial cells. *Nature Cell Biology* **17** (3), pp.276-287.

Davenport, R.J., Wuite, G.J., Landick, R. and Bustamante, C., 2000. Single-molecule study of transcriptional pausing and arrest by E. coli RNA polymerase. *Science* **287** (5462), pp.2497-2500.

de Duve, C., 1971. Tissue fraction-past and present. *The Journal of Cell Biology* **50** (1), 20D-55D.

dela Paz, N.G., Melchior, B. and Frangos, J.A., 2017. Shear stress induces Gαq/11 activation independently of G protein-coupled receptor activation in endothelial cells. *American Journal of Physiology-Cell Physiology* **312** (4), C428-C437.

Demmerle, J., Innocent, C., North, A.J., Ball, G., Müller, M., Miron, E., Matsuda, A., Dobbie, I.M., Markaki, Y. and Schermelleh, L., 2017. Strategic and practical guidelines for successful structured illumination microscopy. *Nature Protocols* **12** (5), pp.988-1010.

Denk, W., Strickler, J.H. and Webb, W.W., 1990. Two-photon laser scanning fluorescence microscopy. *Science* **248** (4951), pp.73-76.

DeRan, M., Yang, J., Shen, C.H., Peters, E.C., Fitamant, J., Chan, P., Hsieh, M., Zhu, S., Asara, J.M., Zheng, B. and Bardeesy, N., 2014. Energy stress regulates hippo-YAP signaling involving AMPK-mediated regulation of angiomotin-like 1 protein. *Cell Reports* **9** (2), pp.495-503.

Dholakia, K., Reece, P. and Gu, M., 2008. Optical micromanipulation. *Chemical Society Reviews* **37** (1), pp.42-55.

Diekmann, R., Wolfson, D.L., Spahn, C., Heilemann, M., Schüttpelz, M. and Huser, T., 2016. Nanoscopy of bacterial cells immobilized by holographic optical tweezers. *Nature Communications* **7**, 13711.

Dong, B., Yang, X., Zhu, S., Bassham, D.C. and Fang, N., 2015. Stochastic optical reconstruction microscopy imaging of microtubule arrays in intact Arabidopsis thaliana seedling roots. *Scientific Reports* **5**, 15694.

Dong, J., Feldmann, G., Huang, J., Wu, S., Zhang, N., Comerford, S.A., Gayyed, M.F., Anders, R.A., Maitra, A. and Pan, D., 2007. Elucidation of a universal size-control mechanism in Drosophila and mammals. *Cell* **130** (6), pp.1120-1133.

Dumbauld, D.W., Lee, T.T., Singh, A., Scrimgeour, J., Gersbach, C.A., Zamir, E.A., Fu, J., Chen, C.S., Curtis, J.E., Craig, S.W. and García, A.J., 2013. How vinculin regulates force transmission. *Proceedings of the National Academy of Sciences* **110** (24), pp.9788-9793.

Dupont, S., Morsut, L., Aragona, M., Enzo, E., Giulitti, S., Cordenonsi, M., Zanconato, F., Le Digabel, J., Forcato, M., Bicciato, S. and Elvassore, N., 2011. Role of YAP/TAZ in mechanotransduction. *Nature* **474** (7350), pp.179-183.

Dwane, S., Durack, E. and Kiely, P.A., 2013. Optimising parameters for the differentiation of SH-SY5Y cells to study cell adhesion and cell migration. *BMC Research Notes* **6**, 366.

Dyba, M. and Hell, S.W., 2002. Focal spots of size λ/23 open up far-field florescence microscopy at 33 nm axial resolution. *Physical Review Letters* **88** (16), 163901.

Edwards, M., Zwolak, A., Schafer, D.A., Sept, D., Dominguez, R. and Cooper, J.A., 2014. Capping protein regulators fine-tune actin assembly dynamics. *Nature Reviews Molecular Cell Biology* **15** (10), pp.677-689.

Elosegui-Artola, A., Andreu, I., Beedle, A.E., Lezamiz, A., Uroz, M., Kosmalska, A.J., Oria, R., Kechagia, J.Z., Rico-Lastres, P., Le Roux, A.L. and Shanahan, C.M., 2017. Force triggers YAP nuclear entry by regulating transport across nuclear pores. *Cell* **171** (6), pp.1397-1410.

Elsum, I.A., Martin, C. and Humbert, P.O., 2013. Scribble regulates an EMT–polarity pathway through modulation of MAPK-ERK signaling to mediate junction formation. *Journal of Cell Science* **126** (17), pp.3990-3999.

Encinas, M., Iglesias, M., Liu, Y., Wang, H., Muhaisen, A., Cena, V., Gallego, C. and Comella, J.X., 2000. Sequential treatment of SH-SY5Y cells with retinoic acid and brain-derived

neurotrophic factor gives rise to fully differentiated, neurotrophic factor-dependent, human neuron-like cells. *Journal of Neurochemistry* **75** (3), pp.991-1003.

Engler, A.J., Sen, S., Sweeney, H.L. and Discher, D.E., 2006. Matrix elasticity directs stem cell lineage specification. *Cell* **126** (4), pp.677-689.

Ernkvist, M., Aase, K., Ukomadu, C., Wohlschlegel, J., Blackman, R., Veitonmäki, N., Bratt, A., Dutta, A. and Holmgren, L., 2006. p130-Angiomotin associates to actin and controls endothelial cell shape. *The FEBS Journal* **273** (9), pp.2000-2011.

Fällman, E. and Axner, O., 1997. Design for fully steerable dual-trap optical tweezers. *Applied Optics* **36** (10), pp.2107-2113.

Fan, F., He, Z., Kong, L.L., Chen, Q., Yuan, Q., Zhang, S., Ye, J., Liu, H., Sun, X., Geng, J. and Yuan, L., 2016. Pharmacological targeting of kinases MST1 and MST2 augments tissue repair and regeneration. *Science Translational Medicine* **8** (352), 352ra108.

Faxen, H., 1922. Der Widerstand gegen die Bewegung einer starren Kugel in einer zähen Flüssigkeit, die zwischen zwei parallelen ebenen Wänden eingeschlossen ist. *Annalen der Physik* **373** (10), pp.89-119.

Felgner, H., Müller, O. and Schliwa, M., 1995. Calibration of light forces in optical tweezers. *Applied Optics* **34** (6), pp.977-982.

Feng, X., Degese, M.S., Iglesias-Bartolome, R., Vaque, J.P., Molinolo, A.A., Rodrigues, M., Zaidi, M.R., Ksander, B.R., Merlino, G., Sodhi, A. and Chen, Q., 2014. Hippo-independent activation of YAP by the GNAQ uveal melanoma oncogene through a trio-regulated rho GTPase signaling circuitry. *Cancer Cell* **25** (6), pp.831-845.

Fernández, B.G., Gaspar, P., Brás-Pereira, C., Jezowska, B., Rebelo, S.R. and Janody, F., 2011. Actin-Capping Protein and the Hippo pathway regulate F-actin and tissue growth in Drosophila. *Development* **138** (11), pp.2337-2346.

Fernandez, S.M. and Berlin, R.D., 1976. Cell surface distribution of lectin receptors determined by resonance energy transfer. *Nature* **264** (5585), pp.411-415.

Fievet, B.T., Gautreau, A., Roy, C., Del Maestro, L., Mangeat, P., Louvard, D. and Arpin, M., 2004. Phosphoinositide binding and phosphorylation act sequentially in the activation mechanism of ezrin. *The Journal of Cell Biology* **164** (5), pp.653-659.

Finer, J.T., Mehta, A.D. and Spudich, J.A., 1995. Characterization of single actin-myosin interactions. *Biophysical Journal* **68** (4 Suppl), 291S-297S.

Fiolka, R., Shao, L., Rego, E.H., Davidson, M.W. and Gustafsson, M.G., 2012. Time-lapse two-color 3D imaging of live cells with doubled resolution using structured illumination. *Proceedings of the National Academy of Sciences* **109** (14), pp.5311-5315.

Flaiz, C., Utermark, T., Parkinson, D.B., Poetsch, A. and Hanemann, C.O., 2008. Impaired intercellular adhesion and immature adherens junctions in merlin-deficient human primary schwannoma cells. *Glia* **56** (5), pp.506-515.

Fletcher, D.A. and Mullins, R.D., 2010. Cell mechanics and the cytoskeleton. *Nature* **463** (7280), p.485-492.

Florin, E.L., Pralle, A., Stelzer, E.H.K. and Hörber, J.K.H., 1998. Photonic force microscope calibration by thermal noise analysis. *Applied Physics A: Materials Science & Processing* **66** (Suppl 1), S75-S78.

Frantz, C., Stewart, K.M. and Weaver, V.M., 2010. The extracellular matrix at a glance. *Journal of Cell Science* **123** (24), pp.4195-4200.

Fu, J., Wang, Y.K., Yang, M.T., Desai, R.A., Yu, X., Liu, Z. and Chen, C.S., 2010. Mechanical regulation of cell function with geometrically modulated elastomeric substrates. *Nature Methods* **7** (9), p.733-736.

Furukawa, K.T., Yamashita, K., Sakurai, N. and Ohno, S., 2017. The epithelial circumferential actin belt regulates YAP/TAZ through nucleocytoplasmic shuttling of merlin. *Cell Reports* **20** (6), pp.1435-1447.

Gailite, I., Aerne, B.L. and Tapon, N., 2015. Differential control of Yorkie activity by LKB1/AMPK and the Hippo/Warts cascade in the central nervous system. *Proceedings of the National Academy of Sciences* **112** (37), E5169-5178.

Galan, J.A. and Avruch, J., 2016. MST1/MST2 Protein kinases: regulation and physiologic roles. *Biochemistry* **55** (39), pp.5507-5519.

Gaspar, P. and Tapon, N., 2014. Sensing the local environment: actin architecture and Hippo signalling. *Current Opinion in Cell Biology* **31**, pp.74-83.

Gaspar, P., Holder, M.V., Aerne, B.L., Janody, F. and Tapon, N., 2015. Zyxin antagonizes the FERM protein expanded to couple F-actin and Yorkie-dependent organ growth. *Current Biology* **25** (6), pp.679-689.

Geiger, B., Spatz, J.P. and Bershadsky, A.D., 2009. Environmental sensing through focal adhesions. *Nature Reviews Molecular Cell Biology* **10** (1), pp.21-33.

Genevet, A., Wehr, M.C., Brain, R., Thompson, B.J. and Tapon, N., 2010. Kibra is a regulator of the Salvador/Warts/Hippo signaling network. *Developmental Cell* **18** (2), pp.300-308.

Giepmans, B.N., Adams, S.R., Ellisman, M.H. and Tsien, R.Y., 2006. The fluorescent toolbox for assessing protein location and function. *Science* **312** (5771), pp.217-224.

Gjorevski, N., Sachs, N., Manfrin, A., Giger, S., Bragina, M.E., Ordóñez-Morán, P., Clevers, H. and Lutolf, M.P., 2016. Designer matrices for intestinal stem cell and organoid culture. *Nature* **539** (7630), pp.560-564.

Glantschnig, H., Rodan, G.A. and Reszka, A.A., 2002. Mapping of MST1 kinase sites of phosphorylation activation and autophosphorylation. *Journal of Biological Chemistry* **277** (45), pp.42987-42996.

Gong, R., Hong, A.W., Plouffe, S.W., Zhao, B., Liu, G., Yu, F.X., Xu, Y. and Guan, K.L., 2015. Opposing roles of conventional and novel PKC isoforms in Hippo-YAP pathway regulation. *Cell Research* **25** (8), pp.985-988.

Goulev, Y., Fauny, J.D., Gonzalez-Marti, B., Flagiello, D., Silber, J. and Zider, A., 2008. SCALLOPED interacts with YORKIE, the nuclear effector of the hippo tumor-suppressor pathway in Drosophila. *Current Biology* **18** (6), pp.435-441.

Gronich, N. and Rennert, G., 2013. Beyond aspirin—cancer prevention with statins, metformin and bisphosphonates. *Nature Reviews Clinical Oncology* **10** (11), pp.625-642.

Grzeschik, N.A., Parsons, L.M., Allott, M.L., Harvey, K.F. and Richardson, H.E., 2010. Lgl, aPKC, and Crumbs regulate the Salvador/Warts/Hippo pathway through two distinct mechanisms. *Current Biology* **20** (7), pp.573-581.

Guck, J., Ananthakrishnan, R., Mahmood, H., Moon, T.J., Cunningham, C.C. and Käs, J., 2001. The optical stretcher: a novel laser tool to micromanipulate cells. *Biophysical Journal* **81** (2), pp.767-784.

Guck, J., Schinkinger, S., Lincoln, B., Wottawah, F., Ebert, S., Romeyke, M., Lenz, D., Erickson, H.M., Ananthakrishnan, R., Mitchell, D. and Käs, J., 2005. Optical deformability as an inherent cell marker for testing malignant transformation and metastatic competence. *Biophysical Journal* **88** (5), pp.3689-3698.

Gunn-Moore, F.J., Welsh, G.I., Herron, L.R., Brannigan, F., Venkateswarlu, K., Gillespie, S., Brandwein-Gensler, M., Madan, R., Tavaré, J.M., Brophy, P.J. and Prystowsky, M.B., 2005. A novel 4.1 ezrin radixin moesin (FERM)-containing protein, 'Willin'. *FEBS Letters* **579** (22), pp.5089-5094.

Gustafsson, M.G., Agard, D.A. and Sedat, J.W., 1999. I5M: 3D widefield light microscopy with better than 100nm axial resolution. *Journal of Microscopy* **195** (1), pp.10-16.

Gustafsson, M.G., 2000. Surpassing the lateral resolution limit by a factor of two using structured illumination microscopy. *Journal of Microscopy* **198** (2), pp.82-87.

Gustafsson, M.G., Agard, D.A. and Sedat, J.W., 2000. Doubling the lateral resolution of wide-field fluorescence microscopy using structured illumination. *Three-Dimensional and Multidimensional Microscopy: Image Acquisition Processing VII* Proc. SPIE **3919**, pp.141-151.

Gustafsson, M.G., 2005. Nonlinear structured-illumination microscopy: wide-field fluorescence imaging with theoretically unlimited resolution. *Proceedings of the National Academy of Sciences* **102** (37), pp.13081-13086.

Gustafsson, M.G., Shao, L., Carlton, P.M., Wang, C.R., Golubovskaya, I.N., Cande, W.Z., Agard, D.A. and Sedat, J.W., 2008. Three-dimensional resolution doubling in wide-field fluorescence microscopy by structured illumination. *Biophysical Journal* **94** (12), pp.4957-4970.

Gustafsson, N., Culley, S., Ashdown, G., Owen, D.M., Pereira, P.M. and Henriques, R., 2016. Fast live-cell conventional fluorophore nanoscopy with ImageJ through super-resolution radial fluctuations. *Nature Communications* **7**, 12471.

Hall, A., 1998. Rho GTPases and the actin cytoskeleton. *Science* **279** (5350), pp.509-514.

Hamaratoglu, F., Willecke, M., Kango-Singh, M., Nolo, R., Hyun, E., Tao, C., Jafar-Nejad, H. and Halder, G., 2006. The tumour-suppressor genes NF2/Merlin and Expanded act through

Hippo signalling to regulate cell proliferation and apoptosis. *Nature Cell Biology* **8** (1), pp.27-36.

Han, X., Li, P., Yang, Z., Huang, X., Wei, G., Sun, Y., Kang, X., Hu, X., Deng, Q., Chen, L. and He, A., 2017. Zyxin regulates endothelial von Willebrand factor secretion by reorganizing actin filaments around exocytic granules. *Nature Communications* **8**, 14639.

Hanahan, D. and Weinberg, R.A., 2011. Hallmarks of cancer: the next generation. *Cell* **144** (5), pp.646-674.

Hansen, C.G., Moroishi, T. and Guan, K.L., 2015. YAP and TAZ: a nexus for Hippo signaling and beyond. *Trends in Cell Biology* **25** (9), pp.499-513.

Harris, A.R., Jreij, P. and Fletcher, D.A., 2018. Mechanotransduction by the Actin Cytoskeleton: Converting Mechanical Stimuli into Biochemical Signals. *Annual Review of Biophysics* **47**, pp.617-631.

Harris, T.J. and Tepass, U., 2010. Adherens junctions: from molecules to morphogenesis. *Nature reviews Molecular Cell Biology* **11** (7), pp.502-514.

Harvey, K.F., Pfleger, C.M. and Hariharan, I.K., 2003. The Drosophila Mst ortholog, hippo, restricts growth and cell proliferation and promotes apoptosis. *Cell* **114** (4), pp.457-467.

Harvey, K. and Tapon, N., 2007. The Salvador–Warts–Hippo pathway—an emerging tumour-suppressor network. *Nature Reviews Cancer* **7** (3), pp.182-191.

Harvey, K.F., Zhang, X. and Thomas, D.M., 2013. The Hippo pathway and human cancer. *Nature Reviews Cancer* **13** (4), pp.246-257.

Hayashi, S. and Okada, Y., 2015. Ultrafast superresolution fluorescence imaging with spinning disk confocal microscope optics. *Molecular Biology of the Cell* **26** (9), pp.1743-1751.

Heilemann, M., Van De Linde, S., Schüttpelz, M., Kasper, R., Seefeldt, B., Mukherjee, A., Tinnefeld, P. and Sauer, M., 2008. Subdiffraction-resolution fluorescence imaging with conventional fluorescent probes. *Angewandte Chemie International Edition* **47** (33), pp.6172-6176.

Heintzmann, R. and Huser, T., 2017. Super-resolution structured illumination microscopy. *Chemical Reviews* **117** (23), pp.13890-13908.

Hell, S. and Stelzer, E.H., 1992. Fundamental improvement of resolution with a 4Pi-confocal fluorescence microscope using two-photon excitation. *Optics Communications* **93** (5-6), pp.277-282.

Hell, S.W. and Wichmann, J., 1994. Breaking the diffraction resolution limit by stimulated emission: stimulated-emission-depletion fluorescence microscopy. *Optics Letters* **19** (11), pp.780-782.

Hell, S.W., 2007. Far-field optical nanoscopy. *Science* **316** (5828), pp.1153-1158.

Heller, I., Sitters, G., Broekmans, O.D., Farge, G., Menges, C., Wende, W., Hell, S.W., Peterman, E.J. and Wuite, G.J., 2013. STED nanoscopy combined with optical tweezers reveals protein dynamics on densely covered DNA. *Nature Methods* **10** (9), pp.910-916.

Helmchen, F. and Denk, W., 2005. Deep tissue two-photon microscopy. *Nature Methods* **2** (12), pp.932-940.

Hergovich, A., Schmitz, D. and Hemmings, B.A., 2006. The human tumour suppressor LATS1 is activated by human MOB1 at the membrane. *Biochemical and Biophysical Research Communications* **345** (1), pp.50-58.

Hess, S.T., Girirajan, T.P. and Mason, M.D., 2006. Ultra-high resolution imaging by fluorescence photoactivation localization microscopy. *Biophysical Journal* **91** (11), pp.4258-4272.

Hilman, D. and Gat, U., 2011. The evolutionary history of YAP and the hippo/YAP pathway. *Molecular Biology and Evolution* **28** (8), pp.2403-2417.

Hindley, C.J., Condurat, A.L., Menon, V., Thomas, R., Azmitia, L.M., Davis, J.A. and Pruszak, J., 2016. The Hippo pathway member YAP enhances human neural crest cell fate and migration. *Scientific Reports* **6**, 23208.

Hirate, Y. and Sasaki, H., 2014. The role of angiomotin phosphorylation in the Hippo pathway during preimplantation mouse development. *Tissue Barriers* **2** (1), pp.1181-94.

Hoffmann, A., zu Hörste, G.M., Pilarczyk, G., Monajembashi, S., Uhl, V. and Greulich, K.O., 2000. Optical tweezers for confocal microscopy. *Applied Physics B: Lasers and Optics* **71** (5), pp.747-753.

Hofmann, M., Eggeling, C., Jakobs, S. and Hell, S.W., 2005. Breaking the diffraction barrier in fluorescence microscopy at low light intensities by using reversibly photoswitchable proteins. *Proceedings of the National Academy of Sciences* **102** (49), pp.17565-17569.

Holzinger, A., 2009. Jasplakinolide: an actin-specific reagent that promotes actin polymerization. *Methods in Molecular Biology* **586**, pp.71-87.

Hong, J.H., Hwang, E.S., McManus, M.T., Amsterdam, A., Tian, Y., Kalmukova, R., Mueller, E., Benjamin, T., Spiegelman, B.M., Sharp, P.A. and Hopkins, N., 2005. TAZ, a transcriptional modulator of mesenchymal stem cell differentiation. *Science* **309** (5737), pp.1074-1078.

Houston, W.V., 1927. A compound interferometer for fine structure work. *Physical Review* **29** (3), pp.478-484.

Hsieh, H.J., Liu, C.A., Huang, B., Tseng, A.H. and Wang, D.L., 2014. Shear-induced endothelial mechanotransduction: the interplay between reactive oxygen species (ROS) and nitric oxide (NO) and the pathophysiological implications. *Journal of Biomedical Science* **21**, 3.

Hua, Y., Sinha, R., Thiel, C.S., Schmidt, R., Hüve, J., Martens, H., Hell, S.W., Egner, A. and Klingauf, J., 2011. A readily retrievable pool of synaptic vesicles. *Nature Neuroscience* **14** (7), pp.833-839.

Huang, B., Bates, M. and Zhuang, X., 2009. Super-resolution fluorescence microscopy. *Annual Review of Biochemistry* **78**, pp.993-1016.

Huang, B., Babcock, H. and Zhuang, X., 2010. Breaking the diffraction barrier: super-resolution imaging of cells. *Cell* **143** (7), pp.1047-1058.

Huang, J., Wu, S., Barrera, J., Matthews, K. and Pan, D., 2005. The Hippo signaling pathway coordinately regulates cell proliferation and apoptosis by inactivating Yorkie, the Drosophila Homolog of YAP. *Cell* **122** (3), pp.421-434.

Huber, L.A., Pfaller, K. and Vietor, I., 2003. Organelle proteomics: implications for subcellular fractionation in proteomics. *Circulation Research* **92** (9), pp.962-968.

Imajo, M., Miyatake, K., Iimura, A., Miyamoto, A. and Nishida, E., 2012. A molecular mechanism that links Hippo signalling to the inhibition of Wnt/β-catenin signalling. *The EMBO Journal* **31** (5), pp.1109-1122.

Imsirovic, J., Wellman, T.J., Mondoñedo, J.R., Bartolák-Suki, E. and Suki, B., 2015. Design of a novel Equi-Biaxial stretcher for live cellular and subcellular imaging. *PloS ONE* **10** (10), e0140283.

Irvine, K.D. and Harvey, K.F., 2015. Control of organ growth by patterning and hippo signaling in Drosophila. *Cold Spring Harbor Perspectives in Biology* **7** (6), a019224.

Ishiuchi, T. and Takeichi, M., 2011. Willin and Par3 cooperatively regulate epithelial apical constriction through aPKC-mediated ROCK phosphorylation. *Nature Cell Biology* **13** (7), pp.860-866.

Ishiuchi, T. and Takeichi, M., 2012. Nectins localize Willin to cell–cell junctions. *Genes to Cells* **17** (5), pp.387-397.

Jaalouk, D.E. and Lammerding, J., 2009. Mechanotransduction gone awry. *Nature Reviews Molecular Cell Biology* **10** (1), pp.63-73.

Jia, J., Zhang, W., Wang, B., Trinko, R. and Jiang, J., 2003. The Drosophila Ste20 family kinase dMST functions as a tumor suppressor by restricting cell proliferation and promoting apoptosis. *Genes & Development* **17** (20), pp.2514-2519.

Jiao, S., Wang, H., Shi, Z., Dong, A., Zhang, W., Song, X., He, F., Wang, Y., Zhang, Z., Wang, W. and Wang, X., 2014. A peptide mimicking VGLL4 function acts as a YAP antagonist therapy against gastric cancer. *Cancer Cell* **25** (2), pp.166-180.

Jungmann, R., Steinhauer, C., Scheible, M., Kuzyk, A., Tinnefeld, P. and Simmel, F.C., 2010. Single-molecule kinetics and super-resolution microscopy by fluorescence imaging of transient binding on DNA origami. *Nano Letters* **10** (11), pp.4756-4761.

Jungmann, R., Avendaño, M.S., Woehrstein, J.B., Dai, M., Shih, W.M. and Yin, P., 2014. Multiplexed 3D cellular super-resolution imaging with DNA-PAINT and Exchange-PAINT. *Nature Methods* **11** (3), pp.313-318.

Justice, R.W., Zilian, O., Woods, D.F., Noll, M. and Bryant, P.J., 1995. The Drosophila tumor suppressor gene warts encodes a homolog of human myotonic dystrophy kinase and is required for the control of cell shape and proliferation. *Genes & Development* **9** (5), pp.534-546.

Kaan, H.Y.K., Chan, S.W., Tan, S.K.J., Guo, F., Lim, C.J., Hong, W. and Song, H., 2017. Crystal structure of TAZ-TEAD complex reveals a distinct interaction mode from that of YAP-TEAD complex. *Scientific Reports* **7** (1), 2035.

Kamble, H., Barton, M.J., Jun, M., Park, S. and Nguyen, N.T., 2016. Cell stretching devices as research tools: engineering and biological considerations. *Lab on a Chip* **16** (17), pp.3193-3203.

Kanchanawong, P., Shtengel, G., Pasapera, A.M., Ramko, E.B., Davidson, M.W., Hess, H.F. and Waterman, C.M., 2010. Nanoscale architecture of integrin-based cell adhesions. *Nature* **468** (7323), pp.580-584.

Kango-Singh, M., Nolo, R., Tao, C., Verstreken, P., Hiesinger, P.R., Bellen, H.J. and Halder, G., 2002. Shar-pei mediates cell proliferation arrest during imaginal disc growth in Drosophila. *Development* **129** (24), pp.5719-5730.

Karimi, A., Yazdi, S. and Ardekani, A.M., 2013. Hydrodynamic mechanisms of cell and particle trapping in microfluidics. *Biomicrofluidics* **7** (2), 021501.

Karpowicz, P., Perez, J. and Perrimon, N., 2010. The Hippo tumor suppressor pathway regulates intestinal stem cell regeneration. *Development* **137** (24), pp.4135-4145.

Khatibzadeh, N., Stilgoe, A.B., Bui, A.A., Rocha, Y., Cruz, G.M., Loke, V., Shi, L.Z., Nieminen, T.A., Rubinsztein-Dunlop, H. and Berns, M.W., 2014. Determination of motility forces on isolated chromosomes with laser tweezers. *Scientific Reports* **4**, 6866.

Kim, K.M., Choi, Y.J., Hwang, J.H., Kim, A.R., Cho, H.J., Hwang, E.S., Park, J.Y., Lee, S.H. and Hong, J.H., 2014. Shear stress induced by an interstitial level of slow flow increases the osteogenic differentiation of mesenchymal stem cells through TAZ activation. *PloS ONE* **9** (3), e92427.

Kim, N., Stiegler, A.L., Cameron, T.O., Hallock, P.T., Gomez, A.M., Huang, J.H., Hubbard, S.R., Dustin, M.L. and Burden, S.J., 2008. Lrp4 is a receptor for Agrin and forms a complex with MuSK. *Cell* **135** (2), pp.334-342.

Kim, N.G., Koh, E., Chen, X. and Gumbiner, B.M., 2011. E-cadherin mediates contact inhibition of proliferation through Hippo signaling-pathway components. *Proceedings of the National Academy of Sciences* **108** (29), pp.11930-11935.

Kim, N.G. and Gumbiner, B.M., 2015. Adhesion to fibronectin regulates Hippo signaling via the FAK–Src–PI3K pathway. *The Journal of Cell Biology* **210** (3), pp.503-515.

Kissil, J.L., Johnson, K.C., Eckman, M.S. and Jacks, T., 2002. Merlin phosphorylation by p21-activated kinase 2 and effects of phosphorylation on merlin localization. *Journal of Biological Chemistry* **277** (12), pp.10394-10399.

Klar, T.A. and Hell, S.W., 1999. Subdiffraction resolution in far-field fluorescence microscopy. *Optics Letters* **24** (14), pp.954-956.

Klar, T.A., Jakobs, S., Dyba, M., Egner, A. and Hell, S.W., 2000. Fluorescence microscopy with diffraction resolution barrier broken by stimulated emission. *Proceedings of the National Academy of Sciences* **97** (15), pp.8206-8210.

Koontz, L.M., Liu-Chittenden, Y., Yin, F., Zheng, Y., Yu, J., Huang, B., Chen, Q., Wu, S. and Pan, D., 2013. The Hippo effector Yorkie controls normal tissue growth by antagonizing scalloped-mediated default repression. *Developmental Cell* **25** (4), pp.388-401.

Kovalevich, J. and Langford, D., 2013. Considerations for the use of SH-SY5Y neuroblastoma cells in neurobiology. *Methods in Molecular Biology* **1078**, pp. 9-21.

Kronenberg, N.M., Liehm, P., Steude, A., Knipper, J.A., Borger, J.G., Scarcelli, G., Franze, K., Powis, S.J. and Gather, M.C., 2017. Long-term imaging of cellular forces with high precision by elastic resonator interference stress microscopy. *Nature Cell Biology* **19** (7), pp.864-872.

Kuroda, M., Wada, H., Kimura, Y., Ueda, K. and Kioka, N., 2017. Vinculin promotes nuclear localization of TAZ to inhibit ECM stiffness-dependent differentiation into adipocytes. *Journal of Cell Science* **130** (5), pp.989-1002.

Labouesse, C., Gabella, C., Meister, J.J., Vianay, B. and Verkhovsky, A.B., 2016. Microsurgery-aided in-situ force probing reveals extensibility and viscoelastic properties of individual stress fibers. *Scientific Reports* **6**, 23722.

Lai, Z.C., Wei, X., Shimizu, T., Ramos, E., Rohrbaugh, M., Nikolaidis, N., Ho, L.L. and Li, Y., 2005. Control of cell proliferation and apoptosis by mob as tumor suppressor, mats. *Cell* **120** (5), pp.675-685.

Laine, R.F., Albecka, A., Van De Linde, S., Rees, E.J., Crump, C.M. and Kaminski, C.F., 2015. Structural analysis of herpes simplex virus by optical super-resolution imaging. *Nature Communications* **6**, 5980.

Lakadamyali, M., Babcock, H., Bates, M., Zhuang, X. and Lichtman, J., 2012. 3D multicolor super-resolution imaging offers improved accuracy in neuron tracing. *PloS ONE* **7** (1), e30826.

Lallemand, D., Curto, M., Saotome, I., Giovannini, M. and McClatchey, A.I., 2003. NF2 deficiency promotes tumorigenesis and metastasis by destabilizing adherens junctions. *Genes & Development* **17** (9), pp.1090-1100.

Lam, W.A., Cao, L., Umesh, V., Keung, A.J., Sen, S. and Kumar, S., 2010. Extracellular matrix rigidity modulates neuroblastoma cell differentiation and N-myc expression. *Molecular Cancer* **9**, 35.

Lapi, E., Di Agostino, S., Donzelli, S., Gal, H., Domany, E., Rechavi, G., Pandolfi, P.P., Givol, D., Strano, S., Lu, X. and Blandino, G., 2008. PML, YAP, and p73 are components of a proapoptotic autoregulatory feedback loop. *Molecular Cell* **32** (6), pp.803-814.

Lauffenburger, D.A. and Horwitz, A.F., 1996. Cell migration: a physically integrated molecular process. *Cell* **84** (3), pp.359-369.

Lee, H.J., Diaz, M.F., Price, K.M., Ozuna, J.A., Zhang, S., Sevick-Muraca, E.M., Hagan, J.P. and Wenzel, P.L., 2017. Fluid shear stress activates YAP1 to promote cancer cell motility. *Nature Communications* **8**, 14122.

Lehtinen, M.K., Yuan, Z., Boag, P.R., Yang, Y., Villén, J., Becker, E.B., DiBacco, S., de la Iglesia, N., Gygi, S., Blackwell, T.K. and Bonni, A., 2006. A conserved MST-FOXO signaling pathway mediates oxidative-stress responses and extends life span. *Cell* **125** (5), pp.987-1001.

Lei, M., Li, Z., Yan, S., Yao, B., Dan, D., Qi, Y., Qian, J., Yang, Y., Gao, P. and Ye, T., 2013. Long-distance axial trapping with focused annular laser beams. *PLoS One* **8** (3), e57984.

Lei, Q.Y., Zhang, H., Zhao, B., Zha, Z.Y., Bai, F., Pei, X.H., Zhao, S., Xiong, Y. and Guan, K.L., 2008. TAZ promotes cell proliferation and epithelial-mesenchymal transition and is inhibited by the hippo pathway. *Molecular and Cellular Biology* **28** (7), pp.2426-2436.

Levine, E.M., Becker, Y., Boone, C.W. and Eagle, H., 1965. Contact inhibition, macromolecular synthesis, and polyribosomes in cultured human diploid fibroblasts. *Proceedings of the National Academy of Sciences* **53** (2), pp.350-356.

Levy, D., Adamovich, Y., Reuven, N. and Shaul, Y., 2008. Yap1 phosphorylation by c-Abl is a critical step in selective activation of proapoptotic genes in response to DNA damage. *Molecular Cell* **29** (3), pp.350-361.

Li, D., Shao, L., Chen, B.C., Zhang, X., Zhang, M., Moses, B., Milkie, D.E., Beach, J.R., Hammer, J.A., Pasham, M. and Kirchhausen, T., 2015b. Extended-resolution structured illumination imaging of endocytic and cytoskeletal dynamics. *Science* **349** (6251), aab3500.

Li, J., Lykotrafitis, G., Dao, M. and Suresh, S., 2007. Cytoskeletal dynamics of human erythrocyte. *Proceedings of the National Academy of Sciences* **104** (12), pp.4937-4942.

Li, W., You, L., Cooper, J., Schiavon, G., Pepe-Caprio, A., Zhou, L., Ishii, R., Giovannini, M., Hanemann, C.O., Long, S.B. and Erdjument-Bromage, H., 2010. Merlin/NF2 suppresses tumorigenesis by inhibiting the E3 ubiquitin ligase CRL4 DCAF1 in the nucleus. *Cell* **140** (4), pp.477-490.

Li, W., Cooper, J., Zhou, L., Yang, C., Erdjument-Bromage, H., Zagzag, D., Snuderl, M., Ladanyi, M., Hanemann, C.O., Zhou, P. and Karajannis, M.A., 2014. Merlin/NF2 loss-driven tumorigenesis linked to CRL4 DCAF1-mediated inhibition of the Hippo pathway kinases Lats1 and 2 in the nucleus. *Cancer Cell* **26** (1), pp.48-60.

Li, Y., Zhou, H., Li, F., Chan, S.W., Lin, Z., Wei, Z., Yang, Z., Guo, F., Lim, C.J., Xing, W. and Shen, Y., 2015a. Angiomotin binding-induced activation of Merlin/NF2 in the Hippo pathway. *Cell Research* **25** (7), p.801-817.

Lian, I., Kim, J., Okazawa, H., Zhao, J., Zhao, B., Yu, J., Chinnaiyan, A., Israel, M.A., Goldstein, L.S., Abujarour, R. and Ding, S., 2010. The role of YAP transcription coactivator in regulating stem cell self-renewal and differentiation. *Genes & Development* **24** (11), pp.1106-1118.

Liang, X.J., Liu, A.Q., Lim, C.S., Ayi, T.C. and Yap, P.H., 2007. Determining refractive index of single living cell using an integrated microchip. *Sensors and Actuators A: Physical* **133** (2), pp.349-354.

Lim, C.T., Dao, M., Suresh, S., Sow, C.H. and Chew, K.T., 2004. Large deformation of living cells using laser traps. *Acta Materialia* **52** (7), pp.1837-1845.

Lin, S., Wang, D., Iyer, S., Ghaleb, A.M., Shim, H., Yang, V.W., Chun, J. and Yun, C.C., 2009. The absence of LPA 2 attenuates tumor formation in an experimental model of colitis-associated cancer. *Gastroenterology* **136** (5), pp.1711-1720.

Ling, C., Zheng, Y., Yin, F., Yu, J., Huang, J., Hong, Y., Wu, S. and Pan, D., 2010. The apical transmembrane protein Crumbs functions as a tumor suppressor that regulates Hippo signaling

by binding to Expanded. *Proceedings of the National Academy of Sciences* **107** (23), pp.10532-10537.

Liu, C.Y., Zha, Z.Y., Zhou, X., Zhang, H., Huang, W., Zhao, D., Li, T., Chan, S.W., Lim, C.J., Hong, W. and Zhao, S., 2010. The hippo tumor pathway promotes TAZ degradation by phosphorylating a phosphodegron and recruiting the SCFbeta-TrCP E3 ligase. *Journal of Biological Chemistry* **285** (48), pp.37159-37169.

Liu-Chittenden, Y., Huang, B., Shim, J.S., Chen, Q., Lee, S.J., Anders, R.A., Liu, J.O. and Pan, D., 2012. Genetic and pharmacological disruption of the TEAD–YAP complex suppresses the oncogenic activity of YAP. *Genes & Development* **26** (12), pp.1300-1305.

Liu, M., Zhang, Z., Sampson, L., Zhou, X., Nalapareddy, K., Feng, Y., Akunuru, S., Melendez, J., Davis, A.K., Bi, F. and Geiger, H., 2017. RHOA GTPase Controls YAP-Mediated EREG Signaling in Small Intestinal Stem Cell Maintenance. *Stem Cell Reports* **9** (6), pp.1961-1975.

Liu, X., Yang, N., Figel, S.A., Wilson, K.E., Morrison, C.D., Gelman, I.H. and Zhang, J., 2013. PTPN14 interacts with and negatively regulates the oncogenic function of YAP. *Oncogene* **32** (10), pp.1266-1273.

Liu, Z., Guo, C., Yang, J. and Yuan, L., 2006. Tapered fiber optical tweezers for microscopic particle trapping: fabrication and application. *Optics Express* **14** (25), pp.12510-12516.

Livet, J., Weissman, T.A., Kang, H., Draft, R.W., Lu, J., Bennis, R.A., Sanes, J.R. and Lichtman, J.W., 2007. Transgenic strategies for combinatorial expression of fluorescent proteins in the nervous system. *Nature* **450** (7166), p.56-62.

Lodish, H., Berk, A., Zipurksy, S.L., Matsudaira, P., Baltimore, D., Darnell, J., 2000. *Molecular Cell Biology 4th Edition*. New York: W. H. Freeman.

Lv, M., Lv, M., Chen, L., Qin, T., Zhang, X., Liu, P. and Yang, J., 2015. Angiomotin promotes breast cancer cell proliferation and invasion. *Oncology Reports* **33** (4), pp.1938-1946.

Ma, B., Chen, Y., Chen, L., Cheng, H., Mu, C., Li, J., Gao, R., Zhou, C., Cao, L., Liu, J. and Zhu, Y., 2015. Hypoxia regulates Hippo signalling through the SIAH2 ubiquitin E3 ligase. *Nature Cell Biology* **17** (1), pp.95-103.

Ma, B., Cheng, H., Gao, R., Mu, C., Chen, L., Wu, S., Chen, Q. and Zhu, Y., 2016. Zyxin-Siah2–Lats2 axis mediates cooperation between Hippo and TGF-β signalling pathways. *Nature Communications* **7**, 11123.

Madan, R., Brandwein-Gensler, M., Schlecht, N.F., Elias, K., Gorbovitsky, E., Belbin, T.J., Mahmood, R., Breining, D., Qian, H., Childs, G. and Locker, J., 2006. Differential tissue and subcellular expressionof ERM proteins in normal and malignant tissues: cytoplasmic ezrin expression has prognostic signficance for head and neck squamous cell carcinoma. *Head & Neck: Journal for the Sciences and Specialties of the Head and Neck* **28** (11), pp.1018-1027.

Maitra, S., Kulikauskas, R.M., Gavilan, H. and Fehon, R.G., 2006. The tumor suppressors Merlin and Expanded function cooperatively to modulate receptor endocytosis and signaling. *Current Biology* **16** (7), pp.702-709.

Mana-Capelli, S., Paramasivam, M., Dutta, S. and McCollum, D., 2014. Angiomotins link F-actin architecture to Hippo pathway signaling. *Molecular Biology of the Cell* **25** (10), pp.1676-1685.

Mao, A.S. and Mooney, D.J., 2015. Regenerative medicine: current therapies and future directions. *Proceedings of the National Academy of Sciences* **112** (47), pp.14452-14459.

Mao, B., Gao, Y., Bai, Y. and Yuan, Z., 2014. Hippo signaling in stress response and homeostasis maintenance. *Acta Biochimica et Biophysica Sinica* **47** (1), pp.2-9.

Mao, X., Li, P., Wang, Y., Liang, Z., Liu, J., Li, J., Jiang, Y., Bao, G., Li, L., Zhu, B. and Ren, Y., 2017. CRB3 regulates contact inhibition by activating the Hippo pathway in mammary epithelial cells. *Cell Death & Disease* **8** (1), e2546.

Martin-Belmonte, F. and Perez-Moreno, M., 2012. Epithelial cell polarity, stem cells and cancer. *Nature Reviews Cancer* **12** (1), pp.23-38.

Médina, E., Lemmers, C., Lane-Guermonprez, L. and Le Bivic, A., 2002. Role of the Crumbs complex in the regulation of junction formation in Drosophila and mammalian epithelial cells. *Biology of the Cell* **94** (6), pp.305-313.

Meng, Z., Moroishi, T. and Guan, K.L., 2016. Mechanisms of Hippo pathway regulation. *Genes & Development* **30** (1), pp.1-17.

Miller, E., Yang, J., DeRan, M., Wu, C., Su, A.I., Bonamy, G.M., Liu, J., Peters, E.C. and Wu, X., 2012. Identification of serum-derived sphingosine-1-phosphate as a small molecule regulator of YAP. *Chemistry & Biology* **19** (8), pp.955-962.

Mills, J.P., Qie, L., Dao, M., Lim, C.T. and Suresh, S., 2004. Nonlinear elastic and viscoelastic deformation of the human red blood cell with optical tweezers. *Mechanics & Chemistry of Biosystems: MCB* **1** (3) pp.169-180.

Mindos, T., Dun, X.P., North, K., Doddrell, R.D., Schulz, A., Edwards, P., Russell, J., Gray, B., Roberts, S.L., Shivane, A. and Mortimer, G., 2017. Merlin controls the repair capacity of Schwann cells after injury by regulating Hippo/YAP activity. *The Journal of Cell Biology* **216** (2), pp.495-510.

Mizuno, T., Murakami, H., Fujii, M., Ishiguro, F., Tanaka, I., Kondo, Y., Akatsuka, S., Toyokuni, S., Yokoi, K., Osada, H. and Sekido, Y., 2012. YAP induces malignant mesothelioma cell proliferation by upregulating transcription of cell cycle-promoting genes. *Oncogene* **31** (49), pp.5117-5122.

Mo, J.S., Yu, F.X., Gong, R., Brown, J.H. and Guan, K.L., 2012. Regulation of the Hippo–YAP pathway by protease-activated receptors (PARs). *Genes & Development* **26** (19), pp.2138-2143.

Mo, J.S., Meng, Z., Kim, Y.C., Park, H.W., Hansen, C.G., Kim, S., Lim, D.S. and Guan, K.L., 2015. Cellular energy stress induces AMPK-mediated regulation of YAP and the Hippo pathway. *Nature Cell Biology* **17** (4), pp.500-510.

Mohanty, S.K., Mohanty, K. and Berns, M.W., 2008. Manipulation of mammalian cells using a single-fiber optical microbeam. *Journal of Biomedical Optics* **13** (5), 054049.

Mohseni, M., Sun, J., Lau, A., Curtis, S., Goldsmith, J., Fox, V.L., Wei, C., Frazier, M., Samson, O., Wong, K.K. and Kim, C., 2014. A genetic screen identifies an LKB1–MARK signalling axis controlling the Hippo–YAP pathway. *Nature Cell Biology* **16** (1), pp.108-117.

Moleirinho, S., Tilston-Lunel, A., Angus, L., Gunn-Moore, F. and Reynolds, P.A., 2013a. The expanding family of FERM proteins. *Biochemical Journal* **452** (2), pp.183-193.

Moleirinho, S., Patrick, C., Tilston-Lünel, A.M., Higginson, J.R., Angus, L., Antkowiak, M., Barnett, S.C., Prystowsky, M.B., Reynolds, P.A. and Gunn-Moore, F.J., 2013b. Willin, an upstream component of the hippo signaling pathway, orchestrates mammalian peripheral nerve fibroblasts. *PloS ONE* **8** (4), e60028.

Moleirinho, S., Chang, N., Sims, A.H., Tilston-Lünel, A.M., Angus, L., Steele, A., Boswell, V., Barnett, S.C., Ormandy, C., Faratian, D. and Gunn-Moore, F.J., 2013c. KIBRA exhibits

MST-independent functional regulation of the Hippo signaling pathway in mammals. *Oncogene* **32** (14), p.1821-1830.

Mönkemöller, V., Øie, C., Hübner, W., Huser, T. and McCourt, P., 2015. Multimodal super-resolution optical microscopy visualizes the close connection between membrane and the cytoskeleton in liver sinusoidal endothelial cell fenestrations. *Scientific Reports* **5**, 16279.

Mori, T., Gotoh, S., Shirakawa, M. and Hakoshima, T., 2014. Structural basis of DDB 1-and-C ullin 4-associated F actor 1 (DCAF 1) recognition by merlin/NF 2 and its implication in tumorigenesis by CD 44-mediated inhibition of merlin suppression of DCAF 1 function. *Genes to Cells* **19** (8), pp.603-619.

Moroishi, T., Hansen, C.G. and Guan, K.L., 2015. The emerging roles of YAP and TAZ in cancer. *Nature Reviews Cancer* **15** (2), pp.73-79.

Müller, P., Langenbach, A., Kaminski, A. and Rychly, J., 2013. Modulating the actin cytoskeleton affects mechanically induced signal transduction and differentiation in mesenchymal stem cells. *PloS ONE* **8** (7), e71283.

Mundel, P. and Reiser, J., 2010. Proteinuria: an enzymatic disease of the podocyte?. *Kidney International* **77** (7), pp.571-580.

Nair, D., Hosy, E., Petersen, J.D., Constals, A., Giannone, G., Choquet, D. and Sibarita, J.B., 2013. Super-resolution imaging reveals that AMPA receptors inside synapses are dynamically organized in nanodomains regulated by PSD95. *Journal of Neuroscience* **33** (32), pp.13204-13224.

Nardone, G., Oliver-De La Cruz, J., Vrbsky, J., Martini, C., Pribyl, J., Skládal, P., Pešl, M., Caluori, G., Pagliari, S., Martino, F. and Maceckova, Z., 2017. YAP regulates cell mechanics by controlling focal adhesion assembly. *Nature Communications* **8**, 15321.

Neil, M.A., Juškaitis, R. and Wilson, T., 1997. Method of obtaining optical sectioning by using structured light in a conventional microscope. *Optics Letters* **22** (24), pp.1905-1907.

Neuhuber, B., Gallo, G., Howard, L., Kostura, L., Mackay, A. and Fischer, I., 2004. Reevaluation of in vitro differentiation protocols for bone marrow stromal cells: disruption of actin cytoskeleton induces rapid morphological changes and mimics neuronal phenotype. *Journal of Neuroscience Research* **77** (2), pp.192-204.

Neuman, K.C. and Block, S.M., 2004. Optical trapping. *Review of Scientific Instruments* **75** (9), pp.2787-2809.

Ni, L., Zheng, Y., Hara, M., Pan, D. and Luo, X., 2015. Structural basis for Mob1-dependent activation of the core Mst–Lats kinase cascade in Hippo signaling. *Genes & Development* **29** (13), pp.1416-1431.

Norregaard, K., Jauffred, L., Berg-Sørensen, K. and Oddershede, L.B., 2014. Optical manipulation of single molecules in the living cell. *Physical Chemistry Chemical Physics* **16** (25), pp.12614-12624.

Nylk, J., Kristensen, M.V.G., Mazilu, M., Thayil, A.K., Mitchell, C.A., Campbell, E.C., Powis, S.J., Gunn-Moore, F.J. and Dholakia, K., 2015. Development of a graded index microlens based fiber optical trap and its characterization using principal component analysis. *Biomedical Optics Express* **6** (4), pp.1512-1519.

Ohashi, K., Fujiwara, S. and Mizuno, K., 2017. Roles of the cytoskeleton, cell adhesion and rho signalling in mechanosensing and mechanotransduction. *The Journal of Biochemistry* **161** (3), pp.245-254.

Ohgushi, M., Minaguchi, M. and Sasai, Y., 2015. Rho-signaling-directed YAP/TAZ activity underlies the long-term survival and expansion of human embryonic stem cells. *Cell Stem Cell* **17** (4), pp.448-461.

Oka, T., Remue, E., Meerschaert, K., Vanloo, B., Boucherie, C., Gfeller, D., Bader, G.D., Sidhu, S.S., Vandekerckhove, J., Gettemans, J. and Sudol, M., 2010. Functional complexes between YAP2 and ZO-2 are PDZ domain-dependent, and regulate YAP2 nuclear localization and signalling. *Biochemical Journal* **432** (3), pp.461-478.

Oka, T., Schmitt, A.P. and Sudol, M., 2012. Opposing roles of angiomotin-like-1 and zona occludens-2 on pro-apoptotic function of YAP. *Oncogene* **31** (1), pp.128-134.

O'Neil, A.T. and Padgett, M.J., 2001. Axial and lateral trapping efficiency of Laguerre–Gaussian modes in inverted optical tweezers. *Optics Communications* **193** (1-6), pp.45-50.

Onken, M.D., Worley, L.A., Long, M.D., Duan, S., Council, M.L., Bowcock, A.M. and Harbour, J.W., 2008. Oncogenic mutations in GNAQ occur early in uveal melanoma. *Investigative Ophthalmology & Visual Science* **49** (12), pp.5230-5234.

Otto, O., Rosendahl, P., Mietke, A., Golfier, S., Herold, C., Klaue, D., Girardo, S., Pagliara, S., Ekpenyong, A., Jacobi, A. and Wobus, M., 2015. Real-time deformability cytometry: on-the-fly cell mechanical phenotyping. *Nature Methods* **12** (3), pp.199-202.

Overholtzer, M., Zhang, J., Smolen, G.A., Muir, B., Li, W., Sgroi, D.C., Deng, C.X., Brugge, J.S. and Haber, D.A., 2006. Transforming properties of YAP, a candidate oncogene on the chromosome 11q22 amplicon. *Proceedings of the National Academy of Sciences* **103** (33), pp.12405-12410.

Paddock, S.W., 1999. Confocal laser scanning microscopy. *Biotechniques* **27**, pp.992-1007.

Pahakis, M.Y., Kosky, J.R., Dull, R.O. and Tarbell, J.M., 2007. The role of endothelial glycocalyx components in mechanotransduction of fluid shear stress. *Biochemical and Biophysical Research Communications* **355** (1), pp.228-233.

Pan, D., 2010. The hippo signaling pathway in development and cancer. *Developmental Cell* **19** (4), pp.491-505.

Panciera, T., Azzolin, L., Fujimura, A., Di Biagio, D., Frasson, C., Bresolin, S., Soligo, S., Basso, G., Bicciato, S., Rosato, A. and Cordenonsi, M., 2016. Induction of expandable tissue-specific stem/progenitor cells through transient expression of YAP/TAZ. *Cell Stem Cell* **19** (6), pp.725-737.

Pantalacci, S., Tapon, N. and Léopold, P., 2003. The Salvador partner Hippo promotes apoptosis and cell-cycle exit in Drosophila. *Nature Cell Biology* **5** (10), pp.921-927.

Paramasivam, M., Sarkeshik, A., Yates III, J.R., Fernandes, M.J. and McCollum, D., 2011. Angiomotin family proteins are novel activators of the LATS2 kinase tumor suppressor. *Molecular Biology of the Cell* **22** (19), pp.3725-3733.

Parsons, J.T., Horwitz, A.R. and Schwartz, M.A., 2010. Cell adhesion: integrating cytoskeletal dynamics and cellular tension. *Nature Reviews Molecular Cell Biology* **11** (9), pp.633-643.

Patterson, G.H. and Lippincott-Schwartz, J., 2002. A photoactivatable GFP for selective photolabeling of proteins and cells. *Science* **297** (5588), pp.1873-1877.

Pearson, M.A., Reczek, D., Bretscher, A. and Karplus, P.A., 2000. Structure of the ERM protein moesin reveals the FERM domain fold masked by an extended actin binding tail domain. *Cell* **101** (3), pp.259-270.

Perkins, T.T., 2009. Optical traps for single molecule biophysics: a primer. *Laser & Photonics Reviews* **3** (1-2), pp.203-220.

Petrilli, A.M. and Fernández-Valle, C., 2016. Role of Merlin/NF2 inactivation in tumor biology. *Oncogene* **35** (5), pp.537-548.

Piccolo, S., Dupont, S. and Cordenonsi, M., 2014. The biology of YAP/TAZ: hippo signaling and beyond. *Physiological Reviews* **94** (4), pp.1287-1312.

Pinkel, D., Landegent, J., Collins, C., Fuscoe, J., Segraves, R., Lucas, J. and Gray, J., 1988. Fluorescence in situ hybridization with human chromosome-specific libraries: detection of trisomy 21 and translocations of chromosome 4. *Proceedings of the National Academy of Sciences* **85** (23), pp.9138-9142.

Plouffe, S.W., Lin, K.C., Moore, J.L.III, Tan, F.E., Ma, S., Ye, Z., Qiu, Y., Ren, B. and Guan, K.-L., 2018. The Hippo pathway effector proteins YAP and TAZ have both distinct and overlapping functions in the cell. *Journal of Biological Chemistry* RA118.002715.

Polacheck, W.J. and Chen, C.S., 2016. Measuring cell-generated forces: a guide to the available tools. *Nature Methods* **13** (5), pp.415-423.

Pollard, T.D. and Cooper, J.A., 2009. Actin, a central player in cell shape and movement. *Science* **326** (5957), pp.1208-1212.

Poon, C.L., Lin, J.I., Zhang, X. and Harvey, K.F., 2011. The sterile 20-like kinase Tao-1 controls tissue growth by regulating the Salvador-Warts-Hippo pathway. *Developmental Cell* **21** (5), pp.896-906.

Poulin, A., Demir, C.S., Rosset, S., Petrova, T.V. and Shea, H., 2016. Dielectric elastomer actuator for mechanical loading of 2D cell cultures. *Lab on a Chip* **16** (19), pp.3788-3794.

Poulin, A., Imboden, M., Sorba, F., Grazioli, S., Martin-Olmos, C., Rosset, S. and Shea, H., 2018. An ultra-fast mechanically active cell culture substrate. *Scientific Reports* **8** (1), 9895.

Pradhan, M., Pathak, S., Mathur, D. and Ladiwala, U., 2016. Optically trapping tumor cells to assess differentiation and prognosis of cancers. *Biomedical Optics Express* **7** (3), pp.943-948.

Praskova, M., Khoklatchev, A., Ortiz-Vega, S. and Avruch, J., 2004. Regulation of the MST1 kinase by autophosphorylation, by the growth inhibitory proteins, RASSF1 and NORE1, and by Ras. *Biochemical Journal* **381** (2), pp.453-462.

Praskova, M., Xia, F. and Avruch, J., 2008. MOBKL1A/MOBKL1B phosphorylation by MST1 and MST2 inhibits cell proliferation. *Current Biology* **18** (5), pp.311-321.

Prickett, T.D., Wei, X., Cardenas-Navia, I., Teer, J.K., Lin, J.C., Walia, V., Gartner, J., Jiang, J., Cherukuri, P.F., Molinolo, A. and Davies, M.A., 2011. Exon capture analysis of G protein-coupled receptors identifies activating mutations in GRM3 in melanoma. *Nature Genetics* **43** (11), pp.1119-1126.

Pullman, J.M., Nylk, J., Campbell, E.C., Gunn-Moore, F.J., Prystowsky, M.B. and Dholakia, K., 2016. Visualization of podocyte substructure with structured illumination microscopy (SIM): a new approach to nephrotic disease. *Biomedical Optics Express* **7** (2), pp.302-311.

Ranade, S.S., Syeda, R. and Patapoutian, A., 2015. Mechanically activated ion channels. *Neuron* **87** (6), pp.1162-1179.

Ratz, M., Testa, I., Hell, S.W. and Jakobs, S., 2015. CRISPR/Cas9-mediated endogenous protein tagging for RESOLFT super-resolution microscopy of living human cells. *Scientific Reports* **5**, 9592.

Rauskolb, C., Pan, G., Reddy, B.V.V.G., Oh, H. and Irvine, K.D., 2011. Zyxin links fat signaling to the hippo pathway. *PLoS Biology* **9** (6), e1000624.

Rauskolb, C., Sun, S., Sun, G., Pan, Y. and Irvine, K.D., 2014. Cytoskeletal tension inhibits Hippo signaling through an Ajuba-Warts complex. *Cell* **158** (1), pp.143-156.

Rayleigh, L., 1874. XII. On the manufacture and theory of diffraction-gratings. *The London, Edinburgh, and Dublin Philosophical Magazine and Journal of Science* **47** (310), pp.81-93.

Regev-Rudzki, N., Wilson, D.W., Carvalho, T.G., Sisquella, X., Coleman, B.M., Rug, M., Bursac, D., Angrisano, F., Gee, M., Hill, A.F. and Baum, J., 2013. Cell-cell communication between malaria-infected red blood cells via exosome-like vesicles. *Cell* **153** (5), pp.1120-1133.

Rego, E.H., Shao, L., Macklin, J.J., Winoto, L., Johansson, G.A., Kamps-Hughes, N., Davidson, M.W. and Gustafsson, M.G., 2012. Nonlinear structured-illumination microscopy with a photoswitchable protein reveals cellular structures at 50-nm resolution. *Proceedings of the National Academy of Sciences* **109** (3), E135-E143.

Remue, E., Meerschaert, K., Oka, T., Boucherie, C., Vandekerckhove, J., Sudol, M. and Gettemans, J., 2010. TAZ interacts with zonula occludens-1 and-2 proteins in a PDZ-1 dependent manner. *FEBS Letters* **584** (19), pp.4175-4180.

Reya, T., Morrison, S.J., Clarke, M.F. and Weissman, I.L., 2001. Stem cells, cancer, and cancer stem cells. *Nature* **414** (6859), pp.105-111.

Ribeiro, P., Holder, M., Frith, D., Snijders, A.P. and Tapon, N., 2014. Crumbs promotes expanded recognition and degradation by the SCFSlimb/β-TrCP ubiquitin ligase. *Proceedings of the National Academy of Sciences* **111** (19), E1980-1989.

Riedl, J., Crevenna, A.H., Kessenbrock, K., Yu, J.H., Neukirchen, D., Bista, M., Bradke, F., Jenne, D., Holak, T.A., Werb, Z. and Sixt, M., 2008. Lifeact: a versatile marker to visualize F-actin. *Nature Methods* **5** (7), pp.605-607.

Robinson, B.S., Huang, J., Hong, Y. and Moberg, K.H., 2010. Crumbs regulates Salvador/Warts/Hippo signaling in Drosophila via the FERM-domain protein Expanded. *Current Biology* **20** (7), pp.582-590.

Roh, M.H., Makarova, O., Liu, C.J., Lee, S., Laurinec, S., Goyal, M., Wiggins, R. and Margolis, B., 2002. The Maguk protein, Pals1, functions as an adapter, linking mammalian homologues of Crumbs and Discs Lost. *The Journal of Cell Biology* **157** (1), pp.161-172.

Rossberger, S., Best, G., Baddeley, D., Heintzmann, R., Birk, U., Dithmar, S. and Cremer, C., 2013. Combination of structured illumination and single molecule localization microscopy in one setup. *Journal of Optics* **15** (9), 094003.

Rouleau, G.A., Merel, P., Lutchman, M., Sanson, M., Zucman, J., Marineau, C., Hoang-Xuan, K., Demczuk, S., Desmaze, C., Plougastel, B. and Pulst, S.M., 1993. Alteration in a new gene encoding a putative membrane-organizing protein causes neuro-fibromatosis type 2. *Nature* **363** (6429), pp.515-521.

Ruska, E., 1986. Ernst Ruska: Autobiography. *Nobel Foundation*.

Rust, M.J., Bates, M. and Zhuang, X., 2006. Sub-diffraction-limit imaging by stochastic optical reconstruction microscopy (STORM). *Nature Methods* **3** (10), pp.793-796.

Sabass, B., Gardel, M.L., Waterman, C.M. and Schwarz, U.S., 2008. High resolution traction force microscopy based on experimental and computational advances. *Biophysical Journal* **94** (1), pp.207-220.

Sansores-Garcia, L., Bossuyt, W., Wada, K.I., Yonemura, S., Tao, C., Sasaki, H. and Halder, G., 2011. Modulating F-actin organization induces organ growth by affecting the Hippo pathway. *The EMBO Journal* **30** (12), pp.2325-2335.

Sarshar, M., Wong, W. and Anvari, B., 2014. Comparative study of methods to calibrate the stiffness of a single-beam gradient-force optical tweezers over various laser trapping powers. *Journal of Biomedical Optics* **19** (11), 115001.

Sauer, M. and Heilemann, M., 2017. Single-molecule localization microscopy in eukaryotes. *Chemical Reviews* **117** (11), pp.7478-7509.

Saxena, V., 2003. Manipulation Microparticle Polystyrene Microparticles as Handles for Optical Manipulation of CATH.a Cells. Stanford Undergraduate Research Journal **2**, pp.39-42.

Schäffer, E., Nørrelykke, S.F. and Howard, J., 2007. Surface forces and drag coefficients of microspheres near a plane surface measured with optical tweezers. *Langmuir* **23** (7), pp.3654-3665.

Scheel, H. and Hofmann, K., 2003. A novel inter action motif, SARAH, connects three classes of tumor suppressor. *Current Biology* **13** (23), R899-R900.

Schermelleh, L., Carlton, P.M., Haase, S., Shao, L., Winoto, L., Kner, P., Burke, B., Cardoso, M.C., Agard, D.A., Gustafsson, M.G. and Leonhardt, H., 2008. Subdiffraction multicolor imaging of the nuclear periphery with 3D structured illumination microscopy. *Science* **320** (5881), pp.1332-1336.

Schlegelmilch, K., Mohseni, M., Kirak, O., Pruszak, J., Rodriguez, J.R., Zhou, D., Kreger, B.T., Vasioukhin, V., Avruch, J., Brummelkamp, T.R. and Camargo, F.D., 2011. Yap1 acts downstream of α-catenin to control epidermal proliferation. *Cell* **144** (5), pp.782-795.

Schoen, I., Hu, W., Klotzsch, E. and Vogel, V., 2010. Probing cellular traction forces by micropillar arrays: contribution of substrate warping to pillar deflection. *Nano Letters* **10** (5), pp.1823-1830.

Schoenberg, D.R. and Maquat, L.E., 2012. Regulation of cytoplasmic mRNA decay. *Nature Reviews Genetics* **13** (4), pp.246-259.

Schröder, M. and Kaufman, R.J., 2005. ER stress and the unfolded protein response. *Mutation Research* **569** (1-2), pp.29-63.

Schroeder, M.C. and Halder, G., 2012. Regulation of the Hippo pathway by cell architecture and mechanical signals. *Seminars in Cell & Developmental Biology* **23** (7), pp. 803-811.

Schueder, F., Lara-Gutiérrez, J., Beliveau, B.J., Saka, S.K., Sasaki, H.M., Woehrstein, J.B., Strauss, M.T., Grabmayr, H., Yin, P. and Jungmann, R., 2017. Multiplexed 3D super-resolution imaging of whole cells using spinning disk confocal microscopy and DNA-PAINT. *Nature Communications* **8** (1), 2090.

Schwartz, M.A., 2010. Integrins and extracellular matrix in mechanotransduction. *Cold Spring Harbor Perspectives in Biology* **2** (12), a005066.

Schwarz, U.S. and Gardel, M.L., 2012. United we stand–integrating the actin cytoskeleton and cell–matrix adhesions in cellular mechanotransduction. *Journal of Cell Science* **125** (13), pp.3051-3060.

Sekar, R.B. and Periasamy, A., 2003. Fluorescence resonance energy transfer (FRET) microscopy imaging of live cell protein localizations. *The Journal of Cell Biology* **160** (5), pp.629-633.

Serrano, I., McDonald, P.C., Lock, F., Muller, W.J. and Dedhar, S., 2013. Inactivation of the Hippo tumour suppressor pathway by integrin-linked kinase. *Nature Communications* **4**, 2976.

Shao, D., Zhai, P., Del Re, D.P., Sciarretta, S., Yabuta, N., Nojima, H., Lim, D.S., Pan, D. and Sadoshima, J., 2014. A functional interaction between Hippo-YAP signalling and FoxO1 mediates the oxidative stress response. *Nature communications* **5**, 3315.

Sharonov, A. and Hochstrasser, R.M., 2006. Wide-field subdiffraction imaging by accumulated binding of diffusing probes. *Proceedings of the National Academy of Sciences* **103** (50), pp.18911-18916.

Shi, X., Yin, Z., Ling, B., Wang, L., Liu, C., Ruan, X., Zhang, W. and Chen, L., 2017. Rho differentially regulates the Hippo pathway by modulating the interaction between Amot and Nf2 in the blastocyst. *Development* **144** (21), pp.3957-3967.

Shimomura, T., Miyamura, N., Hata, S., Miura, R., Hirayama, J. and Nishina, H., 2014. The PDZ-binding motif of Yes-associated protein is required for its co-activation of TEAD-mediated CTGF transcription and oncogenic cell transforming activity. *Biochemical and Biophysical Research Communications* **443** (3), pp.917-923.

Sidenstein, S.C., D'Este, E., Böhm, M.J., Danzl, J.G., Belov, V.N. and Hell, S.W., 2016. Multicolour multilevel STED nanoscopy of actin/spectrin organization at synapses. *Scientific Reports* **6**, 26725.

Siegerist, F., Ribback, S., Dombrowski, F., Amann, K., Zimmermann, U., Endlich, K. and Endlich, N., 2017. Structured illumination microscopy and automatized image processing as a rapid diagnostic tool for podocyte effacement. *Scientific Reports* **7** (1), 11473.

Sigaut, L., von Bilderling, C., Bianchi, M., Burdisso, J.E., Gastaldi, L. and Pietrasanta, L.I., 2018. Live cell imaging reveals focal adhesions mechanoresponses in mammary epithelial cells under sustained equibiaxial stress. *Scientific Reports* **8** (1), 9788.

Silva, E., Tsatskis, Y., Gardano, L., Tapon, N. and McNeill, H., 2006. The tumor-suppressor gene fat controls tissue growth upstream of expanded in the hippo signaling pathway. *Current Biology* **16** (21), pp.2081-2089.

Sim, J.Y., Borghi, N., Ribeiro, A., Sorokina, M., Shcherbakova, O., Ramallo, D., Dunn, A., Nelson, W.J. and Pruitt, B.L., 2012. Uniaxial cell stretcher enables high resolution live cell imaging. *Micro Electro Mechanical Systems (MEMS), 2012 IEEE 25th International Conference*, pp. 854-857.

Sit, S.T. and Manser, E., 2011. Rho GTPases and their role in organizing the actin cytoskeleton. *Journal of Cell Science* **124** (5), pp.679-683.

Skouloudaki, K., Puetz, M., Simons, M., Courbard, J.R., Boehlke, C., Hartleben, B., Engel, C., Moeller, M.J., Englert, C., Bollig, F. and Schäfer, T., 2009. Scribble participates in Hippo signaling and is required for normal zebrafish pronephros development. *Proceedings of the National Academy of Sciences* **106** (21), pp.8579-8584.

Smith, M.A., Blankman, E., Gardel, M.L., Luettjohann, L., Waterman, C.M. and Beckerle, M.C., 2010. A zyxin-mediated mechanism for actin stress fiber maintenance and repair. *Developmental Cell* **19** (3), pp.365-376.

Song, L., Lu-Walther, H.W., Förster, R., Jost, A., Kielhorn, M., Zhou, J. and Heintzmann, R., 2016. Fast structured illumination microscopy using rolling shutter cameras. *Measurement Science and Technology* **27** (5), 055401.

Sorrentino, G., Ruggeri, N., Specchia, V., Cordenonsi, M., Mano, M., Dupont, S., Manfrin, A., Ingallina, E., Sommaggio, R., Piazza, S. and Rosato, A., 2014. Metabolic control of YAP and TAZ by the mevalonate pathway. *Nature Cell Biology* **16** (4), pp.357-366.

Spesyvtseva, S.E.S. and Dholakia, K., 2016. Trapping in a material world. *ACS Photonics* **3** (5), pp.719-736.

Striedinger, K., VandenBerg, S.R., Baia, G.S., McDermott, M.W., Gutmann, D.H. and Lal, A., 2008. The neurofibromatosis 2 tumor suppressor gene product, merlin, regulates human meningioma cell growth by signaling through YAP. *Neoplasia* **10** (11), pp.1204-1212.

Style, R.W., Boltyanskiy, R., German, G.K., Hyland, C., MacMinn, C.W., Mertz, A.F., Wilen, L.A., Xu, Y. and Dufresne, E.R., 2014. Traction force microscopy in physics and biology. *Soft Matter* **10** (23), pp.4047-4055.

Su, T., Ludwig, M.Z., Xu, J. and Fehon, R.G., 2017. Kibra and merlin activate the hippo pathway spatially distinct from and independent of expanded. *Developmental Cell* **40** (5), pp.478-490.

Sun, S. and Irvine, K.D., 2016. Cellular organization and cytoskeletal regulation of the Hippo signaling network. *Trends in Cell Biology* **26** (9), pp.694-704.

Suresh, S., Spatz, J., Mills, J.P., Micoulet, A., Dao, M., Lim, C.T., Beil, M. and Seufferlein, T., 2005. Connections between single-cell biomechanics and human disease states: gastrointestinal cancer and malaria. *Acta Biomaterialia* **1** (1), pp.15-30.

Svoboda, K., Schmidt, C.F., Schnapp, B.J. and Block, S.M., 1993. Direct observation of kinesin stepping by optical trapping interferometry. *Nature* **365** (6448), pp.721-727.

Sydor, A.M., Czymmek, K.J., Puchner, E.M. and Mennella, V., 2015. Super-resolution microscopy: from single molecules to supramolecular assemblies. *Trends in Cell Biology* **25** (12), pp.730-748.

Szymaniak, A.D., Mahoney, J.E., Cardoso, W.V. and Varelas, X., 2015. Crumbs3-mediated polarity directs airway epithelial cell fate through the Hippo pathway effector Yap. *Developmental Cell* **34** (3), pp.283-296.

Tan, J.L., Tien, J., Pirone, D.M., Gray, D.S., Bhadriraju, K. and Chen, C.S., 2003. Cells lying on a bed of microneedles: an approach to isolate mechanical force. *Proceedings of the National Academy of Sciences* **100** (4), pp.1484-1489.

Tapon, N., Harvey, K.F., Bell, D.W., Wahrer, D.C., Schiripo, T.A., Haber, D.A. and Hariharan, I.K., 2002. salvador Promotes both cell cycle exit and apoptosis in Drosophila and is mutated in human cancer cell lines. *Cell* **110** (4), pp.467-478.

Tepass, U. and Knust, E., 1990. Phenotypic and developmental analysis of mutations at the crumbs locus, a gene required for the development of epithelia in Drosophila melanogaster. *Roux's archives of developmental biology* **199** (4), pp.189-206.

Tepass, U., Theres, C. and Knust, E., 1990. crumbs encodes an EGF-like protein expressed on apical membranes of Drosophila epithelial cells and required for organization of epithelia. *Cell* **61** (5), pp.787-799.

Thakur, M.D., Feng, Y., Jagannathan, R., Seppa, M.J., Skeath, J.B. and Longmore, G.D., 2010. Ajuba LIM proteins are negative regulators of the Hippo signaling pathway. *Current Biology* **20** (7), pp.657-662.

Thompson, L.W., Morrison, K.D., Shirran, S.L., Groen, E.J., Gillingwater, T.H., Botting, C.H. and Sleeman, J.E., 2018. Neurochondrin interacts with the SMN protein suggesting a novel mechanism for spinal muscular atrophy pathology. *Journal of Cell Science* **131** (8), jcs211482.

Tilston-Lünel, A.M., Haley, K.E., Schlecht, N.F., Wang, Y., Chatterton, A.L., Moleirinho, S., Watson, A., Hundal, H.S., Prystowsky, M.B., Gunn-Moore, F.J. and Reynolds, P.A., 2016. Crumbs 3b promotes tight junctions in an ezrin-dependent manner in mammalian cells. *Journal of Molecular Cell Biology* **8** (5), pp.439-455.

Toomre, D. and Bewersdorf, J., 2010. A new wave of cellular imaging. *Annual Review of Cell and Developmental Biology* **26**, pp.285-314.

Tremblay, D., Chagnon-Lessard, S., Mirzaei, M., Pelling, A.E. and Godin, M., 2014. A microscale anisotropic biaxial cell stretching device for applications in mechanobiology. *Biotechnology Letters* **36** (3), pp.657-665.

Trofatter, J.A., MacCollin, M.M., Rutter, J.L., Murrell, J.R., Duyao, M.P., Parry, D.M., Eldridge, R., Kley, N., Menon, A.G., Pulaski, K. and Haase, V.H., 1993. A novel moesin-, ezrin-, radixin-like gene is a candidate for the neurofibromatosis 2 tumor suppressor. *Cell* **72** (5), pp.791-800.

Tseng, Y., Kole, T.P., Lee, J.S., Fedorov, E., Almo, S.C., Schafer, B.W. and Wirtz, D., 2005. How actin crosslinking and bundling proteins cooperate to generate an enhanced cell

mechanical response. *Biochemical and Biophysical Research Communications* **334** (1), pp.183-192.

Udan, R.S., Kango-Singh, M., Nolo, R., Tao, C. and Halder, G., 2003. Hippo promotes proliferation arrest and apoptosis in the Salvador/Warts pathway. *Nature Cell Biology* **5** (10), pp.914-920.

van de Hulst, H.C., 1957. *Light scattering by small particles*. Courier Corporation.

Varelas, X., Sakuma, R., Samavarchi-Tehrani, P., Peerani, R., Rao, B.M., Dembowy, J., Yaffe, M.B., Zandstra, P.W. and Wrana, J.L., 2008. TAZ controls Smad nucleocytoplasmic shuttling and regulates human embryonic stem-cell self-renewal. *Nature Cell Biology* **10** (7), pp.837-848.

Varelas, X., Samavarchi-Tehrani, P., Narimatsu, M., Weiss, A., Cockburn, K., Larsen, B.G., Rossant, J. and Wrana, J.L., 2010. The Crumbs complex couples cell density sensing to Hippo-dependent control of the TGF-β-SMAD pathway. *Developmental Cell* **19** (6), pp.831-844.

Verghese, S., Waghmare, I., Kwon, H., Hanes, K. and Kango-Singh, M., 2012. Scribble acts in the Drosophila fat-hippo pathway to regulate warts activity. *PloS ONE* **7** (11), e47173.

Vicidomini, G., Moneron, G., Han, K.Y., Westphal, V., Ta, H., Reuss, M., Engelhardt, J., Eggeling, C. and Hell, S.W., 2011. Sharper low-power STED nanoscopy by time gating. *Nature Methods* **8** (7), pp.571-573.

Visscher, K., Gross, S.P. and Block, S.M., 1996. Construction of multiple-beam optical traps with nanometer-resolution position sensing. *IEEE Journal of Selected Topics in Quantum Electronics* **2** (4), pp.1066-1076.

Vossen, D.L., van der Horst, A., Dogterom, M. and van Blaaderen, A., 2004. Optical tweezers and confocal microscopy for simultaneous three-dimensional manipulation and imaging in concentrated colloidal dispersions. *Review of Scientific Instruments* **75** (9), pp.2960-2970.

Wada, K.I., Itoga, K., Okano, T., Yonemura, S. and Sasaki, H., 2011. Hippo pathway regulation by cell morphology and stress fibers. *Development* **138** (18), pp.3907-3914.

Wang, L., Luo, J.Y., Li, B., Tian, X.Y., Chen, L.J., Huang, Y., Liu, J., Deng, D., Lau, C.W., Wan, S. and Ai, D., 2016. Integrin-YAP/TAZ-JNK cascade mediates atheroprotective effect of unidirectional shear flow. *Nature* **540** (7634), pp.579-582.

Wang, M.M., Tu, E., Raymond, D.E., Yang, J.M., Zhang, H., Hagen, N., Dees, B., Mercer, E.M., Forster, A.H., Kariv, I. and Marchand, P.J., 2005a. Microfluidic sorting of mammalian cells by optical force switching. *Nature Biotechnology* **23** (1), pp.83-87.

Wang, W., Huang, J. and Chen, J., 2011. Angiomotin-like proteins associate with and negatively regulate YAP1. *Journal of Biological Chemistry* **286** (6), pp.4364-4370.

Wang, W., Huang, J., Wang, X., Yuan, J., Li, X., Feng, L., Park, J.I. and Chen, J., 2012. PTPN14 is required for the density-dependent control of YAP1. *Genes & Development* **26** (17), pp.1959-1971.

Wang, W., Xiao, Z.D., Li, X., Aziz, K.E., Gan, B., Johnson, R.L. and Chen, J., 2015. AMPK modulates Hippo pathway activity to regulate energy homeostasis. *Nature Cell Biology* **17** (4), pp.490-499.

Wang, Y., Botvinick, E.L., Zhao, Y., Berns, M.W., Usami, S., Tsien, R.Y. and Chien, S., 2005b. Visualizing the mechanical activation of Src. *Nature* **434** (7036), pp.1040-1045.

Wang, Y., Yu, A. and Yu, F.X., 2017. The Hippo pathway in tissue homeostasis and regeneration. *Protein & Cell* **8** (5), pp.349-359.

Wegel, E., Göhler, A., Lagerholm, B.C., Wainman, A., Uphoff, S., Kaufmann, R. and Dobbie, I.M., 2016. Imaging cellular structures in super-resolution with SIM, STED and Localisation Microscopy: A practical comparison. *Scientific Reports* **6**, 27290.

Wei, X., Shimizu, T. and Lai, Z.C., 2007. Mob as tumor suppressor is activated by Hippo kinase for growth inhibition in Drosophila. *The EMBO Journal* **26** (7), pp.1772-1781.

Wells, C.D., Fawcett, J.P., Traweger, A., Yamanaka, Y., Goudreault, M., Elder, K., Kulkarni, S., Gish, G., Virag, C., Lim, C. and Colwill, K., 2006. A Rich1/Amot complex regulates the Cdc42 GTPase and apical-polarity proteins in epithelial cells. *Cell* **125** (3), pp.535-548.

Westphal, V., Rizzoli, S.O., Lauterbach, M.A., Kamin, D., Jahn, R. and Hell, S.W., 2008. Video-rate far-field optical nanoscopy dissects synaptic vesicle movement. *Science* **320** (5873), pp.246-249.

White, B.D., Chien, A.J. and Dawson, D.W., 2012. Dysregulation of Wnt/β-catenin signaling in gastrointestinal cancers. *Gastroenterology* **142** (2), pp.219-232.

Wiedenmann, J., Ivanchenko, S., Oswald, F., Schmitt, F., Röcker, C., Salih, A., Spindler, K.D. and Nienhaus, G.U., 2004. EosFP, a fluorescent marker protein with UV-inducible green-to-red fluorescence conversion. *Proceedings of the National Academy of Sciences* **101** (45), pp.15905-15910.

Wilhelm, B.G., Mandad, S., Truckenbrodt, S., Kröhnert, K., Schäfer, C., Rammner, B., Koo, S.J., Claßen, G.A., Krauss, M., Haucke, V. and Urlaub, H., 2014. Composition of isolated synaptic boutons reveals the amounts of vesicle trafficking proteins. *Science* **344** (6187), pp.1023-1028.

Willecke, M., Hamaratoglu, F., Kango-Singh, M., Udan, R., Chen, C.L., Tao, C., Zhang, X. and Halder, G., 2006. The fat cadherin acts through the hippo tumor-suppressor pathway to regulate tissue size. *Current Biology* **16** (21), pp.2090-2100.

Willig, K.I., Harke, B., Medda, R. and Hell, S.W., 2007. STED microscopy with continuous wave beams. *Nature Methods* **4** (11), p.915-918.

Wilson, T., 2011. Resolution and optical sectioning in the confocal microscope. *Journal of Microscopy* **244** (2), pp.113-121.

Wu, H., Wei, L., Fan, F., Ji, S., Zhang, S., Geng, J., Hong, L., Fan, X., Chen, Q., Tian, J. and Jiang, M., 2015. Integration of Hippo signalling and the unfolded protein response to restrain liver overgrowth and tumorigenesis. *Nature Communications* **6**, 6239.

Wu, S., Huang, J., Dong, J. and Pan, D., 2003. hippo encodes a Ste-20 family protein kinase that restricts cell proliferation and promotes apoptosis in conjunction with salvador and warts. *Cell* **114** (4), pp.445-456.

Wu, S., Liu, Y., Zheng, Y., Dong, J. and Pan, D., 2008. The TEAD/TEF family protein Scalloped mediates transcriptional output of the Hippo growth-regulatory pathway. *Developmental Cell* **14** (3), pp.388-398.

Xiao, L., Chen, Y., Ji, M. and Dong, J., 2011. KIBRA regulates the Hippo signaling activity via interactions with Lats kinases. *Journal of Biological Chemistry* **286** (10), pp.7788-7796.

Xie, C., Mace, J., Dinno, M.A., Li, Y.Q., Tang, W., Newton, R.J. and Gemperline, P.J., 2005. Identification of single bacterial cells in aqueous solution using confocal laser tweezers Raman spectroscopy. *Analytical Chemistry* **77** (14), pp.4390-4397.

Xin, M., Kim, Y., Sutherland, L.B., Murakami, M., Qi, X., McAnally, J., Porrello, E.R., Mahmoud, A.I., Tan, W., Shelton, J.M. and Richardson, J.A., 2013. Hippo pathway effector Yap promotes cardiac regeneration. *Proceedings of the National Academy of Sciences* **110** (34), pp.13839-13844.

Xu, K., Zhong, G. and Zhuang, X., 2013. Actin, spectrin, and associated proteins form a periodic cytoskeletal structure in axons. *Science* **339** (6118), pp.452-456.

Xu, T., Wang, W., Zhang, S., Stewart, R.A. and Yu, W., 1995. Identifying tumor suppressors in genetic mosaics: the Drosophila lats gene encodes a putative protein kinase. *Development* **121** (4), pp.1053-1063.

Yang, C.C., Graves, H.K., Moya, I.M., Tao, C., Hamaratoglu, F., Gladden, A.B. and Halder, G., 2015. Differential regulation of the Hippo pathway by adherens junctions and apical–basal cell polarity modules. *Proceedings of the National Academy of Sciences* **112** (6), pp.1785-1790.

Yang, L., Taylor, C.M., Rakovich, Y. and McCabe, E.M., 2003. Three-dimensional imaging of microspheres with confocal and conventional polarization microscopes. *Applied Optics* **42** (28), pp.5693-5700.

Yi, C. and Kissil, J.L., 2010. Merlin in organ size control and tumorigenesis: Hippo versus EGFR? *Genes & Development* **24** (16), pp.1673-1679.

Yi, C., Troutman, S., Fera, D., Stemmer-Rachamimov, A., Avila, J.L., Christian, N., Persson, N.L., Shimono, A., Speicher, D.W., Marmorstein, R. and Holmgren, L., 2011. A tight junction-associated Merlin-angiomotin complex mediates Merlin's regulation of mitogenic signaling and tumor suppressive functions. *Cancer Cell* **19** (4), pp.527-540.

Yi, C., Shen, Z., Stemmer-Rachamimov, A., Dawany, N., Troutman, S., Showe, L.C., Liu, Q., Shimono, A., Sudol, M., Holmgren, L. and Stanger, B.Z., 2013. The p130 isoform of angiomotin is required for Yap-mediated hepatic epithelial cell proliferation and tumorigenesis. *Science Signaling* **6** (291), ra77.

Yin, F., Yu, J., Zheng, Y., Chen, Q., Zhang, N. and Pan, D., 2013. Spatial organization of Hippo signaling at the plasma membrane mediated by the tumor suppressor Merlin/NF2. *Cell* **154** (6), pp.1342-1355.

Yokoyama, T., Osada, H., Murakami, H., Tatematsu, Y., Taniguchi, T., Kondo, Y., Yatabe, Y., Hasegawa, Y., Shimokata, K., Horio, Y. and Hida, T., 2008. YAP1 is involved in

mesothelioma development and negatively regulated by Merlin through phosphorylation. *Carcinogenesis* **29** (11), pp.2139-2146.

York, A.G., Parekh, S.H., Dalle Nogare, D., Fischer, R.S., Temprine, K., Mione, M., Chitnis, A.B., Combs, C.A. and Shroff, H., 2012. Resolution doubling in live, multicellular organisms via multifocal structured illumination microscopy. *Nature Methods* **9** (7), pp.749-754.

York, A.G., Chandris, P., Dalle Nogare, D., Head, J., Wawrzusin, P., Fischer, R.S., Chitnis, A. and Shroff, H., 2013. Instant super-resolution imaging in live cells and embryos via analog image processing. *Nature Methods* **10** (11), pp.1122-1126.

Yoshigi, M., Hoffman, L.M., Jensen, C.C., Yost, H.J. and Beckerle, M.C., 2005. Mechanical force mobilizes zyxin from focal adhesions to actin filaments and regulates cytoskeletal reinforcement. *The Journal of Cell Biology* **171** (2), pp.209-215.

Yoshihama, Y., Sasaki, K., Horikoshi, Y., Suzuki, A., Ohtsuka, T., Hakuno, F., Takahashi, S.I., Ohno, S. and Chida, K., 2011. KIBRA suppresses apical exocytosis through inhibition of aPKC kinase activity in epithelial cells. *Current Biology* **21** (8), pp.705-711.

Yu, F.X., Zhao, B., Panupinthu, N., Jewell, J.L., Lian, I., Wang, L.H., Zhao, J., Yuan, H., Tumaneng, K., Li, H. and Fu, X.D., 2012. Regulation of the Hippo-YAP pathway by G-protein-coupled receptor signaling. *Cell* **150** (4), pp.780-791.

Yu, F.X. and Guan, K.L., 2013. The Hippo pathway: regulators and regulations. *Genes & Development* **27** (4), pp.355-371.

Yu, F.X., Luo, J., Mo, J.S., Liu, G., Kim, Y.C., Meng, Z., Zhao, L., Peyman, G., Ouyang, H., Jiang, W. and Zhao, J., 2014. Mutant Gq/11 promote uveal melanoma tumorigenesis by activating YAP. *Cancer Cell* **25** (6), pp.822-830.

Yu, F.X., Zhao, B. and Guan, K.L., 2015. Hippo pathway in organ size control, tissue homeostasis, and cancer. *Cell* **163** (4), pp.811-828.

Yu, J., Zheng, Y., Dong, J., Klusza, S., Deng, W.M. and Pan, D., 2010. Kibra functions as a tumor suppressor protein that regulates Hippo signaling in conjunction with Merlin and Expanded. *Developmental Cell* **18** (2), pp.288-299.

Zender, L., Spector, M.S., Xue, W., Flemming, P., Cordon-Cardo, C., Silke, J., Fan, S.T., Luk, J.M., Wigler, M., Hannon, G.J. and Mu, D., 2006. Identification and validation of oncogenes in liver cancer using an integrative oncogenomic approach. *Cell* **125** (7), pp.1253-1267.

Zhan, L., Rosenberg, A., Bergami, K.C., Yu, M., Xuan, Z., Jaffe, A.B., Allred, C. and Muthuswamy, S.K., 2008. Deregulation of scribble promotes mammary tumorigenesis and reveals a role for cell polarity in carcinoma. *Cell* **135** (5), pp.865-878.

Zhang, H. and Liu, K.K., 2008. Optical tweezers for single cells. *Journal of The Royal Society Interface* **5** (24), pp.671-690.

Zhang, H., Liu, C.Y., Zha, Z.Y., Zhao, B., Yao, J., Zhao, S., Xiong, Y., Lei, Q.Y. and Guan, K.L., 2009. TEAD transcription factors mediate the function of TAZ in cell growth and epithelial-mesenchymal transition. *Journal of Biological Chemistry* **284** (20), pp.13355-13362.

Zhang, H., Deo, M., Thompson, R.C., Uhler, M.D. and Turner, D.L., 2012. Negative regulation of Yap during neuronal differentiation. *Developmental Biology* **361** (1), pp.103-115.

Zhang, H., Li, C., Chen, H., Wei, C., Dai, F., Wu, H., Dui, W., Deng, W.M. and Jiao, R., 2015. SCF Slmb E3 ligase-mediated degradation of Expanded is inhibited by the Hippo pathway in Drosophila. *Cell Research* **25** (1), pp.93-109.

Zhang, L., Ren, F., Zhang, Q., Chen, Y., Wang, B. and Jiang, J., 2008. The TEAD/TEF family of transcription factor Scalloped mediates Hippo signaling in organ size control. *Developmental Cell* **14** (3), pp.377-387.

Zhang, N., Bai, H., David, K.K., Dong, J., Zheng, Y., Cai, J., Giovannini, M., Liu, P., Anders, R.A. and Pan, D., 2010. The Merlin/NF2 tumor suppressor functions through the YAP oncoprotein to regulate tissue homeostasis in mammals. *Developmental Cell* **19** (1), pp.27-38.

Zhao, B., Wei, X., Li, W., Udan, R.S., Yang, Q., Kim, J., Xie, J., Ikenoue, T., Yu, J., Li, L. and Zheng, P., 2007. Inactivation of YAP oncoprotein by the Hippo pathway is involved in cell contact inhibition and tissue growth control. *Genes & Development* **21** (21), pp.2747-2761.

Zhao, B., Ye, X., Yu, J., Li, L., Li, W., Li, S., Yu, J., Lin, J.D., Wang, C.Y., Chinnaiyan, A.M. and Lai, Z.C., 2008. TEAD mediates YAP-dependent gene induction and growth control. *Genes & Development* **22** (14), pp.1962-1971.

Zhao, B., Li, L., Tumaneng, K., Wang, C.Y. and Guan, K.L., 2010. A coordinated phosphorylation by Lats and CK1 regulates YAP stability through SCFβ-TRCP. *Genes & Development* **24** (1), pp.72-85.

Zhao, B., Li, L., Lu, Q., Wang, L.H., Liu, C.Y., Lei, Q. and Guan, K.L., 2011. Angiomotin is a novel Hippo pathway component that inhibits YAP oncoprotein. *Genes & Development* **25** (1), pp.51-63.

Zhao, B., Tumaneng, K. and Guan, K.L., 2011. The Hippo pathway in organ size control, tissue regeneration and stem cell self-renewal. *Nature Cell Biology* **13** (8), pp.877-883.

Zhao, B., Li, L., Wang, L., Wang, C.Y., Yu, J. and Guan, K.L., 2012. Cell detachment activates the Hippo pathway via cytoskeleton reorganization to induce anoikis. *Genes & Development* **26** (1), pp.54-68.

Zhong, M.C., Wei, X.B., Zhou, J.H., Wang, Z.Q. and Li, Y.M., 2013b. Trapping red blood cells in living animals using optical tweezers. *Nature Communications* **4**, 1768.

Zhong, W., Tian, K., Zheng, X., Li, L., Zhang, W., Wang, S. and Qin, J., 2013a. Mesenchymal stem cell and chondrocyte fates in a multishear microdevice are regulated by Yes-associated protein. *Stem Cells and Development* **22** (14), pp.2083-2093.

Zhou, J., Ha, K.S., La Porta, A., Landick, R. and Block, S.M., 2011. Applied force provides insight into transcriptional pausing and its modulation by transcription factor NusA. *Molecular Cell* **44** (4), pp.635-646.

Zhou, X., Wang, S., Wang, Z., Feng, X., Liu, P., Lv, X.B., Li, F., Yu, F.X., Sun, Y., Yuan, H. and Zhu, H., 2015. Estrogen regulates Hippo signaling via GPER in breast cancer. *The Journal of Clinical Investigation* **125** (5), pp.2123-2135.

Zhou, X., Chadarevian, J.P., Ruiz, B. and Ying, Q.L., 2017. Cytoplasmic and Nuclear TAZ Exert Distinct Functions in Regulating Primed Pluripotency. *Stem Cell Reports* **9** (3), pp.732-741.

Appendix A – Primer sequences for qPCR

Table A.1 Forward and reverse primer sequences used for qPCR

Gene (Human)	**Gene-specific primer sequence (5' to 3')**	
	Forward	**Reverse**
Willin	TGAAAACCTGCAGCTCAATG	CTCTGGCCACGAAGCTTAAC
β-actin	CAGGAAGGAAGGCTGGAAGA	GCTGTGCTATCCCTGTACGC

Appendix B – Antibody conditions

Table B.1 Primary antibody conditions for Western blotting

Antibody	Host species	Dilution	Conditions	Company
GAPDH	Mouse	1:20,000	5% BSA/TBS-T	Sigma-Aldrich
Willin	Rabbit	1:100	5% milk/TBS-T	CST
YAP	Mouse	1:300	5% milk/TBS-T	CST
TAZ	Rabbit	1:500	5% BSA/TBS-T	Sigma-Aldrich
AMOT	Rabbit	1:4000	5% BSA/TBS-T	Abcam
Vinculin	Mouse	1:500	5% milk/TBS-T	Abcam
Actin capping protein β	Rabbit	1:500	5% milk/TBS-T	Merck
H3	Rabbit	1:300	5% milk/TBS-T	Proteintech
α-tubulin	Mouse	1:750	5% milk/TBS-T	Sigma-Aldrich
β-actin	Mouse	1:10,000	5% milk/TBS-T	Abcam

Table B.2 Primary antibody conditions for immunocytochemistry

Antibody	Host species	Dilution	Conditions	Company
β-III tubulin	Rabbit	1:750	3% BSA/PBS-T	CST
TAZ	Rabbit	1:100	1% BSA/PBS-T	Sigma-Aldrich
AMOT	Rabbit	1:1000	10% goat serum/PBS-T	Abcam
Vinculin	Mouse	1:250	1% BSA/PBS-T	Merck

Table B.3 Secondary antibody conditions for Western blotting (WB) and immunocytochemistry (ICC)

Antibody	Application	Dilution	Company
Goat anti-mouse IgG HRP	WB	1:10,000	Abcam
Goat anti-rabbit IgG HRP	WB	1:10,000	Abcam
Goat anti-rabbit IgG highly cross-adsorbed Alexa Fluor 488	ICC	1:750	Thermo Fisher Scientific
Goat anti-mouse IgG - FITC	ICC	1:32	Sigma-Aldrich
Cy™5 AffiniPure donkey anti rabbit IgG	ICC	1:1000	Jackson ImmunoResearch

Appendix C – Practical use of the N-SIM

C.1 Calibration

Prior to imaging, calibration of the N-SIM is required for optimal performance.

C.1.1 Alignment of the optical fibre axis

The position of the optical fibre that provides the illumination for SIM is aligned through the objective using micrometre-accuracy positioning screws as follows:

1. A sample of fluorescent beads is used to adjust the z position of the SIM objective to form an in-focus image. This position is then homed, the sample removed, and the objective cleaned.
2. The condenser is removed from the illumination pillar, and the alignment mirror on the illumination pillar moved to the back to expose the laser alignment target.
3. The SIM grating block and objective are removed.
4. The widefield-488 optical configuration is selected on the N-SIM software.
5. Using the IC Capture 2.2 software and the fibre positioning screws, the laser beam is centred on the fibre target.
6. The SIM grating is replaced, and laser alignment repeated.
7. The SIM objective is replaced, and the laser realigned.

C.1.2 Correction ring position adjustment

The SIM objective features an adjustable correction ring that allows correction for spherical aberration due to refractive index mismatch between the coverslip and sample medium. The correction ring must be adjusted if the coverslip thickness or room temperature is changed.

The optimal position of the correction ring is determined as follows:

1. A diffuse sample of fluorescent 100nm beads with 488nm excitation adhered to a coverslip is prepared.
2. The correction ring is set to a specific position (labelled as 0.13-0.19 on the correction ring).

3. The beads are brought into the best focus by fine adjustment of the height of the SIM objective, and the signal intensity altered to be in the linear range of the camera.
4. A single bead is centred in the field of view.
5. A 3μm widefield z stack is imaged around the centre of the bead to yield the microscope PSF.
6. The correction ring is set to the next position and a new image stack acquired.
7. The above is repeated for all correction ring positions.
8. The correction ring is then adjusted to the position yielding the most symmetrical PSF.

C.1.3 Grating focus procedure

The grating focus procedure aligns the focal plane of the SIM grating with the focal plane of the microscope by adjusting the position of the SIM grating block:

1. Following adjustment of the correction ring position, the beads are brought into the best focus.
2. The 'Correction Ring Navi' Wizard is executed to initiate a 3D-SIM z-stack image around the focal plane of the beads.
3. A single bead in the image stack is selected, and the z profile of the bead automatically determined to establish the position of the image plane.
4. The SIM grating is then moved by the microscope piezo to match the image plane.

C.2 Image reconstruction

Initial images acquired with the N-SIM are raw and require reconstruction for removal of the grating. Figure C.1 shows 6 of the 15 raw image tiles obtained prior to reconstruction. The reconstruction algorithm includes three parameters that can be modified by the user: Illumination Modulation Contrast, High Resolution Noise Suppression and Out-of-focus Blur Suppression. The microscope illumination contrast is less than 100% due to aberrations, scattering and absorption, and is set by the user. High resolution noise is enhanced by the reconstruction process, and thus the reconstruction algorithm includes an apodization filter for noise reduction. The out-of-focus blur suppression is a result of the optical sectioning effect of 3D-SIM that removes information outside from the focal plane of the sample. Figure C.2

shows thumbnail options for image reconstruction, with the Illumination Modulation Contrast set as 0.5.

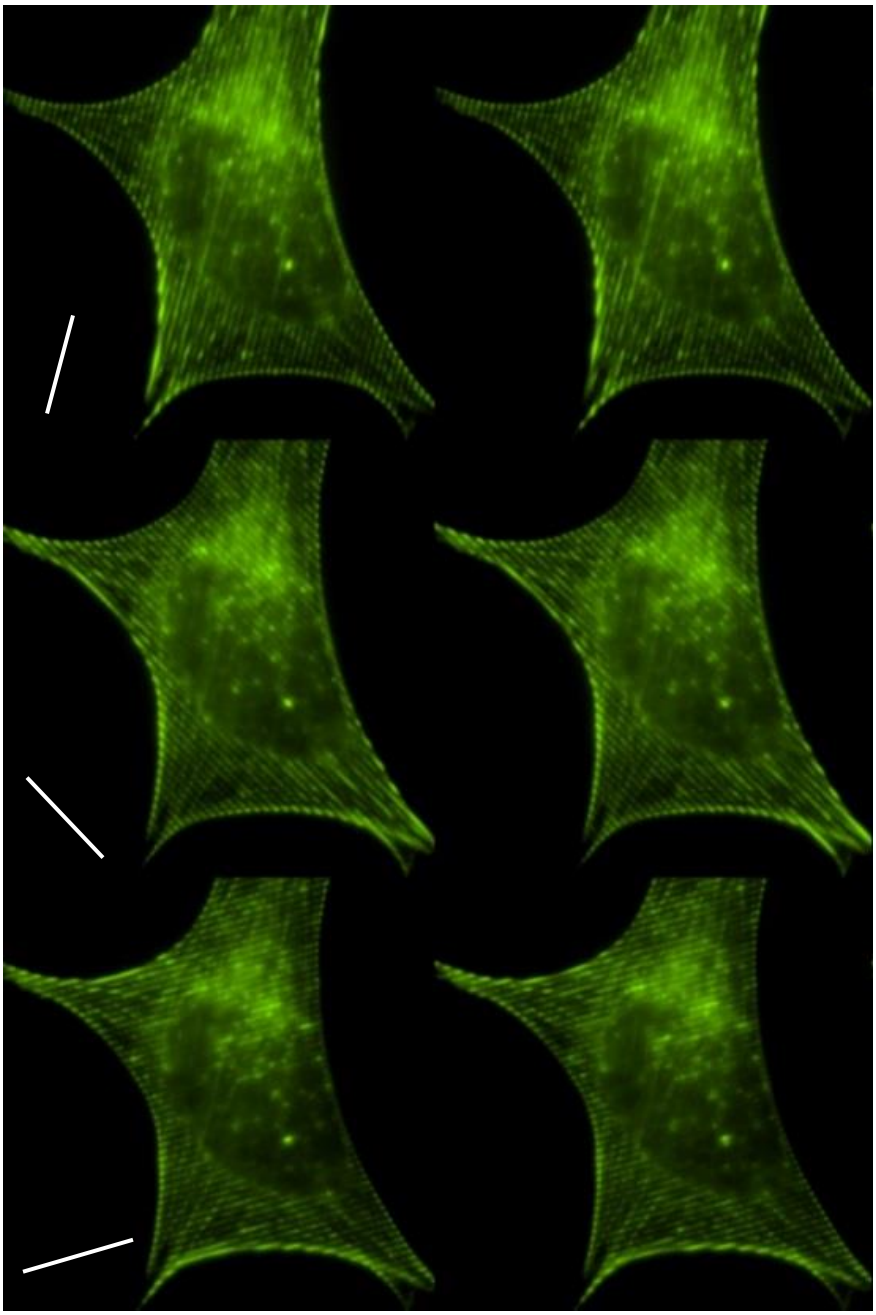

Figure C.1 Raw 3D-SIM images of actin in an SH-SY5Y cell. 6 out of 15 raw image planes are shown. The change in grating angle (denoted by white lines) is shown top to bottom, and the shift in grating phase, left to right.

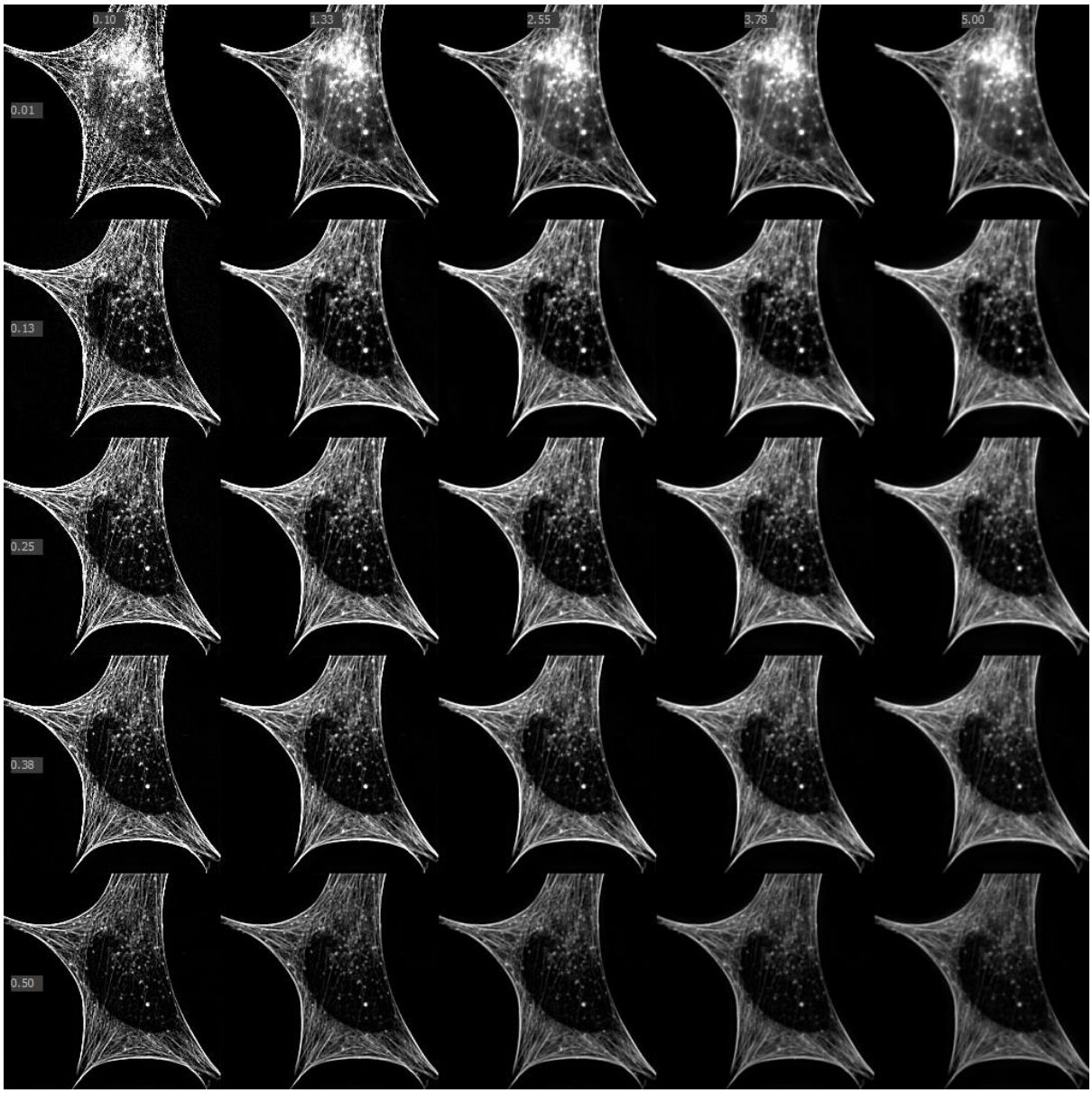

Figure C.2 Thumbnail options for image reconstruction. Left to right: increasing High Resolution Noise Suppression leading to a reduction in high frequency information. Top to bottom: increasing Out-of-focus Blur Suppression leading to a reduction in out-of-focus information.

C.3 Image registration

Chromatic aberration occurs due to the focusing of different wavelengths of light at slightly different positions in the focal plane by the objective lens. To correct for this aberration, image registration is required for 2D images. Image registration is carried out using fluorescent 100nm TetraSpeck beads that absorb and emit several different wavelengths of light. Figure

C.3 shows 3D-SIM images of these beads before and after image registration. The registrations can then be applied to other reconstructed images.

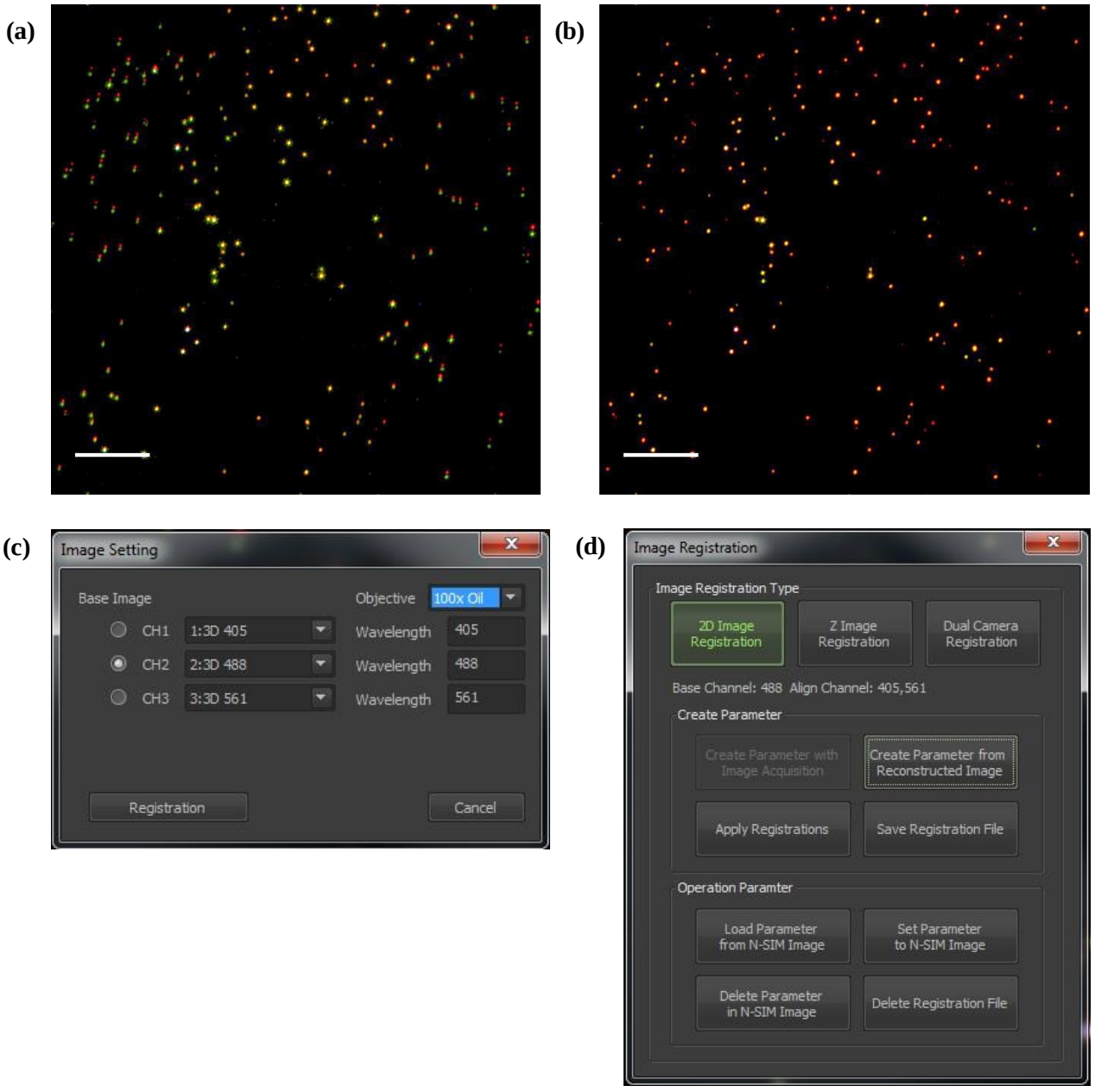

Figure C.3 2D image registration using TetraSpeck beads. **(a)** 3D-SIM image of 100nm TetraSpeck beads pre-registration. **(b)** Image of (a) post-registration. **(c)** Image registration options. **(d)** Application of image registration to 3D-SIM reconstructed images. Scale bar, 5μm.

Appendix D – Production of YAP-GFP cell lines for optical stretching

D.1 Cell line production

ShScr and shWillin SH-SY5Y cells were transfected by nucleofection with a YAP-GFP DNA plasmid (Addgene). Stably fluorescing cells were selected for as described in Chapter 4. Representative images of live shScr-YAP-GFP and shWillin-YAP-GFP are shown in Figure D.1. YAP-GFP appeared largely cytoplasmic in both cell lines.

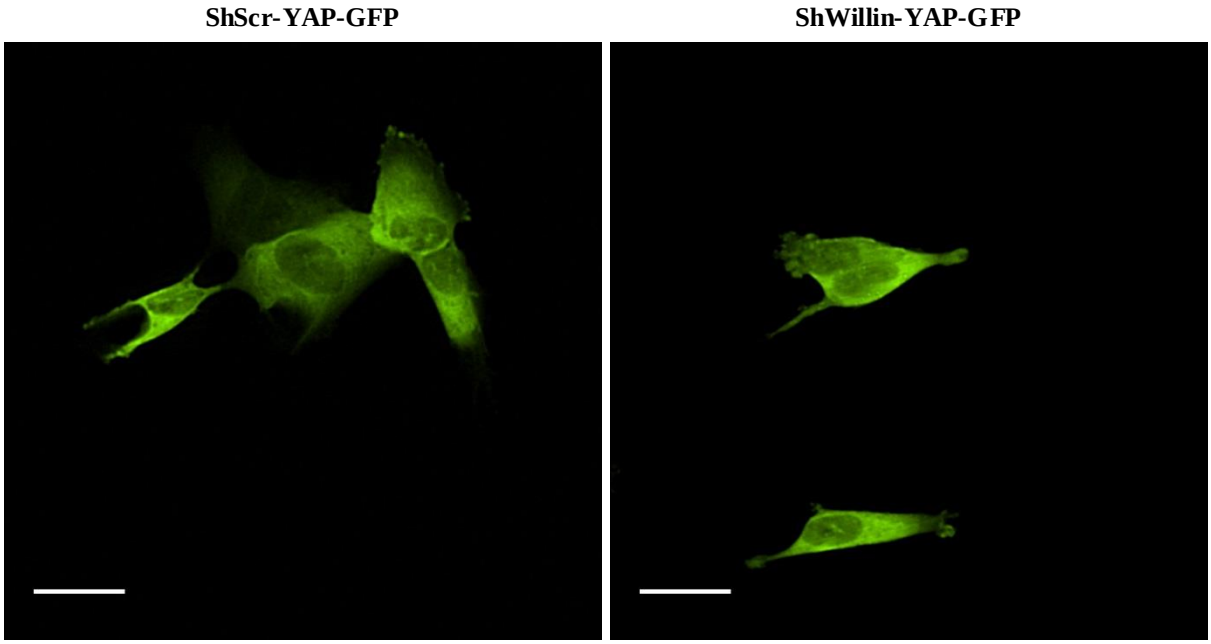

Figure D.1 Live shScr-YAP-GFP and shWillin-YAP-GFP cells imaged under 20x magnification. Scale bar, 25μm; exposure time 287ms.

D.2 Validation of Willin expression

To confirm that Willin expression was unchanged after transfection of shScr and shWillin cells with YAP-GFP, levels of Willin protein in shScr-YAP-GFP and shWillin-YAP-GFP cell lysates were compared to those of shScr and shWillin cell lines by Western blot (Figure D.2). Willin expression levels in shScr and shScr-YAP-GFP cells were comparable, with shScr-YAP-GFP expression levels 92±12% that of shScr cells ($p=0.36$). However, average Willin expression in shWillin-YAP-GFP cells was over 5-fold that in shWillin cells ($p<0.05$)

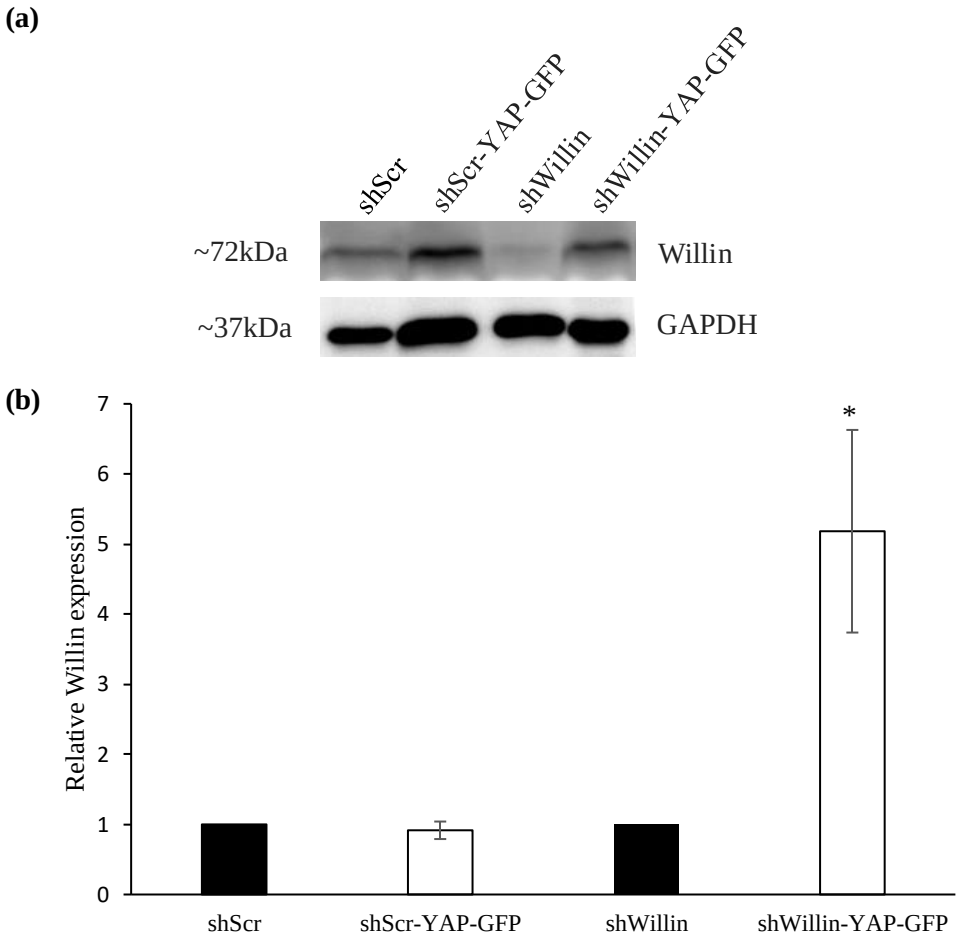

Figure D.2 Relative Willin expression in unmodified and YAP-GFP SH-SY5Y cell lines. **(a)** Representative Western blot Willin protein bands of shScr, shScr-YAP-GFP, shWillin and shWillin-YAP-GFP lysate samples. GAPDH served as a loading control. **(b)** Quantification of Willin expression in shScr, shScr-YAP-GFP, shWillin and shWillin-YAP-GFP cell lines. Willin expression in shSCr-YAP-GFP cells was measured realtive to that of shScr cells, and in shWillin-YAP-GFP cels, relative to that of shWillin cells (n = 3 experimental repeats, error bars indicate standard deviation, * $p<0.05$ as calculated using the two-tailed Student's t-test for shWillin-YAP-GFP vs. shWillin).

Due to the increase in Willin expression after transfection of YAP-GFP into shWillin cells, the YAP-GFP cell lines were deemed unsuitable as a model for tracking YAP in cells expressing altered levels of Willin. This increase in Willin expression may have been due to increased transcription of Willin mRNA owing to alteration of the Hippo pathway by expression of YAP-GFP. Expression of Hippo pathway component CRB3, for example, has been shown to upregulate transcription of Willin mRNA (Mao *et al*. 2017). ShScr- and shWillin-Lifeact-RFP cells were instead used as fluorescent cell lines expressing different levels of Willin for trapping.

Appendix E – Publications

Broadhead, M. J., Bonthron, C., Arcinas, L. V., Bez, S., Zhu, F., Goff, F., Nylk, J., Dholakia, K., Gunn-Moore, F., Grant, S. G., 2018. High-resolution synaptic mapping of the spinal cord reveals regional, developmental and astrocyte-dependent diversity. *eLife*, under review

Tilston-Lunel, A., Rabhi, N., Dey, M., Goff, F., Molerinho, S., Yu, W., Borger, E., Spires-Jones, T. L., Dholakia, K., Stewart, A., Gunn-Moore, F. Expression of the upstream component of the Hippo signalling pathway, Willin/FRMD6, influences mammalian neuronal differentiation. *In draft*